Department of Electrical and Information Engineering

INDUSTRY 4.0

Ph.D. Program

SSD: ING-IND/16-TECHNOLOGIES AND MANUFACTURING SYSTEMS

Final Dissertation

Additive Manufacturing for Electrical Actuation Systems and Sensing

---

by:
Antonio Pavone

<u>Supervisors:</u>

Prof. Gianluca Percoco

Prof. Luigi Tricarico

Coordinator of Ph.D Program:
Prof. Ciminelli Caterina

Course n°37, 01/11/2021-31/10/2024

LIBERATORIA PER L'ARCHIVIAZIONE DELLA TESI DI DOTTORATO

Al Magnifico Rettore
del Politecnico di Bari

Il/la sottoscritto/a_____ANTONIO PAVONE_____ nato/a a ____CONVERSANO_____ il___06/05/1997_____

residente a __RUTIGLIANO___ in via_____Giuseppe Divittorio 8___email__ antonio.pavone@poliba.it ,
pavoneantonio1997@gmail.com _____

iscritto al 3° anno di Corso di Dottorato di Ricerca in _____INDUSTRIA 4.0_____ ciclo__XXXVII__

ed essendo stato ammesso a sostenere l'esame finale con la prevista discussione della tesi dal titolo:

_____Electrical actuation systems and sensing_____

DICHIARA

1) di essere consapevole che, ai sensi del D.P.R. n. 445 del 28.12.2000, le dichiarazioni mendaci, la falsità negli atti e l'uso di atti falsi sono puniti ai sensi del codice penale e delle Leggi speciali in materia, e che nel caso ricorressero dette ipotesi, decade fin dall'inizio e senza necessità di nessuna formalità dai benefici conseguenti al provvedimento emanato sulla base di tali dichiarazioni;

2) di essere iscritto al Corso di Dottorato di ricerca _____IDUSTRIA 4.0_____ciclo_XXXVII__, corso attivato ai sensi del *"Regolamento dei Corsi di Dottorato di ricerca del Politecnico di Bari"*, emanato con D.R. n.286 del 01.07.2013;

3) di essere pienamente a conoscenza delle disposizioni contenute nel predetto Regolamento in merito alla procedura di deposito, pubblicazione e autoarchiviazione della tesi di dottorato nell'Archivio Istituzionale ad accesso aperto alla letteratura scientifica;

4) di essere consapevole che attraverso l'autoarchiviazione delle tesi nell'Archivio Istituzionale ad accesso aperto alla letteratura scientifica del Politecnico di Bari (IRIS-POLIBA), l'Ateneo archivierà e renderà consultabile in rete (nel rispetto della Policy di Ateneo di cui al D.R. 642 del 13.11.2015) il testo completo della tesi di dottorato, fatta salva la possibilità di sottoscrizione di apposite licenze per le relative condizioni di utilizzo (di cui al sito http://www.creativecommons.it/Licenze), e fatte salve, altresì, le eventuali esigenze di "embargo", legate a strette considerazioni sulla tutelabilità e sfruttamento industriale/commerciale dei contenuti della tesi, da rappresentarsi mediante compilazione e sottoscrizione del modulo in calce (Richiesta di embargo);

5) che la tesi da depositare in IRIS-POLIBA, in formato digitale (PDF/A) sarà del tutto identica a quelle **consegnate**/inviate/da inviarsi ai componenti della commissione per l'esame finale e a qualsiasi altra copia depositata presso gli Uffici del Politecnico di Bari in forma cartacea o digitale, ovvero a quella da discutere in sede di esame finale, a quella da depositare, a cura dell'Ateneo, presso le Biblioteche Nazionali Centrali di Roma e Firenze e presso tutti gli Uffici competenti per legge al momento del deposito stesso, e che di conseguenza va esclusa qualsiasi responsabilità del Politecnico di Bari per quanto riguarda eventuali errori, imprecisioni o omissioni nei contenuti della tesi;

6) che il contenuto e l'organizzazione della tesi è opera originale realizzata dal sottoscritto e non compromette in alcun modo i diritti di terzi, ivi compresi quelli relativi alla sicurezza dei dati personali; che pertanto il Politecnico di Bari ed i suoi funzionari sono in ogni caso esenti da responsabilità di qualsivoglia natura: civile, amministrativa e penale e saranno dal sottoscritto tenuti indenni da qualsiasi richiesta o rivendicazione da parte di terzi;

7) che il contenuto della tesi non infrange in alcun modo il diritto d'Autore né gli obblighi connessi alla salvaguardia di diritti morali od economici di altri autori o di altri aventi diritto, sia per testi, immagini, foto, tabelle, o altre parti di cui la tesi è composta.
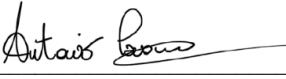
Luogo e data _____18/12/2024_____   Firma _____

Il/La sottoscritto, con l'autoarchiviazione della propria tesi di dottorato nell'Archivio Istituzionale ad accesso aperto del Politecnico di Bari (POLIBA-IRIS), pur mantenendo su di essa tutti i diritti d'autore, morali ed economici, ai sensi della normativa vigente (Legge 633/1941 e ss.mm.ii.),
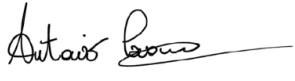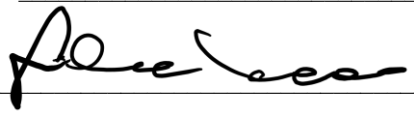
CONCEDE

- al Politecnico di Bari il permesso di trasferire l'opera su qualsiasi supporto e di convertirla in qualsiasi formato al fine di una corretta conservazione nel tempo. Il Politecnico di Bari garantisce che non verrà effettuata alcuna modifica al contenuto e alla struttura dell'opera.
- al Politecnico di Bari la possibilità di riprodurre l'opera in più di una copia per fini di sicurezza, back-up e conservazione.

Luogo e data ____18/12/2024_____   Firma _____

Luogo e data ____18/12/2024_____   Firma Dottorando _____

Firma Relatore _____

Department of Electrical and Information Engineering

INDUSTRY 4.0

Ph.D. Program

SSD: ING-IND/16-TECHNOLOGIES AND MANUFACTURING SYSTEMS

Final Dissertation

Additive Manufacturing for Electrical Actuation Systems and Sensing

by:
Antonio Pavone

Referees   Supervisors:

Prof. Yonas Tadesse   Prof. Gianluca Percoco

Prof.   Ali Zolfagharian   Prof. Luigi Tricarico

Coordinator of Ph.D Program:
Prof. Ciminelli Caterina

Course n°37, 01/11/2021-31/10/2024

Preface

The work shown in the present PhD thesis has been performed at the "Interdisciplinary Additive Manufacturing (IAM) Lab" of the Polytechnic University of Bari, Italy (32 months) and at the "BruBotics - Brussels Human Robotics Research Center" of the Vrije Universiteit Brussel, Belgium, (4 months).

The present PhD thesis refers to the following 7 papers, in which the candidate is first author and co-author, published in international journals.

- "On the Fabrication of modular linear electromagnetic actuators with 3D printing technologies"
  A Pavone, G Stano, G Percoco – Procedia CIRP, V CIRP conference on BioManufacturing, 2022

- "One shot 3D printed soft device actuated using metal-filled channels and sensed with embedded strain gauges"
  A Pavone, G Stano, G Percoco - 3D Printing and Additive Manufacturing, 2023

- "Additive Manufacturing for Soft Electromagnetic Robots: Experimental study to reduce vibration"
  A Pavone, G Stano, G Percoco - International Symposium on Industrial Engineering and Automation, 2023

- "3D Printing of Shape Memory Polymers: Embedding Nichrome-Wires to Enhance Their Performance"
  G Stano, **A Pavone**, G Percoco - Selected Topics in Manufacturing: Emerging Trends from the Perspective of AITeM's Young Researchers, 2023

- "Manufacturing-oriented review on 3D printed lithium-ion batteries fabricated using material extrusion"
  A Maurel, **A Pavone**, G Stano, AC Martinez, E MacDonald, G Percoco - Virtual and Physical Prototyping, 2023

- "Electromagnetic assistance enables 3D printing of silicone-based thin-walled bioinspired soft robots"
  G Stano, A Pricci, **A Pavone**, G Percoco - Additive Manufacturing, 2024

- "Enhancing the sensitivity of 3D printed sensors via ironing and void reduction"
  G Stano, **A Pavone**, MA Jafor, K Matalgah, G Percoco, TJ Fleck - Virtual and Physical Prototyping, 2024

- "Additive Manufacturing of Diels-Alder self-healing polymers: separate heating system to enhance mechanical, healing properties and assembly-free smart structures"
  A. Pavone, S. Terryn, H. Abdolmaleki, A. C. Cornellà, G. Stano, G. Percoco, B. Vanderborght – Additive Manufacturing, 2024

Where No One Has Gone Before.
(Gene Roddenberry, Star Trek ☄)

AKNOWLEDGMENTS

TABLE OF CONTENTS

Summary

ABSTRACT

Additive Manufacturing (AM) has become a key technology for Industry 4.0 due to its cost-effectiveness, low environmental impact, automation, high-level of freedom in fabrication and customization. Particularly, Material Extrusion (MEX), a widely used AM technology, is gaining tremendous interest for the fabrication of smart structures, that can be self-actuated, self-sense, and self-heal, such as soft actuators, sensors, and stimuli-responsive devices. MEX has been employed for its high level of customization, fitting it to extrude non-conventional materials such as functional inks, conductive polymers, and silicone. MEX is ideal for applications in soft robotics, sensors, and even 3D-printed batteries, allowing for advanced integration of multiple functionalities of the printed structures.

In this PhD thesis, MEX technology was used to fabricate several smart structures, such as actuators with embedded sensors, self-healing sensors, and electro- and magnetic-driven structures: a remarkable reduction in fabrication cost, improvement of mechanical and sensing performances, were achieved through innovative fabrication approaches and custom-made 3D printing setups.

First, 3D printed actuators and soft robots with embedded sensors and metal filled channels, actuated via electrical current and magnetic field, were investigated, proving the potentiality of one-shot fabrication of ready-to-use smart structures. Mullins effect of the smart actuators was decreased studying the vibration behavior during of the bending movements: a reduction of 16% was achieved incorporating geometrical ribs in the bending area (joint). Afterwards, the joint was studied and implemented to fabricate a multi-material and multi-actuation finger actuated using: i) shape memory polymer (SMP) heated via embedded electrical Nichrome wire, and ii) tendon driven, resulting in complex movements combining both actuation methods.

To develop and fabricate innovative smart structures, several 3D printing setups and non-conventional materials were studied: a method to improve the printability of silicone (such as pure or with magnetic nano particles) was discovered, implemented a custom-made IDEX 3D printing setup able to extrude at the same time silicone and thermoplastic polymer in the same printing cycle. This setup leverages the electrical Lorentz force in the silicone extrusion head to: i) reduce the printing force (21.08%) enabling thin walled and accurate structures extrusion, and ii) fabricate self-actuated multi-material structures that can move using external stimuli (such as magnetic field). Moreover, a custom-made setup was implemented for increasing the sensitivity of 3D printed multi-material sensors employing rolling technics and studying ironing printing parameters: the latter increased the sensitivity of the 3D printed sensors of 83%, due to 50% void reduction. A new approach to fabricate self-healing smart structures was also explored: a custom-made 3D printing machine capable of extruding both filament- and ink-based self-healing materials was developed. An innovative Separate

Heating System (SHS) was implemented to better control pre-extrusion and extrusion temperatures via PID, resulting in improved mechanical, geometrical, healing (95%), and sensing performance of the 3D printed sensors.

Finally, a comprehensive review of MEX 3D printed batteries was presented, highlighting problems, challenges, and advancement in this new field. The literature review envisions the futuristic possibility of one-shot 3D print devices composed of sensors, actuators and batteries, ready to be used after their removal from the 3D printing platform.

KEYWORDS: Additive Manufacturing, Material Extrusion, Multi-Material Extrusion, Soft Robots, Smart Structures, 3D printed sensors, Bioinspired structures, Self-healing sensor, silicone Extrusion, custom-made 3D printing setups, Electromagnetic Actuation.

1. CHAPTER 1: INTRODUCTION

1.1 Introduction

In recent years, Additive Manufacturing (AM) technologies have started gaining a lot of interest in the industrial fields becoming one of the Key Enabling Technologies (KET) for Industry 4.0 (I4) [1]. As one of the manufacturing processes of the I4.0, AM or three-dimensional (3D) printing presents several features such as flexibility, automation, digitalization, cost reduction, and low environmental impact, which align with the fundamental pillars of the I4.0 [2]. In point of fact, AM offers several benefits in term of industrial "smart" manufacturing: reduction in post-processing and human interventions [3], multidisciplinary and compatibility with other technologies (production systems or internet) opening several opportunities and the challenges in the soft-robotics, sensor, energy, and medical sectors [4]–[6].

In this PhD thesis, the advancement of AM MEX technologies was explored to fabricate smart structures based on the use of electrical and magnetic actuation with embedded sensing systems.
The main idea of the following work is to overcome the classical fabrication of electrical motors and sensors provide ready-to-use 3D printed structures enabling: i) a new class of electrical and electromagnetic actuator with self-sensing capabilities, ii) 3D printed sensors able to deform and adapt to several devices, and iii) sensors self-healing.

- **Traditional actuators and motors: perspective**

The traditional electric motors are electromechanical devices able to convert electrical input energy to mechanical movements through the interaction of electric and magnetic field. Direct current (DC), alternating current (AC), and brushless motors are the main types of industrial electrical motors [7][8]. An advanced type of electrical motors, that differs from traditional ones, are the linear motors: the motion is generated not using rotational movement, but direct translational movement. The rotor and the stator are linearized along a track, makes them particularly useful in application that required precise and controlled motion [9].
Reliability, high efficiency, and time-life are the main advantages of traditional electrical actuation. However, the complexity of their manufacturing and the high production costs lead to study new and innovative fabrication approach such as the use of AM technologies. The 3D printed electric motors overcome the use of traditional rotary or linear configuration of rotor and stator, optimizing internal

geometry using conductive or magnetic composites, such as conductive filaments or magnetic inks. Moreover, the main advantages include cost reduction, high customization, and rapid prototyping (fabrication of all required part in the same printing cycle). At the state of art several 3D printed actuators based on the traditional motion-system are presented: Pavone et al. [10] developed a one-shot 3D printed modular linear motor based on electromagnetic induction and Lorentz force, with a sliding rotor powered using internal Galinstan channels. Mansour at al. [11] fabricated a 3D printed novel miniaturized dual-axis electromagnetic actuator able to manipulate objects using four degree-of-freedom structure. De Leon et al. [12] presents a simple method for creating conductive polymer for 3D select laser sintering to develop a fully 3D printed electrostatic motor fabricated without any metal components.

Table 1.1: Traditional vs 3D printed motors

	Traditional motors	**3D printed motors**
Power efficiency	High	Low
Production costs	High	Low
Materials	Permanent magnets, copper, steel	Conductive polymer, custom composites
Customization	Low	high
Lifespan	Long	Not very long

- **Traditional sensors: perspective**

The traditional industrial sensors convert detecting parameters into electrical or digital signals [13]. The most common sensor classification is based on the measured quantity, such as i) temperature, ii) pressure, iii) speed, or iv) humidity sensors, and on operating principles such as i) electrical, ii) mechanical, iii) magnetic, or iv) chemical [14][15], [16]. Among these, piezoelectric and -resistive sensors are some of the most fabricated, as they allow to detected pressure and mechanical forces [17]. Capacitive sensors also play a key role in measuring pressure and applied forces [18], [19].

While traditional sensors show notable advantages, including i) high accuracy in measuring quantities, ii) durability under extreme environmental conditions, and iii) high lifespan, sensors present several advantages. High production costs, complex manufacturing processes, and rigid design have driven research into new fabrication technologies for sensors [20]. One of these is Additive Manufacturing. Indeed, traditional sensors require numerous manufacturing steps (microfabrication, deposition, assembly, and encapsulation) to fabricate a reliable sensor: on the other hand, AM requires only a single 3D printing cycle to fabricate and encapsulate the sensor directly into the device being analyzed [21]–[23].

	Traditional sensors	3D printed sensors
Design/Customization	Low	High
Production costs	High	Low
Production steps	≥ 4	≤ 2
Materials	Wide choice, but rigidly defined	Conductive polymer, custom composites, high customization of materials
Scalability/Miniaturization	Low	high
Lifespan	Long	Long (but linked to the materials)

- **Additive Manufacturing: perspective**

According to ISO ASTM 52900 Material Extrusion (MEX) is one of the seven AM process groups seems to be most used in several I4.0 fields and is focus of the present thesis.

The MEX physical and working principle is based on the extrusion from one to more materials through a calibrated nozzle to build layer-by-layer a structure. At the state of art, is possible to distinguish three different printing approach: i) filament-extrusion, ii) ink-extrusion, and iii) a combination of both [24], [25]. The first approach named Fused Filament Fabrication (FFF) is based on the extrusion of filament-based materials (solid thermoplastic) using a heated nozzle which completely melted the material before the deposition on a (typically) hot surface (build plate). The second approach namely Direct Ink Writing (DIW) is based on the extrusion of viscous ink, such as silicone-based materials, at room-temperature. The third approach is called hybrid and is typically used for Multi-material Extrusion (M-MEX): one printing-head extrudes the filament-based material and second printing-head extrudes ink-based material [26], [27].

MEX technology is the most widely used 3D printed methods due to several advantages:

i) **Possibility to extrude functional materials**: the materials used in the MEX range from the thermoplastic such as polylactic acid (PLA) or Acrylonitrile butadiene styrene (ABS), to soft materials such as soft thermoplastic polyurethane (TPU) and silicone [28]–[30]. Recently, a new class of materials, named functional, allows several applications in MEX printing: these materials are typically polymer matrix within fillers (carbon nanotubes, graphene, magnetic or copper powders, light- and thermal-responsive elements, self-healing functionalized groups) and semi- o pure conductors such as Galinstan and silver-ink.

ii) **Easy customization of the 3D printer machines**: the flexibility in modifying the 3D printed machine based on MEX technologies enables the researchers to tailor the

equipment for specific applications, such as extrusion of different materials (silicone and thermoplastic using the same machine) [31], [32].

iii) **Use of innovative fabrication methods**: approach such as Start-and-Stop (S&S) allows to combine and insert external elements (sensors, magnets, and wirings) [33], [34] during the printing process.

As matter of facts, MEX is becoming really appealing for the fabrication of 3D printed smart structures able to respond to external stimuli, mimic biological movements, and exhibit self-sensing and self-healing capabilities [35]–[37], features typically of the soft-robots and 3D printed sensors. Smart structures embedded sensing systems within actuation systems during the same printing cycle, enhancing their functionality:

- **Actuation systems**: from an actuation standpoint, MEX printed soft and smart structures mostly based on pneumatic actuation, shape memory polymers (SMPs), shape memory alloys (SMAs), cable-driven actuation, or a combination of them have been studied [38]–[40]. Another actuation method that can bring several advantages to the soft robotic domain is the electrical actuation system, based on the use of electrical and magnetic fields, or the combination of both. The use of electrical or electromagnetic actuation has demonstrated several advantages, such as reduced activation and deactivation times (i.e., return to the original shape) compared to systems based on shape memory polymers or alloys. It has also been shown to reduce noise levels, unlike pneumatic systems, and offers significantly lower energy consumption. The portability, unlike systems that require light sources, heat, or compressed air, makes these systems highly advantageous for both every day and industrial applications (see **Fig. 1.1**) [41]–[43]. Cao et al. 3D printed magnetic actuators [44] using a soft thermoplastic material with magnetic particles to create a magnetic filament for fused deposition modelling setups. Yan et al. [45] fabricated a bionic swimming fish able of underwater operations using electromagnetic driven caudal fin. The latter embedded two soft coils (one for side) composed of silver-ink on soft polydimethylsiloxane (PDMS) substrate and a permanent magnet, obtaining a flapping angle of 4.2° at applied voltage of 8V (with 0.3 mT magnetic field. The fish's body and coils were fabricated through FFF and DIW printers, respectively.

- **Sensing systems**: MEX enables the fabrication of several type of sensors such as piezoresistive and force sensors employing filament- or ink-based conductive materials [46], [47]. Liu et al. [48] developed a custom conductive-ink (electrical conductivity of 1.75×10 6 S m−1) for the fabrication of a wearable piezoresistive pressure sensor through DIW extrusion. The sensor exhibits high sensitivity over a pressure range from 2.8 to 8.1 kPa. Kosir at al. [49] studied the problem of electromagnetic interference (EMI) protection for 3D printed sensors, developing a printing strategy to reduce the signal-noise: in a single printing process sensing element, wiring and connector are including and covers with EMI shielding. Moreover, ironing techniques are employed to reduce the voids of the electrode.
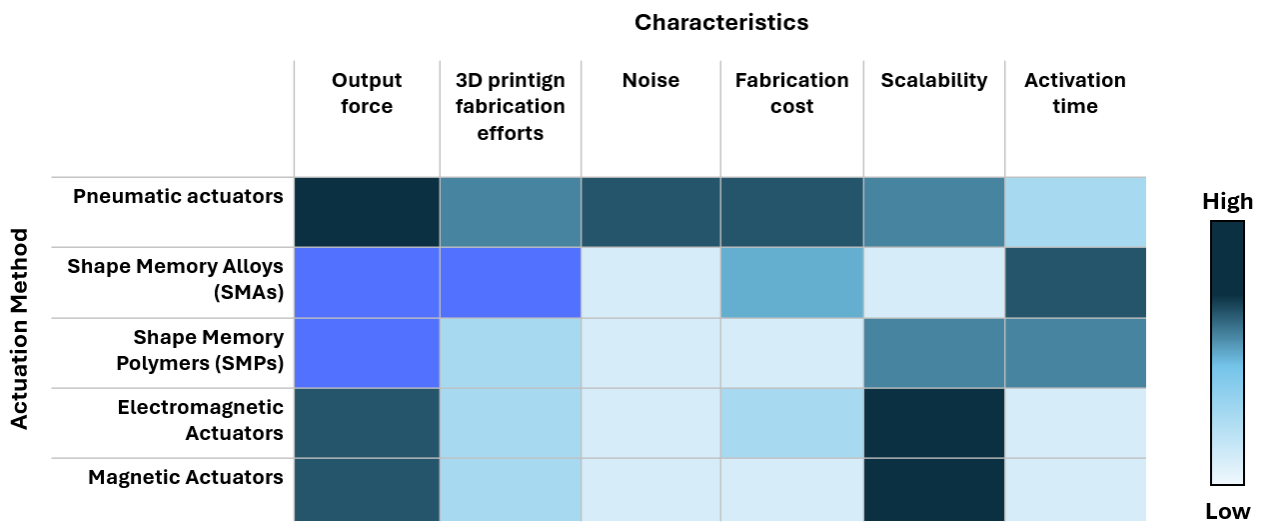
Fig. 1.1: Qualitative comparison between most relevant 3D printed actuation methods in terms of output force, 3D printing fabrication efforts, noise during function, fabrication costs, scalability and activation time.

Another feature making MEX technologies really appealing for the electrical actuation standpoint is the possibility to fabricate 3D-printed batteries [50], [51]. This enables the embedding of the batteries into soft robots and wearable devices, offering advantages in integration, customization, energy efficiency and portability of the devices.

M-MEX CUSTOM 3D PRINTER

CAD

1. Design → 2. Customization → 3. Fabrication → 4. Smart structures

1 SLICING

FILAMENT- AND INK-BASED

SENSING AND ACTUATION
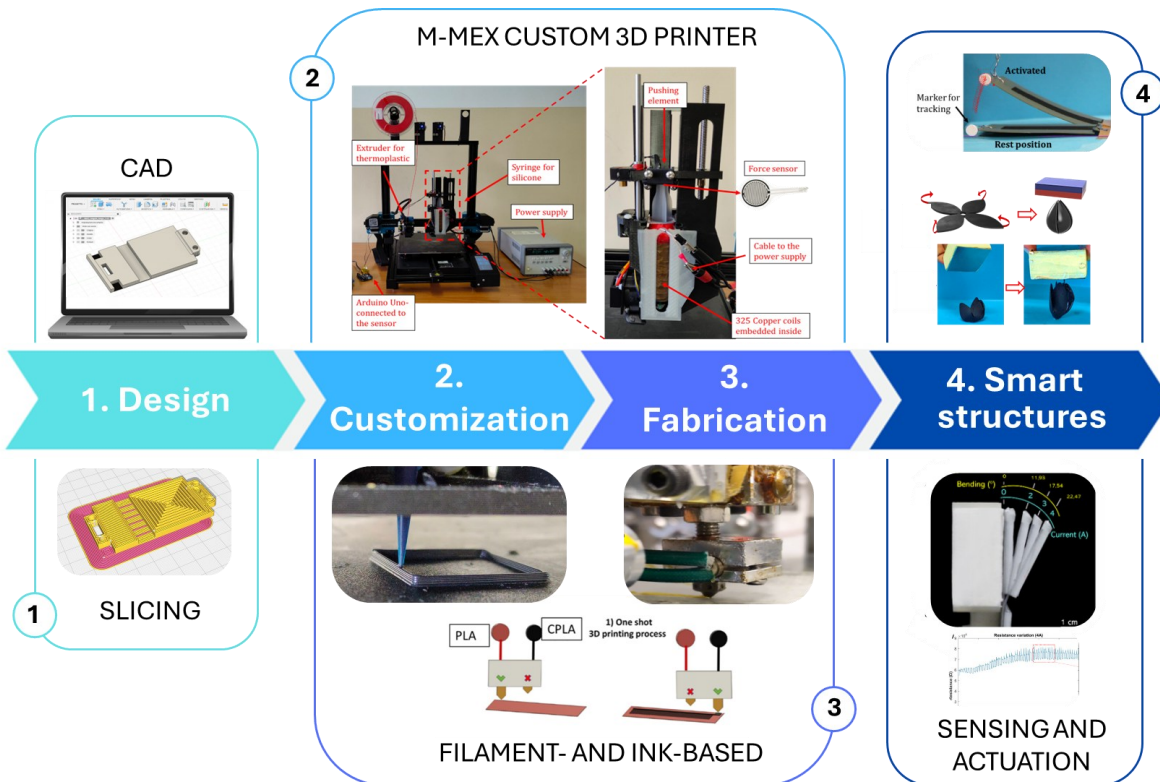
Fig. 1.2: Graphical main idea of the present PhD thesis.

1.2 Storyline of the research

During the Ph.D. research period, which culminates in the present thesis, significant progress has been made in advancing the Additive Manufacturing approaches for smart structures.

Motivated by the aspiration to create innovative solutions in soft robotics, this work has focused on demonstrating the potential of 3D printing to fabricate ready-to-use smart structures that seamlessly integrate electrical and/or magnetic actuation with real-time sensing capabilities. This thesis represents a critical step forward in transforming conceptual ideas into tangible, high-performance systems.

This research begins by presenting the state of art, focusing on recent advancement in the field of electro and electromagnetic soft actuator, analysing the limits and the potentialities of current devices and the possibility to integrate actuation systems, sensing and energy device in the same 3D printed smart structure (Chapter. 1). The research question, *"How can this electromagnetic soft device function effectively?"*, serves as the guiding focus of Chapter 2. In this chapter, multiple approaches are explored to advance the development of electrothermal shape memory polymer (SMP) actuators, electromagnetic actuators, and bio-inspired soft robots. These efforts aim to demonstrate the efficacy of electrically driven systems fabricated using Additive Manufacturing (AM) technologies. The same methodology was applied to explore new customized approaches for material extrusion-based

fabrication, aimed at developing structures based on magnetic actuation and the use of electrical systems to enhance 3D printing fabrication. The question, *"How can electric current be utilized to improve the printing of unconventional materials?"*, drives the research in Chapter 3 (e.g., investigates the use of Lorentz forces for printing magnetic silicone and thermoelectric control for self-healing materials). Moreover, the possibility to embedding sensor in the actuator structure, enhancing the sensor capabilities (sensitivity), led to thing about all-in-one structures that include energy storage system too (chapter 4).

In conclusion, the central aim of this research was to address the question: *"Why not design smart structures that embedded actuation, sensing, and energy storage systems, all integrated within a single printing cycle and ready to use when removed from the print bed?"* This question has guided the development of innovative solutions in AM, culminating in the fabrication of fully functional soft robotics and smart structures that are fabricated using unconventional materials and one-shot approach.

1.3 Scope of the thesis

The purpose of the present thesis is the advancement of Additive Manufacturing MEX technologies for the fabrication of smart structures based on the use of electrical and magnetic actuation with embedded sensing systems.

The main idea of the following work is the fabrication (using the design for additive manufacturing) of one-shot (ready-to-use) soft robotics structures ready to be activated using electric and magnetic external stimuli after remotion from the 3D printer build plate, and to provide real-time feedback thanks to the embedded sensing systems (3D printed sensors).

To achieve these goals, several points have been studied: i) multi-material MEX of actuation systems based on electrically driven, ii) multi-material MEX of sensors, iii) customization of 3D printing machine in order to fabricated smart structure based on silicone and self-healing extrusion, and iv) increasing the fabrication process and the efficiency of actuators and sensors (e.g. increase of electrical sensitivity). In **Fig. 1.2** the graphical idea of the present thesis.

1.4 Structure of the thesis

This work is organized as following:

- Chapter 2 is named *"Electro- (and) magnetic actuation"* and describes the innovative actuation systems used in soft robotics and smart structures based on Additive Manufacturing fabrication and electro-magnetic actuation.

- Chapter 3 named *"Custom-made MEX setups and fabrication approaches for processing non-conventional materials: magnetic-ink, self-healing polymers, and electrically conductive polymers"* presents the development of custom-made 3D printers modified in order to extrude non-conventional materials for innovative fabrication approaches for 3D printing smart structures and sensors.

- Chapter 4 is named *"Future trends: energy storage for MEX structures"* and describes the fabrication of supercapacitors and battery fabricated through 3D printing.

Chapter 1 and Chapter 5 are written respectively as introduction and conclusion for the thesis.

2. CHAPTER 2: ELECTRO- (AND) MAGNETIC ACTUATION

2.1 Introduction of the chapter

In recent years, additive manufacturing (AM) technologies have been largely exploited for the fabrication of smart structures (soft robot and sensing) [52], [53]: several advantages such as reduction in assembly tasks, fabrication cost, and time can be achieved.

Particularly, Fused Filament Fabrication (FFF) is one of the most widespread technologies within Material Extrusion (MEX) family, for the fabrication of the (soft) actuators [40], [54], [55]. FFF is based on the extrusion of thermoplastic material through one or more heated nozzles. This method enabling the fabrication of multi-material actuators with embedded sensor in conjunction with i) the extrusion of conductive material [46] and ii) one-shot fabrication [56], making FFF very appealing for the fabrication of 3D printing soft actuators.

From an actuation standpoint, three-dimensional (3D) printed soft actuators mostly based on pneumatic actuation [57], [58], light and radiation actuation [59], shape memory polymers (SMPs) [60], shape memory alloys (SMAs) [61], cable-driven actuation [62], or a combination of them have been studied [63]. Another actuation method that can bring several advantages to the soft robotic domain and which is innovative and challenging for the fabrication of smart structures is the electrical actuation [64]. It is possible consider two possible family of electrical actuation systems: i) pure electric [65] and ii) electromagnetic (EM) actuation systems [44], [66] .

An example of actuation systems is the electrothermal SMP, activated used embedded electrical wires [67], [68]. The SMPs are a very promising class of actuators because of i) lower cost, ii) possibility to enable greater recovery deformation, iii) biodegradability, and iv) possibility to respond to more multiple stimuli [69] (even though one of the most studied domains is the temperature stimulus [70]). The SMP working mechanism is here described: its initial shape can be modified to a temporary shape, deforming the SMP at a fixed temperature above the glass transaction (Tg) temperature of the materials, named switching temperature (Ts). Cooling down the SMP, the temporary shape will be fixed: if the polymer is heated again above the Tg temperature, the SMP recovers its initial shape [71], [72]. The phenomenon of shape memory effect (SME) is a complex transformation observed in two types of SMP [73], [74]: (i) traditional one-way SMP, which transition is from original shape to a deformed shape and vice versa, and (ii) two-way [75], [76] or more [77] SMP, which can remember the original shape and switch between two or more distinct shape, typically between a low-

temperature and high-temperature shapes. On one hand, SMPs do not required particular and complicated system to work such as cables, motors or pneumatic compressors, but on the other hand their activation is possible through external heat source [78] (often provided via oven and warm water) resulting in a lack of feasibility for real-life scenarios. A new challenge in soft robotics is the fabrication of SMP smart structures fabricated with embedded resistive wires, to improve SMPs usage [31], [79]. The low Tg (50– 65 °C) of Polylactic Acid (PLA) makes it the most used thermoplastic polymers to fabricate SMPs [71] in Fused Filament Fabrication (FFF) technology. In general, FFF printing parameters (infill and pattern) that affect recovery time and recovery rate of SMP structures has been largely studied [73], [80], [81] . Cesarano et al. [82] analysed the SMP response at different time–temperature combinations and programming parameters. Ehrmann et al. [83] performed mechanical destructive tests and investigate the recovery rate of PLA sample changing infill patterns and percentage. Roudbarian et al. [84] improved the shape memory effect (SME) of PLA by following multi-layered and multi-material approaches. Yang et al. [85] improved physical properties of 3D-printed SMP parts by tuning appropriate process parameters. Moreover, a new way to exploit the SME in FFF structures is the fabrication of structures composed of SMP parts and links made of non-shape memory material actuated with tendon driven [31]. A hybrid actuation system brings several benefits such as i) increased bending performance, ii) use of two materials with different stiffness degrees in the same printing cycle, and iii) complex movements impossible to achieve using only one actuation system [86], [87].

On the other hand, the innovative EM actuation system can be achieved several advantages, compared to their counterparts such as: 1) portability (only batteries need to be involved), 2) noise reduction (making them really appealing for wearable application), 3) fast response (SMPs require some minutes), and 4) no need of cooling systems (SMAs and SMPs require cooling systems to speed up the actuation cycle) [88]. The EM actuation system is generally based on conductive coils composed by copper, gallium, or Galinstan (semiconductive alloy of gallium, indium, and tin). When activated by means flow of electrical current through these coils, the Lorentz force makes the whole actuator move. The Lorentz force can be described by the following equation (1):

$$F = I(L \times B) \tag{1}$$

where F is the Lorentz force, I is the contribution of the current supplied into the coils, L is the vector length of the conductor (coils), and B is the magnetic field generating by the external permanent magnet. Thanks to this latter, placed near the actuator, is possible to control the EM actuator for bending, propelling, grasping and jumping movements. Several examples of soft EM devices can be

found in scientific literature: Do et al. [89], fabricated small-scale EM actuators made up of silicone, eutectic gallium indium droplets, and magnetic powders obtaining a displacement of 1mm and a bending angle of 38°. The proposed device can be employed in the soft robotic field for the fabrication of walking robots or small-scale grippers. Kohls et al [90] developed a bio-inspired EM actuator mimicking Xenia soft coral: the EM soft robot is capable of soft compliant motions because of its architecture: it is based on silicone structures with embedded magnets, which can be attracted or repulsed by a magnetic field generated, thanks to soft gallium coils. Mao et al [91] created a silicone EM actuator equipped with channels filled with gallium to obtain several motions: in particular, they showed that this approach can be successfully exploited for the fabrication of swimming robots, flower inspired robots, and bending structures (a bending of 76° was achieved at $3A$).

AM technologies can be employed for the fabrication of EM actuators resulting in several advantages [92], in particular, Material Extrusion (MEX) technology, well known for being the most inexpensive approach, seems to be very promising and appealing. At the state of the art, three different ways to exploit MEX technologies for the fabrication of EM actuators can be outlined. The first one, called fiber encapsulation consists of the integration of long fibers (copper wires) during the extrusion of thermoplastic materials [93]–[95]: recent progress in this technique [96]–[98] could lay the foundation for a huge exploitation of the following approach. The second method consists of the direct extrusion of a magnetic thermoplastic filament through a calibrated nozzle [99]: Cao et al [44] doped a soft thermoplastic material (shore hardness of $70\,A$) with magnetic particles ($50\%\,wt$) to create a magnetic filament having a diameter of $1.8\,mm$ processable by commercial fused deposition modelling setups. Several bio-inspired structures were additively manufactured (gripper, butterfly, and flower) and tested in conjunction with a commercial magnet. The last method found in scientific literature to exploit MEX technologies for the fabrication of EM actuators consists of the extrusion of conductive inks [45]. The direct ink writing technology is used, and the conductive inks are extruded through a calibrated nozzle over a flexible substrate (i.e., silicone) to create coils that will be activated by means of electrical current to exploit the Lorentz force.

In conclusion, MEX technologies have become popular for the possibility to create smart structures (actuation systems and sensor): the fabrication of sensor units into objects is really appealing for several reasons such as 1) reduction of manufacturing costs, 2) reduction of assembly tasks, and 3) possibility to obtain feedback from objects. Several examples of smart objects manufactured using multi-material MEX technologies can be found in scientific literature: load cell with embedded strain gauges [100], multiaxial force sensor [101], universal jamming gripper with embedded capacitive sensor [102], 3D printed accelerometer [103], and pressure sensor for prosthetic applications [104].

The main chapter is organized as follows: in section 2.2 the embedding Nichrome-Wires to enhance performance of 3D Printed Shape Memory Polymers (SMP) is studied. In 2.3 one-Shot 3D printed Soft device actuated using metal-filled channels and sensed with embedded strain gauge is analysed, and in final section 2.4 un experimental study to reduce vibration of Additive Manufacturing electromagnetic soft robots is discussed.

2.2 Electric actuation: Embedding Nichrome-Wires to enhance performance of 3D Printed Shape Memory Polymers.

In this following study, a new approach based on Star-and-go method have been used to investigated how embedded resistive thermal-conductive metal can enhance the shape property of 3D manufactured complex shape memory smart structures, thereby improving their actuation capability. A multi-material FFF approach in conjunction of start and go method have been used to fabricated structures integrating two different actuation systems in a single manufacturing cycle: SMP parts coupled to soft parts actuated through a tendon-driven system. To further enhance the performance of 3D printed SMP, additively manufactured novel method is introduced: resistive nichrome (NiCr) wires have been embedded inside the 3D printed SMP during the fabrication process (using the stop and go method), in order to make the SMA activation step easier, more feasible and faster.

The main steps was fallowed: i) the SMP stiff part geometry was studied to choose the optimal shape (five different geometrical shapes were 3D printed and tested), thereby enhancing the electrical-heating performances before the fabrication of complete complex structures, ii) the compliance of the several printed stiff structures was tested to estimate the shape fixity and recovery based on consecutive activation (5 cycles) when is applied and not a load (50 or 75 g), iii) the coupling between stiff (SMP) and soft (TPU joint) was studied varying several printing parameters, such as mech overlapping, infill percentage of the soft parts (0.25mm and 80% respectively were the optimal results) and through tensile tests in order to make the SMP-joint interface very strong, vi) finally, several complex motions were obtained when the 3D printed structures (SMP and tendon driven) were activated, resulting appealing for the fabrication of soft robots mimicking animals, and showing that such complex motions are impossible to achieved using only one actuation system.

2.2.1   Materials and methods: Shape Memory Polymers (SMPs) and Tendon Driven characterization

The main idea of the present work is the one-shot fabrication of a complex, hybrid actuated structure combining SMP and tendon driven system, in order to obtained bioinspired motions [105]. To achieve this goal, a multi-material FFF machine, namely Ultimaker 5 (Ultimaker, The Netherlands) was used. the following parts have been fabricated in the same manufacturing cycle: i) stiff parts made up with polylactic acid (PLA), with embedded NiCr wire coils (0.6 mm diameter, maximum temperature 1150 °C), ii) flexible-soft joints made up with thermoplastic polyurethane (TPU). A 0.4 mm nylon tendon and a stepper motor were used to enabling the mechanical driven actuation.

Shape Memory Polymers: Stiff Parts. Before the fabrication of the complete structure, the SMP structure was studied to choose the best shape for the fabrication of the complex finger actuator. The stiff parts were printed using the process parameters listed in **Table 2.1**. In particular, as known from scientific literature [106], low values of printing speed and layer height (lh) increas the quality of the parts: in this work, the printing speed was set at 45 and 25 mm/s respectively for PLA and TPU, and the layer height at 0.1 mm. Moreover, the 45° raster orientation was used to overcome the sinking problem of the empty part (channels to embed resistive wires), and a maximum infill percentage of 100% was used to overcome the low heat diffusivity of the polymer.

Table 2.1: Process parameters

Printing parameters	PLA (Stiff parts)	TPU (Soft parts)
Printing speed (mm/s)	45	25
Infill percentage (%)	100 - Lines	80 - Lines
Raster angle (°)	45	45
Printing temperature (°C)	210	235
Layer height (mm)	0.1	0.1

PLA is characterized by a glass transaction temperature (Tg) between 55 and 65 $°C$ (technical datasheet). Moreover, the start-and-stop (S&S) method [33] was used to embedded the NiCr wire inside the PLA parts: with a G-code modification it has been possible to pause the print, manually embed the wire and finally resume the manufacturing process to cover the NiCr wire, as shown in **Fig. 2.1**.
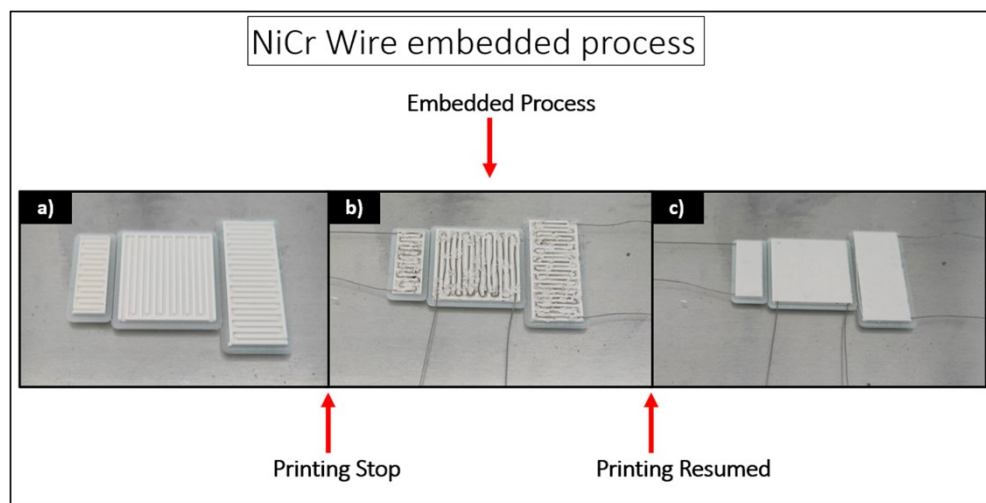
Fig. 2.1: A NiCr embedded process: a) 3D printing process stopped when printing of sample channel is finished; b) embedded NiCr resistance; c) finale sample with embedded resistance after resumed printed.

The embedding of NiCr wire during the S&S is a manual process and strongly related to the operator skills, however it took the authors an average of $2\ min$ to accomplish that. Five different rectangular-sample (R0–) SMA structures, with embedded NiCr wires, have been designed and fabricated to evaluate the best shape in terms of performance. The different SMP structures have been named R01, R02, R03, R04 and R05, respectively with $x-y$ dimensions of $45 \times 18mm, 30 \times 30mm, 28 \times 10mm, 20 \times 30\ mm, 40 \times 10\ mm$ (see **Fig. 2.2**), keeping the thickness unchanged (fixed at $1.8\ mm$).The dimensions of the five different structures have been arbitrarily selected, in order to evaluate i) the repeatability of the embedding process into different geometries, and ii) how the dimensions of the structures affect their performance. Every version of the SMP-stiff part has been monolithically fabricated in a single step printing cycle, resulting time and cost savings: for example, for R01 and R02 the time and cost are respectively 10 and 13 min, and 0.076 and 0.098 $euro$. It is worth mentioning that the spacing among the channel that housed the NiCr wire, has been set equal to 0.6 mm: this value was experimentally found as the minimum value ensuring a good 3D printing quality.
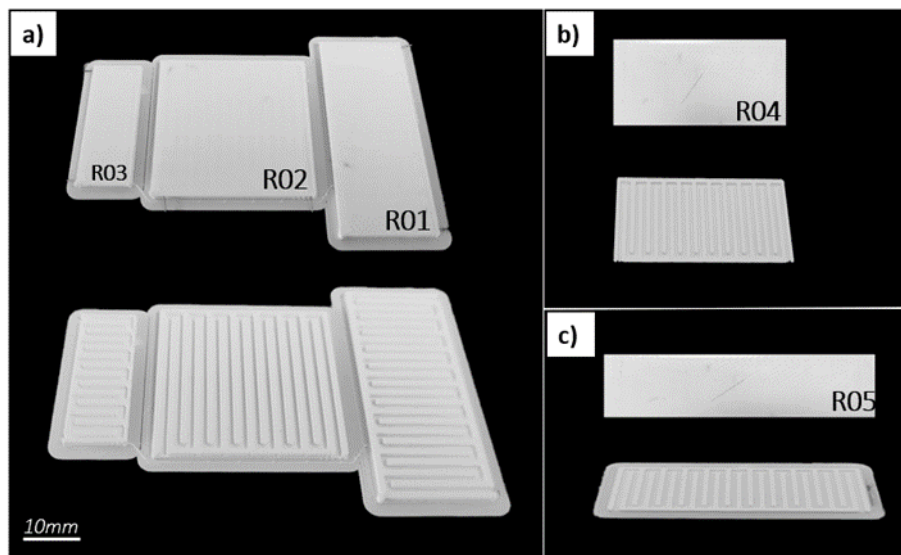
Fig. 2.2: Printed R-sample finished and internal channels.

2.2.2 SMP-Stiff Part Compliance

For the characterization of the SMP-stiff part, the relationship between PLA compliance and local heating was studied. An ad hoc set-up was used to evaluate the compliance factor: a) a power supply to heat up the embedded NiCr resistance, b) a thermal imaging camera to evaluate the temperature of the NiCr wire, c) weight of 50 and 75 g connected to the sample, and d) a digital camera to take pictures at each increment of temperature to calculate the displacement. The temperature of NiCr wire

was incremented, starting from room temperature $Troom$, to Tg and the compliance was calculated at $50, 55, 60$ and $65\ °C$: a continuous current of $1.65A$ (tension of $6.30\ V$) was applied. Each R-sample was tested three times, calculating the standard deviation of the compliance factor for the different temperatures setting (see **Table 2.2**). Moreover, each sample was activated again to test the recovery shape, according to the SME. The compliance factor $C_m \left[\frac{mm}{N}\right]$ was calculated in according to [31], as follows:

$$C_m = \frac{1}{S} \tag{2.1}$$

where S is the stiffness of the part, calculated as the ration of the applied force $F[N]$ and the d is the sample displacement $[mm]$:

$$S = \frac{F}{d} \tag{2.2}$$

Table 3.2: PLA stiff R-samples: compliance factor Cm/Cm0 versus temperature and load

$T\ (°C)$	$\Delta C_m/C_{m0}$ mean (Std. dev)					$Load\ (g)$
	R01	**R02**	**R03**	**R04**	**R05**	
50	2.97 (<0.001)	0.45 (<0.001)	0.43 (<0.001)	1.01 (<0.001)	4.92 (<0.001)	50
	2.31 (0.003)	1.39 (<0.001)	0.60 (0.05)	0.12 (<0.001)	2.68 (<0.001)	75
55	4.02 (<0.001)	1.89 (<0.001)	1.48 (<0.001)	1.22 (0.09)	5.67 (<0.001)	50
	2.92 (<0.001)	2.09 (0.02)	1.36 (0.05)	1.29 (0.003)	4.40 (<0.001)	75
60	5.89 (0.02)	4.04 (0.02)	1.67 (0.002)	2.63 (0.15)	8.23 (0.05)	50
	3.73 (<0.001)	3.43 (0.01)	2.40 (0.002)	3.17 (<0.001)	5.19 (<0.001)	75
65	7.75 (0.12)	6.81 (0.03)	2.24 (0.17)	3.32 (0.02)	9.04 (0.16)	50
	5.12 (0.002)	5.66 (0.02)	4.07 (0.01)	3.98 (0.03)	6.02 (0.06)	75

Starting from $Troom$, associated to C_{mO}, for each tested temperature the absolute compliance (ΔC_m) was calculated. The sample R05 resulting the best in terms of compliance change, showing the maximum absolute compliance factor of 6.02 when $75g$ of load is applied, at $65\ °C$. In **Fig. 2.3** the absolute compliance for all the samples is shown. Additionally, the testing phase has been used to obtain the behavior of the SMP samples at the fist activation (shape transforming phase) and at the second activation (shape recovery phase): such as the compliance testing, two loads (50 and 75 g), generating two forces respectively $F1 = 0.49N$ and $F2 = 0.74\ N$, were used.
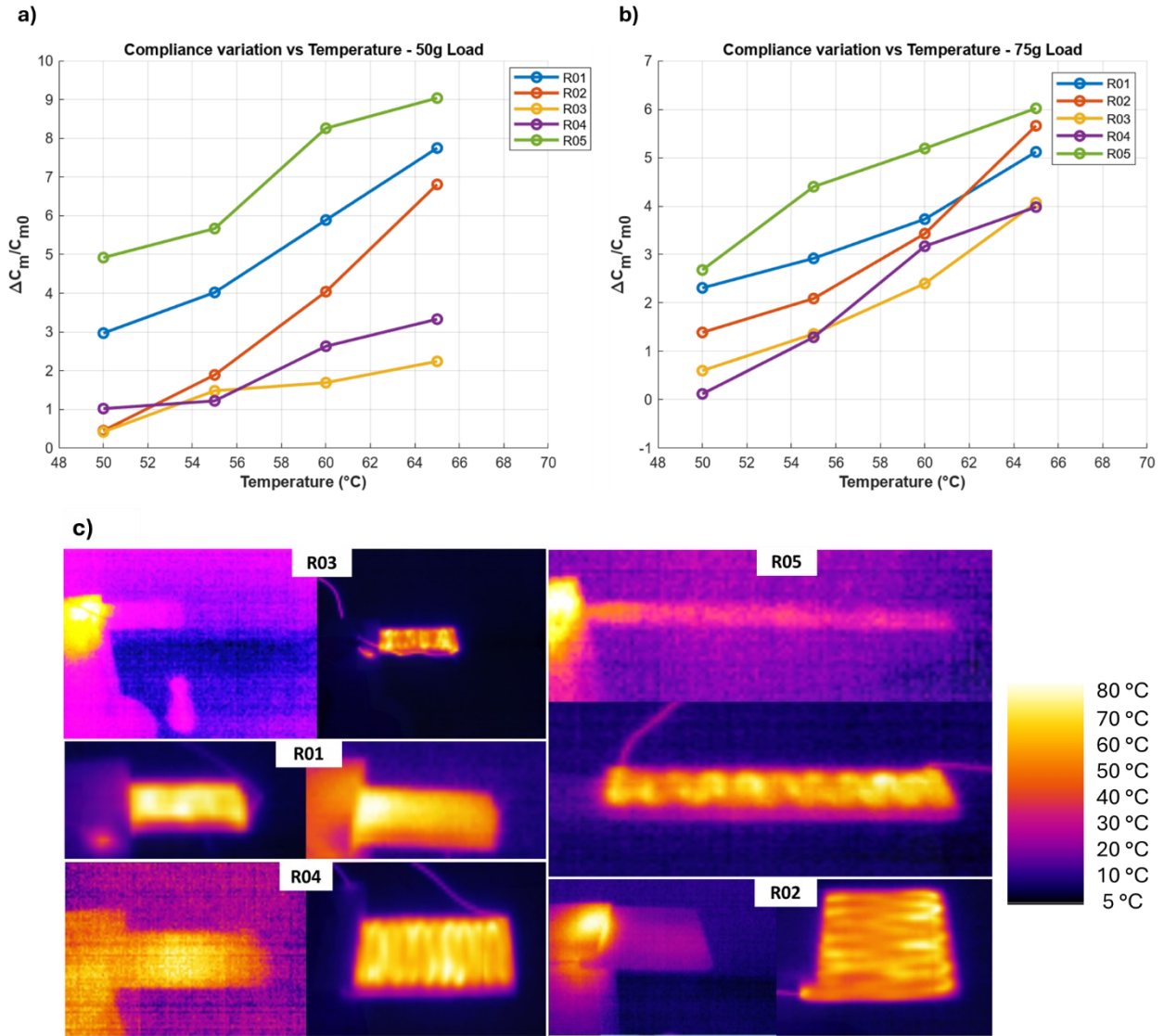
Fig. 2.3: Tested samples: a) compliance variation with 50 g load application during temperature; b) compliance using 75 g load; c) thermal camera analysis used to evaluate the heating propagation inside R0- samples.

For each rectangular sample, the internal NiCr resistance was heated from $Troom$ to $T65\,°C$ switching respectively from the rest position (initial) to final shape position, for each load. After that, each sample (after cooling phase), was re-heated from $Troom$ to $T65\,°C$, respectively from shape position to recovery position (see **Fig. 2.4**). For the above-mentioned temperature values ($50, 55, 60,$ and $65\,°C$) the displacement d was measured for each sample, during each test (see **Table 2.2**). In **Fig. 2.3 c** is showing the heating propagation inside the R0- samples.

A current of $1.65A$ was used. Moreover, the shaping and recovery time were measured to evaluate the actuation time for each sample, as shown in **Fig. 2.6**.

As shown in **Fig. 2.4 e)**, the R05 sample confirms the compliance factor, resulting the only sample with a recovery position almost similar to the initial position. For example, the R05 changes its

displacement from starting position to $d50g = 31.12\ mm$ in $6\ s$ and $d75g = 36.52\ mm$ in $8\ s$ respectively with 50 and 75 g load (see **Fig. 2.4d**). Finally, the R01 and R05 samples was tested in a vertical position to evaluate the bending angle with the application of gravity force (G-Force), as shown in **Fig. 2.5**. On the other hand, in **Figs. 2.4** and **2.5** non-uniform deformation have been obtained: this might lead to unwanted failures during the exploitation of the SMP actuator. Due to the extremely huge design freedom offered from Additive Manufacturing, new shapes can be easily fabricated to overcome this issue.
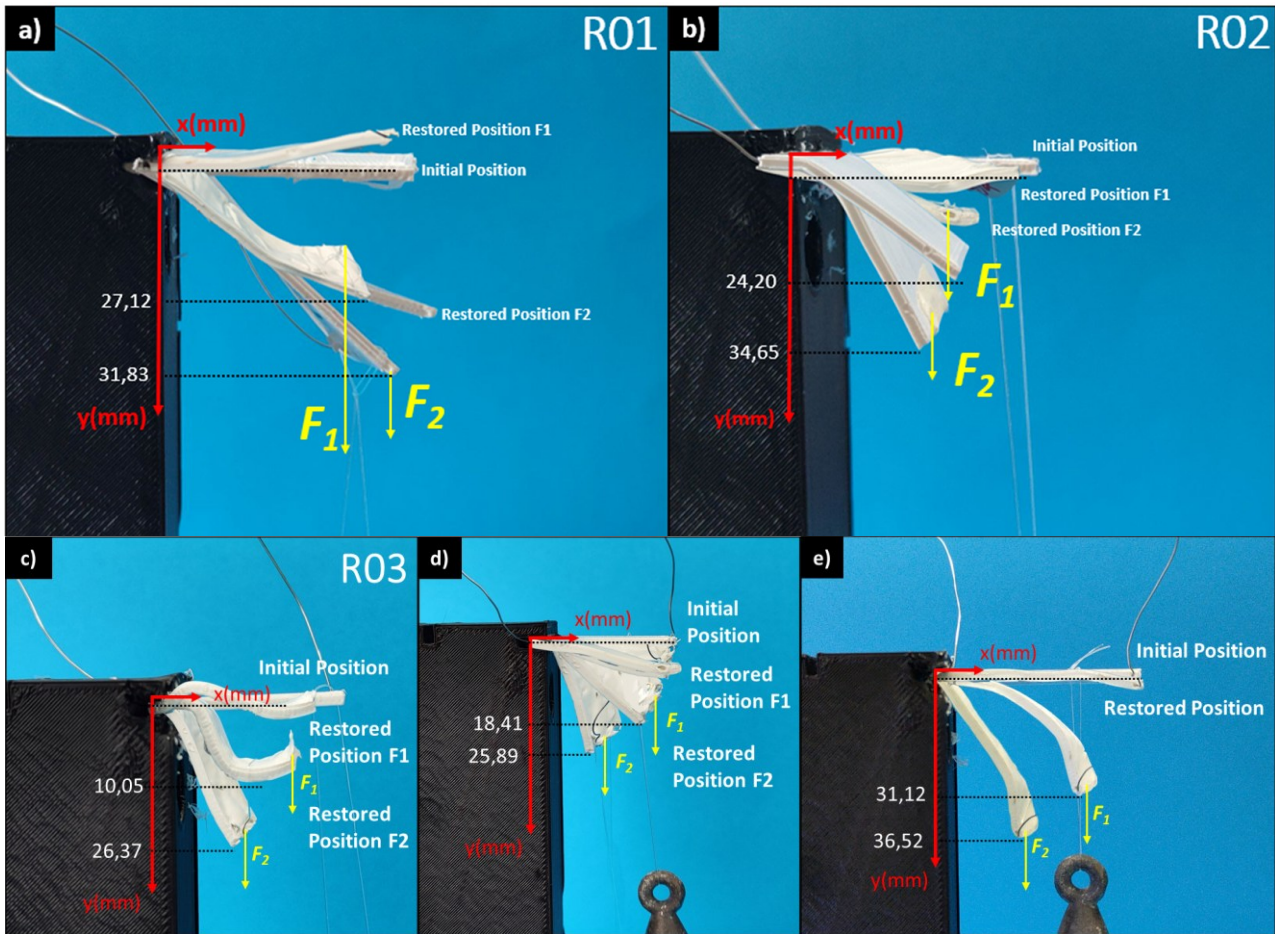
Fig. 2.4: Shape memory effect of tested samples comparing activation (using 50 and 75 g load) and

In conclusion, R05 sample appears to be the best SMP-sample according to the performances shown. The R05 sample results the best in terms of i) absolute compliance factor, ii) SMP behavior with integration of NiCr wire for shape-recovery and iii) low activation and recovery time.

The impact of the manufacturing process on the performance shown by R05 have also been evaluated: five replications of R05 have been fabricated and tested. The standard deviation calculated while applying 75 g for the absolute compliance factor ΔC_m, activation time, and recovery time was respectively 0.7 (mean of 6.3 $\frac{mm}{N}$), 1.3 (mean 7.2 s), and 2.1 (mean of 12.8 s). It stands out that the fabrication process is repeatable and has a very low impact on the performance shown from the SMP

actuators. Also, from a geometric standpoint the R05 samples shows the highest ratio length/width (40 mm/10 mm): this might be related to the improved performances obtained.

The fatigue life on R05 has been characterized: 10 consecutive activation cycles have been performed and the activation position, recovery position, activation time and recovery time were evaluated. In particular, all the four outputs shown a very low standard deviation (statistically not significant for every output), suggesting more cycles are needed to further study the fatigue behavior.

Since the R05 appear to be the most promising sample, two more variables such as Shape fixity and Shape recovery were evaluated based on 5 consecutive experiments performed on the same R05 sample: when applying 75 g as load, a mean shape fixity of 51° (standard deviation of 4.8°) and shepe recovery of 14° (standard deviation of 1.8°) was found. As shown in **Fig. 2.5**, the shape fixity and shape recovery values were calculated with respect to the origin.
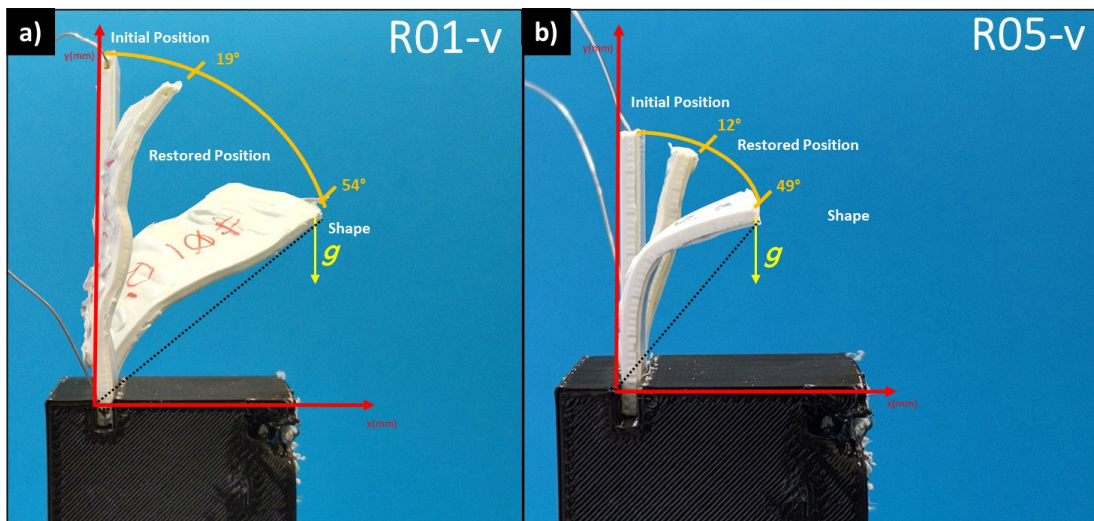
Fig. 2.5: Shape Memory Effect of tested vertical samples comparing activation (using 50 and 75 g
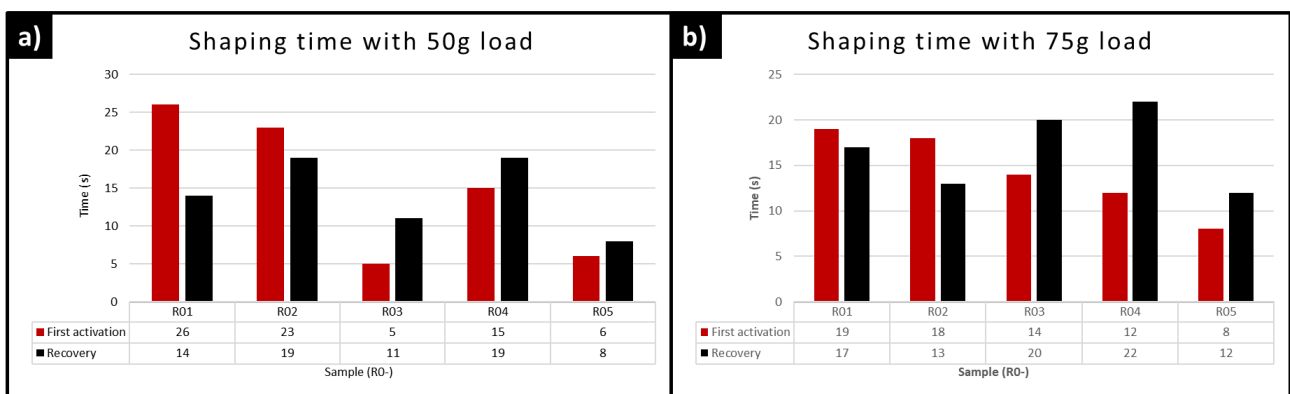
Fig. 2.6: Shaping time of R-sample during the first activation and during the second activation

2.2.3 Soft Joint: Tendon Driven Actuation

The SMP part, in the final version of the dual-mode actuator, is connected with a soft joint made up with TPU 95A, activated via a tendon-driven system (**see Fig. 2.8 a**). In particular, mesh overlapping (mo), infill percentage (ip) and printing temperature of TPU were studied: three values of mesh overlapping were tested ($0.15, 0.20,$ and $0.25\ mm$) combined to 50 and 80% of ip. In according to [107], [108], a T shape of the contact face between PLA and TPU was designed. After printing, the mesh

overlapping and infill percentage were tested with application of three different force of $5, 10, 20\ N$ and $0.25\ mm- 80\%$ were chosen for the following reasons:

- When a mesh overlapping of $0.15\ mm$ (at 50 and 80% of infill percentage) is set (**Fig. 2.7 a**), the adhesion to PLA and TPU was not complete, and it led to the detachment of the joint during the force application.

- Increasing the mesh overlapping to 0.20 and $0.25\ mm$, the adhesion between PLA and TPU increase, although the joint collapse in the range of $10- 20\ N$ when 50% of ip was set (see **Fig. 2.7 b**).

- The 80% of infill percentage is a good compromise between the soft behavior of the joint and the adhesion at the interface, setting $0.25\ mm$ mesh overlapping (see **Fig. 2.7 c, d**).
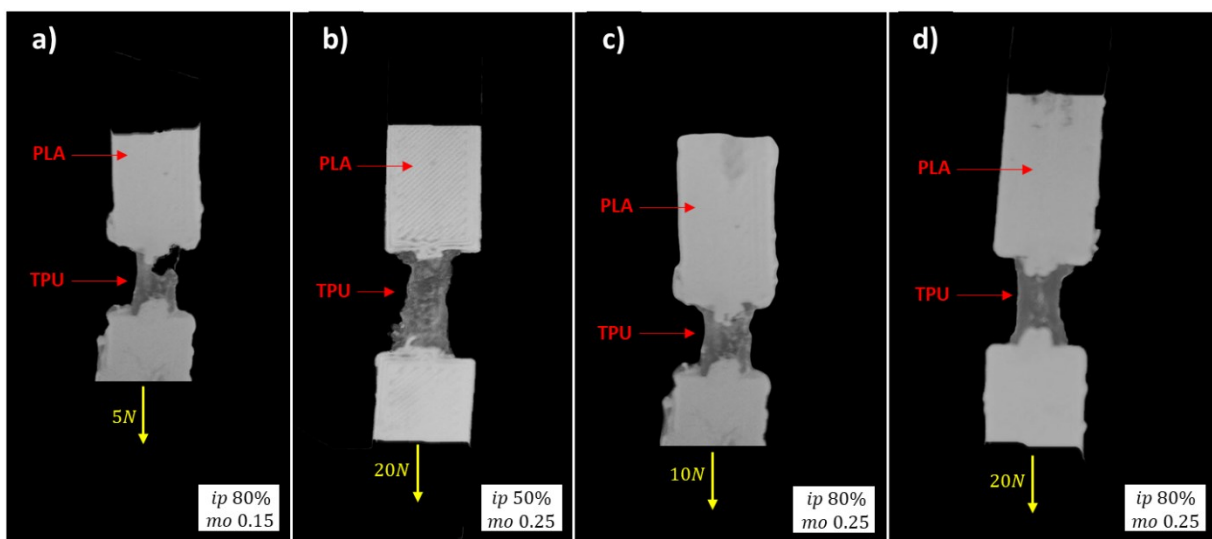
Figure 2.7: Interface TPU-PLA tensile test: a) collapsed joint with application of 5 N and mesh overlapping (mo) sets at 0.15 mm; b) joint dilatation using 50% infill percentage (ip); c) 10 N force application set 80% ip and 0.25 mm of mo; d) 20 N applied force.

With a trial-and-error approach, the printing temperature of TPU was set at $240\,°C$ to increase the adhesion to PLA: it is important to note that when temperature increase, proportional to mesh overlapping (set at $0.25\,mm$) and infill percentage (set at 80%), the joint became very functional and this parameters make the interface between PLA and TPU stronger.
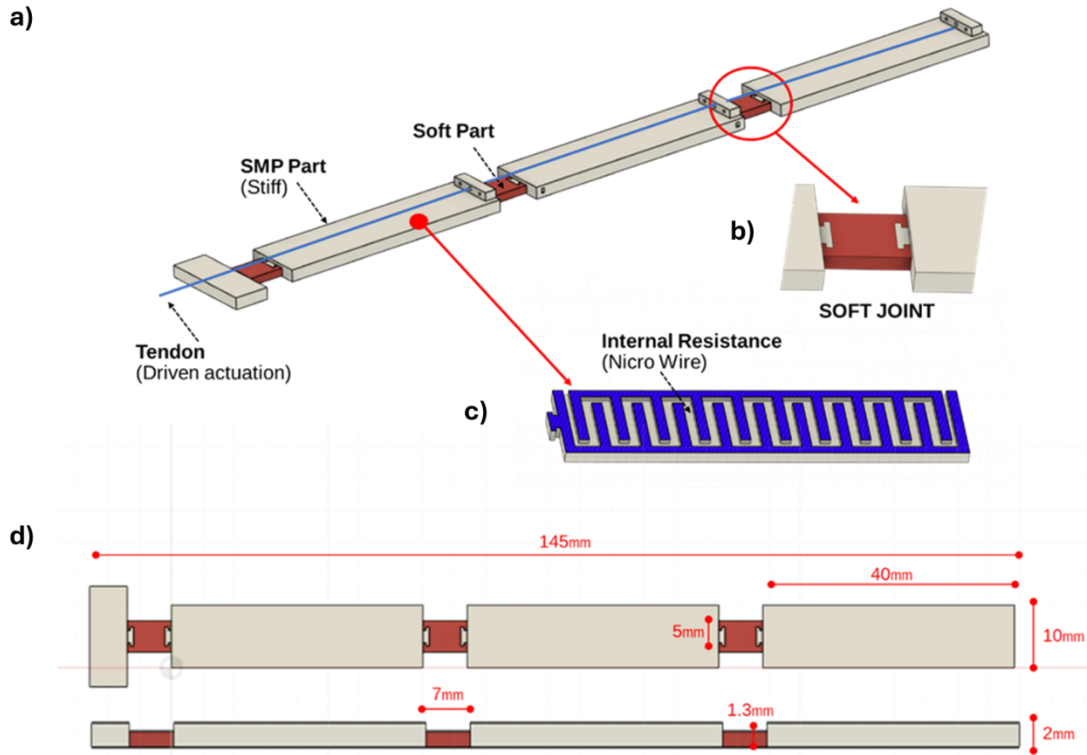
Figure 2.8: Computer Aided Design (CAD) of complex finger structure: a) representation of whole structure; b) interface between soft joint and stiff parts; c) internal channels for NiCr resistance; d) geometrical dimensions of the structure.

2.2.4 Characterization of Dual-Activated (SMPs and Tendon-Driven) Structure and future trends

The proposed structure takes advantage of two actuation systems (SMP and tendon driven) resulting composed of PLA segments (SMP) and TPU segments (tendon driven) connected each other's, as shown in **Fig. 2.8**.

The main reason leading to a dual actuation structure is the possibility to achieve complex motions (i.e. bending, twisting) impossible to achieve using a single actuation system. This structure is characterized by a manufacturing time and cost, respectively of $21\,min$ and $0.89\,Euro$. The fabricated finger was tested three times for each kind actuation system: i) SMP actuation, ii) tendon driven actuation and iii) both actuation (combination of SMP actuation and tendon driven actuation). The tests were performed starting from resting condition (structure laying on the x-axis of **Fig. 2.9**):

1.68 *A* of current (0.72 V of voltage for 5 s) was provided to the NiCr wires to activate the SMP actuation, while a stepper motor was used to pull the tendon wire (tendon-driven actuation).When both electrical actuation systems were used at the same time, as shown in **Fig. 2.9 a**, very complex motions were achieved: both bending and twisting movements were obtained. It is worth mentioning that no damages occurred after the three repetition cycles, however more tests have to be performed to quantify the fatigue behavior on soft robotics actuators.

It is necessary to note that the following limitations were present in this work:

- the number of the tests on the complex actuator are not sufficiently to define a final behavior model, to estimate the right repetition of the movements.

- the tendon driven activation is faster than the SMP activation. An important part of future studies will be the reduction of the cooling time for the SMP by adding external cooling systems such as fan or cold-water channels.
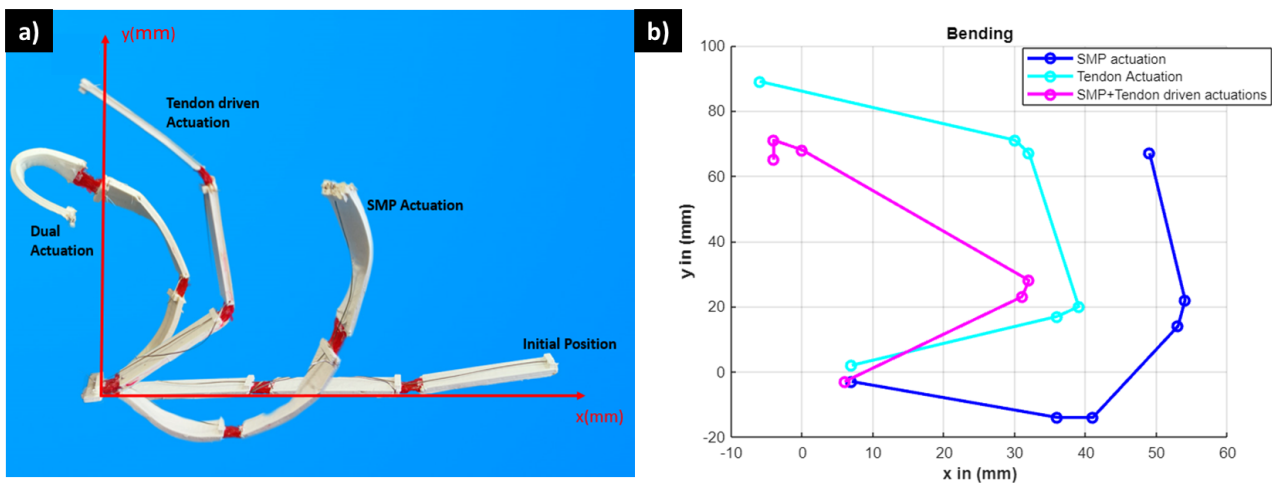
Figure 2.9: Motions of complex finger structure actuated using SMP actuation, Tendon driven actuation and both SMP and Tendon actuation systems: a) real bending actuation; b) software mapping.

2.2.5 Conclusions

In conclusion, a multi-material FFF approach was used for the monolithic fabrication of a smart structure able to perform several unconventional movements, combining two different actuation systems: SMP system and tendon-driven system.

The start and stop method have been successfully used to embed NiCr wires inside SMP structures making them more appealing for real-life scenarios, overcoming the high activation time occurring when hot water or oven are used.

The present work lays the foundation for:

- An extensively usage of FFF technology to fabricate soft robots performing complex motions.

- The fabrication of SMP-based structures with improved performance.

- Further investigation based on modelling the behavior of the proposed SMP actuators in relationship with the process parameters set in the slicing software.

2.3 Electromagnetic actuation system: one-Shot 3D printed Soft device actuated using metal-filled channels and sensed with embedded strain gauge

In this section, the multi-material extrusion (M-MEX) technology is used to fabricate, in a single step, a three dimensional (3D) printed soft electromagnetic (EM) actuator, based on internal channels, filled with soft liquid metal (Galinstan) and equipped with an embedded strain gauge, for the first time.

At the state of the art, M-MEX techniques result underexploited for the manufacture of soft EM actuators: only traditional manufacturing approaches are used, resulting in many assembly steps. The main features of this work are as follows: 1) one shot fabrication, 2) smart structure equipped with sensor unit, and 3) scalability. The actuator was tested in conjunction with a commercial magnet (magnetic field of $1.29\ T$), showing a bending angle of $22.4°$ (when activated at $4A$), a relative error of 0.7%, and a very high sensor sensitivity of $49.7\ \frac{\Omega}{°\,degree}$. Two more examples, showing all the potentialities of the proposed approach, are presented: a jumping frog-inspired soft robot and a dual independent two-finger actuator (IDA).

This work aims to push the role of extrusion-based additive manufacturing for the fabrication of EM soft robots, based on EM actuation system: several advantages such as portability, no cooling systems, fast responses, and noise reduction can be achieved by exploiting the proposed actuation system compared to the traditional and widespread actuation mechanisms (shape memory polymers, shape memory alloys, pneumatic actuation, and cable-driven actuation).

2.3.1 Materials and Methods

The main idea underlying the following research is the one-shot fabrication of a soft EM actuator based on internal channels (filled with Galinstan) and equipped with embedded sensors by using Multi-Material Extrusion (M-MEX) technology. The soft EM actuator, shown in **Fig. 2.10 a–c** is composed of the following parts: 1) a main flexible body, 2) a flexible joint to improve the bending performance, 3) a bottom strain gauge to obtain real-time feedback, and 4) a total of 9 internal channels. In particular, the latter element is crucial to exploit the Lorentz force. The channels have a square profile $(0.8\ x\ 1.3\ )mm$ in accordance to Mao et al [91] and they have been filled up with liquid

soft Galinstan (a liquid alloy composed of 68% $wt.$ gallium, 22% indium and 10% $wt.$ tin), well known for its good electrical performances. After the Galinstan injection, two metal pins have been assembled over the 3D printed connection to hook up the electrical wires. The Galinstan has been purchased by Peguys, Israel. The M-MEX machine Ultimaker 3 (Ultimaker, The Netherlands) in conjunction with two thermoplastic materials has been used. A soft thermoplastic polyurethane (TPU) with a shore harness of 85A and Young's Modulus of 20 MPa has been employed for the flexible parts (main body, joint, and connections for the metal pins), while a conductive polylactic acid (CPLA) with a resistivity of 15 $\Omega * cm$ along the layers and 20 $\Omega * cm$ perpendicular to the layers has been employed for the sensor fabrication.

The TPU (commercial name ''TPU 80A LF'') and CPLA (commercial name ''AlfaOhm'') materials have been purchased, respectively, by BASF SE, Germany, and FiloAlfa, Italy. The overall actuator dimensions along $x-$, $y-$, and $z-axis$ are $(40 \ x \ 73 \ x \ 4.7) \ mm$, while the strain gauge results in 6 tracks and a thickness of $0.4 \ mm$. The main process parameters set during the manufacturing process are listed in **Table 2.3**. Moreover, printing speed and infill percentage have been found to be crucial variables for the channel fabrication. If the channels are not properly fabricated, a Galistan leakage could occur, involving problems during the soft device actuation (impossibility to be activated). Using a trial-and-error approach, a printing speed of 25 mm/s and an infill percentage of 100% were found to ensure a solid channel structure, avoiding Galinstan leakage. An overview on the fabrication of leakage-free channels exploiting MEX technology can be found in Zeraatkar et al [109], Pavone et al [10], and Zeraatkar et al [110]. In particular, the relationship among strain gauge-extruded single-layer thickness (lt) and total number of layers (tl) has been considered. As shown in Stano et al [111], the reduction of tl implies a reduction of the final strain gauge resistance and standard deviation: in this way, electrical power losses will be minimized.

Being the overall strain gauge thickness (SGT) fixed to $0.4 \ mm$, the only way to reduce tl is increasing the single extruded layer thickness (lt) in the slicing software, as shown in **Equation (2.3)**.

$$SGT = lt * tl \qquad\qquad (2.3)$$

A value of lt equal to $0.2 \ mm$ was set; it means that the whole strain gauge is composed of 2 consecutive layers to minimize the welding effect (number of voids between adjacent extruded layers) found in Stano et al [111]. Moreover, further characterizations about the CPLA viscoelastic behavior will be carried out to improve the dimensional accuracy of 3D printed sensors. The strain gauge geometry proposed in Stano et al [100] was used throughout this work; however, recent works pave the way to sinusoidal and wave-based profiles for soft stretchable strain sensors [112].

Table 2.4: Printing parameters set for the fabrication of the EM Actuator

Process parameter	TPU	CPLA
Nozzle size (mm)	0.4	0.8
Layer thickness (mm)	0.2	0.2
Extrusion temperature (°C)	240	260
Printing speed (mm/s)	25	20
Infill percentage (%)	100 (for the channels) 100 (for the joint) 25 (for other parts)	100

The total printing time and cost are, respectively, 97 min and 3.75 €. The main advantages of the proposed manufacturing approach, compared to the main works using MEX technique, to exploit the EM actuation system found in scientific literature and discussed in the introductions are as follows:

1. The EM actuation is achieved by employing a soft metal liquid metal instead of rigid copper wires: in this way, soft devices can be fabricated without recurring to rigid external elements [93], [94].

2. The EM actuation is achieved by employing a soft metal liquid metal instead of extruding thermoplastic composite materials loaded with magnetic fillers.19,20 The main issue related to magnetic thermoplastic materials is their low processability: the magnetic fillers make the whole filament brittle and difficult to be extruded, generally problems like nozzle clogging and breakage of filaments between the 3D printers pushing gears occur. Using the proposed manufacturing approach, all the problems described above have been overcome.

The proposed 3D printed soft EM actuator filled with soft liquid Gallinstan is shown in **Fig. 2.10 d**. The working mechanism of the used M-MEX machine (Ultimaker 3) is shown in **Figure 2.10 e**.
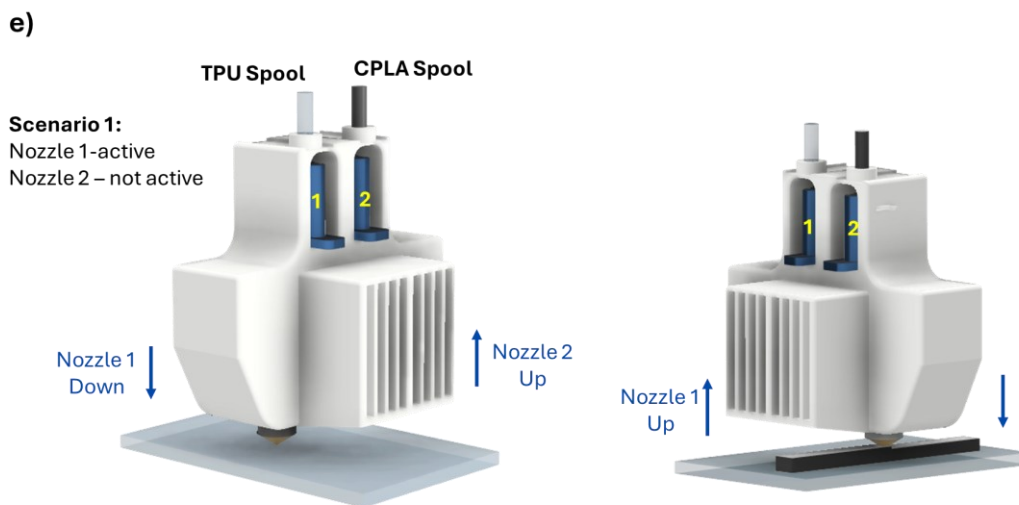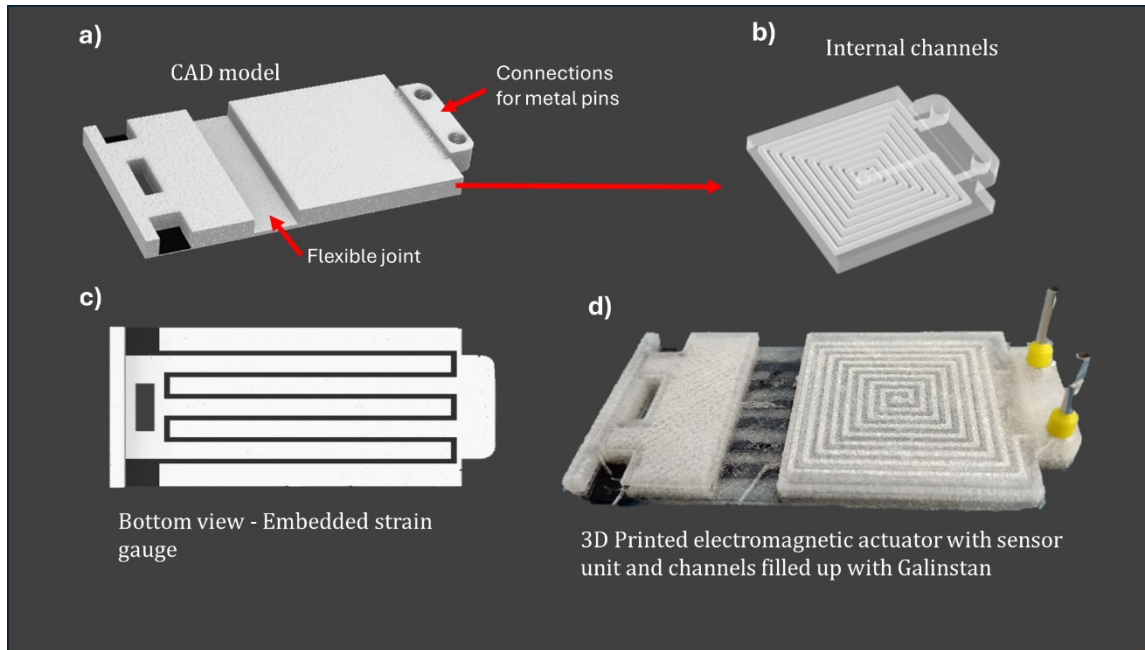
Fig. 2.10: Soft EM actuator: a) CAD model; b) internal channels; c) Bottom view: embedded strain gauge sensor (white = TPU, black= CPLA); d) 3D printed EM soft actuator with embedded sensor and channels filled up with Galinstan; and e) schematic diagram depicting the basic M-MX extrusion working mechanism of Ultimaker 3.

2.3.2 Characterization of the EM Soft Actuator

The proposed 3D printed soft EM actuator was characterized to evaluate 1) bending performance as a function of the applied current and 2) the embedded strain gauge performance. A permanent magnet (purchased by Supermagnete. de, Germany) was used to generate a magnetic field of $1.29 T$.
In accordance to Mao et al [91], the equilibrium Lorentz force equation shown in Equation (2.4) is as follows:

$$F = \frac{2M}{Z_i + Z_{i+1}} \tag{2.4}$$

where Z (mm) is the distance between the permanent magnet and the channels, i is the number of the channel ($i = 1, 2, \ldots, 9$), and M ($m^2 * A$) is the total magnetic moment as shown in Equation (2.5):

$$M = \int I_i B L_i Z_i \tag{2.5}$$

where B (T) is the magnetic field, I is the input current (A), and L (mm) is the length of the main channels.

Three different current inputs ($2A, 3A$, and $4A$) were tested, evaluating the final EM soft actuator bending angle: 10 cycles for every current input were performed. It is worth mentioning that when a current input of $1A$ was provided, the bending motion of the proposed soft EM actuator is neglectable. The testing protocol is as follows:

1. the current is provided to the Galinstan channel for $1 s$ (because of the Lorentz force, the EM soft actuator results in bending motion).

2. After the current is set to $0A$ for $1 s$ (rest time) and the actuator get backs to its initial position, the current is provided again for $1 s$, the whole cycle is repeated $10 \ times$.

The current input providing the best bending performance is $4A$ (**Fig. 2.11 a**): a bending angle of $22.4°$ is obtained, resulting in, respectively, 35.4% and 46.9% higher than the bending angle obtained at $3A$ and $2A$. The standard deviation has been calculated on 10 cycles, resulting really low for every

current input (standard deviation of 0.21° at $2A$, standard deviation of 0.16° at $3A$, and standard deviation of 0.17° at $4A$) (**Fig. 2.11 b, c**).

When a current input of $4A$ is provided, a relative error (e), a good metric to evaluate the accuracy in terms of bending of the proposed actuator, was found to be 0.7%. The low relative error makes the proposed EM soft device appealing for applications requiring high accuracy, such as biomedical and industrial devices.

The strain gauge performance has been analysed: the best current input, namely $4A$, has been provided to the EM actuator for a total of 100 consecutive cycles. The current is provided for $1\ s$, followed by an off period of $5\ s$, for a total of 100 times. Two electrical wires have been welded to the strain gauge pads and connected to the benchtop multimeter (GW Instek, GDM-8341), which in turn was connected to the laptop to collect data.

From the testing phase, it stands out that the strain gauge change of resistance is characterized by two phases: an initial phase in which the change in resistance tends to grow and a second phase where it is stable (**Fig. 2.11 d**). It is possible to explain the two different phases as follows: during the first phase, the overall change in resistance constantly grows for the first 28 cycles because of the 1) Mullin effect and 2) material (TPU) hysteresis.

After the $28th$ cycle, a stabilization in the material hysteresis and mitigation of the Mullins effect occur and the change in resistance of the embedded strain gauge result stable. In particular, the sensitivity (s) of the strain gauge throughout the second phase (stability phase) is $49.7\ \frac{\Omega}{°\,degree}$ and R2 is equal to 0.96. In particular, the high sensitivity allows the exploitation of the proposed EM actuator without recurring to any resistance amplifier. The following results suggest that the proposed 3D printed soft EM actuators need to be trained for 28 cycles before the usage, to obtain consistency in the bending behavior.

It is worth mentioning that the training phase (28 cycle) mostly depends on two factors: 1) size of the device (changing the size, the amount of training cycles can change) and 2) material properties: every material (even different kinds of TPU) is characterized by different viscoelastic properties, affecting the bending behavior of the EM soft device. Every soft EM device fabricated with the proposed approach needs to be initially tested to understand when the stabilization phase (in terms of consistency in the bending behavior) occurs.

Further work will focus on the fatigue analysis of the proposed soft EM device, paying particular attention at the interface adhesion among CPLA and TPU when the device is subject to repetitive cycles. The embedded strain gauge has been used to obtain real-time feedback; in the future, it can be used to create closed control loops, improving the automation degree of the proposed EM soft actuator.
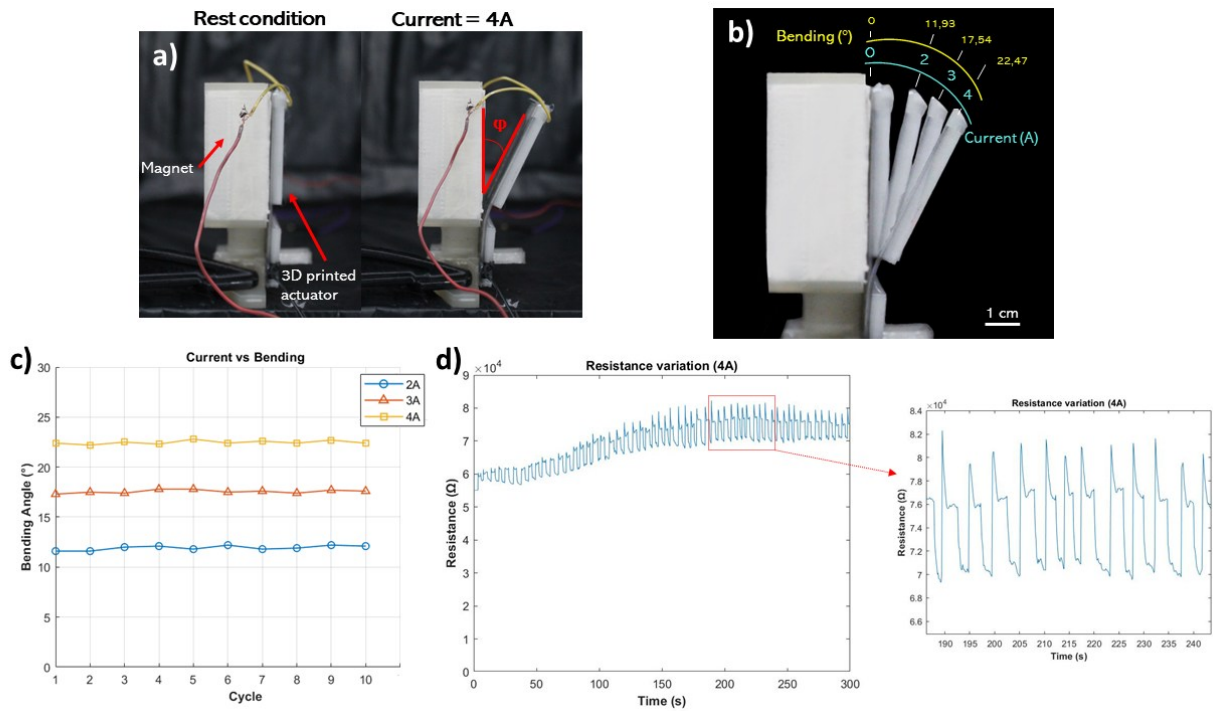
Fig. 2.11: Characterization of the EM soft actuator. a) Working principle of the soft EM actuator with current input of 4A; b) Observed bending angle as a function of the current inputs; c) Comparison of the bending angle at the current input variation versus number of cycles; d) Embedded sensor behavior: resistance variation at 4A current input.

2.3.3 EM applications: Bio-Inspired Frog Robot and Independent Dual Actuator (IDA)

To prove the potentialities of the proposed manufacturing approach, two different applications have been developed: a jumping bio-inspired soft frog (**Fig. 2.12 a**) and an independent dual actuator (IDA) (**Fig. 2.13 a, b**).

The bio-inspired jumping soft frog was used to demonstrate that the proposed EM soft device can be employed for soft robotics applications: nowadays, a challenging topic concerns the fabrication of animal-based soft robots capable of crawl, jump, and swim [113], [114]. The frog-inspired soft EM robot is based on a core main body equipped with internal channels filled with Galinstan (the same of the EM soft actuator shown in EM Actuator Characterization section) and four legs (one for each corner of the main body) designed with flexible TPU joints to improve jumping motions. TPU was used to manufacture the soft frog, setting the same printing parameters listed in **Table 2.3**.

The jumping performance of the soft EM frog has been evaluated, in terms of position in the $x-$ and $y-space$ and repeatability.

The soft EM frog body was placed parallel to the permanent magnet on the horizontal plane: the centre of the magnet is fixed as the zero of the axis system for each orientation. Four different orientations were tested: North, South, Right, and Left.

The following testing protocol was used: for each orientation, one by one, a single input current of $4A$ (the current input providing the best result in Section 2.3.2) is provided to the Galinstan channel, and the soft EM frog results in jumping movement. Subsequently, the current is set to $0A$ for $10\,s$ and the frog soft robot is placed at $x = 0$ and $y = 0$. The whole cycle is repeated three times for each orientation.

A virtual marker for each leg was used to evaluate the x- and y-position (Fig. 3b) of the soft frog: the jumping movement is substantially repeatable, and in **Table 2.4,** the standard deviation of each leg (1–4), for every orientation (North, South, Right, and Left), is listed. The standard deviation has a random behavior: for the x-position, the standard deviation ranges from 1 to $5\,mm$, and for y-position, it ranges from 1 to $10\,mm$. The mean (x- and y-position) standard deviation for North; South; Right; and Left orientation is, respectively, $(3.72; 3.69)\,mm$, $(4.79; 7.53)\,mm$, $(3.14; 3.76)\,mm$, and $(3.01; 7.16)\,mm$, as shown in **Fig. 2.12 c**. The following outcomes indicate that the presented EM bioinspired soft robot can be employed as jumping robot; moreover, future works will focus on the modelling, simulation, and control aspects of the jump motion.

A great advantage offered by M-MEX technique and in general by AM methods concerns the possibility to fabricate assembly-free device that can be scaled up and down [114].

To demonstrate that the proposed fabrication method is suitable for small size, non-assembly EM soft actuator, an IDA was designed and fabricated. The EM-based IDA takes inspiration from human fingers: they are connected to the hand, and they can be activated both independently and simultaneously. The proposed IDA device is composed of two TPU fingers connected to each other at the base: each finger is $50\,mm$ long and $23\,mm$ wide and composed of nine internal channels (which will be filled up with Galinstan after the fabrication step) and one bottom strain gauge sensor. The distance between the two fingers is 4 mm. The possibility to selectively choose which finger will be activated is really appealing and can find applications in many fields such as 1) on-off switching devices for button without human intervention and 2) swimming robot (mimicking fish fins).

Another important aspect of the proposed IDA is related to the presence of two different strain gauges (one for each finger), which provide feedback (change in resistance) when the fingers are activated.

The IDA device was characterized to evaluate 1) bending performance and 2) the embedded strain gauge performance: only a $4A$ input current was used for the tests.

Table 2.4: Jumping movement evaluation

Orientation		Mean position		Standard deviation	
		x (mm)	**y (mm)**	**x (mm)**	**y (mm)**
Nord	**Leg 1**	-23.15	80.51	4.61	1.34
	Leg 2	52.36	68.17	4.34	5.91
	Leg 3	42.49	5.35	3.24	5.64
	Leg 4	-43.25	7.58	2.71	1.90
Sud	**Leg 1**	-99.73	-35.49	2.39	11.70
	Leg 2	-57.24	39.02	6.80	7.79
	Leg 3	26.21	0.470	2.56	6.03
	Leg 4	-23.86	-78.45	7.42	4.58
Est	**Leg 1**	-15.47	37.84	3.01	1.08
	Leg 2	22.56	-0.58	2.29	2.29
	Leg 3	0.14	-8.05	1.43	7.13
	Leg 4	49.89	-75.22	5.83	4.53
West	**Leg 1**	-104.02	34.56	1.39	3.23
	Leg 2	-23.51	64.64	3.38	9.27
	Leg 3	8.64	-16.98	2.74	10.87
	Leg 4	-76.22	-46.96	4.54	5.28

The current input has been provided (from a rest zero-position, with $0A$ for finger 1 and finger 2, as shown in **Fig. 2.13 c**) for a total of 10 *cycles* (single cycle: current on for 1 s and off for 1 s) in three different configurations:

1. Only the finger 1 has been activated (**Fig. 2.13 e, f**).

2.	Only the finger 2 has been activated (**Fig. 2.13 d**).

3.	Both the fingers 1 and 2 have been simultaneously activated.

A mean bending angle of 15.5° (standard deviation of 0.4°) and 15.4° (standard deviation of 0.6°) were found when only the finger 1 and the finger 2 were separately actuated.

As shown in **Fig. 2.14 a**, the strain gauge sensitivity of the finger 1 when activated (finger 2 not activated) is 3.67 $\frac{k\Omega}{°degree}$ ($R^2 = 0.96$), while the strain gauge sensitivity of finger 2 (Fig. 5b) when activated (finger 1 not activated) is 3.84 $\frac{k\Omega}{°degree}$ ($R^2 = 0.93$).

The whole IDA device has been fabricated in a single step cycle resulting, respectively, in a manufacturing time and cost of 72 min and 3.06 €: it consists of two strain gauges (CPLA material) and two soft (TPU material) bodies.

Full advantages have been taken from the M-MEX approach: a comparison is here provided with the same IDA device fabricated in a modular way (two separate soft bodies, two separate strain gauges, and a connection structure). In this case, the 3D printing cost is 4.57 € (1.68 € for every soft body, 0.54 € for every strain gauge, and 0.13 € for the connection structure), and the manufacturing time is 140 min (48 min for every soft body, 27 min for every strain gauge, and 7 min for the connection structure). On top of that, four manual assembly tasks are required: assembly of the two soft bodies with the connection part (2 tasks), and assembly of the two strain gauges in the bottom part of each soft body (2 tasks).

It is possible to assume a total manual assembly time of 30 min for a total manufacturing cost and time of 4.57 € and 150 min. It is important to point out that the human operator cost/minute has not been considered. The exploitation of the M-MEX approach, in this specific case, lead to a reduction in cost and time, respectively, of 14.65% and 55.2%, proving all the potentialities of the proposed 3D printing method.
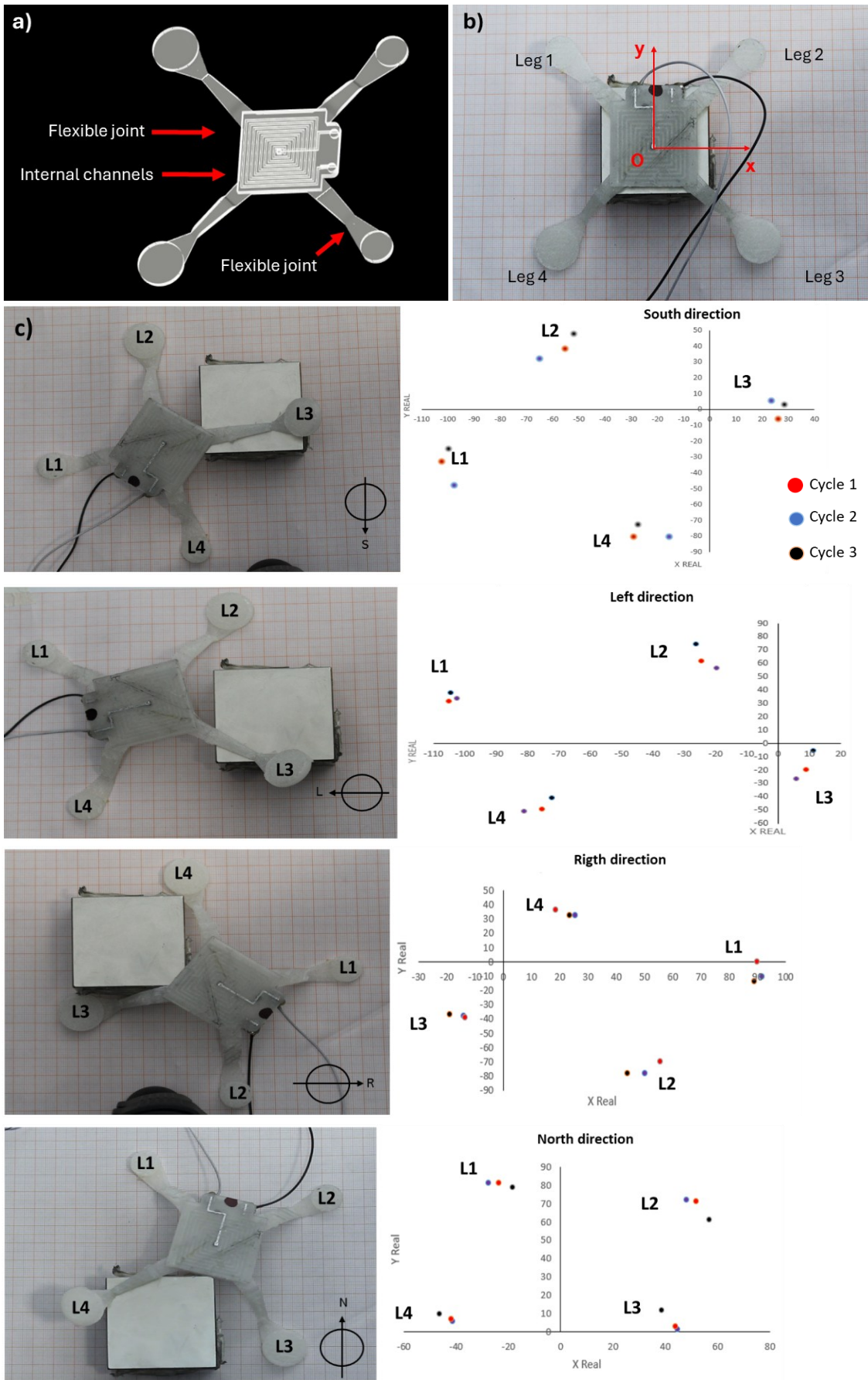
Fig. 2.12: Bio-inspired EM soft Frog: a) CAD of the soft Frog; b) Rest position (at 0 A); c) characterization of jumping motion at four different frog orientation: North-, South-, Right-, Left-direction.

CAD model

Embedded sensor - Bottom view
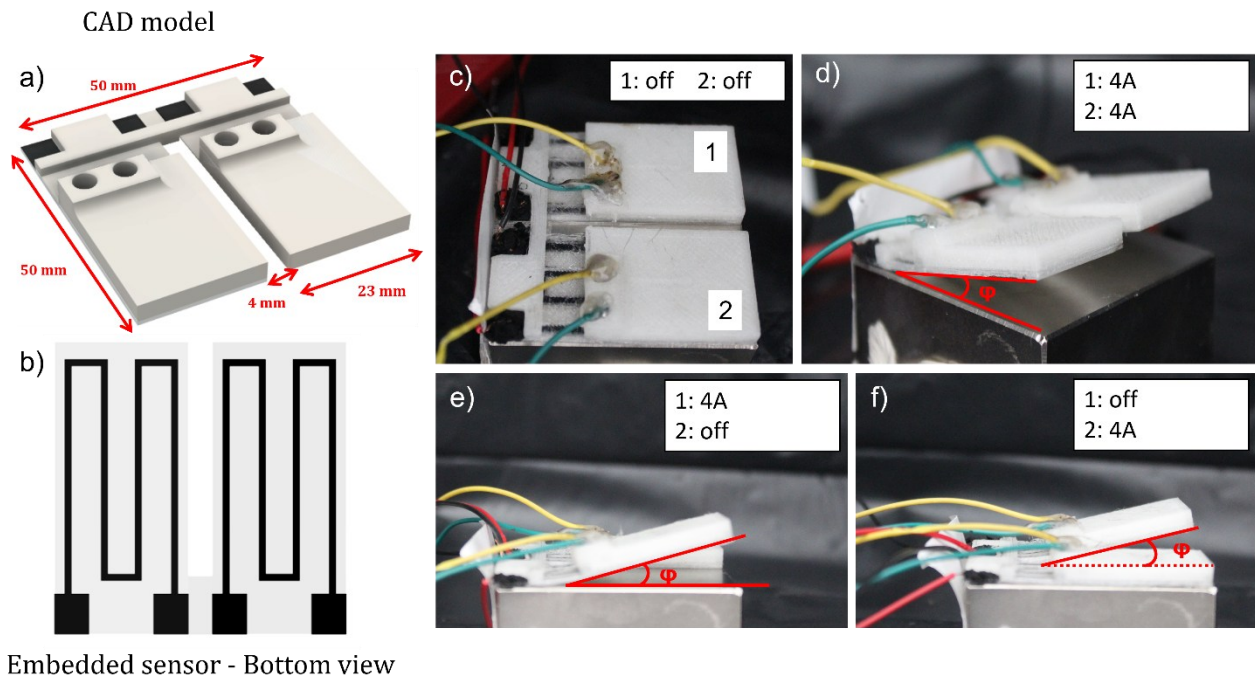
Fig. 2.13: Independent Dual soft EM Actuator (IDA) and characterization: a) CAD of the proposed IDA; b) Bottom view of the embedded strain gauge sensors; c) zero-current input for fingers 1 and 2; d) 4A current input provided to both the fingers: bending of both the fingers; e) bending of finger 1: 4A current input provided to finger 1 and 0A current input provided to finger 2; f) bending of finger 2: 4A current input provided to finger 2 and 0A current input provided to finger 1. IDA, independent dual actuator.
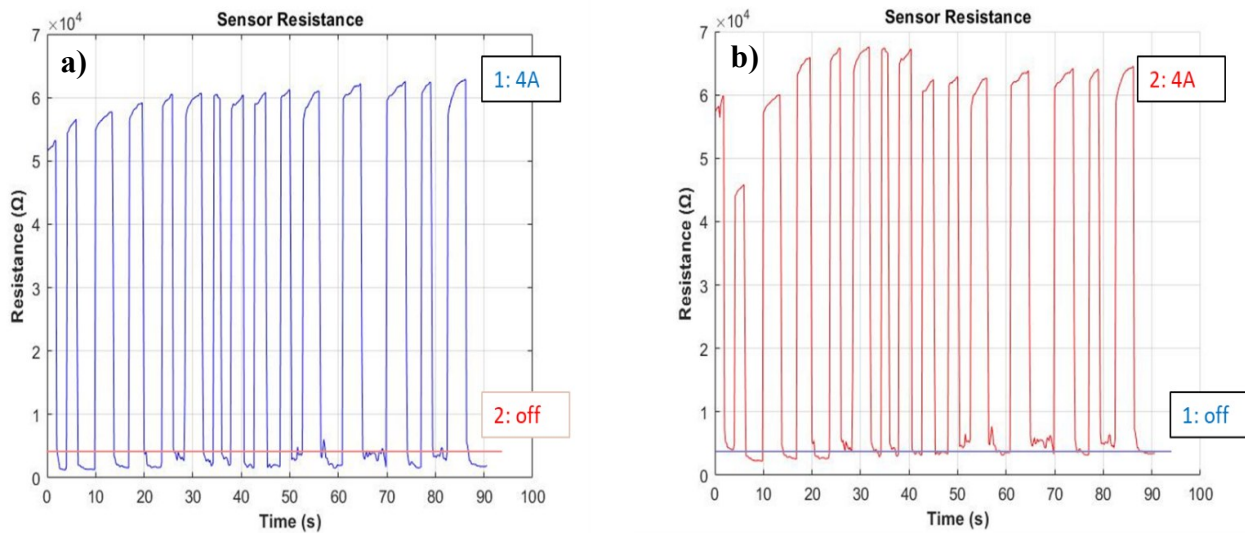
Fig. 2.14: Strain gauge sensitivity: a) Resistance variation (strain gauge sensitivity) of Finger 1 when activated (finger 2 not activated; b) Resistance variation of Finger 2 when activated (finger 1 not activated).

2.3.4 Conclusions

This work demonstrates the advantages offered by the M-MEX AM process for the fabrication of soft EM actuators: even though this class of actuator is really appealing for soft robotic applications, it results, at the state of the art, still underexploited.

The main benefit of the proposed manufacturing approach consists in the monolithic fabrication of the soft EM device equipped with 1) internal channels (filled up with liquid metal Galinstan) and 2) an embedded strain gauge sensor. As a matter of fact, manufacturing steps and assembly tasks have been abruptly reduced, making M-MEX technology suitable for the fabrication of the proposed soft EM devices.

A soft EM actuator used for bending purpose has been characterized showing a bending angle of $22.4°$ and a very low relative error of 0.7%, while the 3D printed embedded strain gauge sensitivity was found to be $49.7 \frac{\Omega}{°degree}$. Two more examples have been presented: a soft frog-inspired EM robot and a dual finger independent actuator (IDA) equipped with two separate strain sensors. The latter can be used for industrial application such as EM switcher. It was also proved that the usage of the M-MEX approach for the fabrication of the dual independent actuator (IDA) with embedded sensors resulted in a reduction of 14.65% and 55.2% in manufacturing time and cost, compared to a modular MEX approach.

In conclusion, the outcomes of this research lay the foundation for a huge exploitation of M-MEX technology (and AM technologies, in general) for the fabrication of EM devices equipped with sensors. Future studies on device failure in terms of delamination and energy consumption will be explored.

2.4 Electromagnetic actuation system: experimental study to reduce vibration of Additive Manufacturing electromagnetic soft robots

The aim of the present section is the study of the bending behavior of the soft EM device, which was fabricated using Material Extrusion (MEX) technology and discussed in detail in the previously section 2.3. Due to a lack in the scientific literature on the exploitation of MEX technology for the fabrication of soft EM-based devices, this section 2.4 seeks to reduce this gab by studying how vibration affect the behavior of the presented EM actuator.

The main contribution of this study is the vibration reduction of additively manufactured soft EM robots: the vibration has been reduced of 16% by using a joint composed of soft ribs. A Design of Experiment (DoE) approach has been used and ribs orientation, thickness, and spacing has been studied (the optimal combination was achieved using horizontal orientation, 2 mm of thickness, and 1 mm of spacing). The reduction in vibration of soft EM robots, lays the foundation for the usage of MEX technology to fabricate this new appealing class of robots.

2.4.1 Background: fabrication of the EM device

In the precedent section 2.3 and in [56] a 3D printed soft Electromagnetic actuator (henceforth, it will be referred to as SEMA) was fabricated. As in shown in **Fig. 2.10** (see section 2.3.1) and **Fig.2.15**, the SEMA is composed of the following parts:

    i)   Flexible body made up of Thermoplastic Polyurethane (TPU), a flexible material (Young modulus of $205 \, MPa$).

    ii)   A bottom strain gauge made up to Conductive Polylactic Acid (C-PLA) with nanotube of carbon.

    iii)   A TPU soft joint to improve the bending performance.

    iv)   Internal channels filled up with metal liquid soft Galinstan. In this work a copper spiral wire was used in substitution of Galinstan coils.

The overall dimensions of SEMA are $(40 * 79 * 4.7) \, mm$, respectively along x-,y-,z- axis. The Multi-Material Extrusion (M-MEX) Ultimaker 3 (Ultimaker, The Netherland) was used to fabricate

the SEMAs in conjunction with One-Shot fabrication to delete the assembly manual tasks and to reduce the printing time and costs. In the past work, with trial-and-error approach, the optimal parameters were found: the TPU printing parameters such as speed, nozzle size, infill percentage and layer height were set respectively $20\ mm/s, 0.4\ mm, 100\%$ and $0.2\ mm$, in order to reduce the welding effect and increase the dimensional accuracy of the SEMA.

The SEMAs were tested using a permanent magnet $(B\ =\ 1.29T)$ and three different current input were provided to the coils: $2, 3$ and $4\ A$. The $4\ A$ current input providing the best bending performance obtaining an angle of $22.4°$ with a good accuracy and repetition: only 0.7% relative error was found for a total of 100 tested cycles. From a testing phase it is stand out a sensitivity of $49.7\ \frac{\Omega}{°degree}$ value of resistance, provided to the strain gauge printed sensor. Moreover, a scalability was tested, designed and fabricated an independent dual actuator, obtaining the same results in term of bending and resistance sensitivity of the above-mentioned SEMA.

During the tests of the first design of SEMAs, a flexural vibration was noted: the present work aims to studied and minimized the vibration during the bending, working on the geometry joint part.
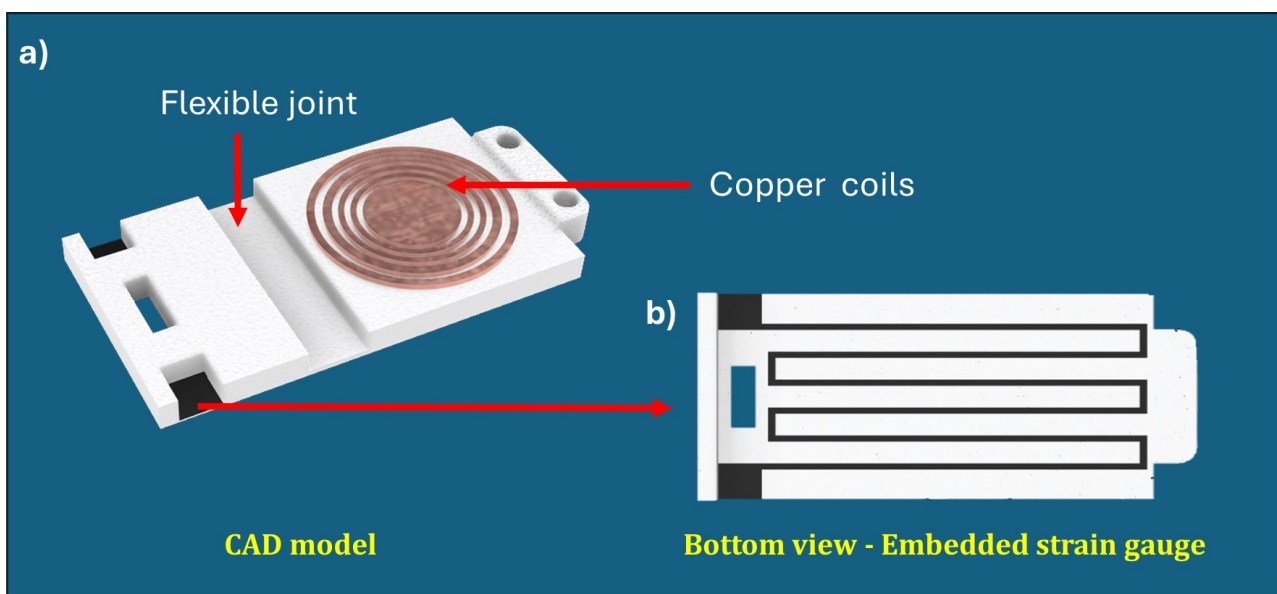
Fig. 2.15: Soft Electromagnetic Actuator (SEMA) with embedded strain gauge: a) Computer Aided Design (CAD) model of SEMA; b) bottom view of embedded strain gauge sensor.

2.4.2 Joint Characterization

To minimize the joint vibration, the geometrical upgrades were performed: first, joint thickness (Sg) and joint length (Lg) were studied and tested (see **Fig. 2.16 c**) in order to choose the best joint dimension to increase the bending performance. Secondly, two different configurations (horizontal

and 45°) of structural ribs were designed and tested (see **Fig. 2.16 a, b**) to minimize the bending flexural vibration. Each geometrical variation was evaluated using the Design of Experiment (DoE). The setup used in [115] was added of a slow-motion HD video cam, used to capture the bending of the tested SEMAs: the single frames (using 240 fps sampling) were processed by the software Tracker in order to evaluate the bending vibration during time variation.
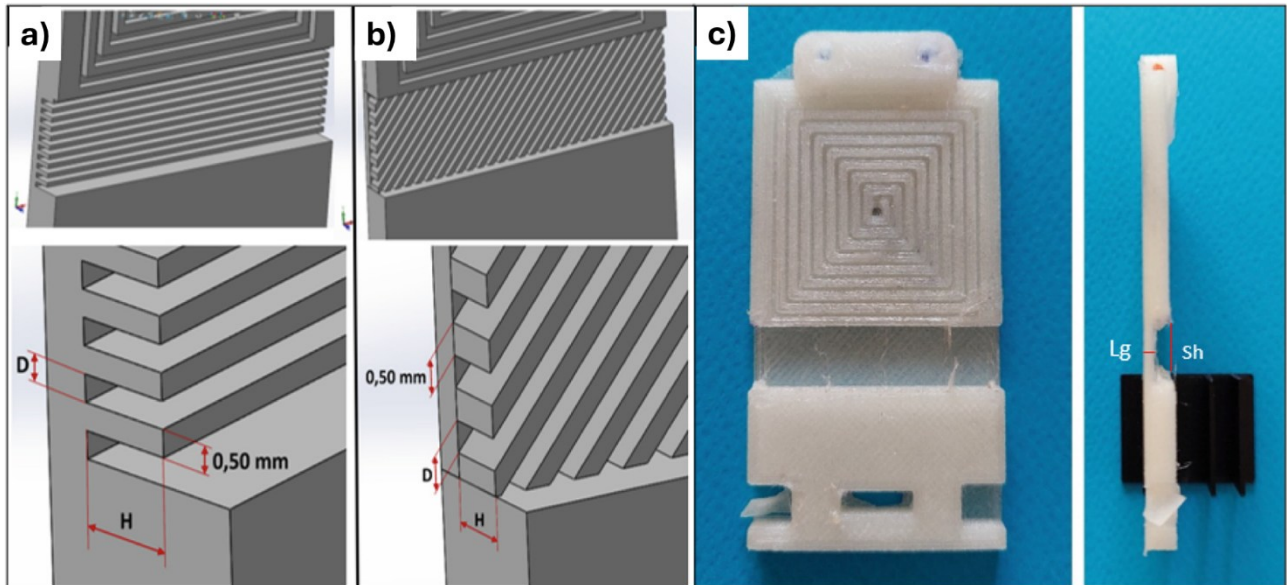
Fig. 2.16: Joint geometry: a) Computer Aided Design (CAD) of horizontal ribs add to joint; b) CAD of 45° ribs add to joint: c) SEMA and joint without ribs.

2.4.2.1 Joint dimensions characterization

Nine different SEMA samples were printed combining three values of joint length $(6, 8,$ and $10)$ mm with three values of joint thickness $(1, 2,$ and $3)$ mm: 23 factorial plan provides the best values of Lg and Sh, respectively 10 mm and 1 mm. In the **Table 2.5** the DoE factors were shown.

The bending was measured fixed the vertical axis (Y), and the applicated force was considered impulsive. The Tracker measured points (photograms of the bending) were interpolated with a spline curve such as in **Fig. 2.17 c, b**, respectively with $(Lg = 10$ mm and $Sh = 1$ $mm)$, and $(Lg = 10$ $mm,$ and $Sh = 3$ $mm)$. From the graphs it is possible to point out the value of the regime bending (θ_r), that is $12.82°$ for the optimal configuration of the joint $(Lh = 10,$ and $Sh = 1)$, that results 0.91 than the worst case, like shown in **Table 2.6**.

Table 2.5: Factorial plan of fist DoE for choose the optimal joint dimensions.

Factors	Levels		
	-1	0	+1
Lg (joint length) [mm]	6	8	10
Sh (joint thickness) [mm]	1	2	3

Table 2.6: Regime bending ϑr [deg] correlated to the different Lg and Sh combination.

Combination	Lg	Sh	θr [deg]
1	-1	-1	8.31
2	-1	0	1.70
3	-1	+1	1.04
4	0	-1	11.91
5	0	0	1.83
6	0	+1	0.96
7	+1	-1	12.81
8	+1	0	2.47
9	+1	+1	0.91

Finally, the bending was evaluated studying the taper index (λ) in Eq. (2.6):

$$\lambda = \frac{L_g}{S_h} \tag{2.6}$$

where Lg is the joint length and Sh is the joint thickness. **Fig. 2.17 a** shown the variation of regime bending (θ_r) compared to the taper index. When Sh is fixed to $1\,mm$ and Lg to $10\,mm$, the following conclusion can drown:

- The maximum tape ratio was achieved (red marker) between the several tested SEMA samples.

- Fixed *Lg* to 10 *mm*, when the *Sh* decrease the joint vibration decrease and the tail curve in **Fig. 2.17 a** fades out.
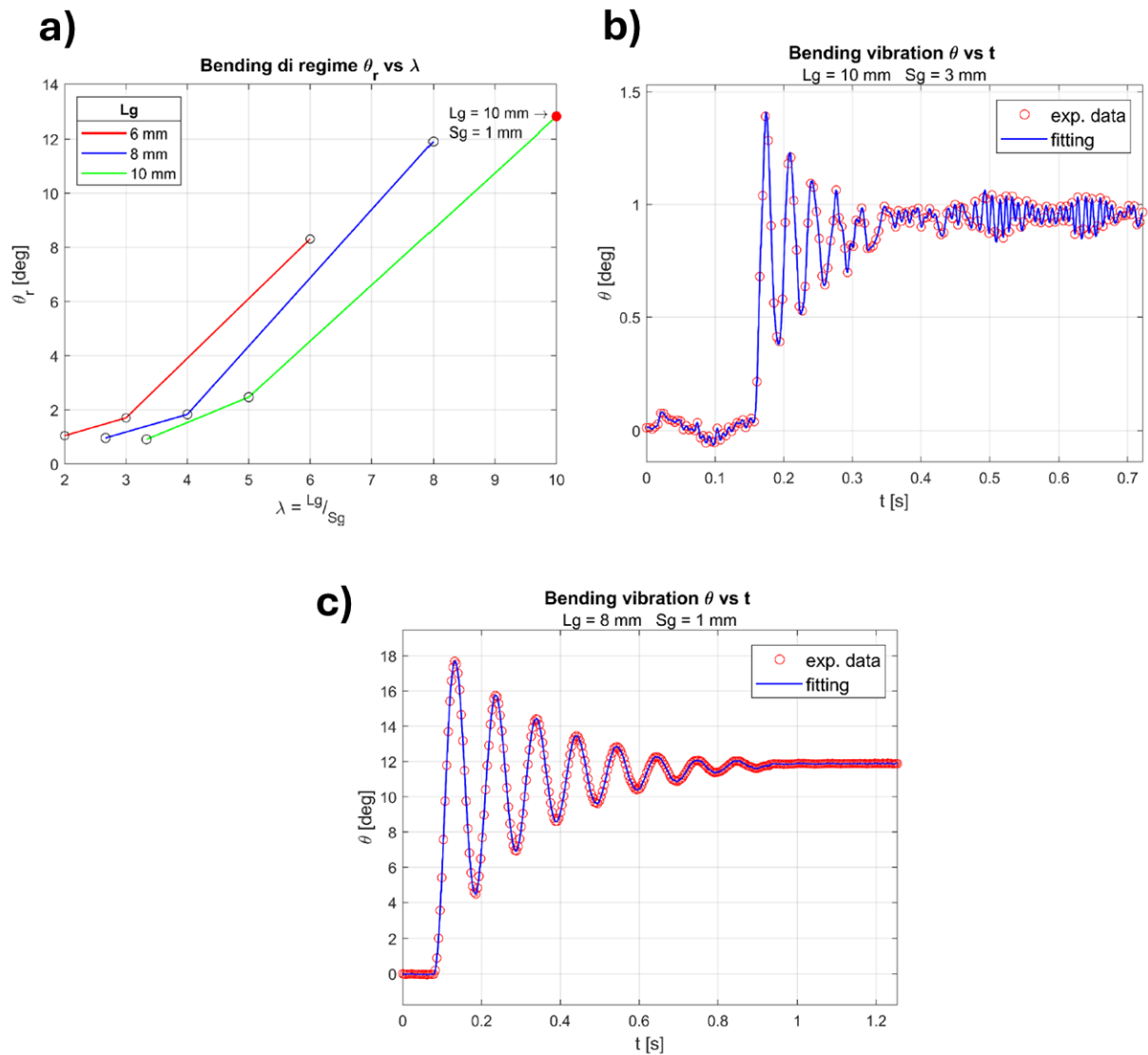
Fig. 2.17: bending behavior of SEMA at: a) variation of regime bending (θ_r) compared to the taper index; b) bending vibration vs time (case Lg = 10 mm and Sh = 3 mm); c) bending vibration vs time (case Lg = 8 mm and Sh = 1 mm).

2.4.3 Ribs characterization

The optimal geometrical configuration of the soft joint that maximize the bending angle was achieved in the previously paragraph. Although, the joint vibration was higher: two different type of ribs was design and tested to decrease the vibration. Using the one-shot fabrication, the ribs was added to the joint, re-designed the same: the main idea is that when the joint is fitted with a solid part (ribs) the vibration fall down. To evaluate this idea, two different design was tested: i) horizontal ribs (**Fig. 2.18 a**) and ii) 45° ribs (**Fig. 2.18 b**).

For the first type of ribs configuration, 2^2 DoE was done: the ribs height (H) and ribs gap (D) were choose like a factor, respectively each one with two levels (2 and 3) mm and (0.5 and 1) mm. The same factors and levels were used to the second ribs configuration (45°). See **Table 2.7**.

Table 2.7: Factorial plan of DoE to evaluate the optimal combination of Horizontal and 45° ribs.

	Factors	Levels	
		-1	+1
Horizontal ribs	H (Ribs height) [mm]	2	3
	D (Ribs gap) [mm]	0.5	1
45° ribs	H (Ribs height) [mm]	2	3
	D (Ribs gap) [mm]	0.5	1

2.4.3.1 Horizontal Ribs Characterization

Three samples for each combination of level and factors were printed in order to evaluate the regime bending means and the standard deviation (see **Table 2.8**). In **Fig. 2.18** the individual values measured experimentally, using interpolation curve (spline), are shown: each graph includes 3 curves for the three tested sample for each DoE configuration (combination).

The distance (D) between the ribs is the most influent parameter, such as shown to the Pareto Chart (**Fig. 2.19 a**). Moreover, the factor H, passing to level −1 at level +1, has a very small influence respect to the factor D. Indeed, in **Fig. 2.19 b** is show the negative slope line the results in decrease passing from level −1 to level +1, while a positive slope line leads to an increase in the value from the level −1 to level +1.

From the plan, several conclusions can be draws:

- Using H = 2 mm and D = 1 mm the lower banding variation (−2.4%) was achieved.

- The vibration was reduced in according to the reduction of log decrement (+16%)

- The D factor is the most influent value for the reduction of the joint vibration.

Fig. 2.18: Bending vibration vs time for different values of H and D respectively: a) (2 and 1) mm;b) (3 and 1) mm; c) (3 and 0.5) mm; d) (3 and 0.5) mm.
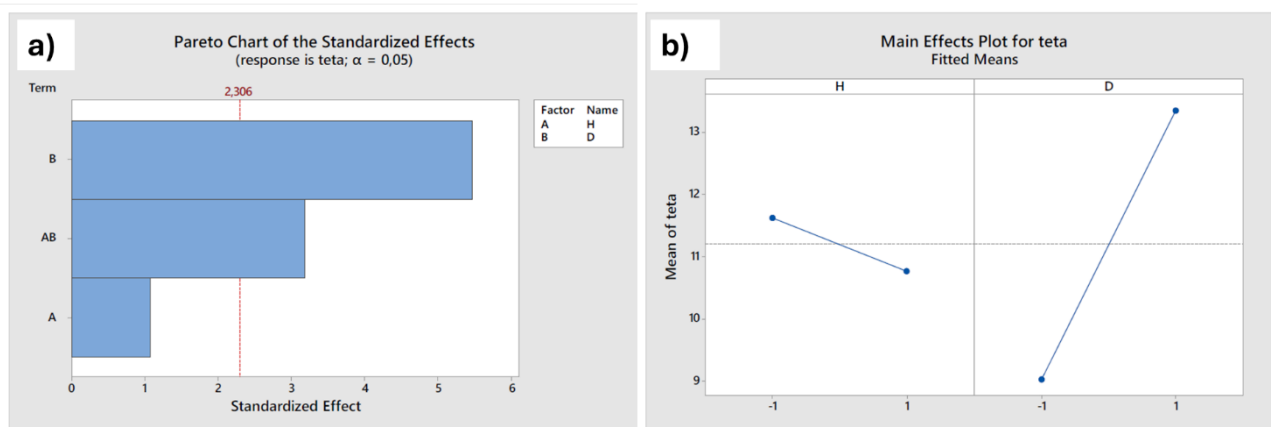
Fig. 2.19: Design of Experiment (DoE) Horizontal ribs results: a) Pareto Chart; b) Main effects plot.

Table 2.8: Regime bending and Log decrement for each combination and repetition tested using Horizontal ribs.

	Combination	A (H)	B (D)	Replication [deg] n1 [deg]	n2 [deg]	n3 [deg]	μ [deg]	σ [deg]	Δθr, %	σ/μ%
Regime Bending	1	-1	-1	8.77	10.82	12.57	10.72	1.9	-16.4	17.8
	2	1	-1	6.12	7.62	8.28	7.34	1.11	-42.8	15.1
	3	-1	1	13.45	11.45	12.64	12.51	1.01	-2.4	8.1
	4	1	1	15.39	14.36	12.81	14.19	1.3	10.6	9.2
Log decrement	1	-1	-1	8.77	10.82	12.57	10.72	1.9	-16.4	17.8
	2	1	-1	6.12	7.62	8.28	7.34	1.11	-42.8	15.1
	3	-1	1	13.45	11.45	12.64	12.51	1.01	-2.4	8.1
	4	1	1	15.39	14.36	12.81	14.19	1.3	10.6	9.2

2.4.3.2 45° Ribs Characterization

Likewise, to the study of the previously paragraph, the 45° ribs were studied printing three sample for each factorial combination $(H = 2, D = 0.5), (H = 2, D = 1), (H = 3, D = 0.5)$, and $(H = 3, D = 1)$ mm. The regime bending vibration was evaluated for each combination (**Fig. 2.20**) and repetition in order to evaluate the means and the standard deviation, like shown in **Table 2.9**.

In contrast to the results of the horizontal ribs, the 45° do not minimize the joint vibration during the bending: the third combination $(H = 2, D = 1)$ mm presents the minimum value percentage of the log decrement (+8.9) but is 50% lower than the horizontal reduction vibration.

From the factorial 2^2 DoE, H and D factors exceed the threshold of the alpha level (α), the red dotted line in Fig. 7 a: this has a statistically important effect on the variation of the regime bending; the term mixed AB has not relevant. Using the 45° ribs, the impact on the vibration bending is similar for both H and D factors: passing from level -1 to level $+1$, H factor has an influence comparable to the factor D (higher slope curve determines a significant variation on the response). Negative slope line means a decrease in the value of the response (in this case the speed bending) when D passing from level -1 to level $+1$. See **Fig. 2.21 b**.

Concluding, the plan shows that the 45° ribs like geometrical solution does not minimize the bending vibration: any combination of levels, does not improve the degree of bending compared to the previously DoE. The degree of bending achieved for all combinations of levels is therefore much worse cause the inclination of such ribs tends to stiffen the joint for the friction between the ribs.
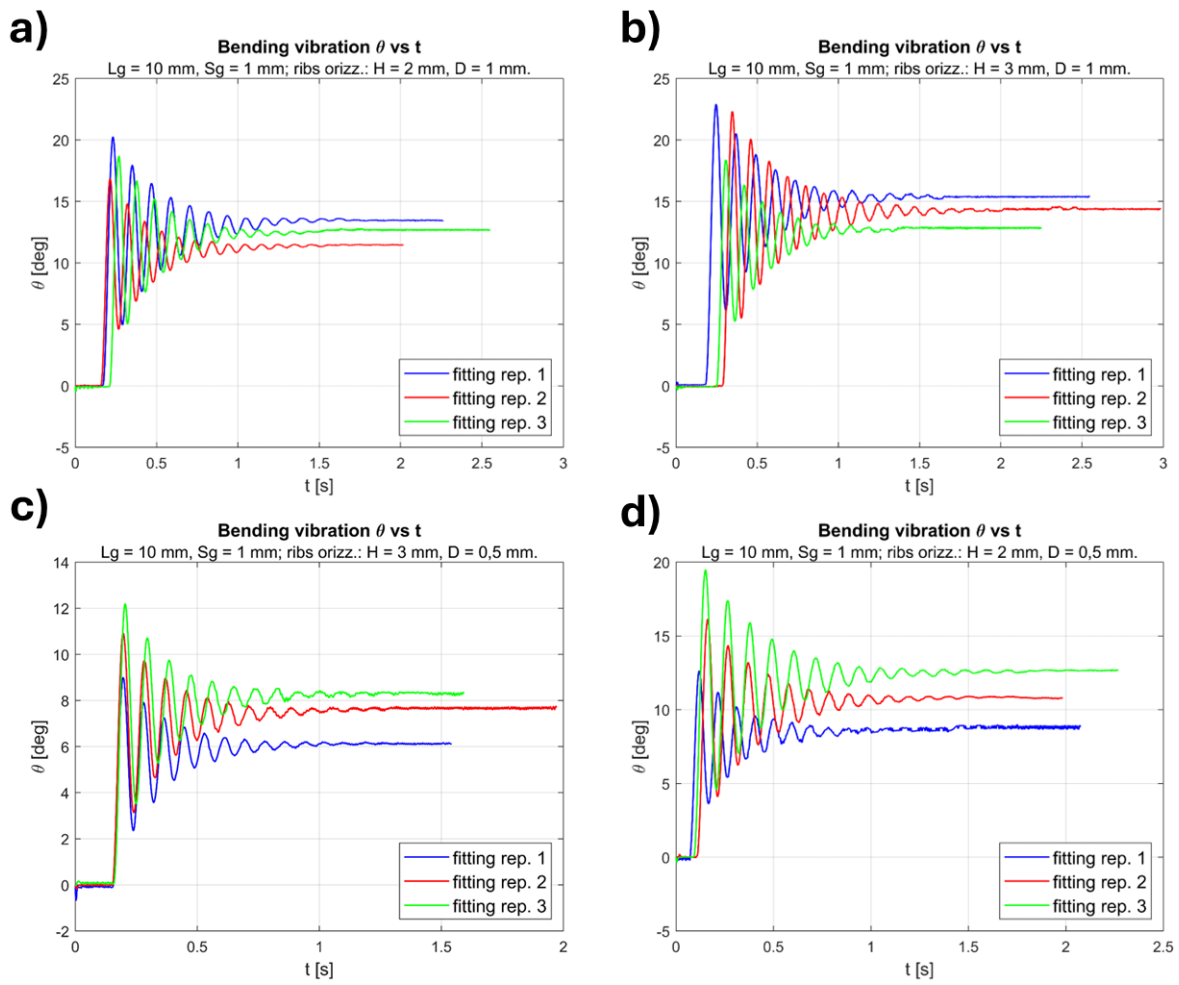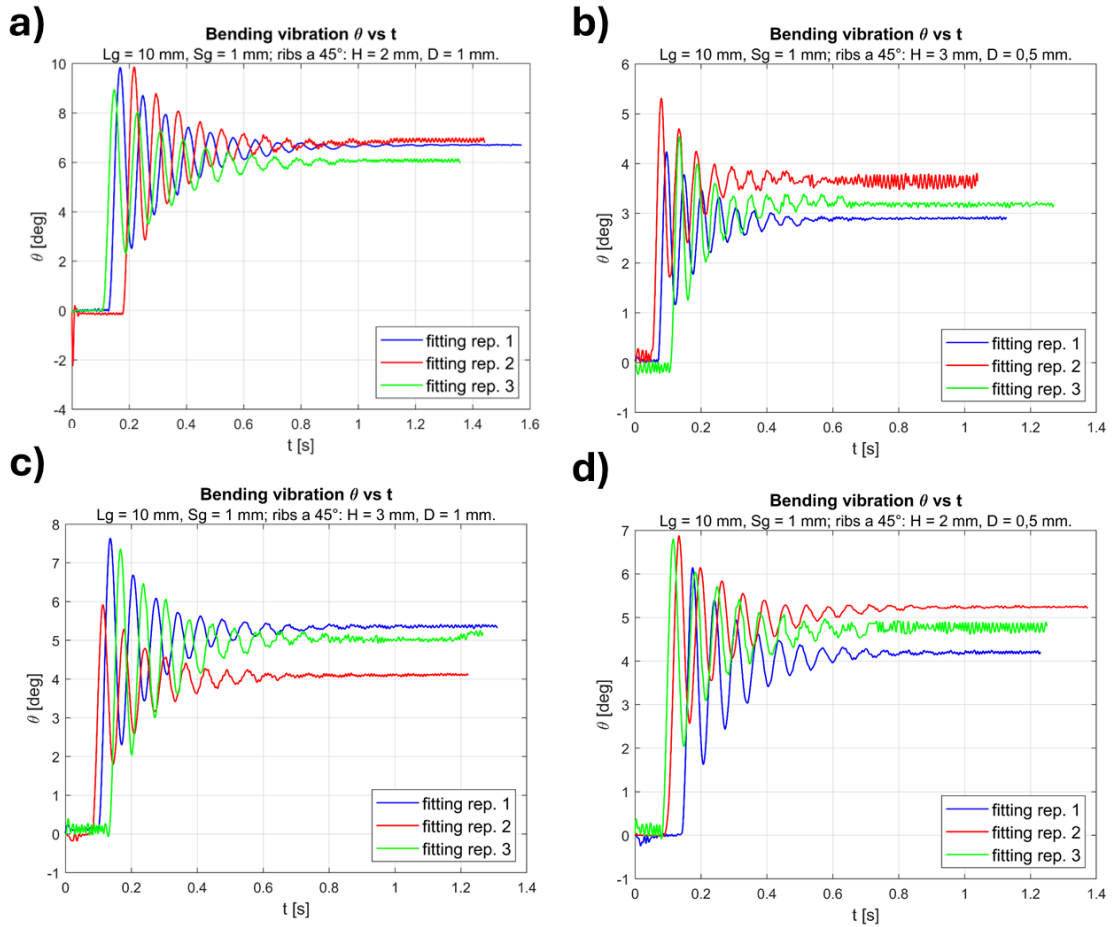
Fig. 2.20: Bending vibration vs time for different values of H and D respectively: a) (2 and 1) mm; b) (3 and 0.5) mm; c) (3 and 1) mm; d) (2 and 0.5) mm.
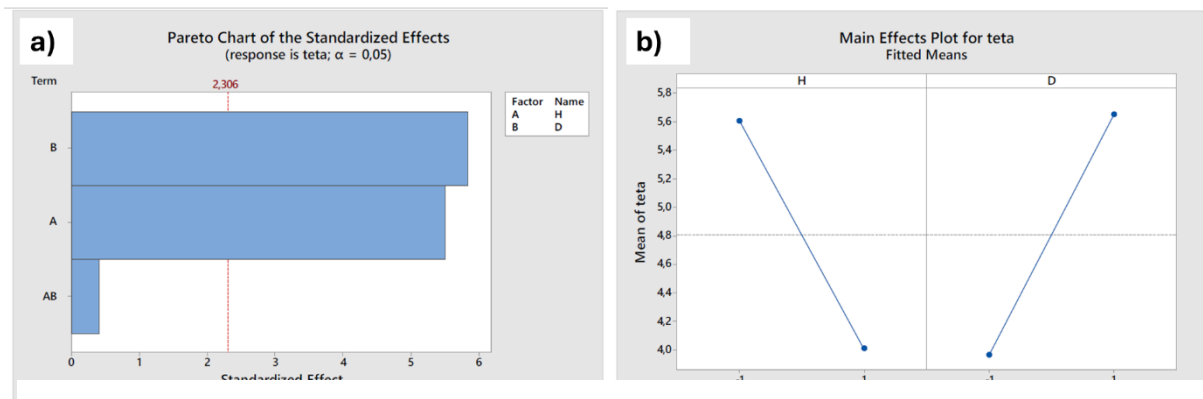
Fig. 2.21: Design of Experiment (DoE) 45° ribs results: a) Pareto Chart; b) Main effects plot.

Table 2.9: Regime bending and Log decrement for each combination and repetition tested using 45° ribs.

	Combination	A (H)	B (D)	Replication [deg]			μ [deg]	σ [deg]	Δθr, %	σ/μ%
				n1 [deg]	n2 [deg]	n3 [deg]				
Regime Bending	1	-1	-1	4.21	5.22	4.68	4.7	0.5	-63.3	10.71
	2	1	-1	2.87	3.62	3.2	3.32	0.38	-74.8	11.76
	3	-1	1	6.65	6.84	6.04	6.51	0.42	-49.2	6.45
	4	1	1	5.32	4.06	5.01	4.8	0.66	-62.6	13.71
Log decrement	1	-1	-1	0.521	0.532	0.354	0.469	0.1	16.6	21.3
	2	1	-1	0.367	0.508	0.737	0.538	0.187	33.7	34.7
	3	-1	1	0.473	0.44	0.401	0.438	0.036	8.9	8.3
	4	1	1	0.588	0.435	0.505	0.51	0.077	26.7	15.1

2.4.4 Conclusions

In conclusion, in the present work soft EM devices by employing TPU and a commercial grade MEX machine have been fabricated and characterized. The main problem of EM soft robots is the high vibration during their usage making them unreliable for accurate tasks. For this reason, the vibration behavior has been studied and a way to reduce it without recurring to any external damper has been provided. Taking full advantage of the huge geometric freedom related to AM technologies, some ribs have been fabricated to reduce vibration. According to the implemented DoE, ribs orientation (horizontal and 45°), thickness (2 and 3 mm) and spacing (0.5 and 1 mm) have been studied and a reduction of vibration of 16% was obtained using the optimal combination of horizontal orientation, 2 mm of thickness, and 1 mm of spacing. This result makes additively manufactured soft EM robots very appealing for grasping operations: future works will be focused on the fabrication of gripping systems based on EM actuation systems.

3. CHAPTER 3: CUSTOM-MADE MEX SETUPS AND FABRICATION APPROACHES FOR PROCESSING NON-CONVENTIONAL MATERIALS: MAGNETIC-INK, SELF-HEALING POLYMERS, AND ELECTRICALLY CONDUCTIVE POLYMERS

3.1 Introduction of the chapter

As discussed in the previously chapter (chapter 2), Material Extrusion (MEX) technique has emerged as a leading technology for fabricating complex polymeric structures that are challenging to produce using traditional methods. These include non-assembly mechanisms, smart structures with embedded sensors [116], [117] and soft robots [43], [52]. Conversely, the complex polymer structures and the development of novel composite materials requires the study of innovative MEX setups (such as machine modifications of hardware and/or software parts) and advanced fabrication approaches (such as 3D printing strategies, printing parameters, and post-process) [118]. Indeed, recent studies have highlighted the importance of optimizing MEX setups to enhance the rheological, mechanical and 3D printing properties of such innovative polymers [21], [119].

Particularly, this chapter focuses on the novel MEX setups and fabrication approaches for non-conventional materials such as magnetic-ink, self-healing polymers, and electrically conductive polymers.

- **MAGNETIC-INK**

Novel applications based on the extremely high design freedom owing to the leveraging of silicone-based MEX include traditional and variable stiffness artificial muscles [120], [121], bio-inspired robots [122], soft robots capable of out-of-plane motions [123], meniscus implants [124], and electrothermally actuated 4D printed silicone robots [125]. Numerous researchers have successfully sought to enhance the potential of silicone-based MEX technology. Hamidi and Tadesse [126] studied an innovative way to create supports by employing carbohydrate glasses to fabricate hollow structures. After the fabrication process, the sacrificial support was dissolved, and the silicone structures were pneumatically actuated with a bending angle of 70°. However, the fabrication of the tall silicone structures is still underexploited because the heat used to cure the extruded silicone only comes from the building plate. The most viable solution to overcome this issue is by assembling the external heating elements near the nozzle to locally cure the extruded silicone, thereby enabling the fabrication of the tall structures [127]–[129] . The exploitation of silicones characterized by different

curing mechanisms, such as moisture curing and UV light, is another method for fabricating tall structures [130]–[133]. Manufacturing structures with external elements integrated during the fabrication process to enhance the functionality of 3D printed objects has made the MEX technology extremely appealing [31], [33], [134], [135]. Bodkhe et al. created a custom-made setup to jointly extrude silicone and incorporate shape memory alloy (SMA) wires [61] to create structures with embedded actuation systems. A new wave based on smart materials capable of performing motions (walking, bending, and crawling) in response to external stimuli has recently emerged [136]–[139]. It reduces the assembly tasks required to fabricate structures, thereby resulting in reduced manufacturing time and cost savings. A novel approach employed to fabricate extremely soft smart structures capable of reshaping and reprogramming their architecture involves creating custom-made silicone mixed with magnetic fillers (i.e., NdFeB), which is extruded using MEX technology and actuated by an external magnetic field. The flexibility of the MEX technology and the high degree of customization of the extrusion setups permit the integration of an external electromagnet (or permanent magnet) assembled near the nozzle tip, thereby generating a magnetic field acting on the extruded silicone [119], [140], [141]. The magnetic fillers inside the silicone are oriented based on the direction of the magnetic field, thereby creating magnetic anisotropy. It is noteworthy that the magnetic field affects only a limited amount of silicone inside the syringe (only the material flowing out from the nozzle tip, thus not producing any remarkable effect during the fabrication). Owing to the magnetic anisotropy, different parts of the structure exhibit different behaviors while exposed to an external magnetic stimulus, thus resulting in complex and unconventional motions of the overall structure [118], [140], [142]. To push silicone MEX technology towards a new mass-production dimension, besides simulation works aimed at understanding the rheological behavior of the extruded silicone [143]–[146], numerous studies correlating process parameters to silicone performance have been performed. Colpani et al. found that the final accuracy of the extrudate silicone strands was positively and negatively linked to an increase in the build plate temperature and deposition rate [147], respectively. Plott et al. correlated the printing strategies (infill line direction) with the formation of voids in the silicone samples, and the mechanical performance. They pointed out that orienting the extruded lines at 0∘ had the worst performance owing to the tangency voids and poor edge surface finish [148]. Walker et al. performed a peeling test to correlate the interlayer adhesion with the single extruded bead cure percentage and found that the degree of adhesion between the consecutive layers increased at low curing rates [149]. The layer height parameter (also known as layer thickness), as for the widespread filament- MEX [150], plays a key role in determining the overall printing forces involved during the extrusion of silicone. Low values of the layer height parameter ($0.1\ mm$) are required to increase the layer adhesion and thereby the mechanical

properties, decrease the number of intralayer voids, fabricate structures with a very high level of detail and accuracy, and fabricate thin-walled structures. However, by setting low values for the layer height, the force involved in the 3D printing process abruptly increases, thereby resulting in numerous problems, such as over-extrusion, poor accuracy, and the impossibility of printing non-rounded toolpaths [146], [151].

- **SELF-HEALING POLYMERS**

Polymer structures are susceptible to damage in various applications: overloads, impacts, or sharp objects can cause cracking, ruptures, or cuts, while cyclic loading can induce fatigue, ultimately leading to failure. In 3D printed structures, these damages often occur faster due to the presence of defects (e.g. air pockets or contaminants), insufficient interlayer adhesion or porosity, hereby resulting in limited structural integrity and lifespan [152], [153]. In this context, extrudable self-healing polymers could potentially overcome these problems, by introducing self-healing capabilities in 3D printed structures [35], [37], which can be extrude using custom-made setups.

Self-healing polymers are smart materials having the unique ability to self-repair damages, cracks, and cuts by means of a self-healing mechanism which is either extrinsic or intrinsic [154]. Extrinsic self-healing polymers are not able to heal themselves: the incorporation of healing agents (capsule-base or vascular-based) triggers the healing process after damage [155]. 3D printing has been leveraged on to create these extrinsic self-healing polymers, enabling to incorporate microchannels or pockets that hold healing agent [156]. Alternatively, intrinsic self-healing are based on reversible bonds [157], [158], including dynamic covalent bonds such as the dissociative Diels-Alder reaction or the associative transesterification reaction, or physic-chemical bonds such as hydrogen bonds. Consequently, the healing capability is intrinsic to the polymer, excluding the need for a healing agent. Unlike for extrinsic self-healing polymers, their intrinsic self-healing capability can be completely recovered after healing, allowing for multiple damage-healing cycles on the same location. Self-healing polymers based on the Diels-Alder reaction, like those resulting from the cyclo-addition reaction of furan and maleimide, are well-known for combining mechanical strength and stability, with self-healing at moderated temperatures [159]–[161]. For example, Li et al. [162] developed a shape memory and self-healing materials incorporating thermoplastic polyurethane in the covalent adaptative networks epoxy, based on Diels-Alder reactions, for enhance both the material's strength ($35\ MPa$) and the healing properties. Safaei et al. have illustrated that by using off-stoichiometric maleimide-to-furan ratios leads to an acceleration of the self-healing process due to an excess of furan, enabling autonomous self-healing in ambient conditions (e.g. at $25\ °C$) with near perfect recovery of their mechanical properties and this in a reasonable time frame (e.g. a couple

of hours) [163]. They have used this approach to construct self-healing soft robotic structures, including a soft bionic hand, that heal from macroscopic damages without any external intervention while recovering their full performance [164].

Moulding-based fabrication techniques, also referred to as formative manufacturing, have been largely employed for the fabrication of self-healing polymeric structures since such process results to be fast to implement [159], [165]; on the other hand, these techniques are characterized by several drawbacks: i) lack of design flexibility, ii) lack of scalability, iii) many assembly tasks for the fabrication of multi-material structures [166]. Material Extrusion (MEX) 3D printing, especially filament-based and ink-based methods, has emerged as a viable solution for overcoming these issues [71], [167]. Roels et al. [168] presented a novel filament-based MEX approach to 3D print self-healing elastomers based on Diels Alder reaction. The authors fabricated and tested several 3D-printed grippers and concluded that using Diels-Alder polymers in 3D printing leads to parts with increased isotropy in their mechanical properties (isotropy in fracture stress as high as 86%). This improvement is results from a reduced porosity due to the low viscosity of the Diels-Alder polymer in its liquid state, as well as from interlayer covalent bonding between print layers. In another work, Li et al. [169] developed a series of poly(urethane-ureaamide) elastomers with self-healing and shape memory capabilities for filament-based MEX: the reduction of warpage and increasing of mechanical properties (tensile strength and Young's modulus) were studied and optimized by means of process parameters and material properties. Considerable efforts have been made towards the increase of mechanical properties, the reduction of anisotropy, and enhancement of layers adhesion for self-healing structures processed through MEX [170], [171]. As a matter of fact, Wang et al. [172] customized a commercial filament-based MEX machine by adding near-infrared (NIR) light, to heat the freshly extruded layer: in this way the temperature of every extruded layer was increased, thereby enhancing interfacial bonding strength between consecutive extruded layers.

Despite the tremendous interest gained from filament-based MEX for processing self-healing polymers, a new wave based on the leverage of ink-based MEX is becoming very popular due to some intrinsic features such as i) the possibility of extruding soft inks doped with different fillers [90], [173], ii) the possibility to couple soft inks with rigid materials [119] and iii) the fabrication of thin-walled structures [27], [174]. Another great advantage of ink-based MEX is the overcoming of a huge problem negatively affecting filament-based MEX, namely the filament breakage between the pushing gears (feeding mechanism) [42], [150], [175]. Such behavior results to be predominant when custom-made materials, with no additives, are prepared and extruded. Lastly, ink-based MEX excludes the need for extensive pre-processing of the polymer in a high-quality filament, which is both economical and ecologically beneficial. For all these reasons, ink-based MEX could potentially

be an excellent fit for the extrusion of self-healing structures. Another advantage of intrinsic self-healing polymers based on thermoreversible bonds, such as those utilizing the Diels-Alder reaction, is their thermo-mechanical reprocessability. They degel above their degelation temperature ($Tgel$) allowing them to be reshaped and reprocessed [176]. Diels-Alder-based self-healing polymers, in particular, exhibit exceptionally low viscosity in their degelled liquid state, making them ideal candidates for recyclable ink for ink-based MEX [177]. However, this requires customized ink-based MEX, equipped with an adequate heating system that liquifies the Diels-Alder polymer prior to extrusion and deposition. Moreover, this additional temperature control during the deposition of ink-based materials enhances the mechanical properties of the printed parts, such as the layer adhesion and isotropy [149], [178], [179]. As a matter of fact, Yuan et al. [180] embedded a heating element around the syringe barrel to keep a constant extrusion temperature of $120°C$: in this way, the ink viscosity was controlled, and self-healing structures have been successfully fabricated. Furthermore, the printed parts exhibited a tensile strength of $77\ MPa$ and healing rate after damages up to 85%. Similarly, a syringe wrapped with a heating element (70°C) for a custom-made UV-light-assisted ink-based MEX setup was used by Kuang et al. [35]. They 3D printed a shape-memory and self-healing structures with semicrystalline thermoplastic incorporated inside semi-interpenetrating polymer network elastomer, demonstrating the potential of 3D printing for creating stretchable structures with in-plane isotropic properties, capable of reaching elongations of up to 600%. High-precision extrusion control was achieved by Yang et al. [181]: they extruded a custom DA-based ink was by utilizing a modified syringe equipped with a heating element ($130 - 138°C$) and an additional cooling mechanism, such system resulted to be extremely effective to reduced anisotropy and simultaneously improve printing accuracy across various printing directions.

- **ELECTRICALLY CONDUCTIVE POLYMERS (for piezoresistive sensors)**

Both custom-made setup and multi-nozzle extrusion commercial machines has been used to create assembly-free structures with embedded sensors capable of detecting various kinds of external stimuli [182], and conductive element for 3D printed batteries (see Chapter 4).

Despite recent advances in the fabrication of piezoelectric [49], [183] and capacitive sensors [102], [184], [185] manufactured via the MEX technique, MEX piezoresistive sensors continue to have the potential to impact the sensor community at large due to (i) the possibility to sense multiple variables (i.e. force, strain, bending, torque and so on) and (ii) the possibility to be embedded inside thermoplastic-based components with ease [186]–[188]. Piezoresistive sensors operate based on the change of electrical resistance when deformed and are typically manufactured by either employing

commercial or custom-made conductive materials composed of a thermoplastic matrix doped with conductive fillers (i.e. carbon black, carbon nanotubes, etc.) [189]–[194].

The multi-material MEX approach has been used to fabricate several robotic systems capable of detecting multiple stimuli. Wang et al. [195] fabricated a foldable magnetic soft robot with an embedded piezoresistive sensor in a single manufacturing process, capable of changing electrical resistance every time the robot was folded. Other works have developed 3D printed gripper systems with embedded sensors [196]. Stano et al. fabricated a polycaprolactone (PCL)-based finger with an embedded strain sensor capable of detecting the position in the x-y space [31]. Singh et al. [197] fabricated a bellow with a piezoresistive ring-shaped sensor providing displacement feedback through a change in its electrical resistance. Matharu et al [198] employed 3D printed piezoresistive flexible sensors to obtain feedback from a jellyfish-like soft robot while swimming.

Piezoresistive sensors have been studied as a means to bridge the gap with other sensors manufactured with traditional technologies in terms of performance. Maurizi et al. experimentally validated a quasi-static model to calibrate 3D printed piezoresistive sensors integrated inside polylactic acid (PLA) structures [199]. Arh et al. [200] used the Bridgman model to determine the dynamic piezoresistivity coefficients in different orientations, allowing future modelling regardless of the orientation of the embedded sensor inside the dielectric structure. 3D printed piezoresistive sensors capable of detecting bending angle are extremely attractive and have risen as one of the most promising application points for multi-material MEX. Such sensors have been embedded inside (i) soft structures used as grippers to manipulate fragile objects, (ii) rehabilitative and wearable devices [6], [201]–[204]. Despite all the aforementioned benefits, piezoresistive sensors prepared via MEX technique still suffer of poor sensitivity and conductivity. At the state of the art, three main strategies have been employed to address such problem. The first strategy relies on the sensor geometry optimisation: as shown in [205]–[207] the sensor design can be actively used to improve the sensor sensitivity by concentrating the bending in small sections. The second way to improve the sensitivity in 3D printed piezoresistive sensors is based on the material modification: the creation of 3D conductive networks inside the thermoplastic matrix [208] and the usage of different conductive fillers such as graphene nanoplatelets and silver nanoparticles [209] has been proven to greatly increase sensor sensitivity. The third method to improve the sensitivity of 3D printed piezoresistive sensor is based on the optimisation of printing process parameters [111], [210]: Stano et al. [21] studied two fabrication approach to increase the sensitivity of the 3D printed sensors. They use first a custom-made roll setup applied at the extrusion head and secondly used a ironing printint parameter. Palmic et al [211] demonstrated that the conductivity can be improved by setting a layer height value ranging between 0.15 and 0.3 mm. Goh et al [212] demonstrated the direct correlation between infill type and

sensitivity of piezoresistive sensors. Their work found that a deposition direction of 45, and 0° provided the best results in terms of sensitivity. All of the methods found in literature do not take into account the layer adhesion and porosity issues that negatively affect sensors produced via MEX, and mainly focus on the chemical aspect of the raw material being processed, as well as optimisation of design and process parameters.

The following Table 3.1 summarized the custom setups and fabrication approaches of the non-conventional material discussed above.

Table 3.1: Custom materials, setups and fabrication approaches used to extrude non-conventional polymers.

	Custom material	**Custom setups**	**Fabrication approaches**
Magnetic inks	[119], [120], [123], [124]	[41], [102], [123], [124]	[109], [130], [131], [132]
Self-healing polymers	[144], [145], [146], [151]	[154], [163], [18], [164], [213]	[150], [155]
Conductive polymers	[171], [177], [191], [192]	[101]	[178], [179], [189], [190], [192], [193], [194], [195]

The chapter 3 is organized as follows: in section 3.2 electromagnetic assistance to enables 3D printing of silicone-based is discussed. In section 3.3 several innovative printing approaches to increase sensors sensitivity were studied. Finally, a custom-made setup to extrude self-healing materials for sensors fabrication is presented in section 3.4.

3.2 Custom MEX setup: Electromagnetic assistance enables 3D printing of silicone-based thin-walled bioinspired soft robots.

In this study, a novel methodology to reduce the printing force when printing at low values of the layer height (0.1 mm) is shown. By employing the innovative proposed approach, an overall force reduction of 21.08% is achieved. The method used to reduce the printing force is based on the use of magnetic ink (Ecoflex 00–10 silicone mixed with Fe_3O_4 nanopowder), which is extruded using a custom-made syringe equipped with 325 copper coils. When the copper coils are supplied with electrical current (4.5 A), a new force is introduced in the system, known as the electromagnetic force (F_{EM}), which is oriented in the opposite direction to the counter-pressure force (F_{C-P}) and the force generated in the syringe (F_S). This way, F_{EM} reduces the overall printing force, thereby enabling the extrusion of the silicone at a low layer height (Fig. 3.1).

Several thin-walled and complex-shaped silicone structures have been manufactured, in addition to bio-inspired soft robots. The latter (including a humanoid finger, knee-based system, bistable actuator, and spider-inspired robot) have been fabricated by extruding stiff thermoplastic material and silicone in the same cycle, thereby proving the completion of the proposed manufacturing approach based on force reduction. In addition, not only the magnetic nanopowder (Fe_3O_4) facilitates the extrusion of the silicone by reducing the overall printing force, but it also allows the fabrication of functional soft structures capable of performing motions in response to magnetic stimulus.
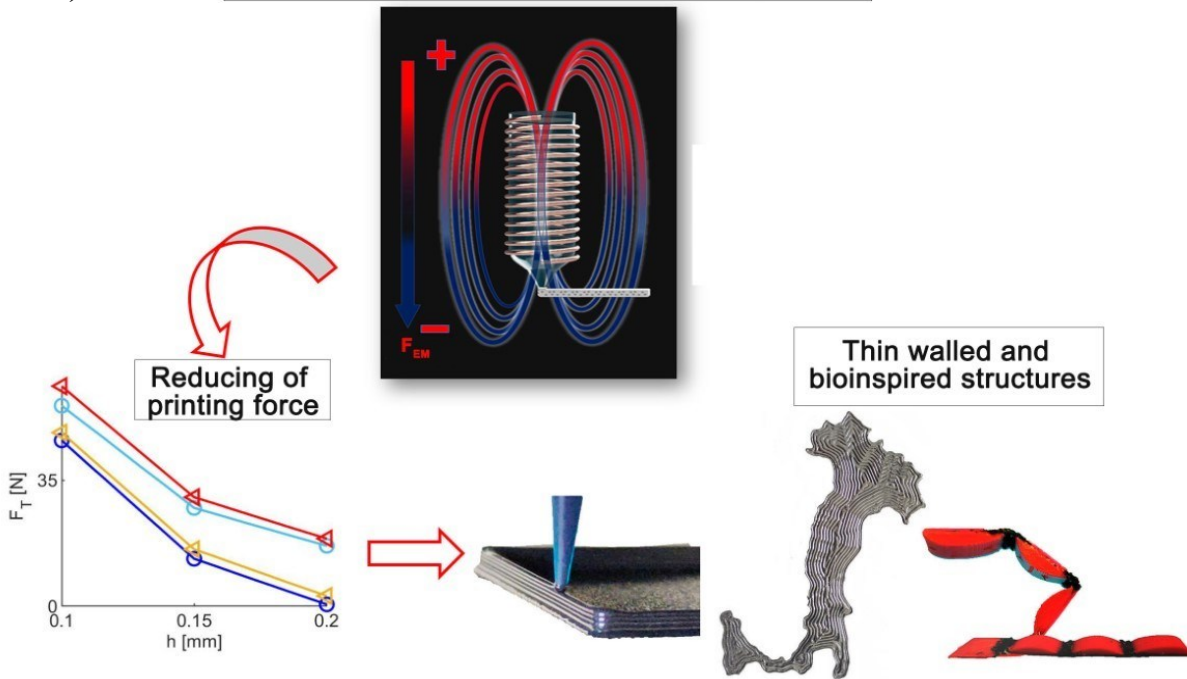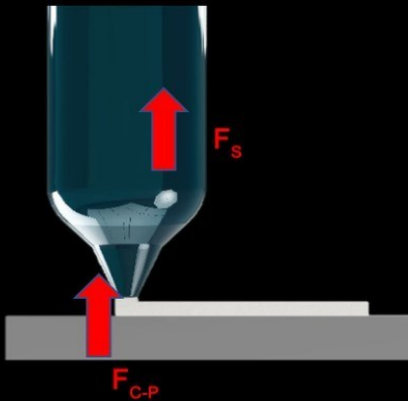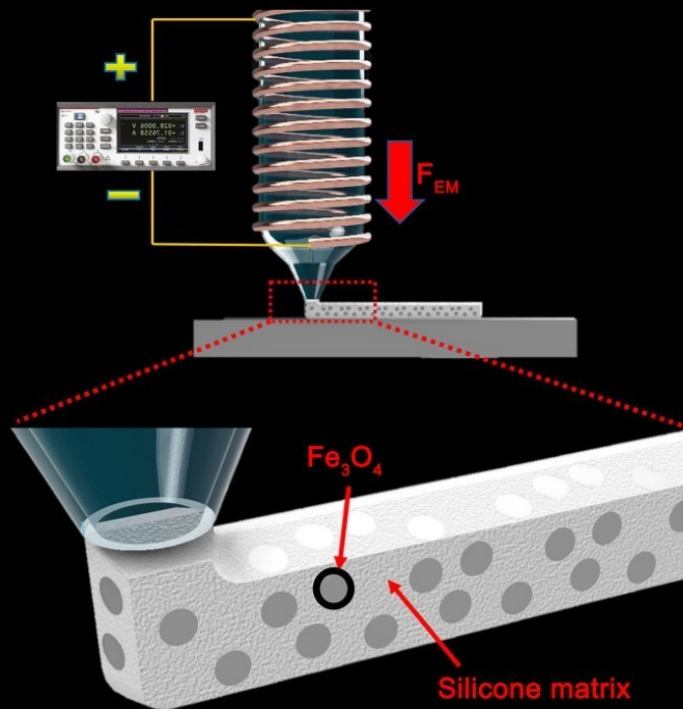
Fig. 2.1: Electromagnetic assisted Additive Manufacturing of magnetic ink for force reduction: a) workflow of the present research and b) comparison between the conventional material extrusion approach to fabricate silicone-based structures and the proposed approach, wherein a new force (electromagnetic force) has been introduced into the system.

3.2.1 Materials and methods

3.2.1.1 Goal of the current research

The ultimate goal of this research is to reduce the overall printing force while extruding silicone-based material at low layer heights ($0.1 \, mm$), thereby enabling the fabrication of thin-walled structures and improving the level of detail achievable in silicone-based MEX by reducing over extrusion problems, as shown in **Fig. 3.1 a**. At the state of the art, silicone has been successfully 3D printed by recurring to MEX setup, but high values of layer height (ranging between $0.5 \, mm$ and $1 \, mm$) are generally set [27], [123], [126]: when lower values are set, the overall printing force abruptly increases resulting in the skewing of the material during the deposition, over-extrusion problem and impossibility to fabricate thin-walled structures. In MEX techniques (both filament- and ink-based), the direct correlation between layer height and layer by layer adhesion has been extensively studied in the last decade, ubiquitously proving that the smaller the layer height the better the adhesion [214]–[217]. Higher interlayer adhesion means improved mechanical properties, fatigue behavior and less delamination problems [130], [148]. On the other hand, when extruding a layer of silicone (k) at low value of layer height (i.e., $0.1 \, mm$), the printing force is extremely high, which is accountable for skewing and deforming the previously deposited layer ($k - 1$). This behavior results to be predominant when the previously extruded layers are thin, thereby making the fabrication of thin-walled structures extremely challenging [151]. The present research proposes a fabrication methodology aiming at overcoming such issues, thereby allowing the extrusion of silicone-based material at low values of layer height.

As shown in **Fig. 3.1 b**, the forces that occur while extruding silicone using conventional MEX technology are: i) the force generated inside the syringe F_s and ii) the counter-pressure force F_{C-P} due to the interaction between the extruded silicone bead and substrate (either the build plate or previously extruded silicone layer). Moreover, the two forces are oriented upward (pointing in the opposite direction of the build plate). The overall total printing force, F_T, is calculated as the sum of the two contributions, expressed as follows (eq. 3.1):

$$F_T = F_s + F_{C-P} \tag{3.1}$$

It should be noted that F_T is linear because it represents the force equilibrium under the syringe nozzle, but both F_S, and F_{C-P} are nonlinear terms since they depend on the solution of Navier-Stokes equations.

F_T can reach high values while extruding at very low layer heights (0.1 mm), thereby resulting in several problems, such as low printing accuracy and skewing of thin-walled structures. To overcome these problems, the authors investigated a method to reduce F_T while printing at low layer heights. To achieve this goal, a new force acting in the opposite direction to F_S and F_{C-P} has been introduced in the system, also known as the electromagnetic force F_{EM}: because it is oriented downwards, as shown in **Fig. 3.1 b** (pointing towards the build plate), it reduces the overall total printing force:

$$F_T = F_s + F_{C-P} - F_{EM} \qquad (3.2)$$

Since F_{EM} acts as a subtractive term, the proposed approach requires less pushing force to extrude soft ink compared to traditional fabrication approach, for the same process parameters. The proposed approach, based on leveraging F_{EM} to reduce F_T (21.08% at a layer height of 0.1 mm), which enhances the extrusion of low layer-thickness silicone structures, has been made possible by recurring to the following artifacts:

1. The silicone was mixed with magnetic nanopowder (Fe_3O_4), having an average size of 53 nm.
2. The syringe used to extrude silicone was equipped with copper coils connected to a power supply to provide electrical current during the extrusion process.

The interaction between the electrical current flowing inside the copper coils (attached to the syringe) and magnetic ink (inside the syringe) generated. The Ecoflex 00–10 silicone was mixed with different $wt\%$ Fe_3O_4, as detailed in Section 3.2.1.2 and Appendix A (section A1). A numerical model capable of predicting force contributions as a function of several process parameters was created and experimentally validated. The custom-made 3D printing machine was also equipped with strain sensors to measure the actual printing force (see Appendix A, section A2) to validate the model and prove the benefits related to the electromagnetic-assisted fabrication approach.

3.2.1.2 Magnetic ink preparation

Commercial Ecoflex 00–10 silicone (Smooth-On, INC Macungie, PA, USA) was employed throughout the study and was successfully extruded using MEX systems [123], thereby revealing its excellent performance in terms of the elongation at break. To provide magnetic properties to the silicone necessary for the leveraging of F_{EM}, commercial Fe_3O_4 magnetic nanopowder (average

nanopowder dimension of $53\ nm$) was added to Ecoflex 00–10 in different weight percentages ($wt\%$). Four different concentrations were tested: $0, 10, 20,$ and $30\ wt\%$. An upper limit of $30\ wt\%$ was arbitrarily chosen: it represents a good compromise between softness of the final ink and magnetic properties required to leverage F_{EM}. As a matter of fact, a higher $wt\%$ of Fe_3O_4 would involve better magnetic properties, and in turn a higher reduction of F_T, but on the other hand it would abruptly reduce the flexibility and softness of the final ink. To ensure the fully dispersion of Fe_3O_4 magnetic nanopowder inside the silicone, the procedure detailed in [218] was followed: at first, Ecoflex 00–10 was prepared by adding parts A and B in a $1:1$ ratio inside a glass container. Afterwards, the desired $wt\%$ of the magnetic nanopowder was added and a glass road was used to constantly stir the slurry (part A, part B, and magnetic nanopowder) for a total of $3\ min$. Further, a degasser (BACOENG, $85\ L/min$) was employed to remove the air bubbles trapped in the silicone matrix: the final slurry was placed in the vacuum chamber for a total of $3\ min$. This step is crucial when extruding silicone using MEX technology, since unwanted air bubbles result in inconsistent extruded beads and an increase in the force required to push the silicone out from the nozzle. The test performed to demonstrate the lack of sedimentation of Fe_3O_4 nanopowder inside the silicone matrix, is described in the Appendix A (section A1, and Fig. A1). It is worth mentioning that the proposed approach involves the use of magnetic ink, which is characterized by mechanical properties that are slightly different from those of pure silicone. The pure Ecoflex 00–10 and Ecoflex 00–10 mixed with $30\ wt\%\ Fe_3O_4$ were mechanically characterized (tensile tests conducted in accordance with ASTM D412), and similar mechanical properties were obtained, except for a reduction in the ultimate tensile strength (UTS) by 12.7%. The reason for this slight reduction is the increase in the solid phase owing to the magnetic fillers inside the soft silicone matrix. Here, a minimal decrease in the softness of the pure silicone is required to reduce the printing force and obtain thin-walled and highly detailed structures.

3.2.1.3 Rheological characterization

Each silicone ink, prepared with different amounts of magnetic nanopowder, was characterized from a rheological standpoint using an MCR 702 rheometer (Anton Paar, Graz, Austria). The data obtained from the rheological characterization were used to create a numerical model capable of predicting the values of F_S and F_{C-P} as a function of the layer height, as described in Section 3.2.1.1. During silicone characterization, the shear rate values ranged from $0.1\ to\ 350\ 1/s$, and a single rheological curve was determined in $2\ min$, which lasted lesser than the silicone pot life at room temperature

(approximately 30 min, based on the material datasheet). Three replicates were performed for each concentration of Fe_3O_4 and the mean values with error bars are shown in **Fig. 3.2 a**.

From the rheological characterization, the following conclusions can be drawn:

1. According to **Fig. 3.2 a**, the dynamic viscosity is negatively correlated with the shear rate (regardless of the magnetic $wt\%$), thereby showing the conventional behavior characteristic of shear-thinning fluids such as silicone.

2. For pure Ecoflex 00–10 ($0\ wt\%$ of Fe_3O_4), the dynamic viscosity was almost constant at very low shear rates (Newtonian regime), whereas at higher shear rates, a gradual transition to the powerlaw regime was observed.

3. By increasing the nanopowder content, a more remarkable power-law behavior was observed. As expected, the dispersed solid phase (Fe_3O_4 nanopowder) increased the macroscopic dynamic viscosity in the shear regime.

Additionally, frequency sweep rheological tests have been performed: storage modulus (G') and loss modulus (G'') have been characterized at different values of angular frequency (ω) ranging from $0.1\ to\ 100\ rad/s$. As shown in **Fig. 3.2 b**, G'' results to be at least one order of magnitude higher than G' at high values of omega, for every ink composition (from pure silicone up to silicone mixed with $30\ wt\%$ of Fe_3O_4). This behavior demonstrates that the viscous effects dominate over the elastic ones. Such outcome has been leveraged for the formulation of the numerical model, based on the assumption of neglecting the elastic behavior of the inks.
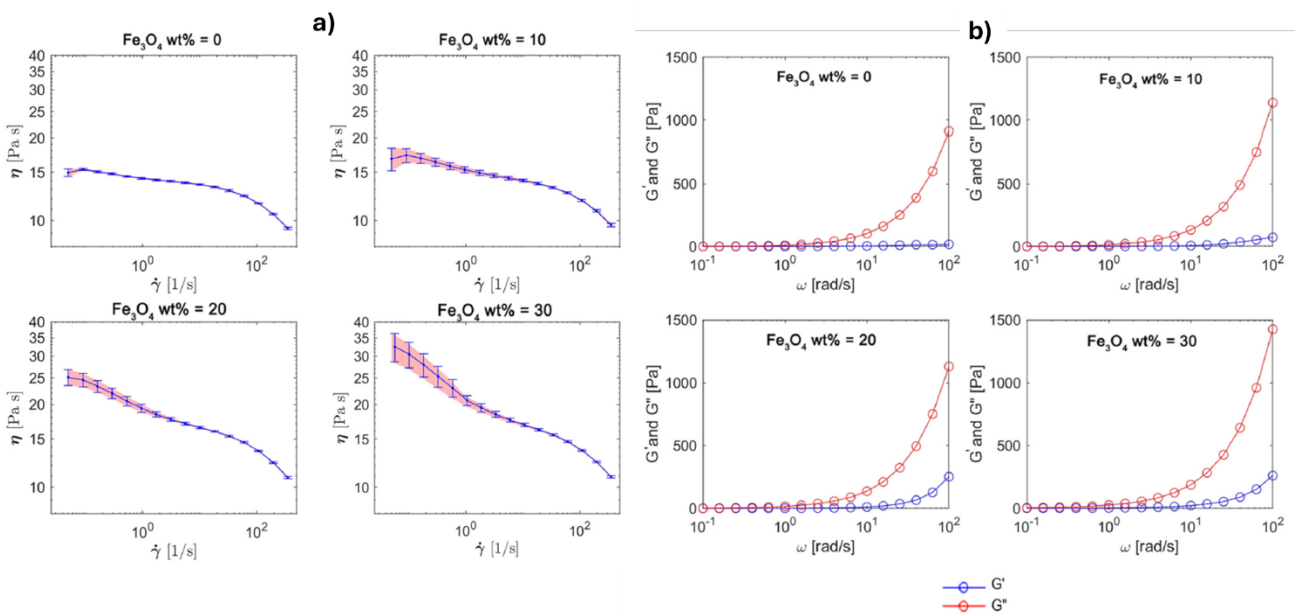
Fig. 3.2: a) Dynamic viscosity as a function of the shear rate for the four different concentrations of magnetic nanopowder, and b) Storage modulus (G') and loss modulus (G'') for the four different concentrations of magnetic nanopowder.

3.2.1.4 Custom-made 3D printing setups

A commercial dual-extruder 3D printer (Sovol SV04, Sovol, United States) based on MEX technology was modified to enable the extrusion of magnetic ink through a calibrated nozzle by implementing the proposed approach based on the leverage of F_{EM}. The 3D printer used throughout the present study was equipped with two independent print heads to process thermoplastic filaments. Only the print head located on the right side was modified to extrude silicone, while that of the left was kept unchanged. In this way, structures comprising thermoplastic and silicone materials can be fabricated in a single-step manufacturing cycle without assembly tasks.

The working mechanism underlying the extrusion of the magnetic ink and leverage of F_{EM} are based on the following elements:

1. A stepper motor (Creality NEMA 17 BJ42D15–26V50) was connected to a lead screw to generate linear motion.
2. A custom-made pushing part connected to the lead screw pushes the syringe piston, thereby resulting in silicone extrusion through a calibrated nozzle connected to the syringe.
3. A custom-made syringe holder.
4. A custom-made syringe equipped with 325 copper coils connected to a power supply and an electrical current of 4.5 A was provided to generate the F_{EM} acting on the magnetized silicone.
5. A heating element was placed near the nozzle and equipped with a fan to blow heat over the extruded silicone to assist the local curing process. A heated built plate was also used as a curing source.

The custom-made syringe used to extrude magnetic ink was equipped with a force sensor to record the forces during the extrusion process, while a commercial force sensor with a resolution of 0.1 N was employed. More details on the data acquisition are provided in the Appendix A (section A2). Owing to its low thickness, the force sensor was placed between the pushing part and syringe piston, and the same method shown in [42] was used to measure all the force contributions F_{C-P}, F_S, F_T, and F_{EM} while extruding based on the conventional and proposed approaches. **Fig. 3.3** shows the custom-made 3D printing machine used to reduce the printing force while extruding ink.

3.2.1.5 Process parameters set for model validation

A nozzle diameter of $1.02\ mm$ was employed in the experimentation phase, and a line width equal to the nozzle diameter was set in the slicing software. The following nozzle size was arbitrarily chosen since it represents a good compromise between good level of detail (low values of extrudate width) and low manufacturing time, however smaller and bigger nozzles can be employed as in **Fig. 3.8**. A low printing speed equal to $10\ mm/s$ was also set in conjunction with a build plate temperature equal to $70\ \circ\ C$. The latter is a crucial parameter in the 3D printing of silicone because it is the main tool for curing extruded silicone. Here, a lower temperature cannot cure the silicone rapidly, thereby resulting in the impossibility of maintaining the desired shape. However, a higher build plate temperature results in the unwanted curing of the silicone inside the plastic nozzle. In addition to the build-plate temperature, another heating source was used to extrude more complex and taller structures: an additional heating element was assembled near the nozzle. The additional heating element was coupled with a fan to blowheat over the extruded silicone.
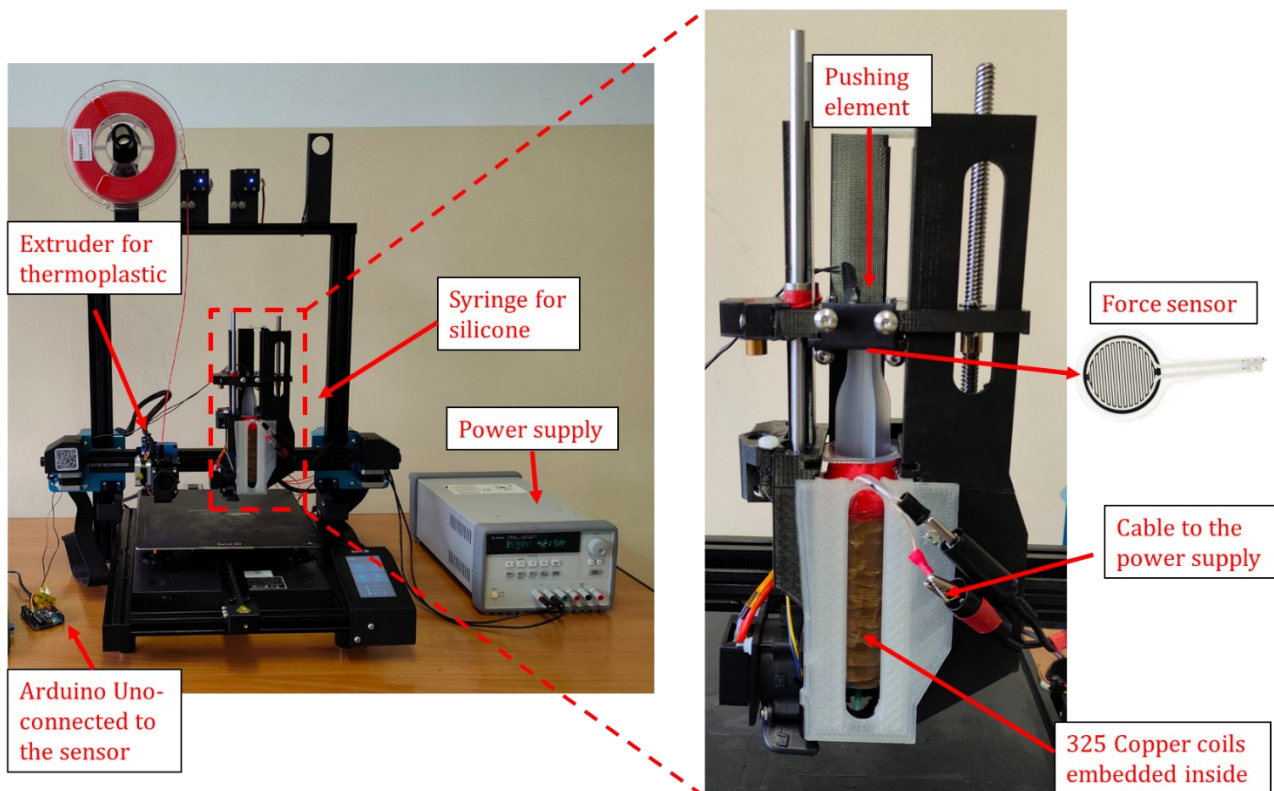
Fig. 3.3: Custom made Material Extrusion setup capable of monolithically extruding ink and thermoplastic material in the same manufacturing cycle. The syringe reservoir is equipped with 325 copper coils connected to a power supply (4.5 A) to leverage the electromagnetic force to reduce the overall printing force. A force sensor has been placed between the syringe piston and the pushing element to record force values and validate the numerical model.

3.2.2 Results of the proposed approach

3.2.2.1 Numerical model to predict 3D printing forces

The silicone-based MEX process has been numerically modeled using the finite element method (FEM)-based software "COMSOL Multiphysics" v. 5.5 (Fluid Flow Module) to predict the impact of every force contribution (F_S and F_{C-P}) on the overall printing force F_T. Further, the proposed approach, based on the leverage of F_{EM} to reduce the total force while extruding at low values of layer height ($0.1\ mm$), has been modeled as well, thereby revealing a maximum force reduction of 21.08% (from the experimental phase) compared to the conventional 3D printing approach. To model the force generated inside the syringe F_S, the isothermal single-phase fluid flow in the nozzle was modeled under the following boundary conditions:

- Velocity inlet: A fully developed flow was imposed, and under a prescribed value of the volumetric flow rate, COMSOL evaluated a parabolic-like inlet velocity profile. This condition was more representative of the experimental setup because force measurements were performed under steady-state conditions.
- No slip: There is no relative motion between the fluid and nozzle walls.
- Symmetry axis: This permits the study of a 3D problem using a 2D axisymmetric model.
- Pressure outlet: A zero-average pressure was imposed at the nozzle outlet and the fluid flow was assumed to be fully developed.

It should be noted that, throughout the whole research, the fluid extruded by the syringe (both pure silicone and magnetic ink) has been modeled as a generalized Newtonian fluid: the shear-thinning behavior shown in **Fig. 3.2 a** has been considered when modeling F_S, and F_{C-P}. The nozzle (diameter of $1.02\ mm$) used to extrude the magnetic ink comprised two tapered sections, while the overall pressure drop (ΔpN) was used to calculate F_S. The geometrical and computational domains are shown in **Fig. 3.4 a**, and **b**. The syringe-pushing area is expressed as:

$$A_S = \frac{\Pi D_S^2}{4} \tag{3.3}$$

Here, D_S is the syringe piston diameter (**Fig. 3.4 g**). The pressure drop along the nozzle axis ΔpN can be expressed as:

$$\Delta_{P_n} = \int_0^L \frac{\partial p}{\partial z_n}\, dz_n \tag{3.4}$$

where Z_N is the direction of the nozzle axis direction, as shown in **Fig. 3.4 b**. The syringe contribution to the extrusion force is expressed as:

$$F_s = A_s \Delta p_N \tag{3.5}$$

To model the counterpressure force F_{C-P}, layer deposition over the build plate was simulated using 2D COMSOL simulations (**Fig. 3.4 c,d,e,** and **f**). All the different silicone compounds (different $wt\%$ of Fe_3O_4) were characterized from a rheological standpoint. The dynamic viscosity was negatively correlated to the shear rate (regardless of the magnetic $wt\%$), thereby showing the conventional behavior characterizing shear-thinning fluids, such as silicone [146]. The mean rheological data for each concentration of the magnetic nanopowder (**Fig. 3.2** b) were imported into COMSOL, and cubic interpolation between contiguous points was performed.

Second-order shape functions were used for the flow-field components, whereas first-order shapes were sufficient for obtaining pressure information. The pressure drop below the syringe nozzle (Δp_C) could be obtained by integrating the pressure gradient along the z_C-direction, as shown in **Fig. 3.4 f**:

$$\Delta_{P_c} = \int_0^{\frac{D_{(ext)}^n - D_{ext}}{2}} \frac{\partial p}{\partial z_C} dz_C \tag{3.6}$$

After finding Δp_C, the counterpressure force can be expressed as:

$$F_{C-P} = A_s \Delta p_C \tag{3.7}$$

Here, As is the syringe pushing area expressed in (3.3). To model the counter-pressure force F_{C-P}, the following boundary conditions were applied:

- Velocity inlet: A fully developed flow was imposed, and under a prescribed value of the volumetric flow rate, COMSOL evaluated a parabolic-like inlet velocity profile.
- No slip: There was no relative motion between the fluid and the nozzle wall (Upper wall: a fixed velocity V_P equal to 10 mm/s was set. Lower wall: the built plate is assumed to be stationary).
- Pressure outlet: fully developed flow with zero average pressure.

The total printing force F_T in the conventional silicone MEX is the sum of the syringe and counterpressure contributions expressed as:

$$F_T = F_s + F_{C-P} \tag{3.8}$$

To reduce the total hydrodynamic printing force F_T, the authors proposed a novel approach based on the leverage of a new force oriented in the opposite direction compared to F_S and F_{C-P}. The new force introduced into the system is the electromagnetic force F_{EM} and due to its orientation, it will be deducted from F_T, resulting in a force reduction. F_{EM} can be leveraged using two main artifacts: i) silicone filled with magnetic nanopowder and ii) custom-made syringe equipped with copper coils connected to a power supply to provide electrical current during the extrusion process. The F_{EM} acting on the magnetic ink and pushing it towards the build plate can be expressed as follows:

$$F_{EM} = NL_C Bi \tag{3.9}$$

where N is the number of copper coils around the syringe (dimensionless), L_C the overall coil length (m), B the magnetic field of the magnetized silicone inside the syringe (T), and i the current applied to the copper coils (A). Throughout the study, N, LC, and i were fixed at $325, 35.36\ m$, and $4.5\ A$, respectively. The B parameter depends on the $wt\%\ Fe_3O_4$ inside the silicone, which was experimentally determined (using a Hall effect sensor) to be $118.57\ \mu T, 213.97\ \mu T$, and $379.12\ \mu T$ at $10\ wt\%$, $20\ wt\%$, and $30\ wt\%$, respectively. Further, the F_{EM} contribution reduced F_T, which in turn was expressed as follows:

$$F_T = F_s + F_{C-P} - F_{EM} \tag{3.10}$$

To summarize, the total printing force shown in Eq. (3.10) depends on three main force contributions; every term of such equation, in turn, depends on process parameters, operating parameters, material and setup. In particular, i) F_s depends on the nozzle geometry, flow rate and material rheology, ii) F_{C-P} depends on the layer height, printing speed, material rheology and flow rate, and iii) F_{EM} depends on the coil geometry, magnetic field of the magnetic ink, and applied current.

3.2.2.2 Reduction of printing force

The proposed approach to reduce the overall printing force (along with the numerical model) was experimentally validated, and a piezoresistive force sensor was employed (placed between the machinepushing element and syringe piston, as shown in **Fig. 3.3**, to record the force values throughout the 3D printing process under several printing conditions. Due to transient effects, the initial $0.2\ s$ of the extrusion process have been discarded from the final force computation. The force

value associated to every experiment was computed as the average force value from $0.2\ s$ up to $7\ s$ (end of the extrusion).

A $70\ mm$ long and $1.02\ mm$ wide (equal to the nozzle diameter), silicone bead was extruded over the build plate to evaluate the force contribution and validate the numerical model. The process parameters presented in Section 3.2.1.5 remained unchanged throughout the validation phase. A methodology similar to the one proposed in [219] has been used to record every force contribution, more details about the way every force contribution was recorded and computed can be found in the Appendix A (section A2). Four different ink compositions of Fe_3O_4 have been tested namely $0\ wt\%, 10\ wt\%, 20\ wt\%,$ and $30\ wt\%$. For every composition, two different values of the volumetric extrusion flow rate (Q) were tested $(0.1\ and\ 0.2\ mL/min)$. The reason for testing two values of Q is to prove the robustness of the proposed approach, which can reduce the overall printing force regardless of the set flow rate value. Although the aim of this study is the reduction of F_T at low layer height (i.e., $0.1\ mm$), three different layer height values were tested $(0.1\ mm, 0.15\ mm, and\ 0.2\ mm)$ to demonstrate the consistency and repeatability of the proposed approach.

All the plots referring to $Q = 0.1\ mL/min$ are shown in the present section. Regarding $10, 20, and\ 30\ wt\%$ of Fe_3O_4, all the experiments were repeated under two different conditions: i) without generating F_{EM} (conventional approach) and ii) by applying electrical current to the copper coils to generate F_{EM} (proposed approach). Pure silicone $(0\ wt\%)$ was tested only based on the conventional approach because insufficient magnetic nanopowders made the proposed approach unworkable. For each combination (volumetric flow rate, layer height, conventional approach, and proposed approach), three replicates were performed, thus portraying a very low standard deviation. A total of 126 samples were 3D printed and the force values were recorded.

In **Fig. 3.5 a**, the overall total printing force F_T as a function of the three layer height values $(0.1\ mm, 0.15\ mm, and\ 0.2\ mm)$ is shown, at all $Fe_3O_4\ wt\%$. For both Q values, a good correspondence between the numerical model and experimental data was observed, not only when printing under conventional conditions but also when leveraging the proposed approach.

Here, a maximum accuracy of 98.44% was achieved. Several factors can account for the discrepancy between the data predicted by the numerical model and that experimentally obtained, such as the fluctuations in environmental conditions (temperature and humidity) and vibrations occurring during the fabrication process. Further, **Fig. 3.5 a** shows the reduction of the force obtained while exploiting the proposed approach based on the electromagnetic force F_{EM}. Particularly, using $30\ wt\%\ Fe_3O_4$ silicone, F_T reduced by 28.57%, while extruding at a layer height of $0.1\ mm$ (the main objective of this study is the reduction of the force at low value layer height) and flow rate of $0.1\ mL/min$ (leveraging the proposed approach). Under similar printing conditions ($h = 0.1\ mm\ and\ Q = $

0.1 mL/min) the reduction of the force obtained while using silicone mixed with 10 $wt\%$ Fe_3O_4 and 20 $wt\%$ Fe_3O_4 was 9.84% and 16%, respectively. The increase in Fe_3O_4 $wt\%$ resulted in a larger decrease in F_T because the F_{EM} contribution (which is deduced from F_T, as shown in Eq. (3.2)) is directly correlated to B (as shown in Eq. (3.9)), thereby increasing with the content of the magnetic nanopowder. On the other hand, based on the conventional approach, F_T slightly increased with an increase in $Fe_3O_4wt\%$ (for every layer height value) because of the higher dynamic viscosity of the ompound (**Fig. 3.2 a**). A comparison between the base Ecoflex 00–10 and silicone filled with 30 $wt\%$ Fe_3O_4 (greatest reduction in force) is shown in **Fig. 3.5 b**.

Despite the increase in the dynamic viscosity, the F_{EM} contribution is predominant, thereby resulting in a considerable decrease in F_T. A maximum reduction in F_T equal to 21.08% was achieved by employing the proposed approach (30 $wt\%$ Fe_3O_4) compared to the conventional approach (base Ecoflex 00–10) at the lowest layer height value of 0.1 mm ($Q = 0.1$ mL/min). In fact, the proposed approach (silicone filled with magnetic nanopowders and a modified extrusion setup) resulted in a considerable reduction in the force, when compared to not only the extrusion of the magnetic ink based on the conventional approach, but also the extrusion of pure Ecoflex 00–10.

Here, all the experiments were performed on the 30 $wt\%$ magnetic nanopowder-based silicone (characterized by the highest FT reduction) when employing the proposed manufacturing method (4.5 A has been provided to the copper coils surrounding the syringe) at two different values of Q (0.1 and 0.2 mL/min). **Fig. 3.5 c** shows every force contribution at the three-layer height values (the F_{EM} contribution depends on the setup and is constant for each layer height), and the following conclusions can be drawn: i) a good correspondence was achieved between every force contribution predicted using the model and actual data obtained from the experimental phase, ii) the layer height values only affected F_{C-P} (reduction of 51.46% when switching from 0.1 to 0.15 mm at $Q = 0.1$ mL/min), iii) F_{EM}, as expected, was almost similar while extruding at $Q = 0.1$ and 0.2 mL/min because it depended neither on the volumetric flow rate nor on the layer height.

Rather, it only depended on the material composition ($wt\%$ of Fe_3O_4), iv) only F_S depended on the volumetric flow rate Q, but its impact on F_T was very low compared to F_{C-P} and F_{EM}, and v) at low values of layer height, the main contribution to increase F_T is given by F_{C-P}.
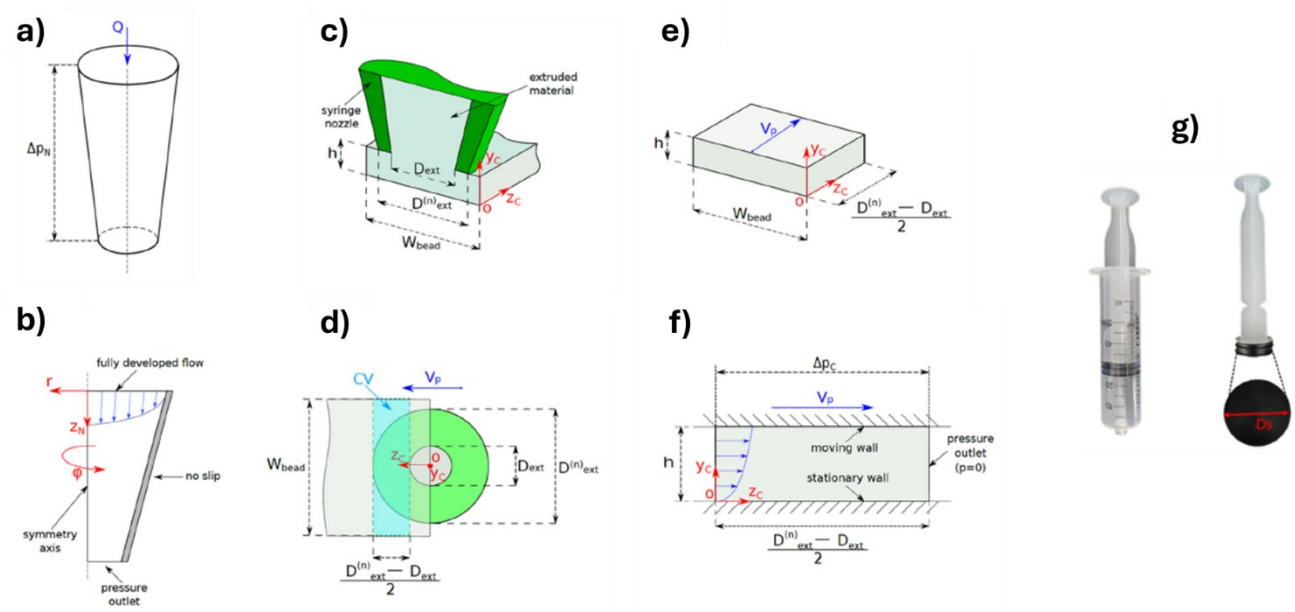
Fig. 3.3: Modeling of forces occurring during the extrusion of silicone. a) Geometry of the nozzle, where the pressure drop along the nozzle axis is shown. b)Boundary conditions for the numerical simulation of the flow inside the nozzle. c) Schematic representation of the layer deposition, with the respective variables involved in the extrusion process. d) Control volume for the solution of the governing equations of the layer deposition. e) Schematic representation of the extrudate, with the respective variables involved. f) Boundary conditions for the numerical simulation of the layer deposition. g) Syringe piston diameter.
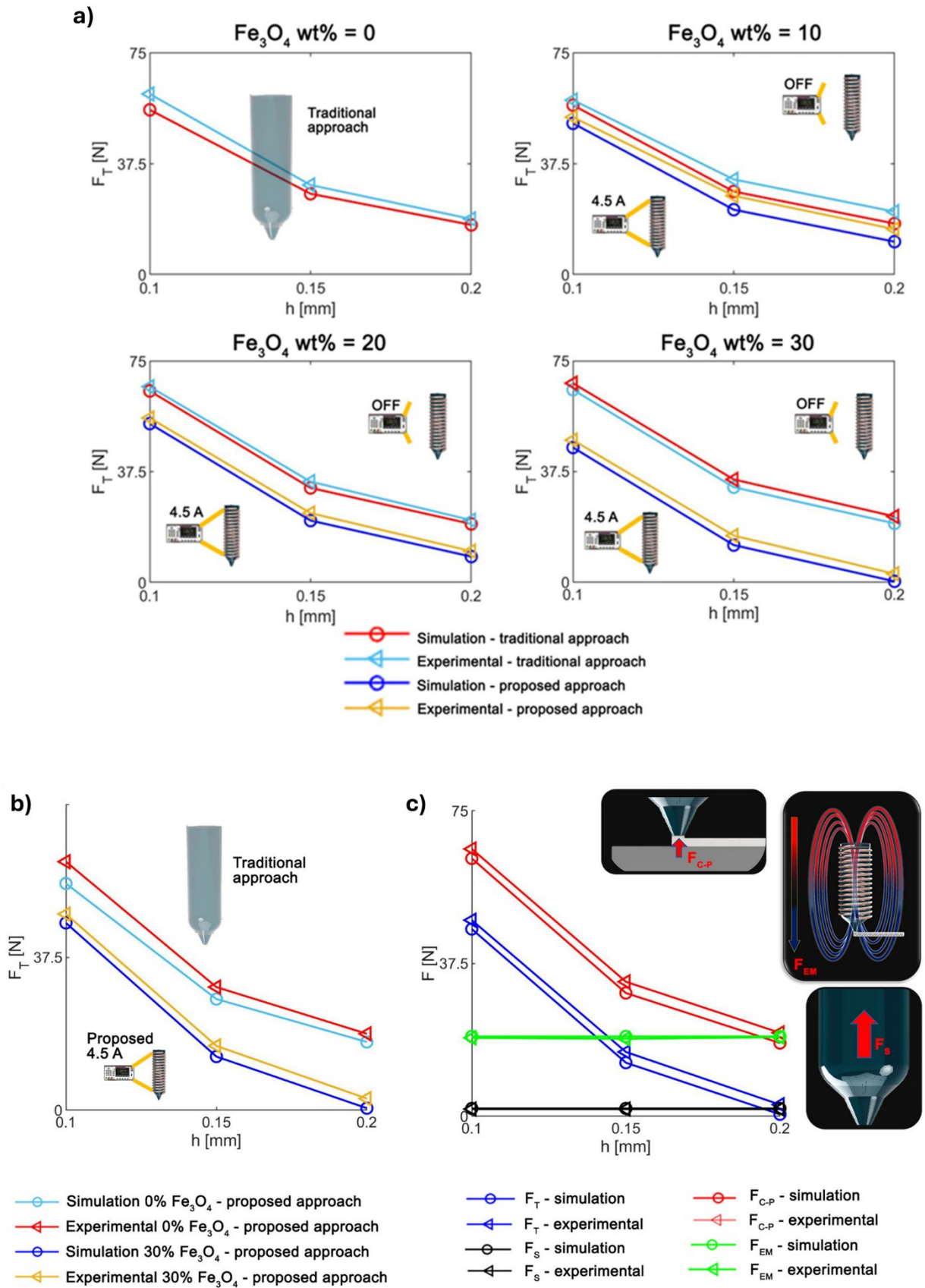
Fig. 3.4: Reduction of the total printing force using the proposed electromagnetic approach: a) Total printing force FT vs layer height (h) at Q=0.1 mL/min, for different wt% of Fe3O4 when using the traditional and proposed approach. Here, the numerical and experimental results are shown. b) Comparison between the overall FT and layer height (h) in the conventional approach for pure Ecoflex 00–10 (no magnetic filler) and the best result of the proposed approach (silicone+30 wt % Fe3O4). c) All three different force contributions when extruding 30 wt% Fe3O4 silicone using the proposed approach (leveraging the electromagnetic force) vs the layer height (h), at Q=0.1 mL/min.

3.2.2.3 Electromagnetic-assisted approach setup to 3D print complex and bioinspired silicone-based structures

To further demonstrate all the potentialities of the proposed electromagnetic-assisted method, several structures were 3D printed by setting a layer height of $0.1\ mm$ ($Q\ equal\ to\ 0.1\ mL/min$). A nozzle with a diameter of $0.8\ mm$ was used, and a printing speed of $10\ mm/s$ was set. The slicing software Ultimaker Cura 4.11 (Ultimaker, The Netherlands) was used to set the desired process parameters and generate g-code files. Particular attention has been paid to the layer height parameter: since the minimum z-resolution of the custom-made MEX setup after all the modifications, resulted to be $0.08\ mm$, a layer height of $0.1\ mm$ was set to safely avoid z-axis related problems.

- Thin-walled structures

As shown in **Fig. 3.6 a**, a thin-walled structure (wall thickness equal to the nozzle diameter) was fabricated with no distortions, as well as complex and unconventional geometries, such as the *Italian country shape*, a *snowflake-shaped* structure, and a thin-walled (wall equal to $0.8\ mm$) gyroid structure. As shown in **Fig. 3.6 b, c, d**, all the 3D printed silicone-based structures were characterized by non-rounded nozzle toolpaths. Particularly, the Italian country shape was also fabricated by employing the pure Ecoflex 00–10 based on the conventional approach (no electromagnetic force) to provide a comparison with the level of detail achievable with the proposed approach, and numerous distortions were observed together with the impossibility of replicating the exact CAD file. It should be noted that, for both the manufacturing approaches shown in **Fig. 3.6 d**, the same printing parameters were set (i.e., h equal to $0.1\ mm$, Q equal to $0.1\ mL/min$, and line width equal to the nozzle size namely $0.8\ mm$) demonstrating the effectiveness of the reduction of force (21.08%) in fabricating complex geometries with high level of details. When extruding at $0.1\ mm$ of layer height, in accordance with the traditional MEX-based silicone approach, more material come out from the nozzle (compared to the theoretical flow rate set in the slicing software) because of the high printing force.

For this reason, the extruded lines are thicker, thereby resulting in the impossibility to retain the desired shape because of the over-extrusion problem. Such issue results to be successfully addressed by employing the proposed approach based on the printing force reduction, as shown in **Fig. 3.6 d**.
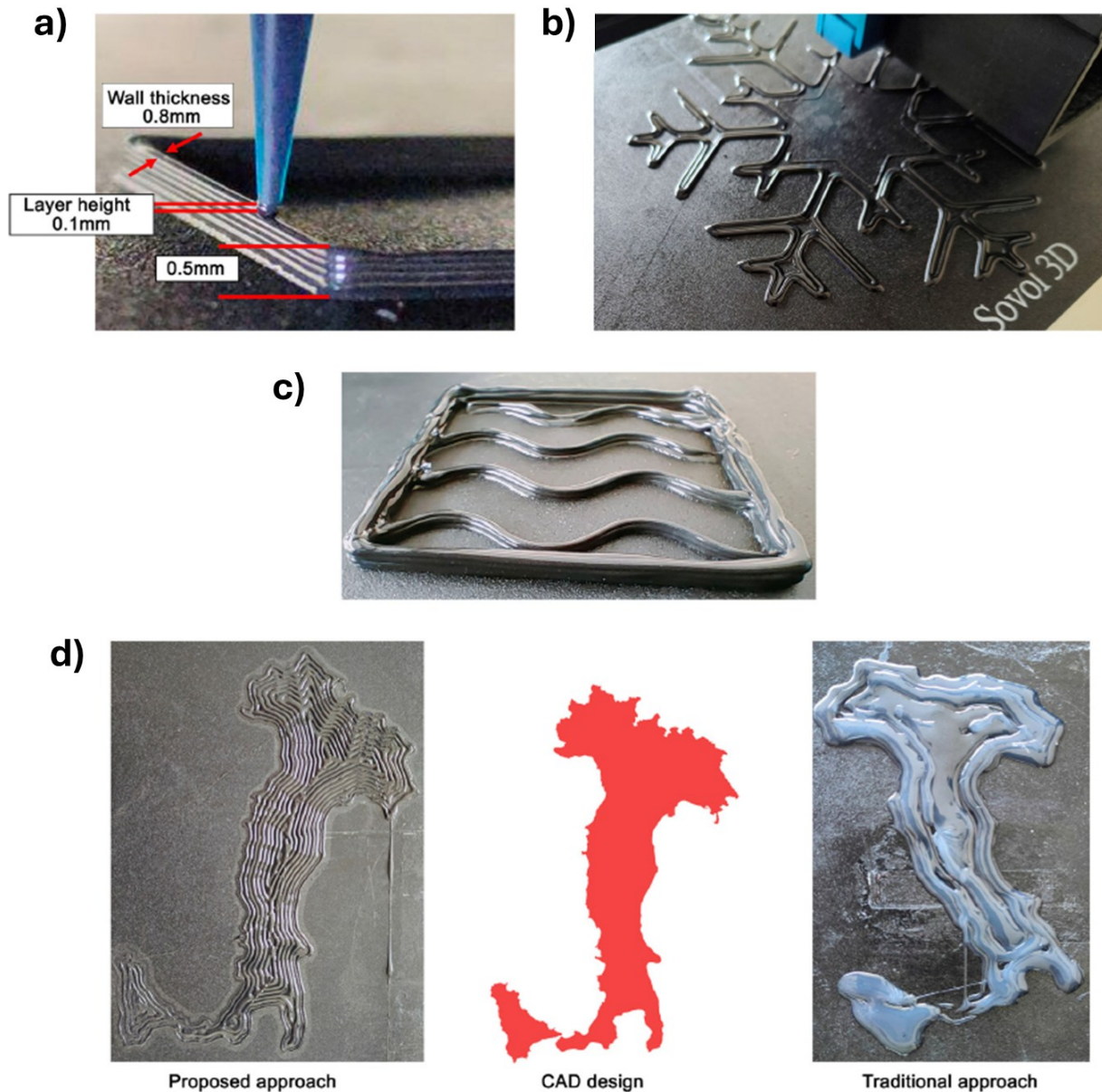
Fig. 3.5: 3D printing of thin-walled and complex structures. a) thin-walled structure, b) snowflake, c) thin-walled gyroid structure, and d) Italian country shape: itis possible to evaluate the high details achieved using the proposed approach and the low detail quality obtained when using the traditional approach (the same printing parameters were used when printing with both the approaches).

- Printing quality improvement

The proposed ink (Ecoflex 00–10 mixed with 30 $wt\%$ of Fe_3O_4) exhibits a different dynamic viscosity compared to pure Ecoflex 00–10 (as shown in **Fig. 3.2 a**), resulting in higher printing quality. For this reason, the effect of the proposed fabrication approach has been tested only on the ink (Ecoflex 00–10 mixed with 30 $wt\%$ of Fe_3O_4) which resulted to provide the higher force reduction (21.08%). The structure shown in **Fig. 3.7 a** (*horse race* with complex features) was fabricated under three different scenarios: i) recurring to traditional silicone MEX approach (the

copper coils were not provided with current), ii) providing the copper coils with 3.5 A, and iii) providing the copper coils with 4.5 A, namely the current input with the higher force reduction. As shown in **Fig. 3.7 a**, the proposed manufacturing approach abruptly increased the overall level of detail, even when extruding only Ecoflex 00–10 mixed with 30 $wt\%$ of Fe_3O_4. As expected, the worst result in terms of printing quality was obtained when the copper coils were not provided with current, thereby resulting in the impossibility to fabricate the desired shape. On the other hand, when 3.5 A were provided and a F_{EM} of 13.6 N was recorded, a great improvement in the overall printing quality was obtained. As a matter of fact, the best result was achieved when providing 4.5 A to the copper coils and exploiting a F_{EM} of 19.2 N: a magnification on the horse head (**Fig. 3.7 a**) clearly shows the increased level of detail achievable with the proposed approach. The main reason underlying such improvement in printing quality, when switching from providing 0 A to 4.5 A (namely F_{EM} equal to 0 N, and F_{EM} equal to 19.2 N), results to be strictly related to the overcoming of the over-extrusion problem. The magnetic field generated by the copper coils (acting on the magnetic ink inside the nozzle), better direct and compress the ink flow during the extrusion process, thereby reducing the swelling phenomenon occurring when the materials is pushed out of the nozzle. This behavior can be clearly seen in **Fig. 3.7 b**: when printing without providing current to the copper coils, two main over-extrusion- based defects such as i) waves on the walls and ii) impossibility to fabricate 90-degree corners, occur. Such defects result to be overcome by exploiting the proposed manufacturing approach (providing 4.5 A to the copper coils), since F_{EM} facilitates the extrusion by reducing the overall printing force and in turn the swelling problem.

In particular, **Fig. 3.7 b** shows a comparison between the same 3 layers thin-walled structure (wall width equal to the nozzle size, namely 0.8 mm and layer height equal to 0.1 mm) fabricated by employing Ecoflex 00–10 mixed with 30 $wt\%$ of Fe_3O_4, in accordance with the traditional and proposed approach. All the structures shown in **Fig. 3.7 a**, and **b** have been fabricated by using the process parameters listed in **Table 3.2**.

Table 3.2: Process parameters set for the fabrication of the structures shown in Fig. 3.7.

Process parameter	Value
Layer height (mm)	0.1
Flow rate (mL/min)	0.1
Line width (mm)	0.8
Nozzle size (mm)	0.8
Printing speed (mm/s)	10

a)

| Electromagnetic Force 0 N (0 A) | Electromagnetic Force 13.6 N (3.5 A) | Electromagnetic Force 19.2 N (4.5 A) |
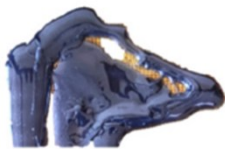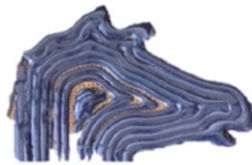
b)

Traditional approach
(Copper coils at 0 A)
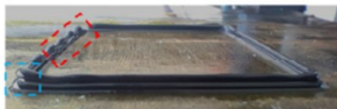
Overextrusion defects due
to high extrusion force

Waves on the walls   Impossibility to fabricate 90
degree corner

Proposed approach
(Copper coils at 4.5 A)

Overcoming overextrusion due
to the reduced printing force

No waves   Desired shape

Fig. 3.6: Electromagnetic assistance to improve the printing quality, tested on the proposed soft ink (Ecoflex 00–10 +30 wt% of Fe3O4 . a) Effect of different current inputs (0 A, 3.5 A, and 4.5 A) provided to the copper coils to generate electromagnetic force on the printing quality, and b) benefits of the proposed approach in overcoming over-extrusion problems when a layer height of 0.1 mm is set.

- Nozzle scalability

It should be noted that the *proposed electromagnetic-assisted* approach is nozzle size free: smaller and bigger nozzles can be employed, as shown in **Fig. 3.8**.

On one hand the usage of small nozzles (i.e. $0.2\ mm$) allow the fabrication of high detailed structures, but on the other hand the fabrication time abruptly increases. To prove the nozzle scalability achievable with the proposed electromagnetic approach, the same structure (star shaped structure with sharp features) has been fabricated by employing three different nozzle diameters: $0.2\ mm$, $1.02\ mm$, and $2\ mm$. The same manufacturing parameters have been set for every printing scenario (flow equal to $0.1\ mL/min$, printing speed equal to $10\ mm/s$, and layer height equal to $0.1\ mm$) and the final structure results to be composed by a total of three layers (total structure thickness of $0.3\ mm$). As shown in **Fig. 3.8**, the smaller nozzle ($0.2\ mm$) produces the best result in terms of x-y resolution but at the same time it takes $9.3\ minutes$ to fabricate the whole structure, while the medium nozzle ($1.2\ mm$) represents a good compromise between fabrication speed and resolution.

- Soft structures

Further, the proposed approach presents two additional advantages. Because Ecoflex 00–10 silicone was mixed with magnetic nanopowder to reduce F_T, it can be directly employed for the fabrication of fast-transforming soft robots actuated using an external magnetic field, as shown in [118], [142], [218]. A flower-inspired magnetic structure was 3D printed and activated using a permanent magnet (magnetic field of $1.2\ T$), as shown in **Fig. 3.9 a, b**. Several other nature-inspired actuators, such as Venus flytrap bistable structures [220] and flexible tensegrity structures [221], can be fabricated with a very high level of detail (by setting a low layer height) and thin walls, fully exploiting the additive manufacturing philosophy.

The custom-made MEX machine permits not only silicone extrusion but also thermoplastic filaments in the same manufacturing cycle and is leveraged to create bio-inspired structures. As shown in **Fig. 3.3**, the 3D printing system used throughout the whole research is equipped with both a filament-based nozzle and a syringe, thus allowing the fabrication of layers composed of two materials (thermoplastic filament and magnetic ink). A stiff thermoplastic material, acrylonitrile butadiene styrene (ABS), was extruded in conjunction with magnetic ink to create small-scale soft robots. To improve the adhesion between magnetic ink and ABS, the mesh overlapping parameter was set equal to $0.2\ mm$. Such parameter overlaps adjacent extruded strands of magnetic ink and ABS and it was proven to increase the mechanical strength between soft and stiff materials in MEX technology [108]. It is worth mentioning that also mechanical interlocking systems greatly increase the interface toughness between silicone and thermoplastic [222]. As shown in **Fig. 3.9 c**, a musculoskeletal system mimicking the human knee was fabricated using ABS for the two bones and magnetic ink for the soft cartilage joint connecting the bones. The proposed 3D printed knee has a circular shape with a diameter, overall height, and joint height of $8\ mm$, $40\ mm$, and $0.4\ mm$ (namely four extruded

layers), respectively. Using the same approach (stiff parts of ABS and soft joints of magnetic ink), a bioinspired finger actuated by using a nylon tendon-driven system (connected to a stepper motor) was fabricated and actuated, as shown in **Fig. 3.9 d**. The proposed finger uses the design rules detailed in [223] and exhibits a considerable resemblance to its counterpart (the human finger) when bent. This remarkable behavior was observed because of the extremely soft silicone joints connecting the two rigid segments and capable of absorbing stress, as with the human fingers. Most robotic fingers do not exhibit such harmonious and bio-inspired behavior, which is required to create humanoid soft robots capable of mimicking human behavior. A direct comparison between a bio-inspired finger fabricated with the proposed approach and its counterpart (traditional silicone 3D printing approach) is provided in **Fig. A4** (see Appendix A), showing the improved performance in terms of bending behavior achievable with the electromagnetic-assisted Additive Manufacturing technique.

Moreover, a small bistable structure (overall height and thickness equal to $25\ mm$ and $2.5\ mm$, respectively) composed of ABS and magnetic ink was fabricated, as shown in **Fig. 3.9 e**. When actuated by means of an external magnetic field (see movie S6), the bistable actuator could switch from the stable equilibrium state 1, to a new equilibrium state 2. When the magnetic field was removed, the structure stayed in its state 2 without any power input; the state 1 was restored by applying again an external magnetic field, but in opposite direction (compared to the first one). Additionally, a small-scale spider-inspired soft robot composed of four legs (magnetic ink) connected through a mechanical interlocking to a central stiff body (ABS) was monolithically fabricated. Each leg is composed of two magnetic ink layers of $0.1\ mm$, resulting in an overall leg thickness of $0.2\ mm$. The proposed soft robot was moved inside a tiny tube (diameter of $10\ mm$) by using an external magnetic field, as shown in **Fig. 3.9 f**. It should be noted that the locomotion mechanism of the proposed soft robot is different from the locomotion of spiders found in nature: the magnetic legs are attracted by the external magnetic field generated by the permanent magnet (moved outside the tiny tube) resulting in the dragging of the whole soft robots towards the direction of the permanent magnet. By exploiting such mechanism, the proposed soft robot can be moved in two directions (back and forth). Small-scale silicone robots (overall thickness of 0.1–$0.2\ mm$) capable of navigating in narrow environments are extremely challenging to manufacture by recurring to traditional silicone 3D printing since the minimum achievable layer height value to avoid manufacturing problems is generally 0.3–$0.4\ mm$.

The spider-inspired robots demonstrate the impact of the proposed electromagnetic-assisted method in the soft robotic field: extremely tiny robots, fabricated with ease, could be used to explore tight and confined spaces. Detailed dimensions of the soft robots presented in **Fig. 3.9** are shown in the Appendix A (section A3).

The proposed approach has several advantages in the soft robotics field, as the rigid structures can be coupled with very small and precise silicone joints (this task has been made possible by reducing the printing force) to obtain motions that recall those found in nature. Additionally, the proposed electromagnetic-assisted approach allows the jointly extrusion of soft ink (low thickness and high level of details) and stiff material, in a single shot fabrication step, thereby enabling the manufacture of assembly-free bio-inspired soft robots. Such feature, results to be impossible to be achieved with traditional fabrication approaches, where multiple assembly tasks are needed to bond silicone and stiff materials.
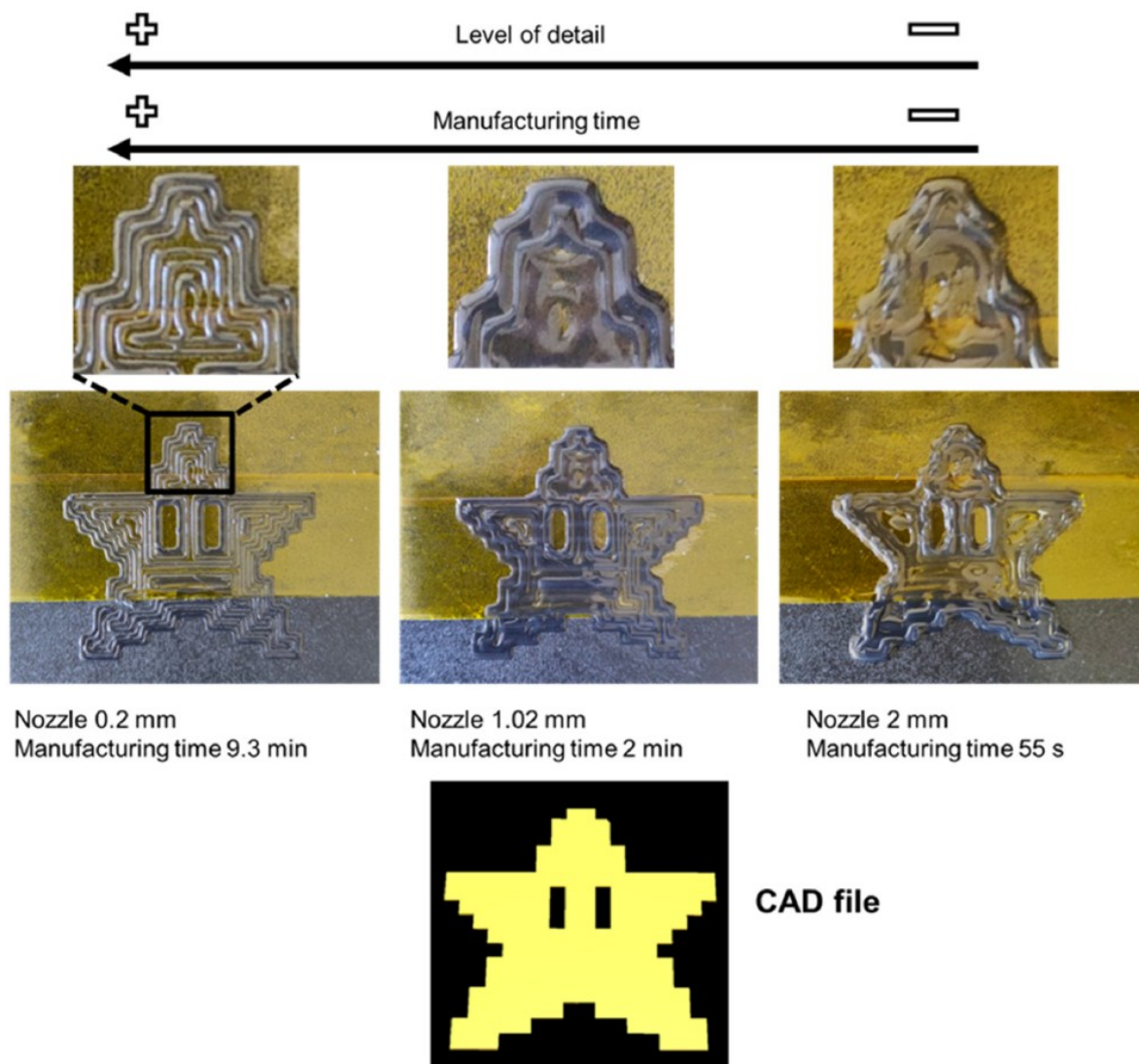
Fig. 3.7: Nozzle scalability. Fabrication of star shaped structure using 0.2 mm, 1.02 mm, and 2 mm nozzle diameter. In particular, the increased level of detail is shown, as well as the increased manufacturing time when employing a 0.2 mm nozzle.

a)

b)

c)

10mm

d)

Tendon

Soft joint

Stiff passive structur

10mm

Activated

Rest position

Human finger

e)

Stable state 1

Stable state 2

f)

Time = 0s
Spider x position = 0mm

Time = 9s
Spider x position = 78mm
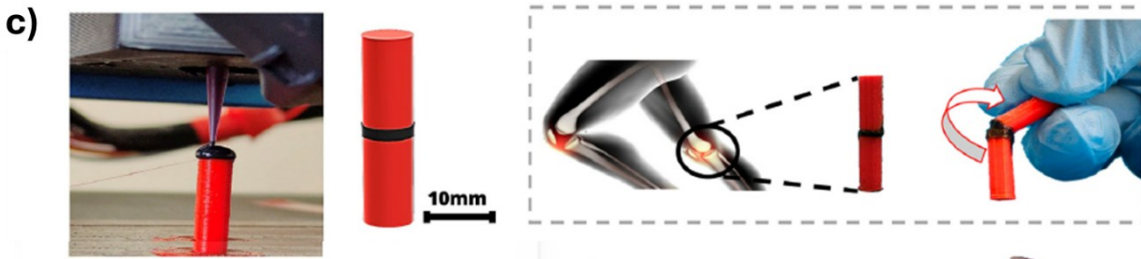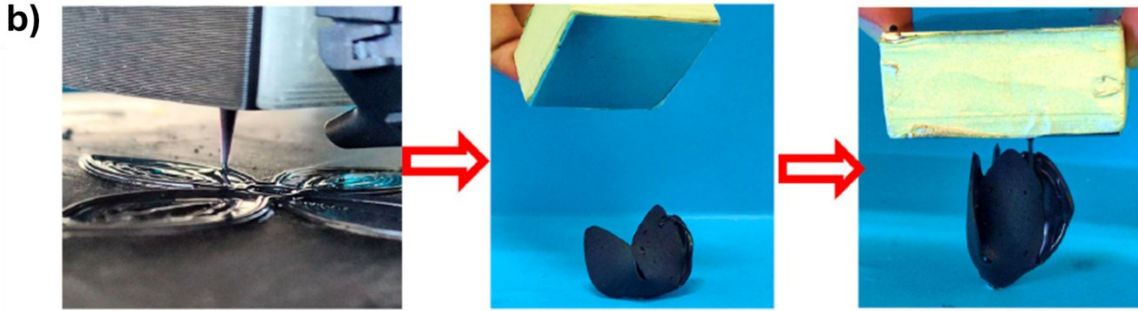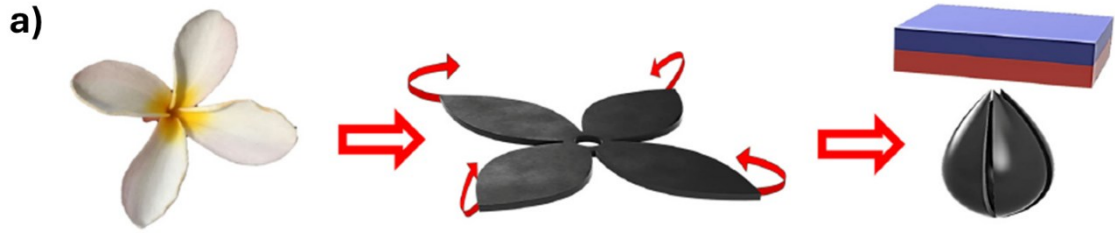
Fig. 3.8: Application to the soft robotics field. a) Schematic representation of the magnetic flower actuation by means of an external magnetic field, b) proposed 3D printed magnetic soft flower and actuation, c) knee-like structure fabricated by jointly extruding stiff ABS (red) for the two bones and soft silicone (black) for the joint. d) 3D printed bio-inspired finger fabricated by jointly extruding stiff ABS (red) and magnetic ink (black) in the same 3D printing cycle. The finger was activated by a tendon-driven system, resembling the human counterpart bending motion. e) 3D printed bistable structure fabricated by jointly extruding stiff ABS (red) and magnetic ink (black): it has been activated using an external magnetic field. f) Spider-inspired soft robot composed of four legs (magnetic ink) and a central stiff body (ABS) fabricated in the same manufacturing cycle. When magnetically activated, the spider-inspired soft robot is capable of navigating in tight and confined spaces.

3.2.3 Conclusions

The novel electromagnetic-assisted approach proposed in this study enables the additive manufacturing of silicone-based structures at low layer heights ($0.1\ mm$) because of a considerable reduction in the overall printing force. Here, the latter was reduced by leveraging a new force introduced into the 3D printing system, referred to as the electromagnetic force (F_{EM}). The proposed manufacturing approach requires some modifications both from a machine (custom-made syringe equipped with 325 copper coils) and material (the silicone needs to be mixed with magnetic filler) standpoint. A remarkable reduction in the printing force by 21.08% ($19.27\ N$) was achieved by employing Ecoflex 00–10 silicone mixed with $Fe_3O_4\ wt\% = 30$ when extruded at a layer height of $0.1\ mm$ and flow rate Q of $0.1\ mL/min$.

In traditional silicone additive manufacturing, when high printing forces are involved (i.e., at low values of layer height), the syringe piston applies high pressure to the ink inside the syringe, resulting in high friction between ink and syringe walls. This makes the fabrication of high detailed structures extremely challenging. Such problem is overcome with the proposed electromagnetic-assisted approach: F_{EM} exerts a pushing effect on the ink causing its motion from the syringe towards the nozzle, thereby reducing F_T. Further, a numerical model was created, thereby resulting in a 94.76% accuracy in terms of predicting F_T under the aforementioned printing conditions. The reduction of F_T allowed the authors to 3D print: (i) multilayers thin-walled structures (the wall is equal to the nozzle diameter) and (ii) complex shapes with nonrounded toolpaths. The proposed manufacturing method has two additional benefits: (i) soft robots (comprising magnetic ink) can be directly actuated by employing an external magnetic field after removal from the build-plate and (ii) the custom-made MEX machine can extrude the magnet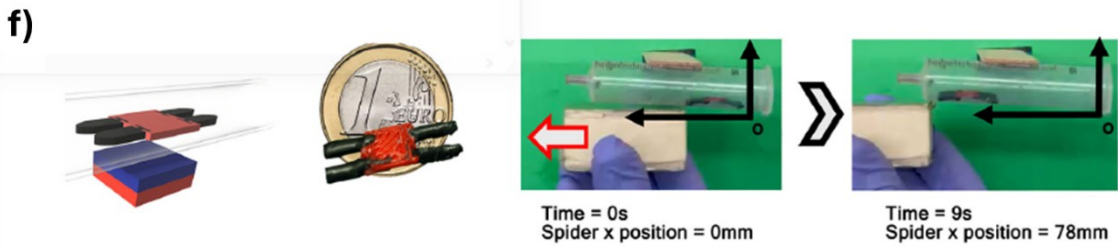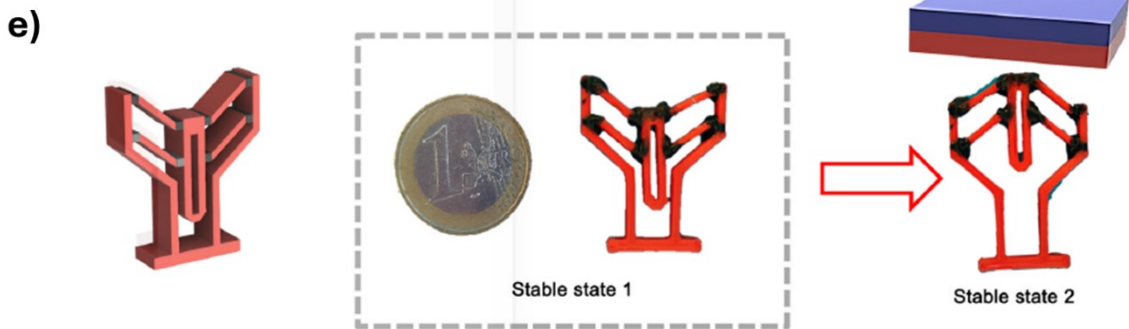ic ink and thermoplastic material simultaneously, and bio-inspired structures (musculoskeletal systems) were fabricated by coupling ABS passive stiff structures with soft silicone joints.

A summary of the main results of this study is presented in **Table 3.3**. The proposed electromagnetic-assisted method can be used to facilitate the extrusion of several highly viscous inks [224], [225] and be potentially translated to any type of MEX technology (i.e., filament- and pellet-based), thereby pushing the role of additive manufacturing beyond its current limitations and towards a new mass-

production dimension. Another key benefit of the extrusion of extremely thin layers, made possible by the proposed approach, is the improvement of the interlayer adhesion since the wetting area among consecutive layers increases, and in turn, the mechanical properties increase too, bridging the gap with the counterpart fabrication technology [214], [216].

Future works will be focusing on the development of suitable methodologies and setups for the interlayer adhesion characterization (i.e. peeling tests) of structures fabricated with the proposed approach at low values of layer height (i.e., $0.1\ mm$). Ultimately, the proposed approach lays the foundation for more reliable exploitation of inexpensive silicone-based MEX (thin-walled structures, complex shapes with non-rounded toolpaths, small-scale soft robots, and bio-inspired structures) that can be fabricated with improved resolution and a greater level of detail.

Table 3.3: Summary of the main results of this study

Feature	Proposed approach	Traditional approach
Material	Ecoflex 00-10 + 30% Fe_3O_4	Ecoflex 00-10
Forces involved	$F_S,\ F_{C-P}, F_{EM,}$	$F_S,\ F_{C-P}$
Total Printing force at h=0.1 mm	48.71 N (Reduced by 21.08%)	67.43 N
Ultimate tensile strength (UTS)	0.48 MPa	0.55 MPa
Fabrication of thin-walled and high detail structures	Allowed	Challenging
Accuracy of the numerical model in predicting FT (h=0.1 mm, Q=0.1 mL/min)	96.76%	94.76%
Self transforming magnetic soft robots	Allowed	Not-allowed
Assembly-free small scale soft robots composed of soft ink and stiff materials	Allowed	Not-allowed

3.3 Fabrication approach for conductive polymers: Enhancing the sensitivity of 3D printed sensors via ironing and void reduction

In the present work, the problem of poor electrical performance in 3D printed piezoresistive sensors was addressed by using a novel approach based on the improvement of the layer-by-layer adhesion, proving that a strong correlation between sensor sensitivity and interlayer voids occurs. The ironing strategy which results to be an extremely effective, simple and inexpensive method was employed to successfully improve the sensitivity in 3D printed piezoresistive sensors: such strategy can also be potentially used in conjunction with the three methods (see section 3.1) widely exploited in scientific literature.

This strategy, still underexploited, makes the conductive tracks compact via the application of heat and pressure with the hot-end, which increased the sensitivity by 82.7%. The findings at the macro scale have been correlated to the internal microstructure of the sensor by employing an X-Ray Computed Tomography (CT) system, discovering a porosity reduction of 59.4%. This simple technique can be leveraged to fabricate smart structures with enhanced performance to detect small changes in force, bending and displacement. The adhesion-centered approach, based on the reduction of voids by means of mechanical pressure, presented in the present research could be potentially used also in conjunction with traditional methods to enhance sensitivity and fabricate high performance sensors.

3.3.1 Material and methods

3.3.1.1 Printing strategy to improve sensitivity

Throughout the work herein, piezoresistive strain sensors were fabricated using a commercial dual extruder MEX machine (Ultimaker S5, Ultimaker, The Netherlands) and two commercial filaments: a conductive polylactic acid (CPLA) for the sensor and a traditional PLA for the dielectric substrate. In particular, the CPLA material (Protopasta, USA) is composed of a matrix of PLA doped with carbon black particles, in a weight percentage ($wt\%$) higher than the percolation threshold, making the whole composite material electrically conductive, with an electrical resistivity in the build direction (z axis) of $115\ V/cm$ according to the datasheet.

The sensor design is shown in Figure 1(a), which is composed of:

1. a non-conductive PLA substrate (green) having a thickness, width, and length of $0.4, 52.8,$ and $100 \, mm$, respectively, and

2. the conductive CPLA sensor (black), which is composed of four tracks, each one having an active length of $50 \, mm$, width of 1.6, thickness of $0.4 \, mm$ and spacing of $3.2 \, mm$.

Two $0.8 \, mm$ nozzles have been employed to extrude both materials. It should be noted that a line width of $0.8 \, mm$ was set and a layer thickness of 0.2 was chosen (every track is composed of two consecutive extruded layers, as shown in **Fig. 3.10 b**). An infill type of 'line' with a 90° direction was set in the slicing software in order to obtain every single track of the sensor to be composed of two adjacent extruded beads. It should be noted, that the infill type and directionality have both been shown to affect the sensitivity of 3D printed sensors [212] but it was not considered in the present research, as the focus of this study centres around an interlayer adhesion approach to address the sensitivity problem. Other printing process parameters are listed in **Table 3.4**. The slicing software Ultimaker Cura 4.11 was used to set the process parameters and generate .gcode files.

The proposed sensor can be exploited to detect multiple stimuli, such as strain and force. Among all the possible ways to leverage 3D printed piezoresistive sensors, a growing interest is risen in the field of bending angle measurements [226], especially to sense soft and bio-inspired robotic hands and grippers [212], [226]. 3D printed bending sensors meets the pressing requirement of soft robotics, making AM the leading manufacturing technology in such field. For this reason, the authors designed the proposed sensor to be employed as bending sensors, thus the sensitivity can be expressed as follows (equation 3.11):

$$s = \frac{\Delta R}{\Delta \alpha} \tag{3.11}$$

where $\Delta R \, (\Omega)$ represents the change in electrical resistance, while $\Delta \alpha$ represents the corresponding change in bending angle ($degree$).

An increased sensitivity implies a sensor can detect small changes in bending angles, which is beneficial for many applications such as biomedical, robotics, structure monitoring, non-destructive tests [31], [34], [227]. In accordance with recent progress in scientific literature, the interlayer adhesion of consecutive extruded layers can be expressed as follows [228]:

$$\sigma = \sigma_0 + \sigma_d \tag{3.12}$$

where σ_0 is the strength developed due to the wetting, while σ_d is the strength developed due to the diffusion.
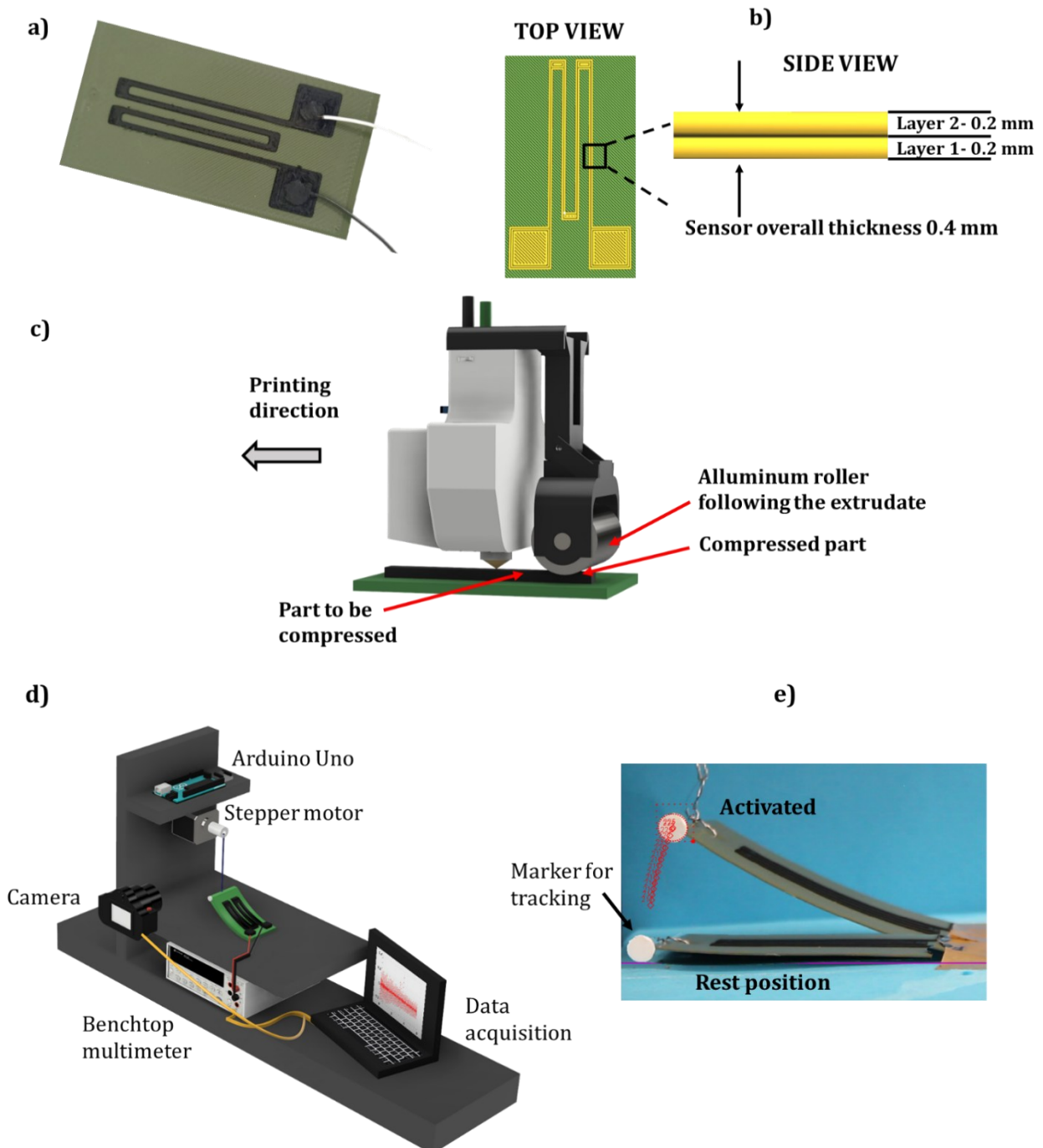
Fig. 3.9: a) 3D printed sensor composed of non-conductive PLA substrate (green) and CPLA sensor tracks (black), b) sensor in the slicing software: manufacturing strategy, c) roller strategy: a roller for compression is attached to the print head, d) custom-made characterization setup and e) Sensor in the Tracer software to calculate the bending angle by using a marker for tracking.

Improving interlayer adhesion could imply a reduction in the void content, in turn, providing a better path to the current to flow. As such, there are two primary mechanisms used herein to improve the interlayer adhesion and, in turn increase the interlayer adhesion: applying pressure on the extruded layer (to increase the wetting area) and increasing the temperature at the interface between two layers (to increase the polymer chain diffusion).

As a consequence of Equation (3.12), the 3D printed piezoresistive sensors were printed under the following conditions:

i) ***As-is***: the process parameters described in **Table 3.4** have been used for the CPLA. This reflects the printing condition commonly used in scientific literature for the fabrication of piezoresistive sensors and smart structures when employing MEX machines and conductive PLA [210].

ii) ***Roller***: a metallic (aluminium) roller was added to the print head to immediately follow the just extruded conductive material and compress it (see **Fig. 3.10 c**). The roller (wider than the nozzle tip) was assembled $3\ cm$ behind the nozzle to allow the total compression of the extruded material. As shown in the scientific literature [214], [229]–[231], this kind of approach based on the increase of the wetting area involves a reduction of voids and an improvement of the mechanical properties of samples prepared via the MEX technique. The roller applied a force of $8.3\ N$ to the sample (measured by using a commercial force sensor).

iii) ***Ironing***: it repeats the last extruded layer by passing the hot nozzle over it (see **Fig. 3.11 a**). The last extruded layer is then compressed and heated up again. In this way, not only the wetted area is supposed to increase (due to the mechanical pressure applied by the nozzle), but also the polymer chain diffusion is supposed to improve since the last layer is locally heated up when the ironing is performed. The following parameters related to ironing have been set: pattern equal to zig-zag, line spacing equal to $0.05\ mm$, flow equal to 7%, ironing distance from the edge equal to $0.2\ mm$ and nozzle temperature when performing ironing equal to $90°C$. The ironing temperature was chosen with a trial-and-error approach, such that the temperature represents a compromise between the lower limit defined by the glass transition temperature (the ironing temperature has to be higher to improve the healing time) and the upper limit defined by the melting temperature (the ironing temperature has to be lower to avoid re-melting the material and significantly distorting the sample geometry).

It should be noted that the main differences between the roller and ironing is that in the roller case

the tool applying pressure is external to the AM system and the metallic roller needs to be manually assembled. For the ironing approach, the tool applying pressure is the nozzle itself. In the ironing approach, the nozzle can also be heated in order to reheat the previously extruded layer and improve the intralayer adhesion. A schematic representation of the ironing strategy is provided in **Fig. 3.11 a**. As described in Section 3.3.1.1, the ironing strategy was proven to be extremely efficient in reducing intralayer voids, resulting in a great sensitivity improvement: in **Fig. 3.11 b,** a schematic of the mechanism underlying such outcome is provided. Three sensors for each printing condition have been manufactured and tested to consider the variability due to the additive manufacturing process. The effects of the printing strategies (i.e. as-is, roller and ironing) on the sensitivity of sensors have been analysed by employing a custom-made characterisation setup, shown in Figure 1(d). Electrical wires have been soldered to the sensor pads and connected to a benchtop multimeter (GW Instek, GDM 8341), which in turn was connected to MATLAB (The Mathworks, Inc.) to record the resistance change throughout the whole test. The top part of the sensor was connected, by using nylon wire, to a stepper motor (NEMA 17) instructed through Arduino Uno. The stepper motor performs 13 cycles per minute; every cycle is composed of a forward movement followed by a backward movement, both performed at 300 RPM, which corresponds to a bending angle of the structure of $14.2 \, degree$ (see **Fig. 3.10 e**). The test was run for $6 \, min$ ($78 \, cycles$). A digital camera (Canon EOS 400D) was employed to record the test, and a white marker in the form of a pin was attached to the edge of the sensor to process the video through a video analysis and motion tracking open-source software (Tracker, OSP – Open Source Physic, USA) and obtain the bending angle of the sensor for every cycle (see **Fig. 3.10 e**).

Table 3.4: Main process parameters set for the fabrication of the sensors, regardless of the printing strategy (as-is, ironing, roller).

Printing parameter	CPLA (sensor)	PLA (substrate)
Layer thickness (mm	0.2	0.2
Printing temperature (°C)	240	205
Printing speed (mm/s)	25	50
Flow (%)	110	100
Infill type	Line (90°)	Line (45°)
Number of external perimeters	0	3
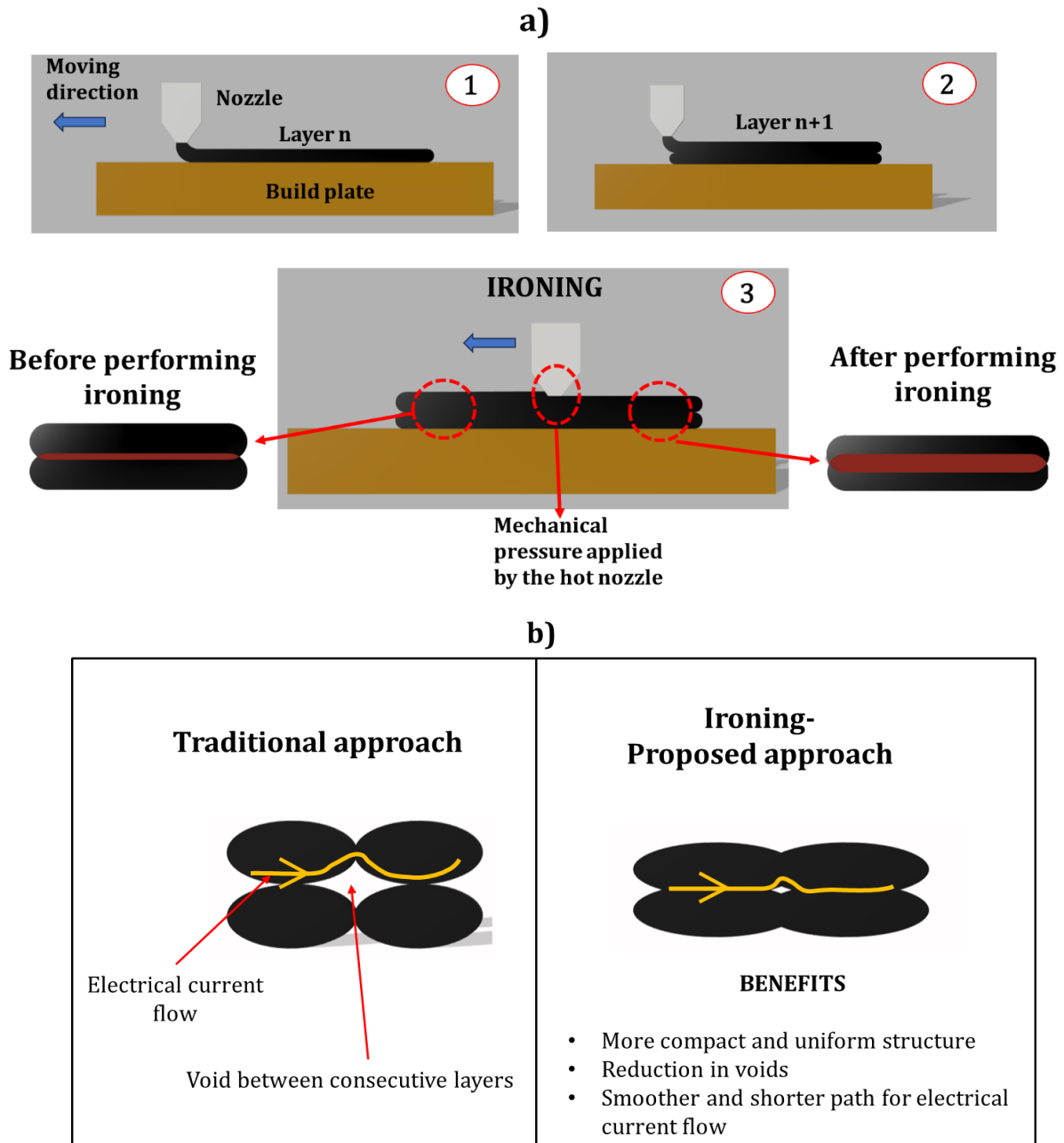
Fig. 3.10: a) Step by step description of the ironing strategy and b) mechanism underlying the better sensitivity achieved with the proposed approach based on the ironing strategy.

3.3.1.2 Microstructure evaluation

Two different microscopic studies have been performed to correlate the improvement in sensitivity with the internal microstructure in terms of voids reduction and improvement of the bond width. It is worth mentioning that both the microscopic evaluations have been performed, only considering 'ironing' and 'as-is' conditions since they respectively represent the best and worst results in terms of sensitivity (see Section 3.1). For this reason, the 'roller' condition was not considered.

CT scans were conducted using the NSI X-3000 X-Ray CT system (North Star Imaging, Microfocus)

to analyse internal voids. A voltage of $50\ kV$ and current of $700\ \mu A$ and a focal spot size of $35\ \mu m$ were employed for all scans, which was used to produce an X-ray beam with a voxel size of $15.82\ \mu m$. A reconstruction software, efX-CT, was employed following CT scan completion, wherein specific sharpness and beam hardening settings were selected for each scan in based on highlighting the void content within the printed material. After the reconstruction process, the data was analysed using Dragonfly's segmentation wizard feature, which makes use of artificial intelligence (AI). The AI module of the software was trained to differentiate between voids (red), the material (yellow) and the background/air (blue) based on variations in greyscale values from the CT scan, as demonstrated in **Fig. 3.12 a**. Following the calibration of the AI feature, the software would autonomously identify similar greyscale values across all slices of the scanned sample, performing segmentation.

The region of interest area (voids) is then analysed and calculated for each slice and plotted relative to the depth of the sample (as discussed in Section 3.3.2.2).

Three 'ironing' and three 'as-is' samples were then analysed, and the results in terms of void reductions were correlated with the improved sensitivity. All the samples prepared for CT scans were composed of five beads (every bead was $0.8\ mm$ wide, same dimension of the nozzle used to extrude CPLA) and five layers (every layer was $0.2\ mm$ tall, same layer thickness set for throughout the whole research). In addition to X-ray CT analysis, as the ironing strategy applies mechanical pressure to extruded layers, the microscopic image analysis of sample cross sections were performed to verify if it was translated in an increased bond width. A Dino-Lite Edge 3.0 (Dunwell Tech Inc.; California, USA) digital microscope was used to calculate the wetting factor between consecutive layers, in accordance with Equation (3.13) proposed in [228], as shown in Equation (3.13):

$$f_{wetting} = \frac{Bond\ width}{Fiber\ width} \tag{3.13}$$

where bond width (mm) represents the contact length between layer n and layer n + 1, and fibre width (mm) represents the width of the single layer (theoretically, it should be equal to the nozzle diameter), as schematically represented in Figure 3(b). A total of three CPLA test coupons (two beads, two layers) with and without performing ironing have been 3D printed. Each test coupon was sectioned every $5\ mm$ using an IsoMet Low-Speed Saw (Buehler Ltd., Illinois, USA) to cut five small pieces and manually polished using $400, 600, 1000, 2000, 3000$ grit sandpapers sequentially. For ease of cutting in the low-speed saw, each test coupon was cast in the PRO-SET INF-114 infusion resin and

hardener (Gougeon Brothers, Inc. MI, USA) and was cured for $24\ h$ in the room temperature. The low-speed saw was used at a low rotation per minute to avoid disturbing the test surface.

Material (CPLA)

Voids

a)

Air/background

Cross section

b)

Fiber width

Layer n+1

Bond width
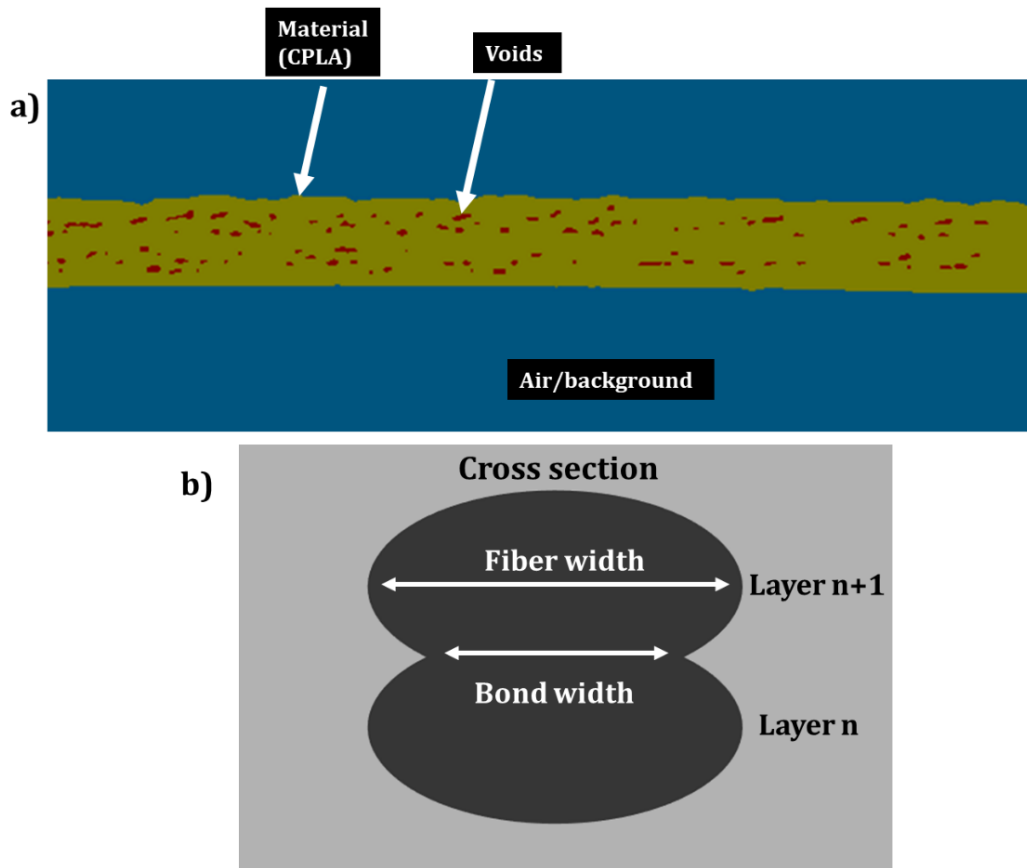
Layer n

Fig. 3.11: a) User painted slice showcasing the three different features used to calculate porosity (void percentage) from X-Ray CT scans and b) graphical representation of the bonding between two consecutive extruded layers.

3.3.2 Results and discussion

3.3.2.1 Sensitivity improvement

The relationship between sensitivity and the three different extrusion strategies detailed in Section 3.3.1.2 (as-is, roller and ironing) has been studied by cyclically bending the sensor 78 times at a frequency of 0.002 Hz, as shown in **Fig. 3.10 e**. The main results are shown in **Fig. 3.13**, where the relative change in resistance $\frac{\Delta R}{R_0}$ versus time while bending the sensor has been plotted. Every test has been performed on three different samples for printing strategy, to consider the variability due to the manufacturing process, as well as the testing conditions. From the characterisation test, several conclusions can be drawn. First, the printing artefacts used in accordance with Equation (3.12)

produce an increase in the sensitivity of the sensor. As shown in **Fig. 3.13 a–c**, there is a constant increase in the amplitude of $\frac{\Delta R}{R_0}$ when switching from 'as-is' to 'roller' and from the latter to 'ironing'.
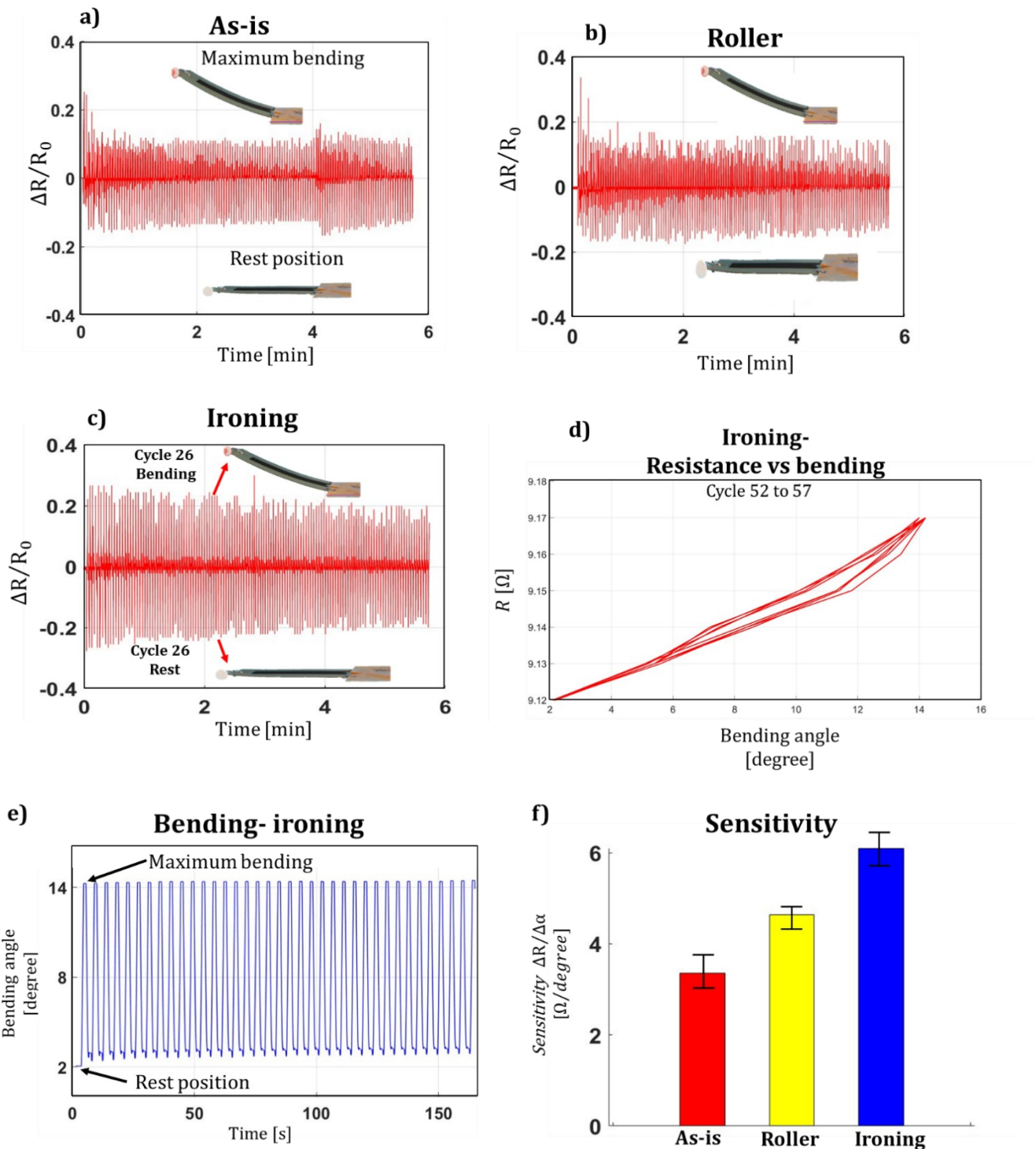
Fig. 3.12: a) Change in relative resistance vs time for as-is sensor, b) change in relative resistance vs time for roller sensor, c) change in relative resistance vs time for ironing, d) Resistance vs bending angle for 'ironing' sample (cycles 52–57), e) bending angle of the sensor during the characterization and f) sensitivity for the three tested printing strategy: ironing produces the best result.

From **Fig. 3.13 a–c**, a slight change in the response of the sensor, $\frac{\Delta R}{R_0}$ over time can be noted. As each

graph represents the average behavior of three identical sensors: such change in the response might be due to the variability affecting the manufacturing process, as well as slight changes in the setup environment during the test (i.e. change of temperature and humidity). An overview of the direct correlation between change in resistance and bending angle, for the 'ironing' sample ($cycles\ 52–57$) is shown in **Fig. 3.13 d**. It should be noted that the proposed characterisation method was consistent, as demonstrated in **Fig. 3.13 e**, in which a maximum bending angle of 14° and rest position angle of 2° was consistently achieved every cycle. As shown in **Fig. 3.13 f**, the sensitivity of the 'as-is', 'roller' and 'ironing' sample is $3.35\ V/degree$, $4.64\ V/degree$ and $6.12\ V/degree$, respectively. The best result is obtained when using the ironing strategy with an improvement of the sensitivity of 83% compared to the as-is sensor is. The standard deviation, calculated on three different samples was found to be lower than $\pm 0.9\ V/degree$ for each case. Additionally of note, while the effect wasn't as marked as the ironing strategy, the roller strategy still produces an improvement of 39% in the sensitivity compared to the 'as-is' scenario.

Additional testing was conducted to further prove the benefit of the ironing strategy over the as-is printing scenario. The two versions of the sensor were tested under the same conditions (motor speed and number of cycles per minute) for $70\ min$. In this case, the raw data of resistance change (Ω) has been plotted as a function of the time without t normalising procedure. **Fig. 3.14**, which shows the performance of the 'ironing' sample, demonstrates that after approximately $30\ min$ of testing, or a total of 390 bending cycles, a stabilisation in the resistance behavior occurs when cyclically bending the sensor. Despite an initial drift behavior of the sensor was observed for the first $30\ min$, stabilisation of the sensors response occurs for the remainder of the 70 min. The drift in resistance in 3D printed conductive polymer sensors is a very common issue that has been shown in literature. To date, no unified theory has been developed to explain this behavior. While not validated, one proposed hypothesis from this work, and in accordance with scientific literature to date [232]–[234], attributes the initial drift being related to Mullin's effect which involves hysteresis and cyclic softening in plastic materials, as well as the viscoelastic effect. In accordance with the Mullins' effect the majority of stress softening happens at the first cycles and sequenced cycles of stretching provoke the same or less stress softening [235]. Another possible mechanism might be related to a change in temperature due to the flow of current inside a conductive material generating heat because of the Joule effect.

Fig. 3.14 shows that when testing the as-is sample for $70\ min$, there is no stabilisation in the change of resistance, rather a constant decreasing drift in sensor response. To quantify the stability and the decreasing trend, the data from minute 30 up to minute 70, or the time window where the ironing

sample showed great stability, have been fitted using a linear regression equation, obtaining respectively:

$$R = -0.0002t + 9195.4 \qquad (3.14)$$

$$R = -0.07t + 11799 \qquad (3.15)$$

Equation (3.14) refers to the ironing sample, while Equation (3.15) refers to the 'as-is' sample. The coefficient of determination, R^2, was found to be 0.96 and 0.89 respectively for the ironing (Equation (3.14), and as-is sample (Equation (3.15), showing that the linear regression model can be used to obtain useful insights about the stability of the proposed sensors. The slope of both curves is the metric used to evaluate the stability related to the change of electrical resistance. If the slope trends to zero (parallel to the x-axis) then the change in resistance of the sensor over time is stable. For the ironing scenario, the slope is $-0.0002\ Vs$, while as for the as-is scenario, the slope is two orders of magnitude higher at $-0.07\ Vs$. The following evaluation suggests how ironing contributed to making
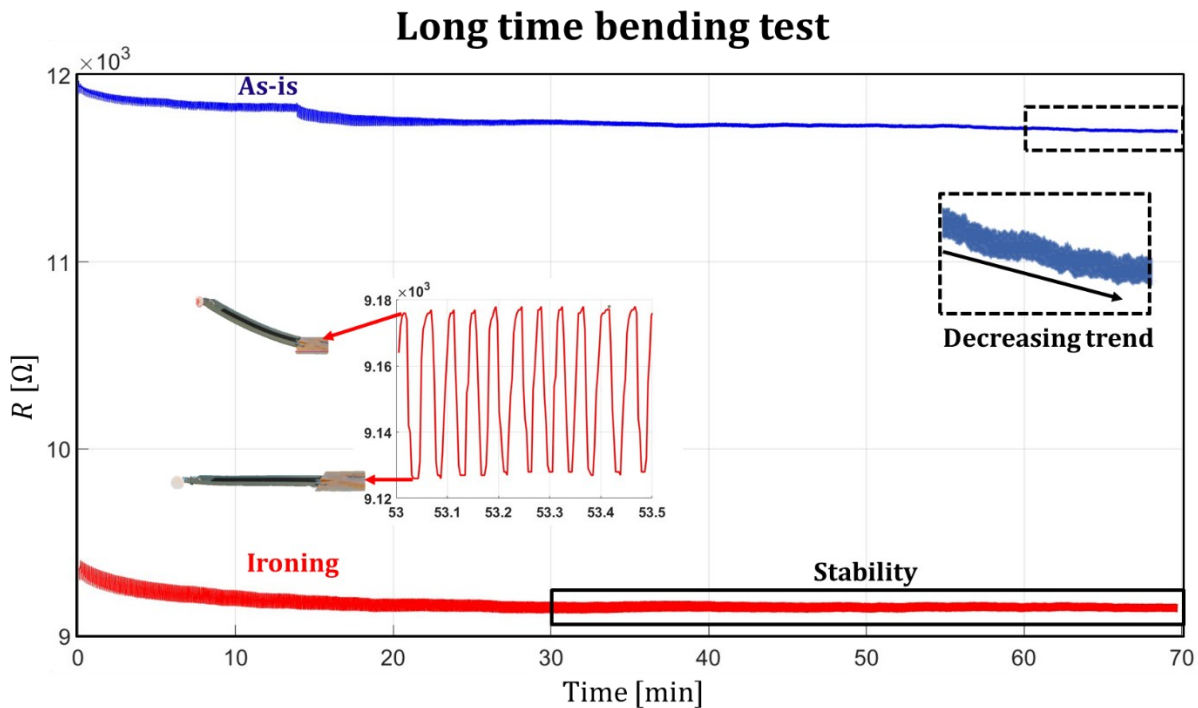
Fig. 3.13: Long time bending test for ironing and as-is: stability after 30 min for ironing sample, and lack of stability for as-is sample.

the sensor stable over time, unlike for the traditional as-is printing as observed in this work.

The improved stability can potentially be attributed to the ironing strategy, by reducing intralayer voids and improving the healing time, resulting in a net improvement of the adhesion between the subsequently deposited layers. When cyclically stressed, a layered structure with weak adhesion

(sensor 'as-is') could exhibit creep behavior, resulting in a decreasing trend of the electrical resistance (**Fig. 3.14**). A detailed explanation of this phenomenon, which increases the stability, is provided in Section 3.3.2.3. Additionally, the 'ironing' sample was also tested at rest (without applying any bending) for a total of $60\ min$, in a controlled environment at $22\ °C$ and no drift in the electrical resistance were recorded. This result is in accordance with the latest finding in scientific literature, where conductive polymer materials used for the fabrication of 3D printed sensors tend to have a strong correlation between electrical resistance and environmental temperature[236], [237]. It should be noted, if the proposed 'ironing' sensors is to be used in an environment with temperature fluctuations, the material coefficient of temperature (TC) has to be taken into account and compensation strategies need to be employed. The 'ironing' sample was also cyclically tested to characterise its life span. A total of $10,000$ bending cycles have been performed at a frequency of $0.002\ Hz$ for a total of $12.82\ h$, and no damages were observed at the end of the test, suggesting that the proposed sensor can be employed for at least $10,000\ cycles$. The ironing sensor resolution and response time were also measured, resulting to be $1.2\ degree$ and $60\ ms$.

In summary, the ironing strategy was shown to be the most suitable way to fabricate 3D printed piezoresistive sensors given the strategies attempted in this work, with the following benefits being achieved:

1. Sensitivity improvement of 83% compared to the traditional 'as-is' printing.

2. Less drift in sensor response after $30\ min$, the slope of $-0.0002\ V/s$ 'ironed' compared against $-0.07\ V/s$ for 'as-is'.

As detailed in Section 3.3.2.2, a reduction of porosity and an increase in the bonding between the conductive layers of the sensor are potential reasons underlying the enhancement of the sensor performances when performing ironing. In particular, the bonding between conductive layers was improved when performing ironing due to: i) the hot nozzle heated up again the last deposited layer activating the polymer chain diffusion and ii) the nozzle applied mechanical pressure on the last deposited layer, resulting in an increased bonding (wetting) area and resulting in a reduction in voids.

On one hand, the ironing strategy abruptly improves the sensitivity of 3D printed sensors, but on the other hand, it makes the strain gauge top surface less smooth compared to the 'as-is' traditional scenario. An industrial profilometer (Mitutoyo SJ-400) was employed to evaluate three different roughness values, namely Ra, Rz and Rq (in accordance with the international standard ISO 1302)

Due to the ironing zig-zag path set in the slicing software, shown in **Fig. 3.15 a, b,** every roughness metric resulted to be increased compared to the traditional 'as-is' scenario, as shown in **Fig. 3.15 c**. Five roughness measurements were taken for every sample with a scan path parallel to the beads, and a not statistically significant standard deviation ($< 0.01\,\mu m$) was found. Therefore, the ironing process was fully characterised, demonstrating improvement in sensitivity at 83% results in a significant increase in surface roughness on the top of the strain gauge surface. It should be noted that this increase in surface roughness would make this approach infeasible for certain applications, such as additively manufactured optics and photonics [238].
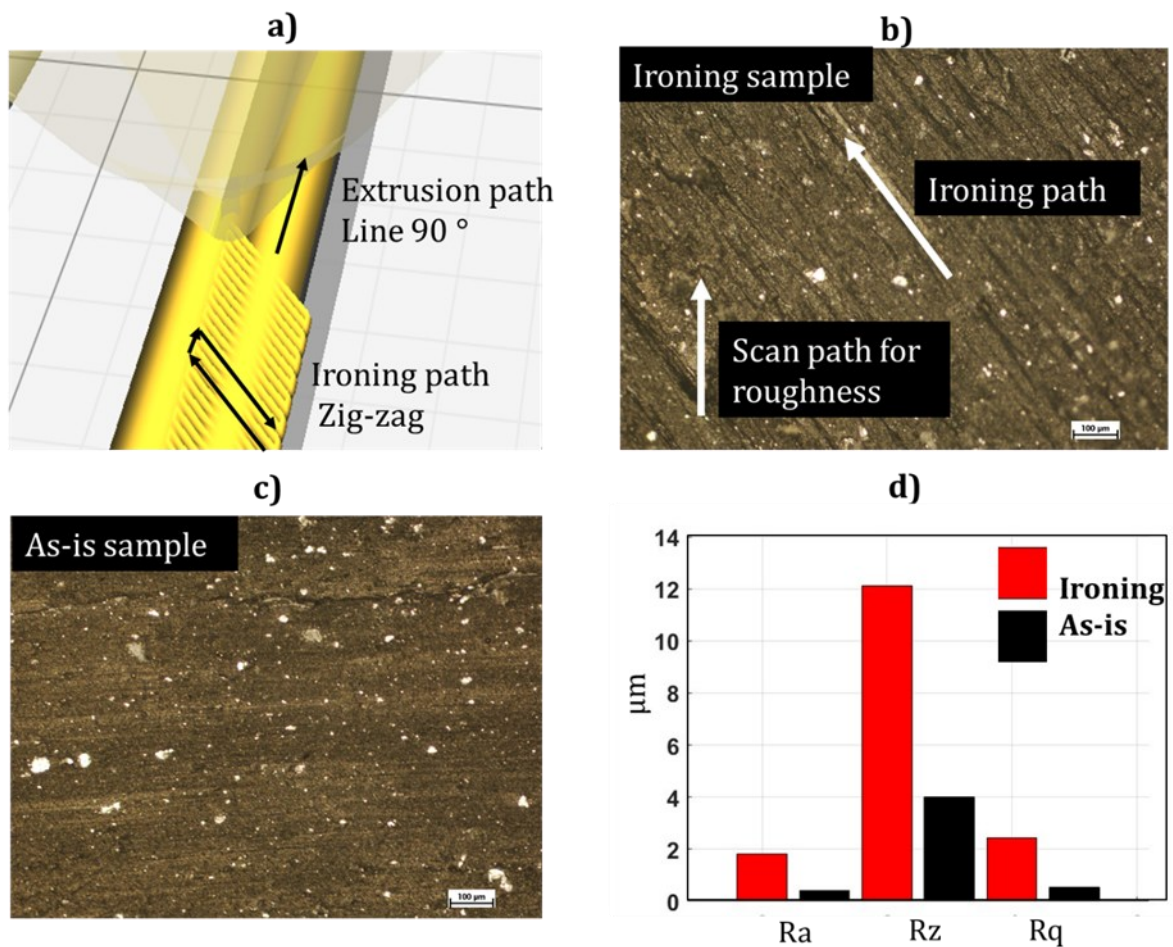
Fig. 3.14: Roughnes evaluation: a) Ironing path simulated into the slicing software, b) Actual ironing path at microscope, c) As-is sample at microscope and (d) Ra, Rz and Rq (ISO 1302) for ironing and as-is samples.

3.3.2.2 Relationship between ironing strategy and microstructural features

In this section, the improvement in sensitivity is deeply investigated from a microscopic standpoint, analysing the void volume fraction among conductive layers and proving that its reduction is strongly correlated to the improved performance of the sensor. All the tests have been conducted on 'ironing' (best sensitivity and stability) and 'as-is' samples (worst sensitivity and stability). A total of three

identical samples for every scenario ('as-is' and 'ironing') have been manufactured and tested, to take into account the manufacturing variability affecting the MEX process.

As described in Section 3.3.2.2, X-Ray CT scan tests were conducted to analyse the void volume percentage, also called porosity. As shown in **Fig. 3.16 a**, a great reduction in void content was achieved when employing the proposed 'ironing' approach, compared to the traditional 'as-is' scenario. **Fig. 3.16 a** plots the porosity of three 'as-is' and three 'ironing' samples as a function of their depth, namely, the thickness of the samples. Every sample was composed of five layers, each one $0.2\ mm$ thick. Depth equal to $0.2, 0.4, 0.6, 0.8$ and $1\ mm$, respectively, refers to layers $1, 2, 3, 4$ and 5 (see **Fig. 3.16 b**). The primary outcomes from the CT scan analysis are listed here as:

- For '*as-is*' samples the void content was dependent on the location, or depth into the sample. At the interface between every layer (i.e. layer 2 at $0.4\ mm$, layer 3 at $0.6mm$ and so on) a spike in void content occurs. In the '*ironing*' samples, the void content is less dependent on the thickness, in which a constant value is recorded throughout the sample. This phenomena is driven by the underlying mechanisms that ironing uses, in which the hot nozzle applies mechanical pressure and thermal energy simultaneously, increasing the bond width between consecutive extruded layers and subsequently reduces the void content at the interface. The traditional printing scenario ('as is') suffers from lower bond width, which is translated into void content spikes at the interface between consecutive layers.

- The void content obtained when employed the proposed approach (ironing) resulted to be 2.8% with a standard deviation of 1.3, while the traditional '*as-is*' scenario was characterised by a porosity of 6.9% with a standard deviation of 2.1. The proposed approach resulted in a reduction in the porosity of 59%. This finding supports the hypothesis that links the improved sensitivity (83%) to a reduction in void content. **Fig. 3.16 c, d,** show cross-sectional images that demonstrate the significant differences in microstructure that can be observed between these samples.

The reduction of porosity (59%) achieved by means of the ironing strategy, makes the conductive structure more compact, which, in turn, is reflected on the conductivity (S/m) of '*ironing*' samples which resulted to be improved of 40.1% compared to '*as-is*' samples. Since the conductive layers have less discontinuity points (less voids), the electrical current path is larger in terms of area and the conductivity is improved. Further investigation has been conducted to correlate the increased sensitivity to microscopic features of the '*ironing*' samples, by analysing the ratio between bond

width and fiber width, as expressed in Equation (3.13). Ideally, the bond width of two consecutive layers should be equal to the fiber width, resulting in a $f_{wetting}$ value equal to 1. As shown in **Fig. 3.17**, there is a clear indication of interface and not complete bonding between the two layers (bond width is smaller than fiber width), as expected from the 'as-is' test coupon. The $f_{wetting}$ values for the five cut sections of the 'as-is' coupon are listed in **Table 3.5**. It is evident that there was no complete wetting between consecutive layers as the average $f_{wetting}$ (0.83) was always lower than 1, which fully agrees with available literature [228]. On the other hand, when performing ironing, there was no distinguishable interface between consecutive layers, indicating complete wetting at the interface. As a matter of fact, the $f_{wetting}$ value, in this case, is considered as 1, indicating increased wetted area. Due to the significant porosity reduction provided by the ironing technique, the authors envision that custom-made nozzles designed to maximise the ironing performance in terms of interlayer adhesion could be fabricated and used to further leverage the ironing strategy.

Table 3.5: Adhesion for 'as-is' samples in five different locations.

Section No	Bond width (mm)	Fibre width (mm)	F$_{wetting}$
1	0.75	0.88	0.85
2	0.69	0.85	0.81
3	0.70	0.83	0.84
4	0.65	0.80	0.81
5	0.63	0.74	0.85

3.3.2.3 Relationship between ironing strategy and improved interlayer diffusion

One of the most important mechanisms accountable for layer-by-layer adhesion is the polymer chain diffusion at the interface between consecutive layers, where more polymer chain diffusion results in higher interfacial adhesion. As shown in Coogan and Kazmer [60], the fraction of diffusion at the interface $\frac{X}{X_\infty}$ can be written as follows:

$$\frac{X}{X_\infty} = \sqrt{6} \left(\int_0^t \frac{1}{\tau_h(T,t)} dt \right)^{\frac{1}{4}} \qquad (3.14)$$

where τ_h (s) represents the total healing time, namely the time at which the diffusion occurs when $T > T_{glass}$. The ironing strategy is executed by passing the hot nozzle over the last extruded layer.

The nozzle temperature was arbitrarily set to 90 °C, while performing ironing. In this way, the last extruded conductive layer, that already cooled down under T_{glass} has been reheated above T_{glass}, enabling further interlayer diffusion.

An experimental setup consisting of a FLIR A700 thermal camera capable of taking infrared (IR) videos was attached to a custom-made frame placed on the top of the machine (the camera lens was parallel to the building plate). All the analyses were performed by focusing on a single region of interest (1 $pixel$) located on the conductive track of the sensor. Videos were taken during the extrusion of the last conductive layer for a total of 120 s, under the two printing conditions studied in this research, namely '*as-is*' and '*ironing*'. As shown in **Fig. 3.18**, for the 'as-is' scenario (traditional printing condition), the temperature of the extruded conductive material was above T_{glass} for a total of 44 s, from $t = 0\ s$ up to $t = 44\ s$. Subsequently, the temperature never rose above T_{glass}, as expected. The behavior of the 'ironing' sample was fundamentally different, in which the temperature went below T_{glass} after 48 s, but after performing ironing the temperature rose again above T_{glass}, from $t = 67\ s$ up to $t = 96\ s$, for a total of an additional 29 s after ironing was completed.

By summarising, the total healing time τ_h, namely the amount of time above T_{glass}, for the ironed sample was 77 s against 44 s for the as-is sample, as shown in **Fig. 3.18 a**. It should be noted that, while performing ironing, the two most important process parameters accountable for increasing the layer temperature above T_{glass} are i) the temperature of the hot nozzle while performing ironing (set to 90°C in this work) and, ii) the ironing speed, namely the speed at which the hot nozzle moves on the last extruded layer (set to 10 mm/s in this work), in that a lower speed results in more heat exchanged with the conductive layer.

This outcome suggests that in the case of ironing, a higher diffusion at the layer interfaces occurs since the healing time (τ_h), namely the time every layer is above T_{glass}, is higher compared to the traditional as-is scenario. As demonstrated in [214], τ_h is a crucial variable to bond (heal) two consecutive layers of polymeric material processed via the MEX approach. th represents the time at which the diffusion between two layers occurs: the higher τ_h, the higher the intralayer adhesion. As such, higher interface diffusion is translated into better adhesion and, in turn, better mechanical properties. It is hypothesised that this phenomenon could be the underlying mechanism driving the improved great stability recorded for the ironed samples. Additionally of note, as the layer adhesion is improved, common problems in layered structures such as delamination and creeping were reduced, resulting in enhanced stability of electrical resistance variation when 3D printed sensors are cyclically stressed.
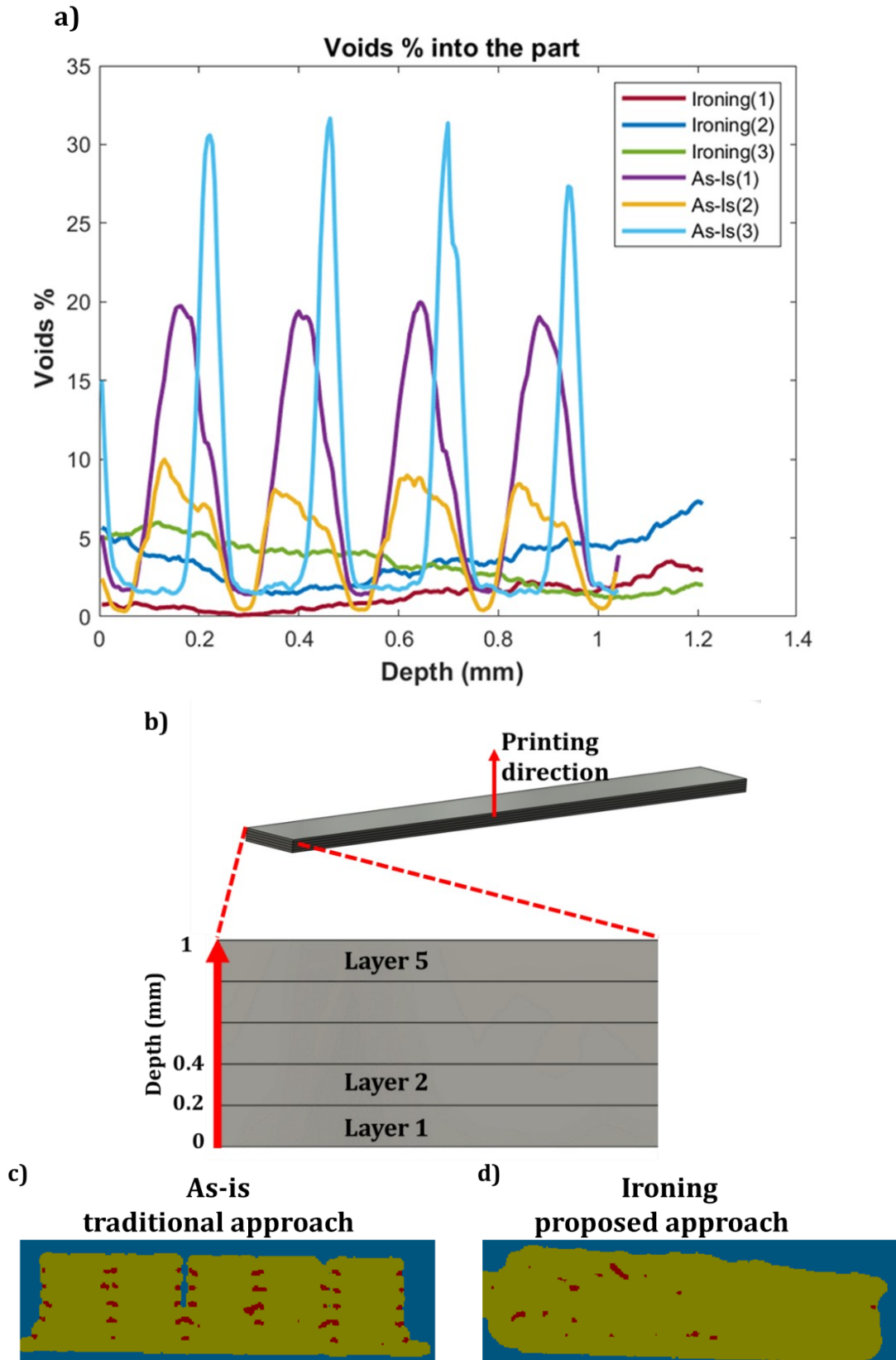
Fig. 3.15: Porosity: a) void content % vs depth (sensor thickness) for three ironing and three as-is samples, b) graphical representation of the correlation between depth and layers, c) CT scan figure showing the voids in the cross section of 'as-is' sample and d) CT scan figure showing the voids in the cross section of an 'ironing' sample.
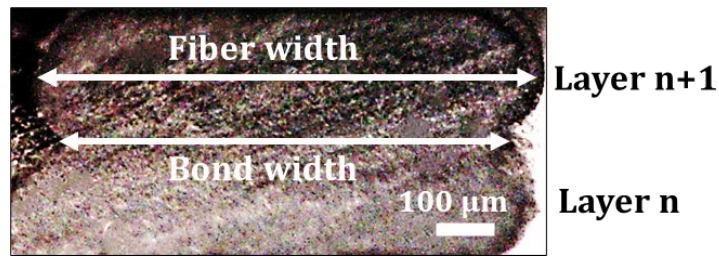
Fig. 3.16: Cross section view of as-is sample using digital microscope:bond width and fibre width are shown at the interface between consecutive extruded layers.
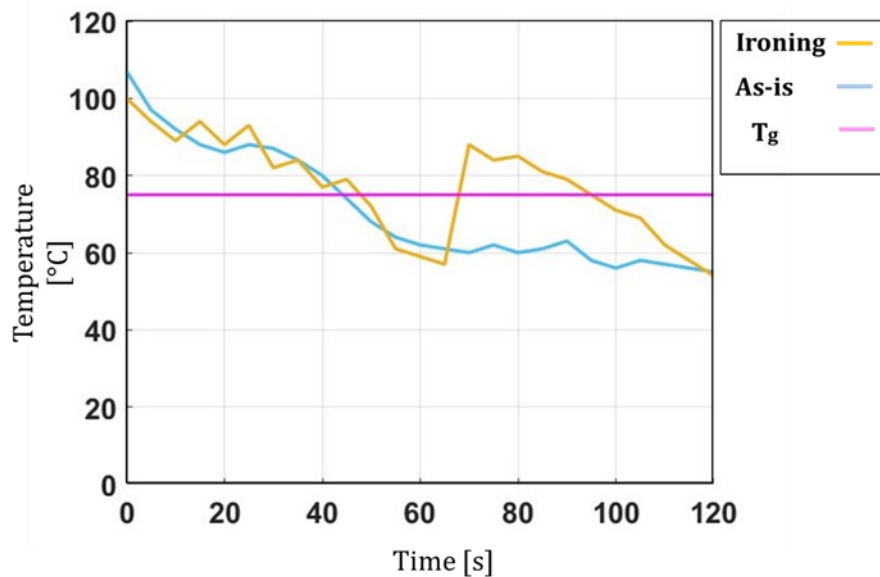
Fig. 3.18: Temperature history profile for ironing, and as-issamples during fabrication with respect to CPLA glass transition (Tg) temperature.

3.3.3 Proposed approach for smart structures

The proposed approach based on the usage of the ironing strategy to improve sensor performance has been used for the fabrication of two proof of concept smart 3D printed devices: a smart self-monitoring structure and a smart auxetic structure. In both cases, the dielectric structure and the conductive sensors have been 3D printed in the same manufacturing cycle, resulting in no assembly steps. A simple prismatic PLA smart structure was manufactured by depositing a piezoresistive sensor onto the main structure to create a force sensor capable of detecting the applied force, as shown in **Fig. 3.19 a**. Two self-monitoring structures were fabricated, respectively, by employing the approach proposed in the present research (ironing) and by using regular printing settings (as-is). Several calibrated weights have been applied on the top of the smart structure (see **Fig. 3.19 a)** and the change in electrical resistance of the sensor was recorded using the same benchtop multimeter.

From **Fig. 3.19 b**, the proposed benefits from the phenomena displayed in this work demonstrate the potential performance increase that can be seen in 3D printed smart structures that employ piezoresistive sensors. The smart structures printed using the ironing approach are capable of detecting a minimum change of force of $0.19\ N$ due to their improved sensitivity as compared to their traditionally printed counterpart. The structure fabricated under traditional printing conditions (as-is) shows a very low sensitivity with a minimum force detection of $1.96\ N$. Due to the increased sensitivity, the proposed approach could be used to 3D printed structural components undergoing loads to obtain real-time data about the applied force.

Another potential use of the proposed approach is related to structural health monitoring in which structural plastic components difficult to be inspected with traditional approaches could be monolithically fabricated with embedded piezoresistive sensors, and the change in electrical resistances could be associated to potential damages in the structure.

Finally, an auxetic structure (geometry proposed in [239]) was 3D printed with an embedded sensor. In this case, the embedded sensor fabricated by using the proposed adhesion-centered approach, was employed to sense displacement, as opposed of bending, showing the wide range of possible applications of 3D printed piezoresistive sensors. The dielectric component of the auxetic device was fabricated by employing thermoplastic polyurethane (TPU), one of the most common soft materials for auxetic devices. The smart auxetic structure is shown in **Fig. 3.20 a**, with two different versions have been created. The first version having the walls of the unit cell (see **Fig. 3.20 b**) equal to $0.8\ mm$, and a second version with walls of $0.4\ mm$. A dual-track piezoresistive sensor was fabricated on the top of the TPU auxetic geometry for both version. The reason for manufacturing two versions of the same auxetic structures is to prove the scalability in terms of sensor width of the proposed approach. For both versions, the ironing strategy was used to enhance the sensitivity. Both versions have been tested by employing an Instron 68TM-10 machine to compress the auxetic structures, while the force, displacement and electrical resistance of the sensor were simultaneously recorded. A maximum force of $50\ N$ was applied. Version one with walls of $0.8\ mm$ exhibited a maximum displacement of $3.8\ mm$, while version two with walls of $0.4\ mm$ exhibited a maximum displacement of $14\ mm$. For both versions, a decrease in resistance occurred while compressing the auxetic device, as expected from the piezoresistive theory. In this case, the change in resistance was correlated to the displacement of the auxetic structure, and for version two (the one exhibiting the highest displacement), a sensitivity of $17.6\ V/mm$ was obtained. The same auxetic structure having a wall thickness of $0.4\ mm$ (the one exhibiting a larger displacement) was also fabricated without applying 'ironing' on the top surface of the sensor, namely according to the 'as-is' scenario. While testing the structure, a delamination of

conductive layers of the sensors occurred at a force of $12\ N$ (displacement of $4.75\ mm$) making the 'as-is' strategy unsuitable for the fabrication of smart auxetic structures undergoing an appreciable amount of compression. Such outcomes are directly correlated to the findings of Section 3.3.2.2, and 3.3.3.2. By leveraging the ironing strategy, a great interlayer adhesion occurs, demonstrated by a void reduction of 59% and an increased healing time (from $44s$ to $77s$).

Auxetic structures have been gaining a lot of popularity since they can efficiently absorb huge amounts of energy and provide several benefits to many fields such as military, biomedical and sport [[240]–[242]. A lack of scientific literature about auxetic devices with embedded sensors motivated the authors to fabricate TPU auxetic shapes with embedded piezoresistive sensors using a monolithic approach. In this way, inexpensive auxetic devices could provide the users additional benefits, such as real-time data related to the displacement of the whole structure, as shown herein, and potentially to the applied force and energy absorbed from the auxetic structure.
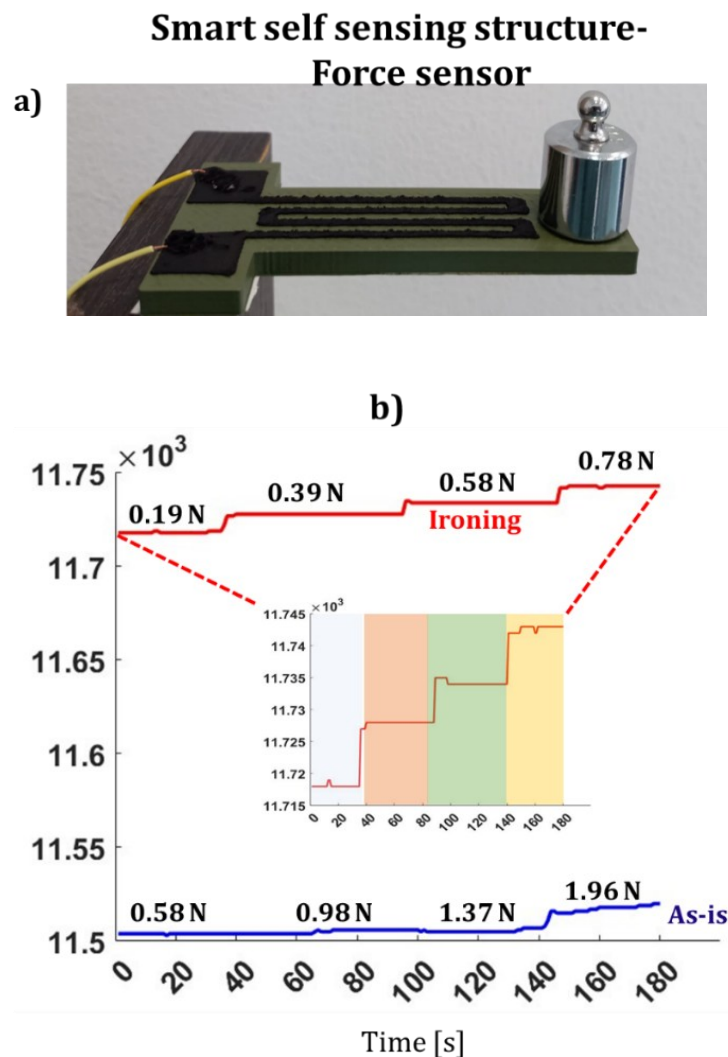
Fig. 3.19: a) 3D printed smart self sensing device (green =PLA, black = CPLA), (b) Response of the structure fabricated using the traditional and proposed approach.
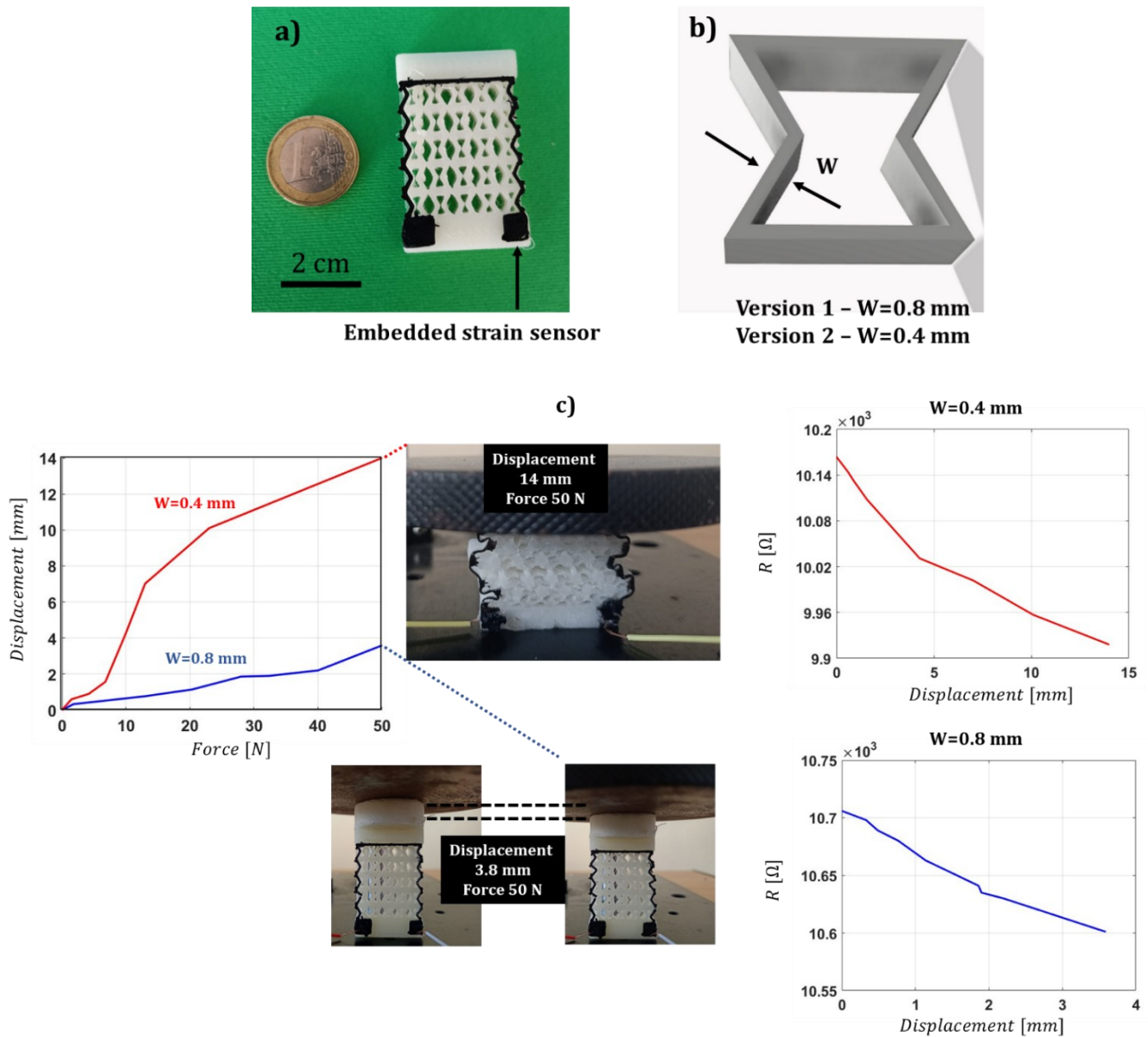
Fig. 3.20: a) 3D printed smart auxetic device, (b) different thickness of the unit cell, (c) characterisation of the two versions of the auxetic device.

3.3.4 Conclusions

The work herein highlights the significance to which the ironing strategy can be used in the fabrication of MEX sensors and smart structures. This very simple and effective method was used to enhance the electrical properties of 3D printed sensors. The ironing strategy does not require any 3D printing machine modifications since it leverages the hot nozzle to 'iron' the previously extruded layer of CPLA by making the structure compact and uniform via the application of heat and mechanical pressure. The ironing process parameter increased the sensitivity of 3D printed sensor by 83% due in part to the mechanical pressure applied from the hot nozzle reduces the voids among consecutive

layers. The reduction of voids has been analysed by using an X-Ray CT scan system, and a porosity reduction of 59% was achieved when performing ironing compared to the traditional as-is printing scenario. Ironed samples also show an increased bond width between consecutive layers almost equal to the fibre width, resulting in an improved wetting factor. The reduction in voids provides a smoother path for electrical current flow. The macroscopic findings, such as higher sensitivity, have been then related to the improved microscopic features, such as decreased void content, of the 3D printed sensors. Lastly, the ironing process parameter was found to improve the stability of electrical resistance when stressing the sensor cyclically. When performing ironing, the hot nozzle heats up the previously extruded layer above its glass transition (T_{glass}) temperature, resulting in an increased healing time (τ_h) of the layer. The increased τ_h means increased polymer chain diffusion, which, in conjunction with the reduction of voids, promotes improvement interlayer adhesion. For this reason, the ironed sample presents good stability in the electrical resistance when mechanically stressed. In conclusion, the ironing parameter could be potentially used every time 3D printed sensors are fabricated via MEX systems to improve their electrical performance without recurring any post-treatments and machine modifications. Future works will be focusing on modelling the sensor performance (i.e. stability) by combining several variables, such as intralayer voids, noise and variability. The main findings of the research are listed in **Table 3.6**.

Table 3.6: Main outcomes presented in this research work.

Proposed Approach (Ironing	Sensitivity	Voids (porosity)	Conductivity	Stability	Healing time (τ_h)
	Improvement of 83%	Reduction of 59%	Improvement of 40.1%	Improved	Increased – 77 s for ironing, 44 s for 'as-is'

3.4 Additive Manufacturing setup: separate heating system to enhance mechanical, healing properties and assembly-free smart structures of Diels-Alder self-healing polymers

An innovative solution to pre-heat self-healing inks directly on board of the MEX machine, by developing a separate heating system (SHS) is proposed in this research: the syringe barrel (self-healing ink reservoir), and nozzle (used to deposit the ink) are independently controlled temperature-wise. The pre-heating problem has been tackled, and systematically analysed by means of the proposed SHS approach, as depicted in **Fig. 3.21**. As a matter of fact, experiments have been conducted to correlate the temperature set on the barrel and nozzle (SHS approach) to: i) printing quality, ii) printing accuracy, iii) mechanical properties, and iv) self-healing performance. The 3D printed parts, fabricated by recurring to the proposed SHS approach exhibit an increase in printing accuracy of 26%, strongly correlated to a remarkable reduction of extrusion force (77% lower), measured during the 3D printing process, compared to the one fabricated according to the traditional approach.

Additionally, the samples fabricated by recurring to the optimal printing conditions (SHS approach) were characterized by a 95% of healing performance, proving the effectiveness of the proposed approach for the fabrication of self-repairing components. Finally, the custom-made MEX machine was also used to jointly extrude a dielectric self-healing ink (from the syringe system) and an electrically conductive self-healing filament (from the filament print head) to create assembly-free smart structures with embedded sensors that shown high sensitivity ($3.10\ \Omega/degree$) and healing performance.
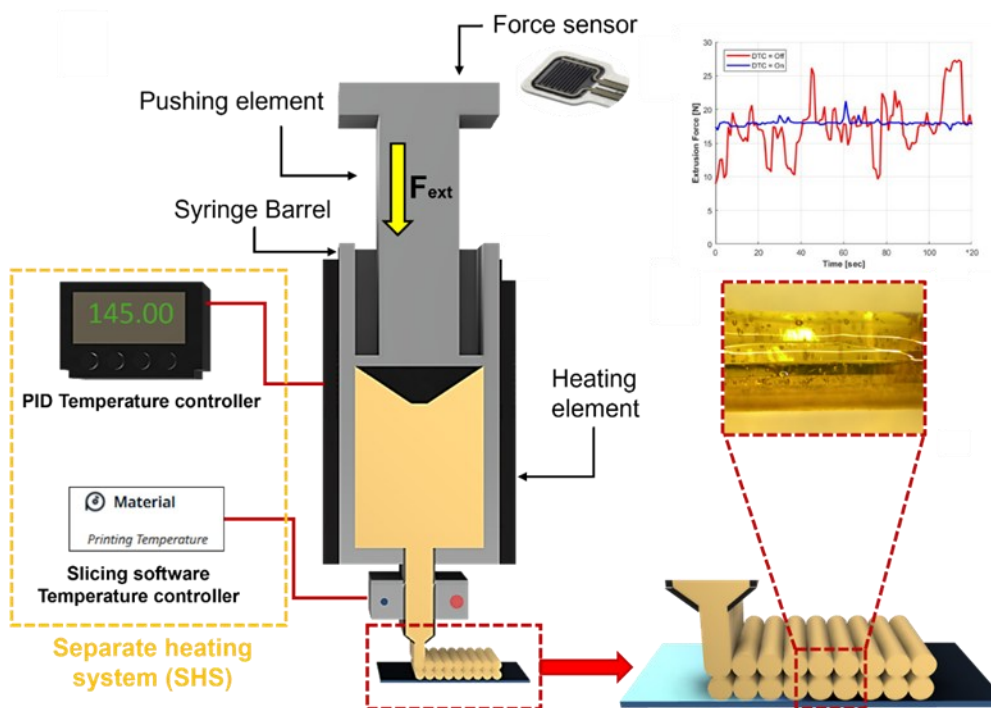
Fig. 3.21: Workflow underlying the present research: schematic of the innovative separate heating system (SHS) used to 3D print Diels-Alder self-healing ink, wherein a real-time force sensor was used to evaluate the extrusion force during the printing.

3.4.1 Materials and methods

3.4.1.1 Self -healing polymers preparation

In this work two different self-healing polymers based on the Diels-Alder reaction between furan and maleimide were used: a dielectric self-healing polymer and an electrically conductive self-healing composite. Their synthesis, materials, composition and characteristics are described in detail below.

Synthesis of the dielectric self-healing polymer is Pripol-based and resulting from the following synthesis steps. First Pripol™ 1040 is reacted via epoxy-carboxylic acid ring-opening with furfuryl glycidyl ether (FGE) in the presence of $0.5\,wt.\%$ zinc acetylacetonate (Zn(acac)2). This reaction is performed in a $1:1$ stoichiometric ratio between the epoxy and the $COOH$ groups. The reaction is carried out for 24 hours at $100\,°C$ under nitrogen, with continuous stirring provided by a magnetic stirrer, yielding a furan functionalized Pripol. This was mixed with DPBM bismaleimide in a $1:1$ stoichiometric furan-to-maleimide ratio. In addition, $1\,wt.\%$ radical inhibitor, more specially 4-tert-butylcatechol, was added to the mixture, after which it was heated to $150°C$ for 5 minutes to dissolve the DPBM and inhibitor, resulting in a transparent mixture. Next the mixture was poured in mould at room temperature, around $25\,°C$. Upon cooling, Diels-Alder crosslinking between the furan

and maleimide leads to the formation of the thermoset network. The synthesis is completed by leaving the thermoset 24 hours at 25°C.

Synthesis of the conductive self-healing composite starts with the furan functionalization of Jeffamine JT5000. This is performed in an epoxy amine reaction by mixing JT5000 with FGE with a 1:1 stoichiometric ratio and heating the mixture at $60\,°C$ for 7 days, followed by 2 days at $90\,°C$. Next, the resulting furan-functionalized Jeffamine is dissolved together with DPBM in chloroform with a $20\,wt.\%$. $5\,wt.\%$ 4-tert-butylcatechl is also added to the mixture. To achieve electrical conductivity, a hybrid filler, composed of $7.5\,wt.\%$ carbon black (Ensaco 360G) and $1.5\,wt.\%$ of nanoclay (Cloisite 15A) is added. All components are added to a well-sealed container that is placed on a mechanic stirrer for 24 hours at ambient conditions to ensure that materials are dissolved and all filelrs are well dispersed. Chloroform is extracted in a vacuum oven at $60\,°C$ for $24\,hours$ after which the mixture is cooled down. Upon cooling, Diels-Alder crosslinking between the furan and maleimide forms the composite network. The synthesis is finalized by allowing the thermoset to sit for $24\,hours$ at $25°C$. More details on the preparation of this composite can be found in [166][243].

Materials: Pripol™ 1040 is a mixture of trimer (77%) and dimer acid monomers (33%) and is supplied by Cargill. It is a viscous liquid with a molar mass of 820 g.mol^{-1} and a functionality of 2.77. JT5000 is a polyetheramine obtained from Huntsmann from the Jeffamine T-series triamines, with a molecular weight of $5712\,g.mol-1$. Furfuryl glycidyl ether (FGE), with a purity of 95 %, was purchased from Sage Chemicals (China) and stored in refrigerated conditions. Zinc acetylacetonate (Zn(acac)$_2$) powder is supplied by Sigma Aldrich. 1,1'-(Methylenedi-4,1-phenylene) bismaleimide (DPBM) with a purity of 95 % was obtained from Sage Chemicals (China). 4-tert-butylcatechol is provided by Sigma Aldrich.

Composition and mechanical characteristics of the dielectric self-healing polymer and the conductive self-healing composite are listed in **Table 3.7** and **3.8**, respectively. In the composition of the network, we approximate that at ambient temperatures the Diels-Alder conversion is equal to 1 (e.g. all maleimide is reacted). The mechanical properties (E, σ_{max} and ε_{max}) were derived by tensile testing, the glass transition temperature via differential scanning calorimetry (DSC) and the degelation temperature via dynamic rheometry (see Appendix B, Section B1).

Table 3.7: Composition of the Diels-Alder polymer and composite

	Initial maleimide concentration $[M]_0$ mol.kg^{-1}	Initial furan concentration $[F]_0$ mol.kg^{-1}	Maleimide-to-furan ratio r /	Diels-Alder concentration [DA] mol.kg^{-1}
Self-healing polymer	1.55	1.55	1	1.55
Self-healing composite	0.49	0.82	0.6	0.49

Table 3.8: Mechanical properties and thermal transitions of the Diels-Alder polymer and composite

	Young' modulus E MPa	Fracture stress σ_{max} MPa	Fracture strain ε_{max} %	Glass transition temperature T_g °C	(De)gelation temperature T_{gel} °C
Self-healing polymer	832	23	12	53	135
Self-healing composite	7.8	3.0	210	-62	115

3.4.1.2 3D printing with Diels-Alder polymers

Unlike traditionally irreversibly, like rubbers or silicones, the Diels-Alder polymers are thermo-mechanically reprocessable thanks to their thermoreversible Diels-Alder crosslinks (**Fig. 3.22**). The 3D printing of these self-healing polymer networks relies on these thermoreversible Diels-Alder crosslinks. When the polymer is heated above its gelation temperature (T_{gel}) the extensive breaking of these reversible crosslinks causes the network structure to break down, resulting in a low viscosity liquid polymer. In this liquid state, the polymer can be reprocessed using various techniques [244], including ink-based MEX as demonstrated in this paper. This solid-to-liquid transition is completely reversible as upon cooling down the Diels-Alder crosslinks are reformed, restoring the polymer network. During 3D printing this allows to solidify on the print bed.
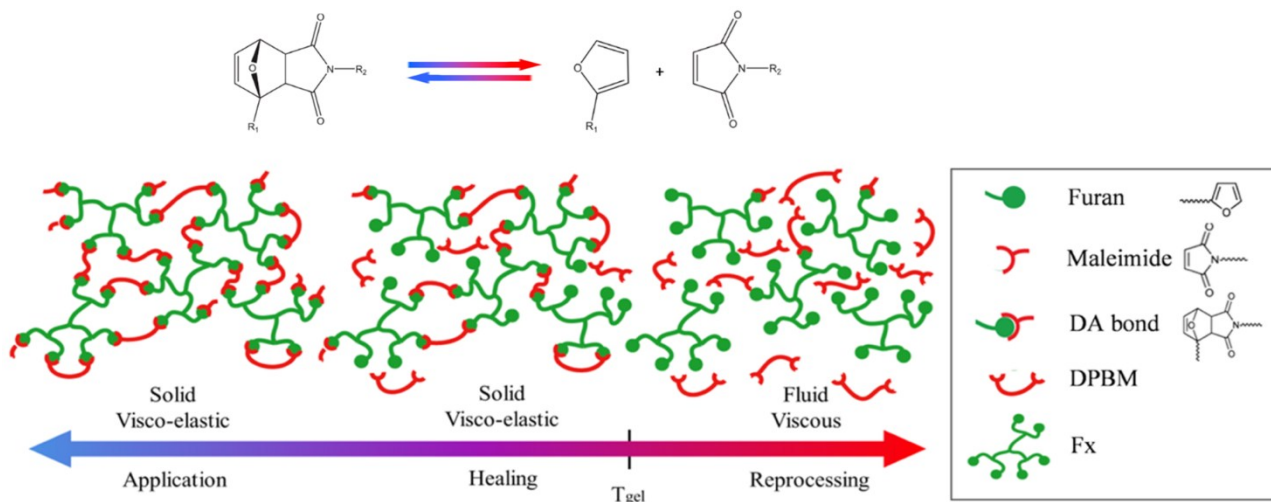
Fig. 3.22: The reversible network structure of the Diels-Alder polymers is formed by Diels-Alder crosslinks. These are thermoreversible crosslinks that upon heating break down. With increasing temperature, the equilibrium of the equilibrium Diels-Alder reaction is pushed to the unbound state, gradually breaking a larger portion of the Diels-Alder bonds into furan and maleimide. Above the gelation temperature (Tgel) extensive breaking of the Diels-Alder bonds leads to a loss of the network structure and a solid-to-liquid transition. Fx is noted as the furan containing compound. For the self-healing polymer this is furan functionalized Pripol, while for the self-healing composite it is furan functionalized Jeffamine.

Consequently, unlike traditional ink-based MEX for network polymers, where monomers are premixed or mixed during printing, this 3D printing process with Diels-Alder polymers involves liquefying an already polymerized polymer network. This offers a significant advantage, as premixing often limits print size due to the polymer beginning to polymerize upon mixing and mixing during printing presents reproducibility challenges due to insufficient blending. Using reversible polymer networks, like the Diels-Alder polymers, allows to synthesize large batches of polymer, of which a part can be liquified during ink-based MEX. Even more importantly, this approach allows for the reprocessing of polymers, enabling the recycling of parts. Nevertheless, it requires more precise temperature control, as discussed in the next section.

3.4.1.3 Separate heating system (SHS)

The ink-based 3D printing of Diels-Alder polymers relies on the reversible degelation of these polymers (e.g., the solid-to-liquid transition). To create ink, the Diels-Alder polymer must be heated above T_{gel}. Therefore, the polymer in the barrel (material reservoir) must be heated above T_{gel}. As illustrated in section 3.4.1.2, the viscosity of the Diels-Alder polymer and the composite is highly temperature-sensitive, necessitating additional controlled heating at the nozzle. For this, the paper proposes an innovative approach aiming at overcoming such issues: the traditional approach involves the use of only one heater element (barrel or nozzle). The proposed one allows 3D printing of self-healing ink-materials using two separate heating elements to independently control the barrel and the

nozzle temperature, as shown in **Fig. 3.23**. It should be noted that the main components of the proposed SHS approach, are detailed in Section 3.4.1.4. The authors used the following nomenclature throughout the whole paper: i) extrusion temperature (Text) refers to the nozzle temperature, required to melt the self-healing polymer (generally, such a temperature is also referred as printing temperature), ii) barrel temperature refers to the temperature (equal to $135\,°C$) set to improve the flowability of the self-healing polymer, on the barrel located on top of the nozzle.

Three values of extrusion temperature (nozzle temperature) were studied, namely $145\,°C, 150\,°C$, and $155\,°C$. It should be noted that below the lower limit ($145\,°C$) the polymer was not completely melted, resulting in clogging problems inside the nozzle, and discontinuous extrusion. On the other hand, above the upper limit ($155\,°C$), the polymer degradation occurs, as well as the loss of the healing behaviour.

3.4.1.4 Custom-made ink-based 3D printer

The main focus of the present research is related to the custom-made 3D printing setup used to extrude the self-healing polymer: a separate heating system (SHS) was implemented, in order to heat up the ink, not only in the nozzle, but also in the syringe barrel (see **Fig. 3.24**):

i) A commercial ToolChanger 3D printer (E3D, Oxfordshire, UK) equipped with four independent direct-driven filament extruders, was modified to enable the extrusion of self-healing ink-based materials. The system is based on a robotic Toll-handler that selectively (based on the .gcode file) approaches, picks and moves a specified extrusion head (parked in the bottom of the 3D printer) per time, allowing the multi-material extrusion. In the present work, only two print heads were used: a non-modified printhead to extrude, and a modified print head to extrude self-healing ink. The latter is extensively described in the supplementary materials; however a metal syringe was employed and the main elements to convert such a commercial filament print head into a system capable of processing ink-based materials, are here described. A stepper motor (Nema E3D) connected to an integrated lead screw to linearize the motion, was fixed using a 3D printed part to the custom plate. Two cylindrical line bars that run into a linear bearing were employed to facilitate the linear translation motion (See **Fig. 3.24 a**).

ii) A custom-made metal pushing part was fixed to the lead screw to push against the syringe piston, thereby allowing the extrusion of the ink-based material.

iii) A 2 mm thick Self-Adhesive Thermal Interface Sheet was used to thermal-isolate the extruder system and the custom plate to the metal syringe, to avoid overheating of the tool-head mechanisms.

iv) A custom-made cooling fan was fixed to the plate in order to only blow air on the extrudate.

v) A commercial extra thin force sensor (see Appendix B, section B2), controlled using an Arduino Uno Board, was placed between the pushing part and syringe piston, to evaluate the printing force.

The custom-made metal syringe used to extrude the self-healing materials was based on 40 ml syringe model and manufactured using a Computer Numerical Control (CNC) machine in aluminum. It should be noted that two reasons led the authors towards the choice of a metal syringe over traditional plastic syringes: i) possibility of heating the self-healing material within the barrel (and not only inside the nozzle), ii) and avoiding melting and deformation issues of the syringe itself. Moreover, the metal syringe simplifies the cleaning tasks of the reservoir without the material adhering firmly to the barrel-walls, other to guarantee an easy extrusion during the material pushing, unlike the traditional plastic syringe. The syringe was designed according to the CNC manufacturing and to easily clean the internal surface. Moreover, the syringe was blocked to the custom plate using only three screws, in order to facilitate the assembly. **Fig 3.23 b** depicts the traditional MEX approach, and the proposed one, enabling a separate temperature control. As shown, in 3.4.1.1, 3.4.1.2, the SHS improves several properties of the extruded ink, such as the printing quality, the geometrical accuracy, the mechanical and healing performances.

To implement the separate heating system (SHS), the syringe was equipped with the following elements:

i) A Barrel cylindrical heater (RS Components, Belgium) controlled using a PID digital temperature controller (Rs Components, Belgium) with internal thermocouple (see Appendix B, section B3).

ii) A heater-block housing a 40 W heater cartridge and a thermocouple, were fixed to the syringe, and controlled through the slicing software.

Finally, the glass build plate, capable of reaching a maximum temperature of 70 °C was used.
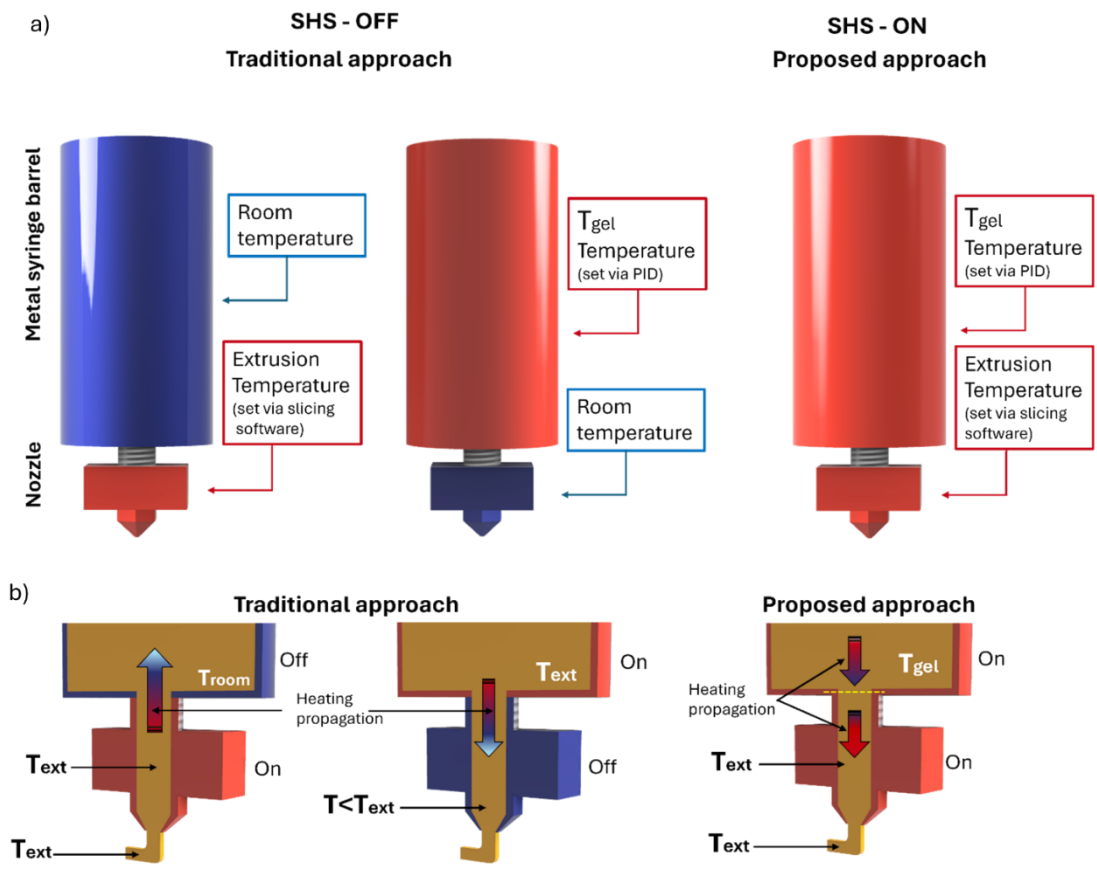
Fig. 3.23: Separate heating system (SHS) proposed approach vs traditional approach: a) in the traditional approach the working temperature of the nozzle (extrusion temperature set via slicing software) or the metal syringe barrel (gelation temperature set via PID) are not set at the same time, on the other hand the proposed approach allows to set the nozzle and the barrel temperatures at the same time controlling better the extrusion of the SH materials, b) the heating propagation using the traditional approach does not ensure proper control over the SH material extrusion while the proposed approach ensure a good control of the temperature (first gelation temperature is set on the barrel and then extrusion temperature is set in the nozzle).
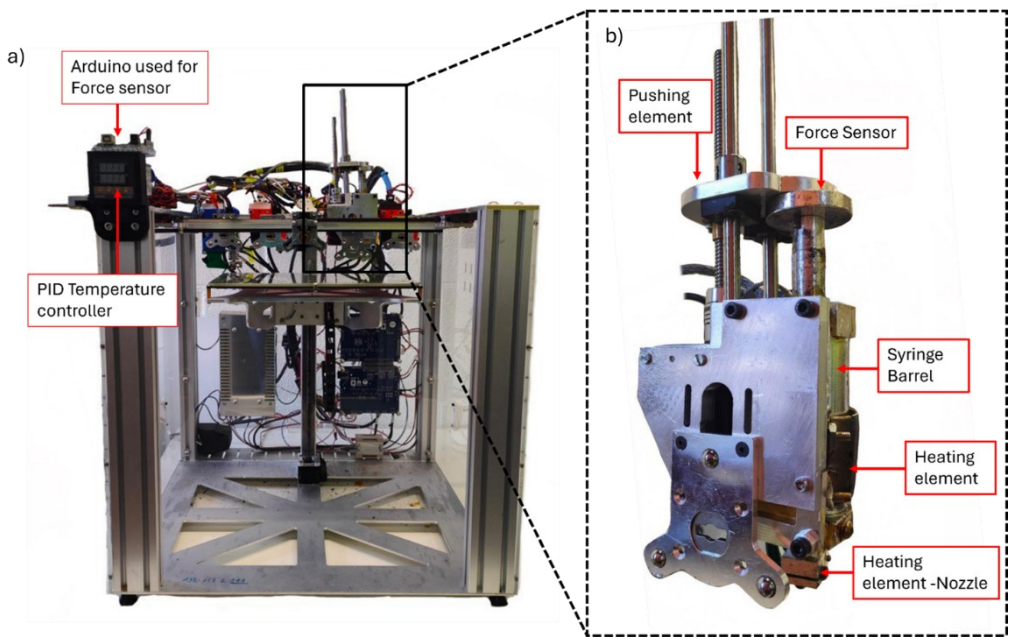
Fig. 3.24: Custom-made material extrusion 3D printed: a) E3D ToolChanger machine modified to extrude filament- and ink-based self-healing materials in the same printing cycle, b) custom-made ink-based heads equipped with metal syringe to extrude the thermoset self-healing.

3.4.1.5 Relationship SHS - Temperature-geometry accuracy

Several easy and complex 2D shapes were printed to evaluate the geometrical accuracy of the 3D printing process by i) changing the nozzle extrusion temperature ($145, 150,$ and $155 \degree C$) and enabling the SHS system ($135\degree C$ of temperature for the syringe barrel was set according to the gelation temperature), and ii) changing the barrel temperature ($145, 150,$ and $155 \degree C$) for the traditional approach (SHS=OFF).

A series of linear single-bead structures and serpentine structures (see Section 3.4.2) with a fixed length of $30\ mm$ were 3D printed (printing time of $120\ s$). The 3D printed structures were compared to the CAD design to evaluate the printed filament width $w_f\ (mm)$ and the relative filament deviation σ_f [245], according to the following equation

$$\sigma_f = \frac{w_f}{d} - 1 \qquad\qquad (3.15)$$

where d is the nozzle diameter used (mm). A modular high-performance stereomicroscope Leica MZ1325 (Leica Microsystems, Wetzlar, Germany) was used to analyze the 3D printed samples, in order to measure the term w_f.

3.4.1.6 Relationship SHS - Temperature-extrusion force

A common problem, negatively affecting MEX is the relationship between layer height and extrusion force, the smaller the layer height of the extrudate, the higher the extrusion force. High values of extrusion force led to unwanted issues, such as over-extrusion, and skewing (especially for thin structures) [119], thereby decreasing the overall quality of the 3D printed parts.

As described in 3.4.1.2, a force sensor (CP 150, RS Components, Belgium) placed between the syringe piston and the pushing part was employed to measure the force while extruding self-healing ink at $0.2\ mm$ of layer height (a good compromise among manufacturing time and accuracy). The most important process parameters set throughout this experimental phase are listed in **Table 3.9**. A nozzle with a diameter equal to $0.8\ mm$ was employed to avoid clogging problems.

The extrusion force was evaluated under two main conditions: when the SHS was ON (proposed approach), and OFF (traditional approach). For every condition, the best extrusion temperature found in the accuracy test, were studied in order to determine the extrusion force. Moreover, the extrusion

force was studied for the proposed approach when the minimum and maximum value of temperature used to melt the self-healing ink, avoiding its decomposition, were set. The temperature of the barrel (in the proposed approach) was set to liquefy the self-healing material avoiding rheological and flowability problems during the 3D printing process [246].

Finally, complex 3D structures were 3D printed by recurring to the optimal condition in terms of force reduction (and the worst) demonstrating the potential of the proposed SHS approach.

Table 3.9: Printing parameters of thermoset self-healing.

Process parameter	Value
Layer height Lh (mm)	0.2
Flow rate Q (mL/min)	0.3
Line width Lw (mm)	0.8
Nozzle diameter d (mm)	0.8
Printing speed (mm/s)	15
Building plate temperature (°C)	60
Barrel temperature (°C)	135

3.4.1.7 Relationship SHS - Temperature-mechanical properties

After demonstrating, all the benefits of the SHS in terms of geometry accuracy, and reduction of extrusion force, the mechanical properties of self-healing ink fabricated with the SHS ON were evaluated. In particular, three different nozzle extrusion temperatures ($145, 150, and\ 155\ °C$) were studied. According to [181], the ASTM D638-14 Type V standard was chosen. Tensile samples were fabricated with two different raster orientations: 0°, and 90° (the design is reported in the Appendix N, section B5).

Once printed, the samples were cured in an oven at $70°C$ for $8\ hours$ and consequently were dried at room temperature for one day in order to increase the crosslinks between layers. A Tinus Olsen 5ST (Tinus Olsen, Redhill, UK) universal machine equipped with 2.5 kN load cell was used to test the 3D printed samples. Moreover, a comparison between the mechanical properties of moulding, traditional and proposed approaches was performed.

3.4.1.8 Self-healing analysis

The self-healing polymer, the Diels-Alder thermoset, heals non-autonomously, requiring a heat stimulus. This necessity arises from the limited mobility in the polymer network under ambient conditions, which, while providing high mechanical strength and stability, necessitates a temperature increase to initiate the healing process. To evaluate the healing performance of 3D printed parts, three rectangular samples $(10x20x0.6\ mm)$ were 3D printed using the best nozzle extrusion temperature $(145°C)$ and recurring to the SHS and were mechanically tested prior to damage and after self-healing. The following damage-healing cycle was adopted:

i) Several micros (partial cutting) and macro (the samples were cut in the middle forming two more parts) damages from 5 to 20 mm were manually inflicted to the printed samples using a cutter. Moreover, an awl with a 3 mm hint of diameter was used to create a circular damage on the top of the samples.

ii) To ensure enough mobility for self-healing the Diels-Alder polymer must be heated above its T_g, which is set at 53 °C. Above this temperature the network behaves as an elastomer, providing mobility for self-healing. Consequently, the samples were heated at $70°C, 8\ hours$ in a controlled oven. In addition, at this temperature a portion of the Diels-Alder crosslinks break, providing reactive maleimide and furan in the network in order to self-heal. Note that this healing temperature remains far below T_{gel} ensuring a solid state and mechanical stability during healing, not compromising any structural integrity of the 3D printed samples.

iii) Afterward, the samples were cooled to room temperature and left to heal under ambient conditions for 24 hours. During the cooling period, the furan and maleimide rebounded, reforming the Diels-Alder crosslinks throughout the polymer network and across the fracture interface. Consequently, the self-healing polymer appeared as good as new, achieving complete healing.

Pristine and healed samples were characterized using tensile testing until fracture with a strain ramp of 1% $per\ minute$. A common approach to assess the self-healing capabilities of polymers, composites or their resulting sensors is by calculating their self-healing efficiency for several parameters, denoted as η_p, formally defined by Equation (3.16):

$$\eta_p = \frac{P_{healed} - P_{damaged}}{P_{pristine} - P_{damaged}} \tag{3.16}$$

Here, property (P) can include mechanical parameters such as Young's modulus (E), fracture strain (ϵ) and fracture stress (σ), toughness. However, also the recovery of electrical and piezoresistive attributes like conductance (C) and sensitivity (S) can be studied based on healing efficiency. In this study, the sensor is severely damaged by being cut in half, resulting in all the aforementioned properties dropping to zero in the damaged state, as shown in Equation (3.17) Healing efficiency is defined as the ratio between the property measured in the nth healed state and its value in the pristine state. Ideally, measuring the healing efficiency of a pristine sensor would yield 100% efficiency for any parameter.

$$\eta_p = \frac{P_{healed}}{P_{pristine}} \tag{3.17}$$

3.4.1.9 One-shot fabrication of assembly-free structures (smart structures)

To demonstrate the potential of the proposed approach two different self-healing materials were extruded in the same manufacturing cycle, to manufacture a multi-material structure. In particular, a dielectric self-healing polymer, and an electrically conductive self-healing composite were employed to fabricate a dielectric structure with an embedded piezoresistive sensor (**Fig. 3.29 a**). The design of the sensor is based on a previously work [21], as shown in **Fig. 3.29 c**. Both the sensing and self-healing performance of the sensor were analysed. The sensor was designed as a bending angle sensor. The relative resistance change $\frac{\Delta R}{R_0}$ was calculated for both the original sensor and the sensor after the healing process. Moreover, the sensitivity S was calculated to evaluate the healing efficiency, as follows:

$$S = \frac{\Delta R}{\Delta \alpha} \tag{3.18}$$

where $\Delta \alpha \, (degree)$ is the bending angle variation and $\Delta R \, (\Omega)$ is the variation of the measured resistance. Electrical wires have been soldered to the sensor pads, and connected to a benchtop multimeter (GW Instek, GDM 8341), in turn connected to Matlab software (The Mathworks, Inc.) to record the resistance change. The sensor was bent by using a nylon wire (connected to the top part of the dielectric structure), connected to a stepper motor (NEMA 17) instructed through Arduino Uno (**Fig. 3.30 b**). The stepper motor performs a forward and backward movement, both at $300 \, RPM$, which corresponds to a bending angle of the sensor of $36.8 \, degree$. The test was run for $45 \, min$ for both the original and healed sensors.

3.4.2 Results

3.4.2.1 Effect of the SHS on geometrical accuracy

In this work a variety of test prints have been demonstrated that the use of separate heating system (SHS) improved the printing quality and the geometrical accuracy, reducing the printing force and kept it constant throughout the printing process. In order to increase and optimize the printability of the ink-based self-heling material, an iterative method was used to determine the optimal process parameters [245]. First, the material was extruded to determine the flow rate Q, varying different printing speed, layer height and nozzle diameters. According to this and the lower viscosity of the ink-based material ($1.9\ Pa.s\ at\ 145°C$) the optimal printing parameters were set such shown in **Table 3.7.** After this, several structures were printed to determine the printing accuracy.

Particularly, in the ink-based 3D printing of self-healing thermosets, parameters such as printing speed and temperature considerably influence both the deposition and the Diels-Alder reaction of the ink [168]. When a lower values of printing speed are set, the quality of the printing increase according to the nozzle extrusion temperature that does not exceed much the T_{gel} of the material [168]: at $145°C$, the ink takes $50\ s$ to degel, which equal a maximal printing speed of *15 mm/s*. This resulted in high-quality and geometry accuracy of 2D and 3D structures printing and minimized layer deformation during the deposition of the next layer. Additionally, maintaining a uniform temperature using the SHS, allows for precise control of the material deposition, thereby enhancing geometrical accuracy. To validate this, several easy 2D linear and snake structures were printed with both the nozzle and the syringe set at the same temperatures. The printed samples were compared with the CAD design. The samples printed with the nozzle temperatures of 145 and $150°C$ resulting in a high-geometrical accuracy (**Fig 3.25 a, b**). On the other hand, the sample printed set the temperature around $155°C$ (**Fig. 3.25** c) presented several geometrical problems in both linear and snake shapes. Indeed, in order for the dimensional and quality accuracy to be acceptable, the extrusion temperature must be set close to the gelation temperature of the ink and the SHS must be on. Nozzle temperature of 145 and $150°C$, when the SHS is active, yield printed beads with the right line width dimension ($0.8\ mm$), respectively with a relative error of 0.06 and $0.15\ mm$ (see **Fig. 3.25 d**). However, exceeding a lot the gelation temperature during the printing (when the nozzle extrusion temperature is set to $155°C$), the structures printed accuracy decrease considerable, and the width of the bead range from 0.12 to

2.45 mm caused clogging problems in the nozzle, with the uncontrollable flow of the ink (see **Fig. 3.25 c**), and the impossibility to print the snake structure.
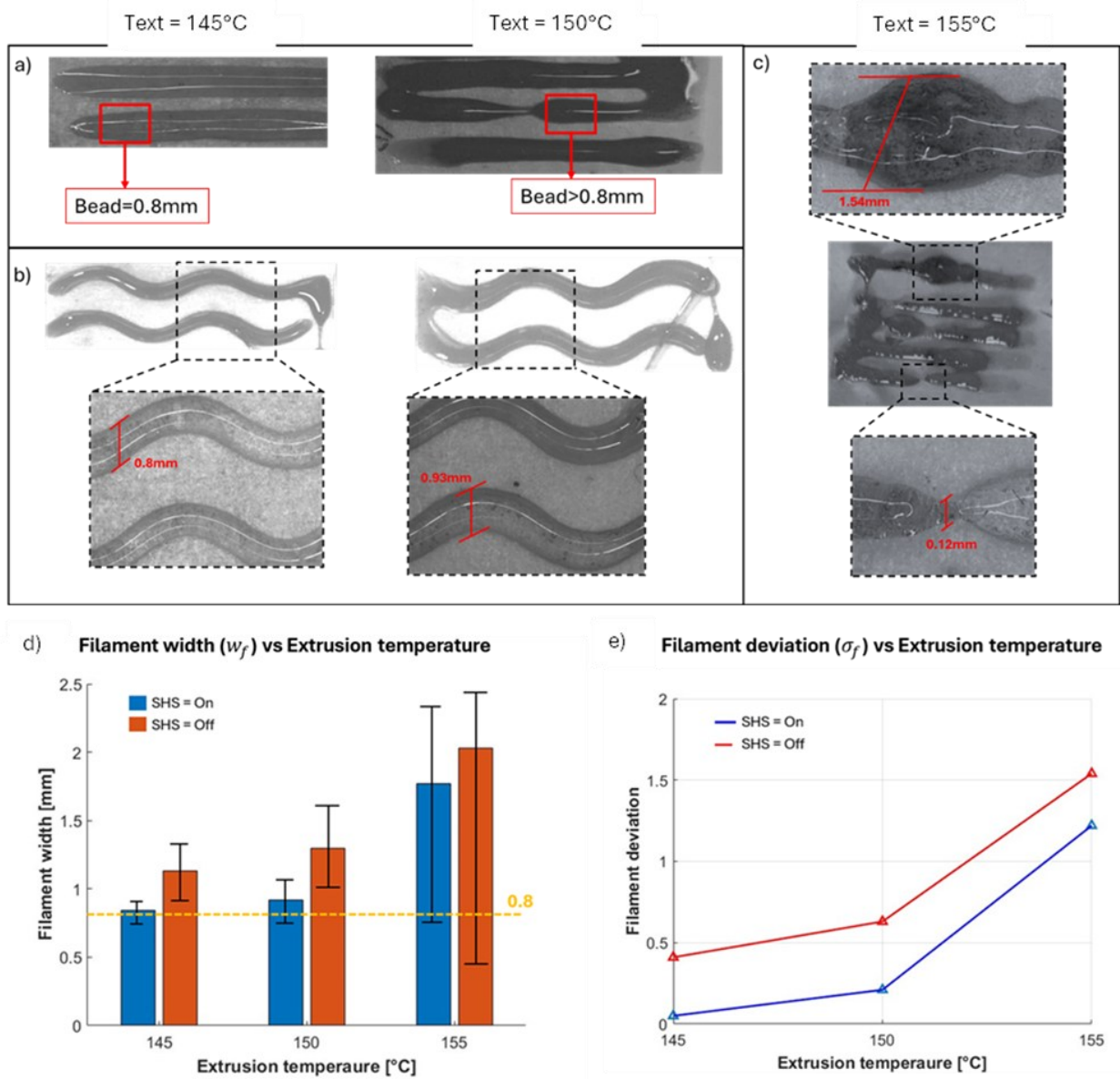
Fig. 3.25: Separate heating system (SHS) to improve the geometrical accuracy: a) printed linear 2D structures (single bead) setting printing temperature at 140 and 150°C, b) printed snake structures at the same temperatures (140 and 150°C), c) extruded bead with worst-case extrusion temperature (155°C), d) extruded filament width increase with various extrusion temperatures (with enable and disable the SHS) resulting in a low geometrical accuracy, and e) the relative filament deviation decreases setting low extrusion temperature resulting in a high geometrical accuracy under both traditional (SHS = Off) and proposed approach (SHS =On).

To better understand the potential of the proposed SHS approach, the geometrical accuracy of the 2D and 3D structures printed (with respect to extrusion temperature variation), the filament deviation and extrusion force (in Section 3.4.1.2) were evaluated. Equation (3.16) was used to evaluate the relative filament deviation (σ_f) of the 3D printed structures, yielding a value close to 0 when the filament deviation (w_f) aligns with the nozzle diameter (d). Twenty linear and snake 2D structures for each

temperature were printed. The comparison of several deviation index at different nozzle printing temperatures is shown in **Fig. 3.25 d**: the better extrusion quality is achieved when the temperature is $145°C$, while the worst-case occurs when the nozzle temperature is set to $155°C$. Furthermore, the use of SHS results in reduced filament deviation of 26% than the traditional approach (several example of accuracy with SHS=OFF (traditional approach) are present in Appendix B, Section B6), such shown in **Fig. 3.25 e**, during the printing, thereby in a high-quality printing due to the almost uniform temperature (inside the nozzle ($145°C$) and the syringe ($135°C$) and the reduction of the extrusion force, how explained in the following section.

3.4.2.2 Effect of the SHS on the extrusion force

The contribute of the extrusion force was calculated setting the process parameters in Table 1 during the fabrication of the samples printed in the previously section. A methodology similar to the one proposed in [119] has been used. In **Fig. 3.26 a**, the printing force as a function of the SHS: i) activated is using the barrel temperature set to $135°C$ and nozzle temperature set to $145°C$, ii) SHS deactivated using only nozzle-traditional approach, and iii) SHS disactivated using only barre-traditional approach, is shown. The extrusion force was evaluated for the best and the worst-case extruded temperature, respectively 145 and $155°C$, when the SHS was enabled. It should be noted that, when the SHS is activated, a very stable force curve is obtained (almost flat), with an average value of force of $17.95\ N$. The good stability is demonstrated by the low value calculated between the maximum and the minimum peak equal to $4.33\ N$. On the other hand, when the SHS is not leveraged a very unstable force curve is measured: despite an average value of force values equal to $17.42\ N$, nozzle-traditional approach, and $17.96\ N$ barrel-traditional approach (which results to be even less than the average value ($17.95\ N$) achieved when employing SHS), the whole measure is characterized by a huge instability. As a matter of fact, the value calculated between the maximum and minimum peak is $18.38\ N$, which is 77% higher than the one calculated when the SHS is used ($4.33N$), for the nozzle-traditional approach, and $10.13\ N$ for the barrel-traditional approach. Moreover, when the SHS was enabled to test the worst-case temperature, it should be noted that the extrusion force gradually increased during the printing cycle, with an average value of the force of $19.06\ N$, which resulted higher than the extrusion force at $145°C$ (see **Fig. 3.26 b**).

As evidence of the impact of the SHS, two complex-shape structures (square-star in **Fig. 3.26 e**, butterfly in **Fig. 3.26 f**, and different shapes in Appendix B, Section B6) were printed. It should be noted that when the SHS is enabled (nozzle printing temperature equal to $145°C$), the printed bead is equal to the line width and the printed square-stars resulting in high-geometrical accuracy and quality

printing (see **Fig. 3.26 d**). On the other hand, the square-star printed disabling the SHS presented several geometrical problems, resulting in a poor-quality printing, such shown in **Fig. 3.26 e**. Similarly, the butterfly printed with SHS activated shows high-quality compared to the printed one without SHS. Moreover, removing the print from the building plate when SHS was deactivated proved more challenging due to inconsistent material deposition.

In conclusion, the proposed SHS approach enables high-quality printers of ink-base self-healing materials, reducing the printing force when both the nozzle and syringe temperature are set lower the $155°C$, enable the fabrication of complex-shape structures. Summarized results of the extrusion force are in **Table 3.10**.

Table 3.10: Extrusion force for each approach.

	Mean value of Extrusion Force	Force instability (Max peak-min peak)
Proposed approach (SHS=On)	17.95 N	4.33 N
Nozzle-Traditional approach (SHS=Off)	17.92 N	18.38 N (77% higher)
Barrel-Traditional approach (SHS=Off)	15.96 N	10.13 N (57% higher)
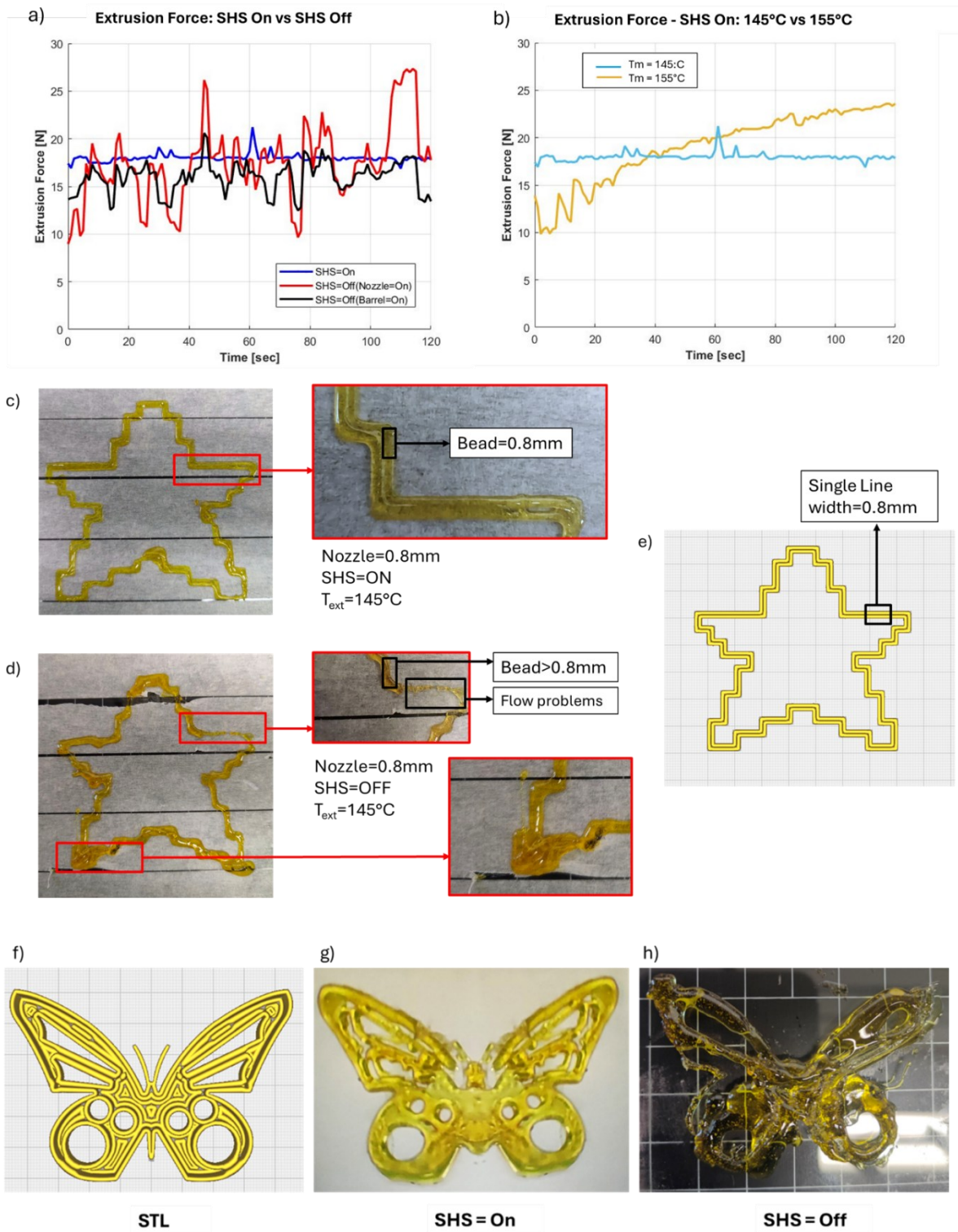
Fig. 3.26: Effect of the SHS on the extrusion force and printing quality: a) extrusion force vs the different printing approach during the printing of samples (in Section S3.2) resulting uniformly when the proposed approach (SHS = On) is enable, b) when SHS is activated the extrusion force at best-case extrusion temperature (145°C) is constant while worst-case of temperature (150°C) lead to an increasing of the force, c) good geometrical accuracy and printing-quality of the complex square-star shape printed enabling SHS (nozzle extrusion temperature equal to 145°C), d) the same square-star printed disabling the SHS showing several problem resulting in a low printing quality, e) CAD design of the square-star, f) butterfly structures CAD design, g) printing-quality of the complex butterfly shape printed enabling SHS (nozzle extrusion temperature equal to 145°C), h) butterfly structure printed setting SHS=Off.

3.4.2.3 Mechanical characterizations

One of the challenges with self-healing thermosets manufactured via MEX lies in achieving isotropic parts and reducing voids between extruded beads and layers [180], [244], which reflects in poor mechanical properties.

As explained in Section 3.4.1.7, the proposed SHS approach was investigated by fixing the barrel temperature to 135 °C, and varying the extrusion temperature (145,150,155°C). On top of that, two printing directions (**Fig. 3.27 f**) for each printing temperature were investigated:

- 90° - parallel to the short axis y of the build plate.
- 0° - perpendicular to the short axis y of the build plate.

The proposed SHS approach, was also compared to both traditional moulding of self-healing ink, and traditional 3D printing (without pre-heating the ink inside the barrel, namely T_{Barrel} equal to room temperature).

Mechanical tests were performed according to the standard described in Section 3.4.1.7.

It should be noted that, according to the accuracy outcomes of Section 3.1, the samples fabricated by setting a T_{ext} of 145 °C resulted in a good geometrical accuracy, while samples fabricated at 150°C, and 155 °C resulted in over extrusion problems, as depicted in **Fig 3.27**.

Several conclusions can be drawn from this characterization:

i) The printing direction is not significant compared to the printing temperature.

ii) The samples printed at 145 and 150°C presented about the same behaviour: the 90° printing direction (**Fig. 3.27 b, c**) support a maximum stress of 23.09 MPa (T_{ext} of 145°C) and 24.10 Mpa (T_{ext} of 155°C). On the other hand, the 3D printed samples fabricated at 0° presented a maximum stress of 22.41 MPa (T_{ext} of 145°C) and a maximum load of 23.10 MPa (T_{ext} of 150°C).

iii) The best results in terms of mechanical properties (UTS) are achieved when T_{ext} is set equal to 145 °C, and 150 °C, and barrel temperature is set to 135 °C (SHS approach). This result is in good agreement with the main fundings of Section 3.2. In particular, when extruding with SHS approach at T_{ext} of 145 °C, an improvement in UTS of

26.57% compared to traditional 3D printing (without SHS) was achieved. Also, a great reduction in standard deviation of 69.2% is obtained. These results clearly indicates that the reduced printing force obtained with the proposed SHS approach, involves better mechanical properties because inter-, and intra- layer voids are reduced due to an improvement in the geometrical accuracy of the extruded layers and beads.

iv) The best UTS results are still achieved when moulding is performed. At the state of the art, moulding technology still provides the higher mechanical performances, as anisotropy and voids do not affect the moulded parts. Anyway, moulding technology can be used only for extremely simple geometries, resulting in a very limited design of the self-healing based components. However, the proposed SHS approach is demonstrated to produce samples with UTS only 5.58% lower than the moulded counterpart, bridging the gap in mechanical performance between moulding and 3D printing.

A summary of the results is provided in **Table 3.11**. Other information about the tested samples is in the supplementary materials, Section B5.

3.4.2.4 Healing

T extrusion of 145 $°C$, found to both improve geometrical accuracy, and mechanical properties, was set in conjunction with T barrel of 135 $°C$ (proposed SHS approach) to 3D print a total of 3 samples to be tested in order to evaluate self-healing performance (using the procedure detailed in the Section 3.4.1.8). Two different types of damage (tears and cuts) were inflicted to the printed sample in order to investigate the healing performance (**Fig. 3.28**). The recovery of the samples was investigated through qualitative and quantitative analyses.

It should be noted that the authors manufactured three samples: sample 1 was completely cut along the width of the sample (See **Fig. 3.28 a-d**), while samples 2, and 3 were damaged by performing both partial lateral and inner cuts (**Fig. 3.28 e-h**).

Samples 2, and 3 exhibited full recovery, displaying only a minor scratch on the surface observed under the microscope in **Fig. 3.28 d**. On the other hand, sample 1 did not achieve complete recovery due to a significant cut. Despite the incomplete recovery, the two parts of the cut were jointed

together, as illustrated in **Fig. 3.28 d**. As a matter of fact, the healing efficiency η of the sample 1, 2 and 3 is respectively 81%, 93% and 95%, as shown in **Fig. 3.29 a.**

The Ultimate tensile strength (UTS) of the healed samples increases when the healing efficiency increases too (**Fig. 3.28 b**): sample 1 presents an UTS of 17.31 MPa before the healing process and 13.95 MPa after the healing process, showing a decreasing of 19,41% in UTS when the sample is healed. On the other hand, samples 2 and 3 showed only a slight decrease of 6.25% and 4.45% in UTS after the recovery process. Moreover, **Fig 3.28 c** shows Young modulus, and strain at fracture of pristine and healed 3D printed samples

Table 3.5: Summary of the mechanical results.

Fabrication approach	Moulding	3D printing Traditional (No SHS)	3D printing Proposed approach (SHS)		
			145 °C	150 °C	155 °C
UTS (MPa)	23.72	15.47	21.07	22.3	17.41
Std. dev. (Mpa)	0.31	0.65	0.20	0.17	0.40
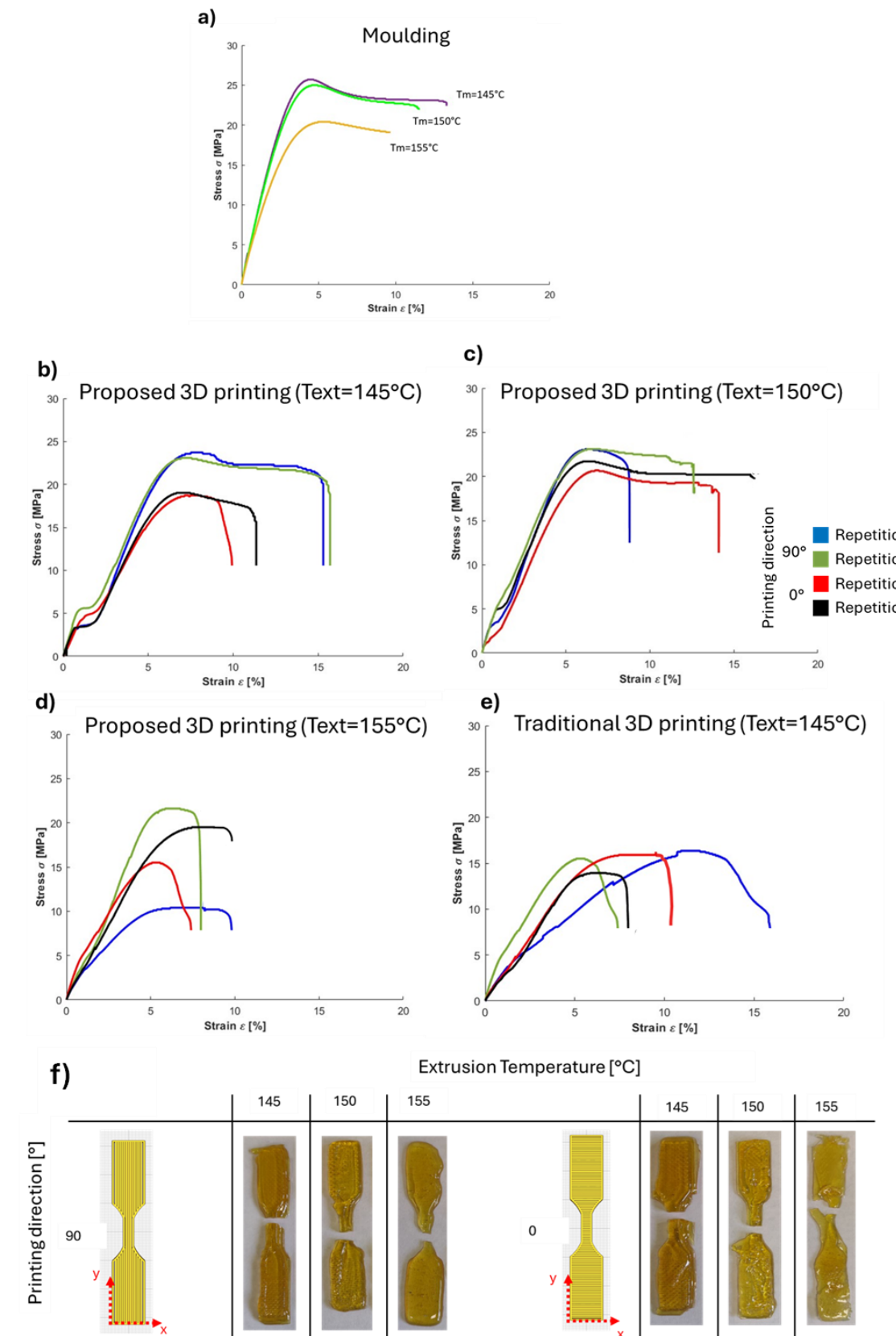
Fig. 3.27: Mechanical properties evaluation of the self-healing materials: a) tensile test (strain vs stress) result of the sample fabricated via moulding, b) tensile test results (strain vs stress) of the samples fabricated using the proposed approach (SHS - nozzle extrusion temperature equal to 145°C), c) tensile test results (strain vs stress) of the samples fabricated using the proposed approach (SHS - nozzle extrusion temperature equal to 150°C), d) tensile test results (strain vs stress) of the samples fabricated using the proposed

approach (SHS - nozzle extrusion temperature equal to 150°C), e) tensile test results (strain vs stress) of samples fabricated using the tradition approach (nozzle extrusion temperature equal to 145°C), f) printed samples.
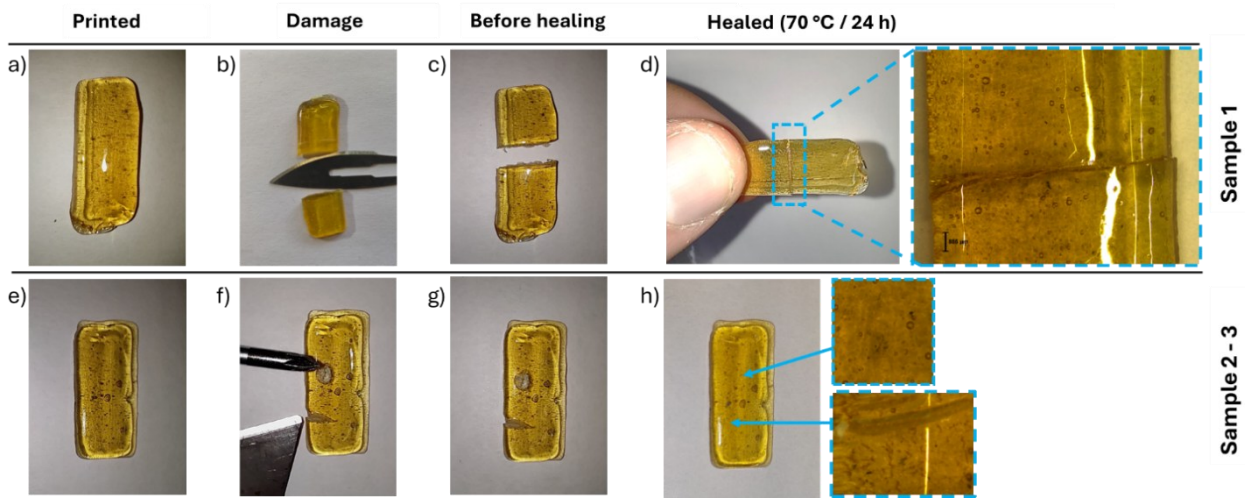
Fig. 3.28: Damage and healing of the printed samples: a) sample 1 pristine (as is printed), b) damage type-cut of the sample 1, c) cut sample 1, d) not completely recovery of the cut sample 1 and macroscopic image, e) sample 2 and sample 3 as printed, f) damage type-tears of the sample 2 and sample 3, g) tears sample 2 and sample 3, h) completely recovery of the sample 2 and sample 3 and microscopic image after the haling..
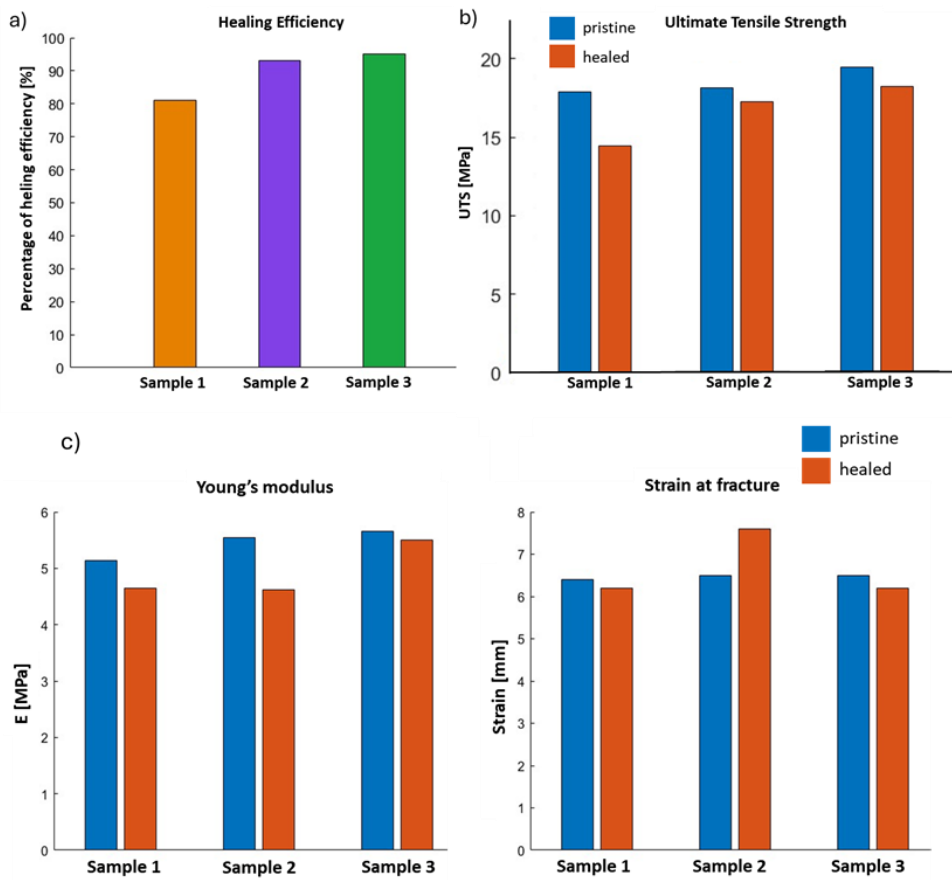
Fig. 3.29: Healing efficiencies of the printed samples: a) healing efficiency of sample 1, 2, and 3 after the recovery, b) Ultimate Tensile Strength (UTS) of the pristine (as is printed) samples resulting 10% higher then the UTS values of the healed samples (after the healing process), c) Young's modulus, stress and strain at fracture of pristine and healed samples.

3.4.3 Dual extrusion of self-healing smart structures

3.4.3.1 Self-healing piezoresistive sensor

The potential of the proposed approach was demonstrated through the fabrication of one-shot multi-material assembly-free piezoresistive sensor. As delineated in section 3.4.1.8, the smart structure was manufactured using two different self-healing (dielectric and conductive) materials. The adhesion properties were qualitatively studied under the microscope. The printing parameters were set as in **Table 3.9** for the dielectric material, according to the best nozzle extrusion temperatures ($145°C$), and in **Table 3.12** for the conductive one. A $0.8\ mm$ nozzle was used to minimize the clogging problem. To maximize the conductivity of the beads of the conductive self-healing material, the sensor was fabricated setting the printing direction equal to 90° (parallel to the y-axis). As shown in **Fig. 3.30 d**, the dielectric self-healing ink (yellow) was extruded employing the SHS approach, followed by the deposition of the conductive self-healing filament-based material atop, resulting in significant qualitative adhesion in both x and y directions as well as between layers.

Table 3.11: Printing parameters of conductive self-healing.

| Process parameter	Value
Layer height Lh (mm)	0.2
Flow (%)	165
Line width Lw (mm)	0.8
Nozzle diameter d (mm)	0.8
Printing speed (mm/s)	5
Building plate temperature (°C)	60
Extrusion temperature (°C)	115

3.4.3.2 Piezoresistive characterization of the printed sensor

To investigate the reproducibility of the ink-based MEX in printing complex multi-material self-healing structures, two sensors were manufactured and characterized. Their absolute resistance, the change in relative resistance $\frac{\Delta R}{R_0}$ and the sensitivity S were analysed and compared (**Fig. 3.30**). Both sensors were subjected to cyclic testing with an angle amplitude of 38.6 $degree$ and a frequency of $0.002\ Hz$. Looking at **Fig. 3.311 a, b**, it is clear that there is a slight difference in piezoresistive behavior between the two pristine sensors. This is emphasized by a difference in their initial resistance R_0 in unloaded conditions and their average sensitivity, plotted in **Fig. 3.30 e**.

Although this demonstrates that the printing process is repeatable to a certain extent, it also indicates that further optimization is needed.
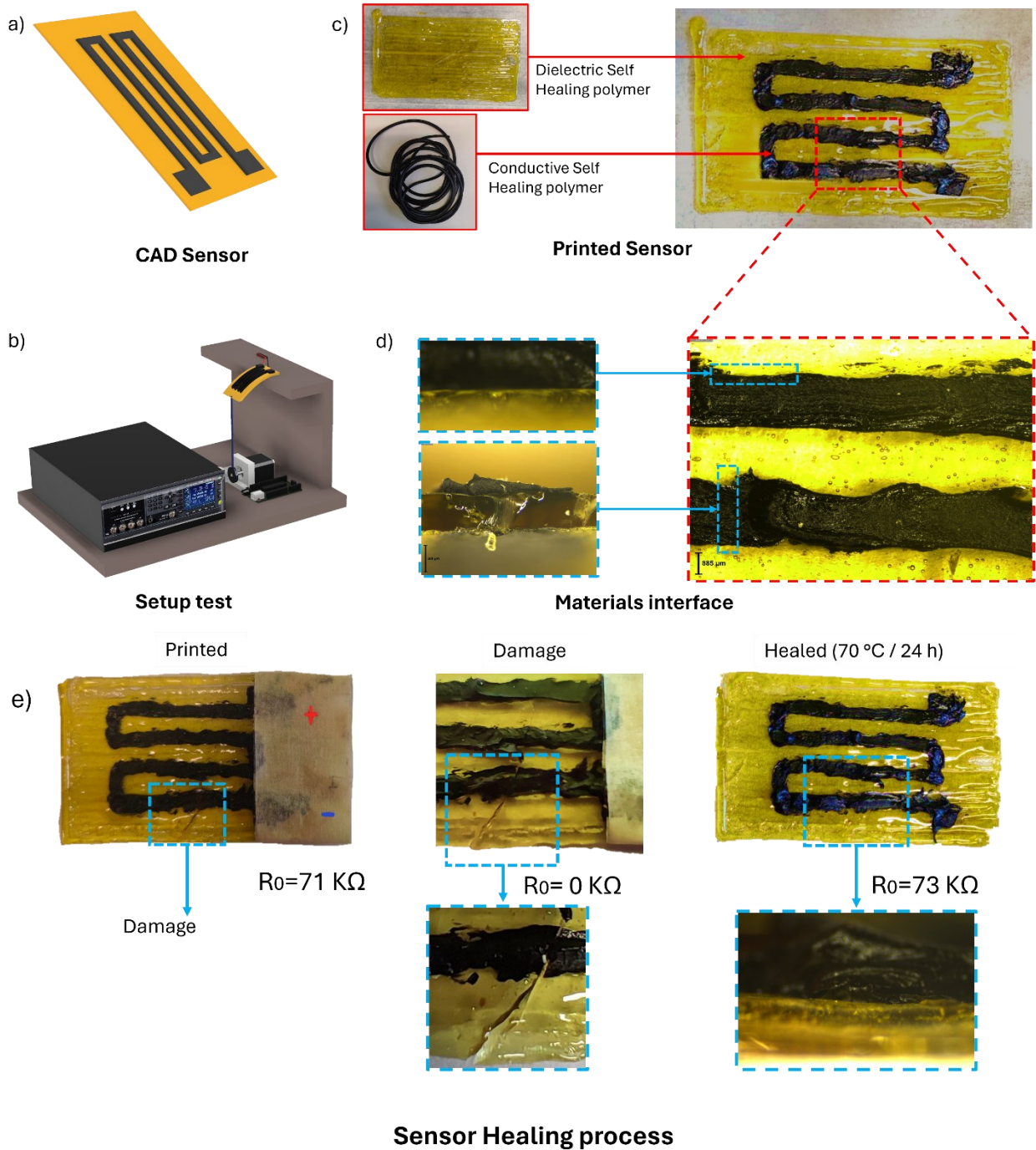
Fig. 3.30: 3D printed self-healing smart structure (sensor): a) CAD sensor composed of non-conductive self-healing ink-based material (yellow) and conductive self-healing filament-base material (black), b) Setup for test the electrical performance of the sensors, c) 3D printed multimaterial sensor, d) adhesion between the materials at the interface, e) before the damage the resistance of the sensors is 71 KΩ and after the healing process the sensors was healed but the resistance increase (73 KΩ).

3.4.3.3 Self-healing characterization of the printed sensor

To analyze the self-healing capacity of the sensor, we investigated the recovery of absolute conductance, the change in relative resistance, and the sensitivity S (**Fig. 3.31**). The sensor was severely damaged as shown in **Fig. 3.30 e**, with a scalpel blade cutting completely through all layers, including both the dielectric and conductive layers. It has to be noted here that before the damage, the sensor resistance (R_0) measured from the connectors was 71 Ω, and it was changed where the damage was inflicted ($R_0 = 0$ Ω). The damaged sensor was heated at $70°C$ for the night, before leaving it to rest for 24 h at room temperature. The new resistance (R_0) of the healed sensor was increased by 2.74%, showing that the self-healing sensor recovers its function after the damage-healing procedure. See **Table 3.12.**

This self-healing analysis was expanded by investigating the recovery of the piezoresistive performance of the sensor after being self-healed (**Fig. 3.30**). As shown in **Fig. 3.31 e**, the average of the sensitivity of the pristine (as-is printed), and the healed sensors is 2.21 $Ω/degree$ and 3.08 $Ω/degree$, respectively. The standard deviation calculated on the two sensors is lower than 0.06 $Ω/degree$ for each case. The best result is obtained by the sensors healed, when an improvement of the sensitivity of 28% was achieved. After the damage of the sensors, the increasing of the temperature inside the oven increases the mobility of the reactive components of the self-healing materials, resulting in an increase of the sensitivity. Moreover, the sensor 1 remains with the higher sensitivity than the sensor 2, even after the healing process.

The proposed self-healing sensor has been benchmarked with the one presented by the authors in [21], which has been fabricated by recurring to filament- MEX, and employing a commercially available electrically conductive polylactic acid (CPLA). It should be said, that a sensitivity almost 50% lower than [21]was achieved in the present research, alongside with a R_0 almost 7 time higher. Such outcomes indicate a reduction in electrical performance (sensitivity, and R_0) is the price to pay to obtain smart polymers capable of healing after a damage. On the other hand, further optimization of process parameters, fabrication strategies, and material chemical composition could definitively result in improved electrical performance.

Table 3.13: Electrical resistance for pristine and healed sensor.

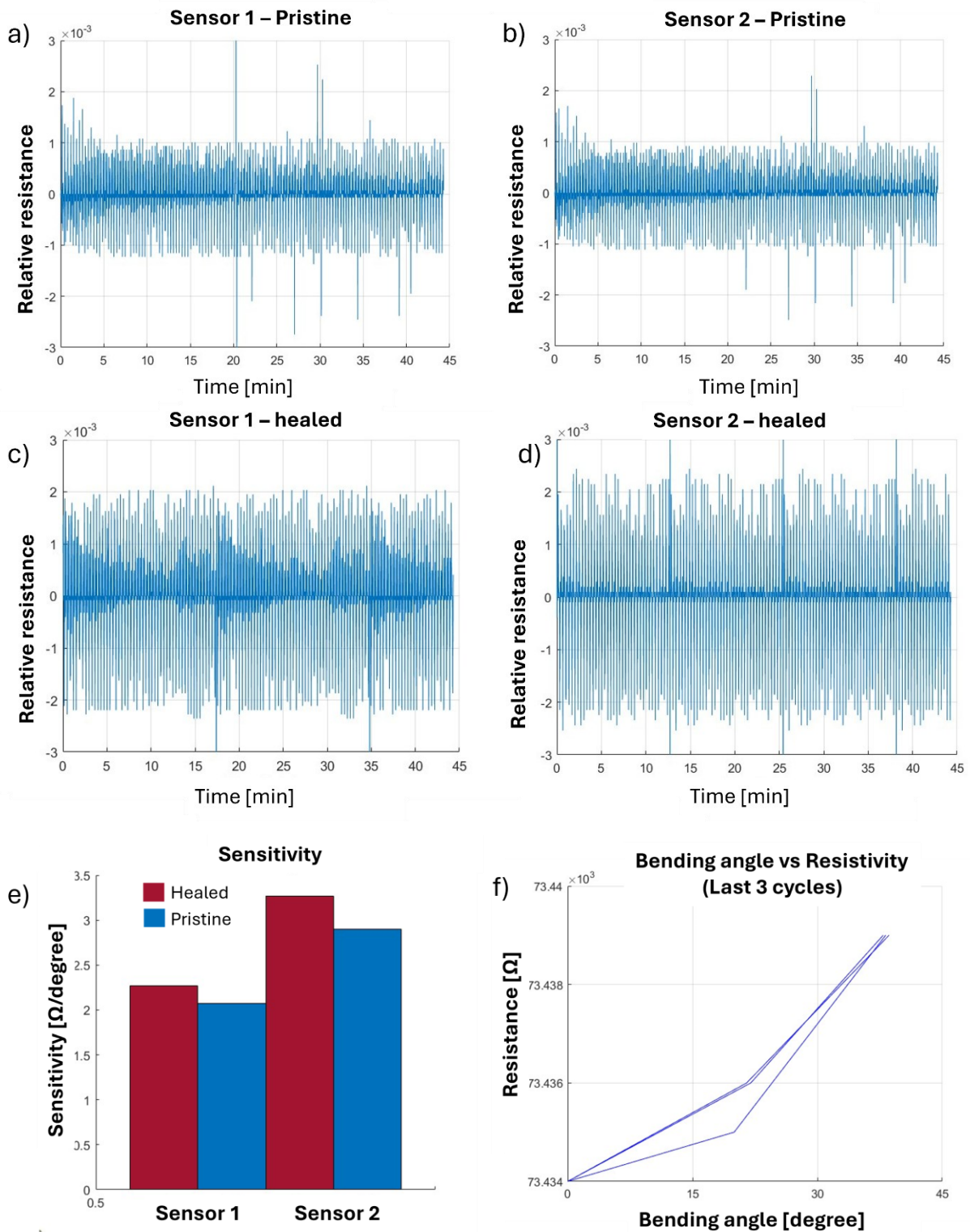| Initial Resistance R0 (Ω)	Pristine	Healed
Sensor 1	71	73
Sensor 2	73	74

Fig. 3.31: Long time test of the 3D printed self-healing smart structure: a) characterization of the pristine (as-is) sensor 1 (relative resistance vs time), and b) pristine (as is) sensor 2, c) evaluation of the electrical performance of the healed sensors 1, and d) sensor 2, e) comparing of the sensitivity of the pristine and healed sensors.

3.4.4 Discussion

The authors demonstrated how the manufacturing strategies impact on the final performance of Diels-Alder self-healing polymers. From one hand, this class of material is highly request for their unique ability to self-heal after a structural damage, thereby increasing the lifespan of the polymeric structure, from the other hand the current material extrusion machines are not flexible enough to properly process such materials. The authors tackled the pre-heating problem, which is not considered in traditional MEX of common polymers, by developing a separate heating system (SHS) capable of pre-heat the polymer inside the barrel (degeletion) and melt the polymer (extrusion) inside the final nozzle.

The main mechanism underlying the correlation between separate heating system and extrusion force reduction (and force fluctuations) is as follow: pre-heating the self-healing ink inside the barrel at degelation temperature greatly reduce the ink viscosity, which in turns, is translated in a reduction of the force required to push the ink through the nozzle. In this way, over extrusion problems are mitigated: as the extruded layers are geometrically more accurate, inter-, and intra-layer voids are reduced, thereby resulting in improved adhesion. The latter was experimentally validated through mechanical, and healing tests: being the adhesion improved both mechanical and healing performance resulted to be improved.

The proposed approach has been benchmarked with traditional MEX of Diels-Alder self-healing polymers, showing superior performance. The increase in performance is strongly correlated to the reduction of the extrusion force achieved with the proposed approach: by reducing extrusion force (and fluctuations of this force) a remarkable increase in accuracy (26%) is obtained, unlocking the 3D printing of complex structure. Moreover, the reduced extrusion force, also led to an improvement in mechanical properties (Young modulus, and ultimate tensile strength) and healing efficiency. The proposed SHS method results effective in manufacturing structural components capable of undergo higher loads, compared to traditional self-healing fabricated via traditional MEX.

The outcomes of this study highlight the importance of controlling the heating of Diels-Alder polymers during the fabrication: the authors envision future MEX setups with more independent heating systems to further improve the flowability of the polymer.

Furthermore, the authors extruded two self-healing polymers (dielectric, and electrically conductive), in the same manufacturing cycle to fabricate a smart structure with embedded sensing strain gauge capable of detecting bending angles. The performance of the self-healing sensors improved slightly following the healing process (due to a re-heating of the polymer), showing their applicability for many applications. It should be said that the sensitivity of such sensors is almost 50% lower than sensors fabricated with traditional electrically conductive polymers. Lower electrical performance, at

the state of the art, represents the price to pay to achieve self-healing. However, future material optimization could create stronger electrical networks inside the self-healing polymer, improving also electrical performance.

Table 3.14: Main findings of the present research.

	Filament deviation (mean error at T=145°C)	Fabrication of complex-shaped structures	Ultimate Tensile Strength (UTS)	Healing efficiency	Mean value of Extrusion Force	Force instability (Max peak-min peak)
Proposed approach (SHS=On)	Decrease of 26% (error 0.06mm)	Yes-Improvement	$2.07 \pm 0.20\ MPa$	95%	17.95 N	4.33 N
Traditional approach (SHS=Off)	Error 0.41mm	No	$1.52 \pm 0.04\ MPa$	89%	17.92 N	18.38 N (77% higher)

3.4.5 Conclusions

The present research proposes a novel temperature-based approach, to improve the extrudability and the performance (both healing, and mechanical) of self-healing inks processed through Material Extrusion. In particular, the Diels-Alder self-healing ink-based material was fabricated through a custom-made MEX setup equipped with a separate heating system (SHS): both the barrel and the nozzle are independently controlled, to preheat (degelation), and melt (extrusion) the ink to guarantee a robust and continuous extrusion. The proposed manufacturing approach has a significant impact on the printing part to enhance the accuracy and the geometrical properties, enabling the fabrication of complex-shape structures with high details. Indeed, the printed part presented an accuracy higher 26% times than the traditional approach.

Moreover, the printing temperature is also found to be significant for the extrusion force and the mechanical properties (when the SHS is enabled). The proposed approach enables the reduction of the printing force ($4.33N$ peak-peak), when both nozzle and barrel temperature are set under $155°C$. The latter condition is also respected for the mechanical property: when the temperature is lower than $155°C$, the UTS is closed to the moulding fabrication. Experiments have also demonstrated very high self-healing property of the printed samples (recovery up to 95%). Finally, the key benefits of the SHS approach were used to fabricate multimaterial smart structures, such as piezoelectric sensors:

the dielectric self-healing ink was extruded from the syringe, and the electrically conductive self-healing filament from the filament print head. The sensor showed good sensitivity before and after the healing procedure, respectively 2.21 $\Omega/degree$ and 3.10 $\Omega/degree$, with an improvement of the sensitivity (29%) after the healing, due to the chemical property of the self-healing ink.

The present work lays the foundation for an extensive use of MEX technology (both filament-, and ink-based) for the fabrication of assembly-free, sensorized structures based on DA self-healing materials.

4. CHAPTER 4: Future trends: energy storage for MEX structures

4.1 Introduction of the chapter

One of the emerging trends and innovative application of 3D printing in the field of electrical devices is the additive manufacturing of elements that can be storage energy, such as supercapacitors and batteries.

Commercial lithium-ion batteries currently involve stacked sheets of electrodes, separator and current collectors, based on two dimensional (2D) designs with restricted geometric freedom (**Fig. 4.1 a**). The electrodes are electronically isolated by a separator membrane infused with a liquid electrolyte responsible for ensuring effective lithium ions (Li^+) ionic conductivity. Through processes of oxidation and reduction, the stored chemical energy is converted into electrical energy. During discharge, Li^+ move from the negative electrode to the positive electrode through the electrolyte, simultaneously releasing electrons (oxidation) from the negative electrode. These electrons then traverse the external circuit to reach the positive electrode (reduction). The reverse reactions occur during battery charging. The terms anode and cathode are commonly used to respectively refer to the negative and positive electrodes, in accordance with the reactions taking place during discharge. Many studies [247]–[251] recently have demonstrated that enhanced battery power performance (enabling faster charging) can potentially be achieved by incorporating intricate three-dimensional (3D) electrode architectures, like the interdigitated gyroidal design depicted in **Fig. 4.1 b, c**. Unfortunately, these complex interdigitated 3D structures cannot be produced using conventional battery manufacturing methods, which typically involve slurry casting. In this context, additive manufacturing (AM) [252], more commonly referred to as 3D printing, is now being considered as a viable solution, and AM was recently employed to print lithium-ion batteries components [51], [251], [253]–[257]. This is because it offers the advantage of creating 3D objectsfrom a digital model through the gradual deposition of material layer by layer. As a result, it holds the theoretical potential to facilitate the production of intricate 3D interdigitated battery components with enhanced electrode surface area, improved lithium ions diffusion and enhanced power performances; however, this represents a significant milestone that is yet to be attained. Moreover, the ability of AM to implement shape-conformable, free-form or structural load-bearing batteries [258]–[265] within a system envelope could maximise the energy storage by leveraging otherwise unused space (**Fig. 4.1 d**) or improve the performance by conforming to application requirements (i.e. anatomy, aerodynamics, etc).

In contrast with traditional manufacturing techniques (casting, moulding, machining), cutting-edge AM technologies have recently enabled the fabrication of complex and intricate designs [266]–[268]. Since the introduction of AM in the 1980s by Charles Hull (stereolithography) , AM had evolved over the years and six additional categories of 3D printing have been introduced according to ISO/ASTM 52900:2015 [269]. Prior to printing, objects must be modelled by means of a computer-aided design (CAD) software resulting in a.stl file [270]. This latter is then introduced into a slicer software to set the adequate printing parameters, thus generating a Gcode file which is executable by the 3D printer. In 2019, according to the yearly report on AM published by the Dutch company 3D Hubs and based on the summarised data provided from ten trustworthy market analysts, the total 3D printing market (including machines, materials, software and services) was estimated to represent $12.1B$, demonstrating an annual 25% growth since 2014. The AM market, doubling every three years, is expected to reach $34.9B$ by 2024. Additive manufacturing has now been employed for a wide range of applications including but not limited to electronics [135], architecture [271], jewelry [272] healthcare [273], aerospace [274], or soft robotics [52]. As the most widely available process in additive manufacturing, material extrusion (ME), was originally invented by Scott Crump, co-founder of the American company Stratasys, and later, increasing in popularity among AM technologies as patents expired and the technology became more affordable with the introduction of the RepRap mission by Adrian Bowyer (Bath University) in 2005 [275], an open-source 3D printer capable of 'replicating rapidly' (RepRap) itself [276]. Disclosed for the first time in 2008, it contributed dramatically to public awareness but also to the emergence of many start-up companies around the world such as Makerbot and Prusa, which created and released their own lower cost 3D printers. Material extrusion includes two different processes: 1) Filament Extrusion (also referred to as Stratasys' trademark Fused Deposition Modeling, or Fused Filament Fabrication) and 2) Ink Extrusion (also referred to as Direct Ink Writing, Robocasting or Liquid Deposition Modeling). See **table 4.1**.

Mechanically relatively simple, both extrusion technologies are based on the deposition of material layer after layer through a needle or nozzle. Classical filament extrusion printers are fed with a thermoplastic filament which is printed by heating the feedstock filament by a few degrees above the melting temperature. On the other hand, ink extrusion consists of an ink or a paste that is deposited by applying a computer-controlled pressure [277]. ME has gained a lot of popularity in recent years for several reasons: (i) the process is inexpensive, (ii) the possibility exists to extrude various materials in the same build volume (multi-materials printing options), (iii) the reduction of manual assembly tasks and (iv) the opportunity to fabricate smart structures [22], [31], [34], [278] with embedded electronic components. Recently, ME has been explored to print energy storage devices.

Since 2013, considerable attention has been given to 3D print lithium-ion batteries due to the capability of building shape-conformable devices, and furthermore, with recent modelling studies suggesting enhanced power performances with complex anode/cathode geometric architectures [248], [249]. Most of these studies have been limited to the printing of single battery component. However, with a view to fabricate a complete functional battery cell via ME 3D printing, remaining challenges are related to the materials feedstock, hardware modification, printing and post-processing parameters optimisation, as well as utilisation of multi-material ME printing options.
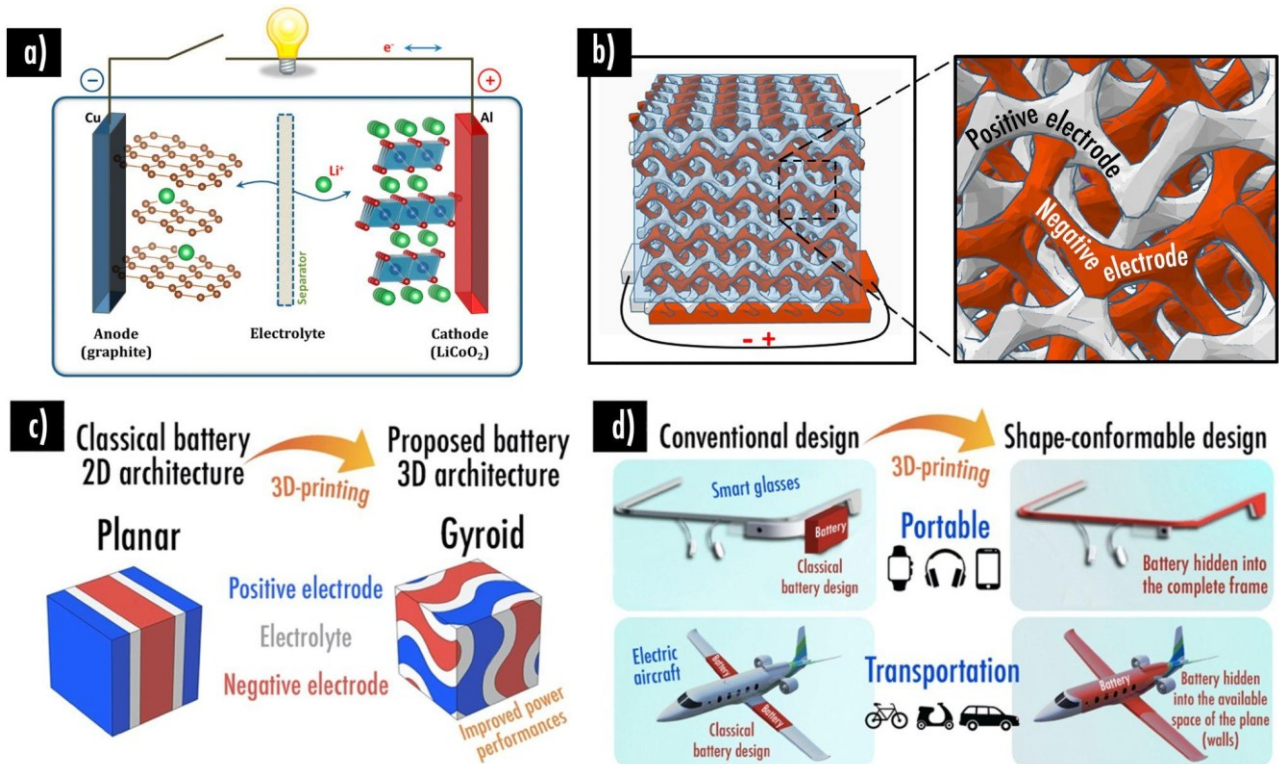
Fig. 4.1: a) Scheme of a conventional lithium-ion battery. Reprinted (adapted) with permission from [264]. Copyright 2013 American Chemical Society; b) Interdigitated gyroidal electrodes [265]; c) Conventional 2D battery architecture and innovative 3D architecture with enhanced power performances now possible thanks to AM [249], [250]. © The Electrochemical Society. Reproduced by permission of IOP Publishing Ltd. All rights reserved ; d) Examples of shape-conformable and structural batteries that can be manufactured thanks to AM [250], [263] . Reprinted (adapted) with permission from [263]. Copyright 2015 American Chemical Society.

In this chapter the future trends about the fabrication of 3D printing batteries is presented (section 41).

Table 5.1: Summary of previous studies on the topic of 3D printed lithium-ion batteries.

AM process	Battery component targeted	Focus of the paper	References
Filament extrusion	Positive electrode	Feedstock material optimization	[249], [261], [262], [269], [279]–[281]
		Printing parameters or post-processing optimization	[262], [269], [282], [283]
	Negative electrode	Feedstock material optimization	[50], [261], [269], [278], [279], [283], [284]
		Printing parameters or post-processing optimization	[50], [282]–[284]
	Electrolyte/Separator	Feedstock material optimization	[269], [279], [280], [285], [286]
		Printing parameters or post-processing optimization	[269], [285]
		Machine modification	[269], [285]
	Current collectors	Feedstock material optimization	[269], [287]
	Full battery	Assembly of independent components	[269], [279], [280]
		Printed in a single step	[269], [279]
Ink extrusion	Positive electrode	Feedstock material optimization	[288]
		Printing parameters or post-processing optimization	[288]–[292]
		Machine modification	[250], [293], [294]
	Negative electrode	Feedstock material optimization	[289], [295]–[301]
		Printing parameters or post-processing optimization	[289], [298]–[300]
		Machine modification	[299]
	Electrolyte/Separator	Feedstock material optimization	[277], [295], [296], [301], [302]
		Printing parameters or post-processing optimization	[302]
		Machine modification	[277], [302]
	Current collectors	Feedstock material optimization	[303]
		Machine modification	[286]
	Full battery	Assembly of independent components	[297]
		Printed in a single step	[289], [296], [304]

4.1 Future trends for energy storage: Manufacturing-Oriented Review on 3D Printed Lithium-ion Batteries Fabricated Using Material Extrusion

In these years, the growing interest in 3D printed energy storage systems stems from a rapid advancement in additive manufacturing of electrical devices and 3D printed materials able to accumulate energy. In this contest, an overview of the state of the art of the material extrusion-based 3D printed batteries is reported in this chapter. A summary of the materials being employed to prepare composite filaments and ink feedstocks for printing battery components, as well as primary manufacturing challenges and the proposed solutions, are discussed. This work also comprehensively describes the common issues encountered when printing composite battery components with extrusion-based machines, and required machine-modifications and optimizations of the printing parameters that have been investigated to facilitate printability and maximize the electrochemical performance of the final multi-material structures. Finally, currently available multi-material extrusion printers are listed and analyzed with consideration for the eventual printing of a complete rechargeable battery in a single non-assembly process.

4.1 Materials for material extrusion 3D printing of batteries

Used as material feedstock for the material extrusion 3D printer, inks and filaments require specific electronic, electrochemical, mechanical, and rheological properties to ensure good printability and adequate electrochemical performance within the printed battery component. As a reminder, a conventional lithium-ion battery assembly consists in a negative and a positive electrode each supported on a current collector, and a separator impregnated with liquid electrolyte (**Fig. 4.1 a**) [264]. In all-solid-state batteries, the separator-liquid electrolyte duo is replaced by a ceramic or polymer-based electrolyte. The functioning mechanism is based on the flow of electrons through an external circuit as a consequence of electrochemical reactions that shuttle lithium ions between the negative and positive electrodes. The variety of possible materials and compositions is a further complication. Hereafter, a summary of the most relevant and recent investigations on extrusion-based 3D printing of lithium-ion battery components is presented, as well as solutions proposed to provide adequate mechanical and rheological properties as well as improved electrical conductivity and electrochemical performance.

4.1.1 Filament extrusion: Outlook of the most relevant advances

Since 2017, filament extrusion has been extensively investigated for lithium-ion battery electrodes printing (**Table 1**). Many groups [42], [261], [262], [278], [279], [285] recently have focused studies on the preparation of composite thermoplastic filaments to feed a classic printer (**Fig. 4.2 a**). A compromise between electrochemical and mechanical strength is usually required. For the electrodes, the electrochemical properties are conferred by the high loading of additives including active material and conductive particles. On the other hand, the mechanical strength must be ensured through the incorporation of a thermoplastic polymer matrix. Striking a balance between electrochemical or electrical performance with sufficient mechanical properties to ensure printability remains a challenge. Through the incorporation of a high loading of fillers within the composite filament, the preparation of a homogeneous composite filament through extrusion and subsequent 3D printing become challenging as the loading percentage but also the density of the fillers will considerably affect the rheological properties of the material coming out of the heated nozzle. To counteract the increase in viscosity (caused by the fillers), the filler amount and/or the printing parameters must be tuned to ensure adequate rheological properties, i.e. a low viscosity after the filament is liquefied, making it easier for the 3D printer nozzle to dispense the melted composite. (50) The deposited material must be able to solidify quickly to reach an efficient build speed, while still ensuring it to well adhere to a previously deposited layer.

First tests with this process were performed by Wei et al. [305] who prepared an acrylonitrile butadiene styrene (ABS) filament loaded with $5.6 \, wt.\%$ of graphene, that could potentially be used as negative electrode in a classical lithium-ion battery. Noteworthy, no battery characterization tests were performed in this initial study. Later on, a commercial graphene-polylactic acid (PLA) filament ($8 \, wt\%$ graphene and $92 \, wt\%$ PLA) was used by Foster et al. [306] to print a $1 \, mm$ thick 3D printed negative electrode disc. A proof of concept was reported, however limited discharge specific capacities (quantifying the overall electric charge that the cell can provide) of $15.8, 6.2, 2.6, 1.1$, and $0.6 \, mAh \, g^{-1}$ of active material were reached at current densities of $10, 50, 70, 100$, and $200 \, mAh \, g^{-1}$ (cycling rate of C/37, C/7, C/5, C/4, and C/2) when tested versus lithium metal respectively, principally as a result of the low ratio of active material within the filament ($103 \, mg$ of active material per cm^3 of composite). With this background, further investigations on electrode printing with filament extrusion were intensively concentrated on the development of bespoke composite filaments containing substantially greater amounts of electroactive particles. The same group later reported the preparation of bespoke PLA/graphene ($wt.\% \, 80/20$) and PLA/nanographite ($wt.\% \, 75/25$)

filaments [306], [307] for their use as negative electrodes. However, at the time of publication, other teams had already advanced further as described hereafter.

The development of PLA/$Li_4Ti_5O_{12}$ negative and PLA/$LiFePO_4$ positive electrode composite filaments was introduced by Ragones et al. [261]. According to the authors, the filaments prepared by extrusion contain ~$50 - 70\%$ of active material, 10% carbon additives and ~$20-40\%$ PLA (weight versus volume percentage was not identified). Tested in half-cells configuration versus Li metal, and impregnated with a classical 1 M $LiPF_6$ in ethylene carbonate:diethyl carbonate ($EC:DEC$ $1:1$ $vol\%$) + 2% vinylene carbonate electrolyte, the printed positive electrode PLA/$LiFePO_4$ exhibited capacities of $60, 50$ and 20 mAh g^{-1} of $LiFePO_4$ at current density of $9, 44$ and 88 μA cm^{-2}, respectively.

Similarly, the development of homemade negative electrode PLA/$Li_4Ti_5O_{12}$/graphene ($vol.\%$ $70/24/6$) and positive electrode PLA/$LiMn_2O_4$/multi-walled carbon nanotubes ($vol.\%$ $80/4/16$) filaments, was reported by Reyes et al. [279]. The authors tuned as high as possible the amount of conductive additives to reach the highest electronic conductivity without degrading printability. Negative and positive half-cells tested vs Li metal presented 0.34 and 0.71 mAh cm^{-3}, at a current density of 10 mAh g^{-1}, respectively. The assembly of the complete lithium-ion battery was finally achieved: 1) by stacking the independent printed electrodes with a separator (**Fig 4.2 b**); 2) in one-single print (components directly printed on top of each other) (**Fig 4.2 c**). Extra commercial pure PLA and copper-based filaments were used as separators and current collectors. The resulting complete lithium-ion batteries were impregnated within a 1 M $LiClO_4$ in an ethyl methyl carbonate/propylene carbonate liquid electrolyte ($EMC:PC$ $1:1$ $vol\%$). The resulting stacked battery from independent components presented a volumetric capacity of about 3.91 mAh cm^{-3} at a current density of 20 mAh g^{-1}, while the lithium-ion battery obtained in a single print exhibited 1.16 mAh cm^{-3} at 20 mAh g^{-1}.

A significant landmark was accomplished in 2018 by Maurel et al. [262], [278] who reported for the first time the development of PLA-based graphite and LFP highly loaded electrode filaments (up to 62.5 $wt\%$ of active material) thus paving the way towards printability of electrochemically promising lithium-ion battery electrodes (**Fig 4.2 a**). Such loadings were achieved through the addition of poly(ethylene glycol) dimethyl ether average Mn~500 (PEGDME500), acting as plasticizer within the composite filaments, as discussed into more details in the next section. In this particular study, a liquid electrolyte composed of 1 M $LiPF_6$ in ethylene carbonate and diethyl carbonate ($EC:DEC$ $1:1$ $wt\%$) and a homemade PLA/PEGDME500/SiO_2 ($66/27/7$ $wt\%$) separator filament (ionic conductivity of $1.20 \times 10 - 4$ S cm^{-1}) were employed. From these optimized filament

compositions, printing of the complete lithium-ion battery was achieved[262]. By tuning the separator infill patterns and density, authors were able to enhance the electrolyte soaking onto the printed structure while preventing short-circuits. Stacked battery from independent printed components showed capacity of 15 $mAh\ g^{-1}$ of LiFePO$_4$ at a current density of 4.25 $mAh\ g^{-1}$ (C/40) while the cell printed in one-single step presented higher reversible capacity values (30 mAh g^{-1} of active material at C/40, corresponding to 15 $mAh\ g^{-1}$ of the total composite or also 6.5 $mAh\ cm^{-3}$ considering both electrodes and separator total volume). In order to improve the liquid electrolyte impregnation, the available electroactive surface area and further electrochemical properties, this same group [284] recently proposed to 3D print electrodes with various infill patterns (gyroid, rectilinear and archimedean chords).

As shown before, most of the works on 3D printed electrodes via filament extrusion have been confined to the galvanostatic cycling of green parts (3D printed electrodes obtained directly after printing). However, recently Valera-Jimenez et al. [282] demonstrated that the specific capacity values of debinded and sintered electrodes (**Fig 4.2 d**) can approach the corresponding theoretical values at reasonable C-rates. For a Li$_4$Ti$_5$O$_{12}$/carbon black electrode sintered at 900 ºC in N$_2$, an average reversible specific capacity of $\approx$ 168 $mAh\ g^{-1}$ (209 $mAh\ cm^{-3}$ for the total volume electrode) centered at $\approx$ 1.5 V, was observed at C/2 rate. For a LiCoO$_2$ electrode cycled at C/10 an average reversible capacity of 129 $mAh\ g^{-1}$ (205 $mAh\ cm^{-3}$ for the total volume electrode) was observed, corresponding to 94% of the theoretical 137 $mAh\ g^{-1}$ (for 0.5 Li$^+$ intercalated). In order to further improve the electrochemical performances of the electrodes, future studies must focus on improving the thermal treatment that allows removal of non-electroactive species, thus creating porosities within the electrodes favoring a) the liquid electrolyte impregnation, b) the electroactive material reachability and c) the resulting overall electrochemical performances. It is worth mentioning that for now, electrochemical performances reported via filament extrusion are limited by the intrinsic first layer resolution limitation. Indeed, as reported previously [287], current layer thickness resolution of classical desktop filament extrusion printers is about 150 $-$ 200 μm for the first layer and down to 50 μm for the successive layers.

Similarly, the preparation of filaments acting as solid polymer electrolyte have been prepared as described hereafter. A 3D printable polyethylene oxide/lithium bis(trifluoromethanesulfonyl)imide (PEO/LiTFSI) filament (2.18 $\times$ 10^{-3} $S\ cm^{-1}\ at\ 90\ °C$) optimized to be used as solid polymer electrolyte in a lithium-ion battery was for example prepared by Maurel et al. [285] In another study, PEO/PLA/LiTFSI with SiO$_2$ or Al$_2$O$_3$ ceramic fillers ($wt\%$ 59: 20: 20: 1) filaments were prepared and printed by Ragones et al. [280], resulting in ionic conductivity values of 8 $\times$

$10^{-5}\,S\,cm^{-1}$ and $3 \times 10^{-5}\,S\,cm^{-1}$ at $120°C$, respectively. Polyethylene oxide often appears as the thermoplastic polymer of choice for the solid polymer electrolyte filament being prepared, due to its helical structure consisting of seven –CH₂–CH₂–O– groups in two turns of the helix [308] which adjust to wrap Li cations coordinated with three ether oxygens, resulting in promising ionic conductivity.
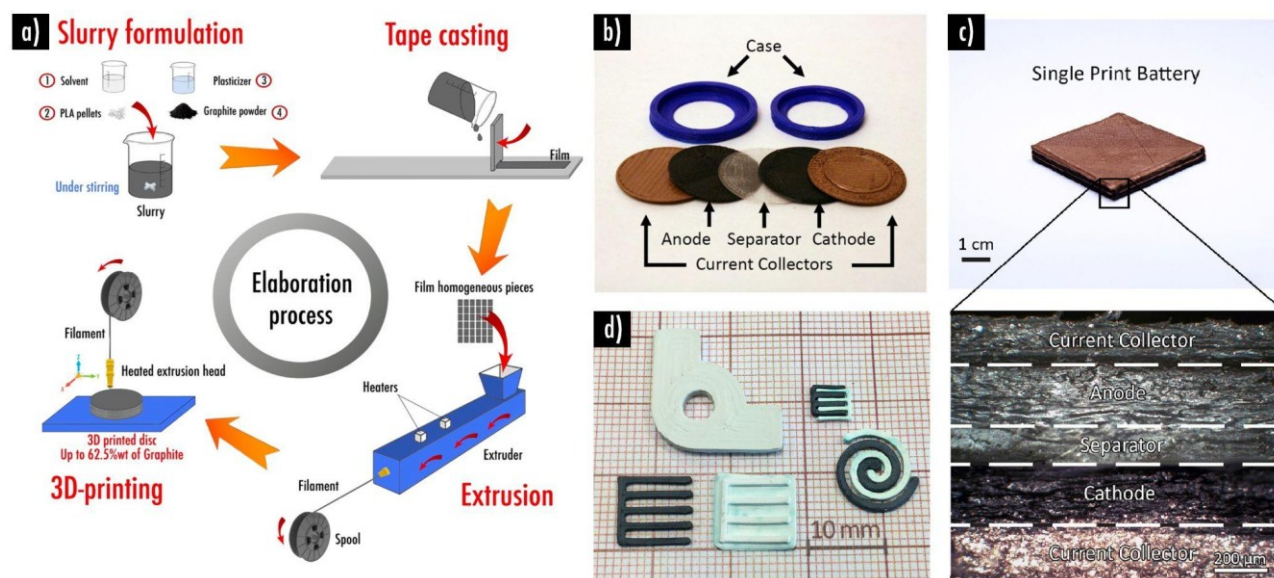

Fig. 4.2: a) Composite filament feedstock preparation and printing. Reprinted (adapted) with permission from [278]. Copyright 2018 American Chemical Society; b) 3D printed independent components and c) complete lithium-ion battery obtained in a single print. Reprinted (adapted) with permission from [279]. Copyright 2018 American Chemical Society; d) Sintered 3D printed Li4Ti5O12 (white) and LiCoO2 (black) electrode components. Reprinted from [282] with permission from Elsevier.

4.1.2 Filament extrusion: Solving the problem of inadequate mechanical properties

While thermoplastic polymers such as PLA, ABS, PP (**Table 4.2**) classically used in filament extrusion provides good tensile strength and flexibility, filaments designed to print electrodes become brittle upon the addition of powder active materials and conductive additives. As a result, printing becomes challenging, as observed in filaments loaded with graphite [278], LiFePO₄ [261], [262] and Li₄Ti₅O₁₂ [261]. To overcome this issue, low-molecular-weight liquid plasticizers with low volatility can be used as reported by Maurel et al. [278]. The action mechanism of plasticizers is to lower the glass transition temperature and the melting temperature of the polymer matrix, which allows it to remain flexible. In general, their chemical composition can be very diverse [309]: azelates, ortho-phthalates, adipates, citrates, benzoates, epoxy esters, glycols and polyethers, to mention a few. In the specific case of battery electrodes, the choice of plasticizer not only depends on the type of polymer matrix, but also of the electrochemical window and the chemical environment inside the battery. To determine the most appropriate plasticizer for PLA-based filaments, Maurel et al. [285] tested four substances: propylene carbonate, acetyl tributyl citrate, poly(ethylene glycol) dimethyl

ether with Mn ~2000 (PEGDME2000) and PEGDME500. The latter was found to be the best match for a printable highly-loaded PLA/graphite filament (optimized final loading was Graphite/carbon black/PLA/PEGDME500 $wt\%$ 49/5/33/13 corresponding to $vol\%$ 37/4/40/19). In contrast, PLA/graphene-based conductive commercial filament without any plasticizer contains a graphene loading of 8 $wt.\%$ only. PEGDME500 was used by Maurel et al. [262], [278] to strengthen the filament mechanical performances and printability while allowing to maximize the electrochemical performances. Once printed, the optimized negative electrode composed of graphite/carbon black/PLA/PEGDME500 (49/5/33/13 $wt\%$) tested in a half-cell vs. Li metal [278], exhibited a reversible capacity of 200 mAh g^{-1} of active material (99 mAh g^{-1} of the total composite, or 154.6 $mAh\,cm^{-3}$) at current density of 18.6 mA g^{-1} (C/20) and 140 mAh g^{-1} of active material (69 mAh g^{-1} of the total composite or also 108.2 mAh cm^{-3}) at current density of 37.3 mA g^{-1} (C/10). On the other hand, the optimized positive electrode made of LiFePO$_4$/carbon black/PLA/PEGDME500 (49/5/33/13 $wt\%$) [261] shown reversible capacity values of about 87 mAh g^{-1} of active material (43 mAh g^{-1} of the total composite or also to 77 mAh cm^{-3}) at current density of 8.5 mA g^{-1} (C/20), 45 mAh g^{-1} of active material (22 mAh g^{-1} of the total composite or also to 40 mAh cm^{-3}) at current density of 17 mA g^{-1} (C/10), and 22 mAh g^{-1} of active material (11 mAh g^{-1} of the total composite or also to 20 mAh cm^{-3}) at current density of 34 mA g^{-1} (C/5). More recently [249], the use of paraffinic oil as plasticizer during the elaboration of polypropylene (PP)/LiFePO$_4$ composite filament was reported. Good printability of a positive electrode containing $wt.\%$ 33/49/13/5 of PP/LiFePO$_4$/paraffinic oil/carbon black was demonstrated. Nevertheless, insignificant electrochemical performances were achieved, caused mainly by the highly energetic printing parameters that were employed resulting in a lack of micro-porosity, and related to a lesser extent to the chemical aversion of the liquid electrolyte with the PP polymer matrix that does not contain any polar groups thus conferring poor affinity with the polar molecules contained in the liquid electrolyte. The printed PP-based electrodes do not swell when soaked in the liquid electrolyte, thus resulting in low ionic conductivity and specific capacity. **Table 4.3** lists potentially suitable plasticizers for PLA, ABS and PP thermoplastic polymers. Note that most of these plasticizers have not yet been tested for battery applications.

The absence of elasticity is an issue during the printing process, but it also appears as a challenge during the cycling of the printed electrodes, often subjected to volume change during the charge-discharge process that can induce cracks and lead to capacity fading. To overcome this issue, another option introduced by Hu et al. [310] consists in using thermoplastic polyurethane (TPU) as polymer matrix due to its excellent flexibility (elongation at break between $300 - 1500\%$; **Table 4.2**) to ensure good elasticity, deformation durability, and structural integrity of the printed electrode during

cycling. The authors (88) prepared TPU-based filaments loaded with LFP, or LTO (optimized loading of TPU/active material/KB $wt\%$ 50/44/6). The printed TPU/LFP positive electrode shown reversible capacity values of about 170 mAh g^{-1} of active material at C/10, 167 mAh g^{-1} at C/5, 152 mAh g^{-1} at C/2, and 125 mAh g^{-1} at 1C. On the other hand, the printed TPU/LTO negative electrode presented reversible capacity values of about 165 mAh g^{-1} of active material at C/10, 155 mAh g^{-1} at C/5, 138 mAh g^{-1} at C/2, and 117 mAh g^{-1} at 1C. Both printed electrodes exhibited remarkable capacity retention, that may be partially explained by the ability of TPU to accommodate the volume change during the lithium ions intercalation and deintercalation processes upon cycling.

Table 4.2: Physical properties of polymers employed in 3D printed of electrodes for lithium-ion batteries. (89)

Polymer matrix	Glass transition temperature (°C)	Melting temperature (°C)	Printing temperature (°C)	Tensile strength (MPa)	Tensile modulus (MPa)	Elongation (%)	Flexural strength (MPa)	Flexural modulus (MPa)	Young's modulus (MPa)
Polylactic acid (PLA)	55-75	164-178; 180-184 (L-PLA)	180-230	52-72; 27-41 (DL); 55-82 (L)	2700-16000	4-6; 3-10 (DL); 5-10 (L)	83	1,000-3,800	3,700-4,100
Acrylonitrile-butadiene-styrene (ABS)	102-107 (acrylonitrile-styrene mesophase) and -58 (butadiene component); 103 (DSC) and 121 (DMA)	220-260	240-270	25-65	1900-2700	8-20	55-125	2150-2300	1810-2390
Polypropylene (PP)	calc.=-15; exp.=-8; -3.2 (isotactic); -9 to -51 (elastomeric)	120-176; 147-158 (metallocene); 160-176 (monoclinic); 140-153 (hexagonal)	225-245	26-32	1,700	10-140	41	1,240-1,600	1,200-2,000
Thermoplastic polyurethane (TPU)	-44 to -66	170-220	205-250	17-66	120-330	300-1500	5.5-75.2	17-1,990	33-72

Table 4.3: Representative plasticizers for the most used polymers in filament extrusion.

Polymer matrix	Plasticizer name	Chemical structure
Polylactic acid (PLA)	Polypropylene glycol	
	Polyethylene glycol	
	Acetyl tributyl citrate	
	Propylene carbonate	
	Glycerol triacetate	
Acrylonitrile-butadiene-styrene (ABS)	Triphenyl phosphate	
	Resorcinol bis(diphenyl phosphate)	
	Diphenyl phosphate	
	Dibutyl phthalate	
Polypropylene (PP)	Paraffinic oil	
	Dioctyl sebacate	
	Polybutene	

4.1.3 Ink extrusion: Outlook of the most relevant advances

Ink extrusion is currently the most employed AM process for lithium-ion battery electrodes 3D printing due to the ability to build highly loaded shape-conformable complex 3D structures with relatively inexpensive machines (**Table 4.1**) [311]. With a view to match adequate rheological properties to allow good printability, ink formulation must be studied thoroughly and a compromise between solvent, binder, electroactive species, and additives such as viscosifier or surfactant is required. Post-processes stages (freeze-drying, debinding, sintering) are commonly employed to allow inks to solidify into the form of the final object. By removing non-electroactive species, enhanced electrochemical performances and electrical conductivity can be obtained. In the case of high-temperature thermal post-treatment, it must be carefully executed as undesirable phase transitions of the electroactive material may occur.

For the first time in 2013, Sun et al. [289] reported the fabrication of a complete 3D printed Li-ion microbattery prepared from $Li_4Ti_5O_{12}$ and $LiFePO_4$ cellulose-based electrode inks (**Fig. 4.3 a**). Active material nanoparticles were suspended in aqueous solutions for the negative and positive electrodes inks respectively. Printed green parts then undergo a sintering step at 600 °C during 2 h under an inert atmosphere to eliminate the organic additives and enable sintering. Promising electrochemical performances were reported for the half-cells: $LiFePO_4$ electrode depicted a specific capacity of 160 mAh g−1 of active material at a current density of 170 mA g−1 (1 C), corresponding to an areal capacity of 1.6 mA cm^{-2} at 1.7 mA cm^{-2}. In parallel, the $Li_4Ti_5O_{12}$ electrode depicted a specific capacity of 131 mAh g−1 of active material at current density of 175 $mAh\ g^{-1}$ (1 C), thus equal to an areal capacity of 1.4 mA cm^{-2} at 1.87 mA cm^{-2}. Based on the same AM process, in 2016 Fu et al. [295] introduced the development of $Li_4Ti_5O_{12}$/graphene oxide (GO) and $LiFePO_4$/GO aqueous inks (**Fig. 4.3 b**). After enduring a freeze-drying step to remove water and strengthen the 3D structures, the electrical conductivity of the electrodes was tuned through the formation of reduced graphene oxide (rGO) upon a sintering step (Ar/H2 at $600\ °C$ for $2\ h$). A polyvinylidene fluoride-co-hexafluoropropylene (PVDF-co-HFP)/Al2O3 ink was prepared to print a separator. After solvent evaporation, it was impregnated with a liquid electrolyte composed of 1 M LiPF6 in ethylene carbonate and diethyl carbonate (EC:DEC 1: 1 vol%) to obtain a gel electrolyte. $LiFePO_4$/rGO and $Li_4Ti_5O_{12}$/rGO half cells were electrochemically tested vs. Li metal at current density of 10 $mAh\ g^{-1}$ (C/17). Specific capacities of 164 and 185 $mAh\ g^{-1}$ of active material were respectively obtained. These electrodes were assembled and the full battery depicted a capacity of about 100 $mAh\ g^{-1}$ 1 at current density of 50 $mA\ g^{-1}$.

In 2018, the fabrication of a LiMn2O4/carbon black/PVDF positive electrode ink ($85.5/6.5/8\ wt.\%$) in N-methyl-2-pyrrolidone (NMP) solvent was reported by Li et al. [290]. After printing, a voltage ($10\ kV$) was applied for $10\ minutes$ to control the electrode microstructure, while drying at $120\ °C$ was implemented to remove the solvent. Resulting structure exhibited enhanced performances ($3.5\ mAh\ cm^{-2}$ at C/10) compared with classical laminated film ($1.8\ mAh\ cm^{-2}$). The same year, printability of a complete lithium-ion battery was demonstrated by Wei et al. [304] by making use of a positive (LiFePO4) and negative (Li4Ti5O12) electrode inks, as well as ultraviolet (UV) curable packaging and separator inks (**Fig. 4.3 c**). Electrodes inks preparation consisted respectively of incorporating $30\ vol\%$ LiFePO4 with $1.25\ vol\%$ Ketjen black (KB) conductive particles, and $30\ vol\%$ Li4Ti5O12 with $1.35\ vol\%$ KB in 1 M lithium bis(trifluoromethanesulfonyl)imide/PC with $1\ wt.\%$ polyvinylpyrrolidone for the positive and negative electrode, respectively. A separator ink of PC/Al2O3/Triton X-100 surfactant was also prepared. After printing, the resulting structure was subjected to a UV-curing post-processing step. Complete printed lithium-ion battery exhibited an aerial capacity of $4.45\ mAh\ cm^{-2}$ (corresponding to $17.3\ mAh\ cm^{-3}$) at a current density of $0.14\ mA\ cm^{-2}$.

Chen et al. [303] used a copper mesh printed via ink extrusion and later sintered as a substrate on top of which lithium metal was electrodeposited as a negative electrode for a lithium-sulfur battery. The copper-based ink consisted of $84.6/0.9/14.5\ wt.\%$ of copper powder, PVDF and NMP, respectively. The positive electrode was a non-printed sulfur-loaded carbon. Gao et al. [291] formulated an NMP-based ink from sulfur composite, PVDF-HFP, carbon nanotubes, and acetylene black in weight ratios $7:2:0.5:0.5$, with a sulfur loading of $5.5\ mg\ cm^{-2}$. High-capacity retention of 87% and 85% after $200\ cycles$ at rates 1C and 2C ($9.2\ mA\ cm^{-2}$ and $18.4\ mA\ cm^{-2}$), respectively, were obtained. Also printing a positive electrode material for lithium-sulfur batteries, Shen et al. [312] employed an ink containing sulfur particles (S8), 1,3-diisopropenylbenzene as copolymer initiator and condensed GO as conductive additive and rheological properties enhancer. Surprisingly, GO also acted as a buffer of the volume changes upon cycling and the sulfur copolymer-graphene architecture exhibited a reversible capacity of $812.8\ mAh\ g^{-1}$ and good cycle performance. On the other hand, Lacey et al. [313] produced positive electrode meshes for lithium-O2 batteries by printing an aqueous ink containing holey graphene powder ($\approx 100\ mg\ mL-1$), that after post-processing becomes holey GO. The 3D printed meshes possessed meso and nanoporosity that enabled pathways for electrolyte and oxygen gas to enhance battery performance. Thanks to these pioneering works, in 2022 Idrees et al. [314] applied this information to produce a negative electrode for zinc-ion batteries. The active material consisted of a composite produced from the pyrolysis of a polymerized metal organic framework containing silicon and zinc (SiOC@Zn) (**Fig. 4.3 d**). The ink was made of active

material, PVDF and KB in an $8:1:1$ *weight ratio*. They found that the interpenetration of the design guides the nucleation of Zn2+ to achieve a superior capacity of 99 $mAh\ g^{-1}$ at 0.45 $A\ g^{-1}$ in half-cell versus zinc metal and helps to control dendritic growth and parasitic reactions that normally hamper the performance of zinc-ion batteries. As it can be deduced, there is still a lot to be done in regard to battery chemistry options other than lithium-ion, and to do so, issues such as inadequate rheological properties and electronic conductivity must be solved first.
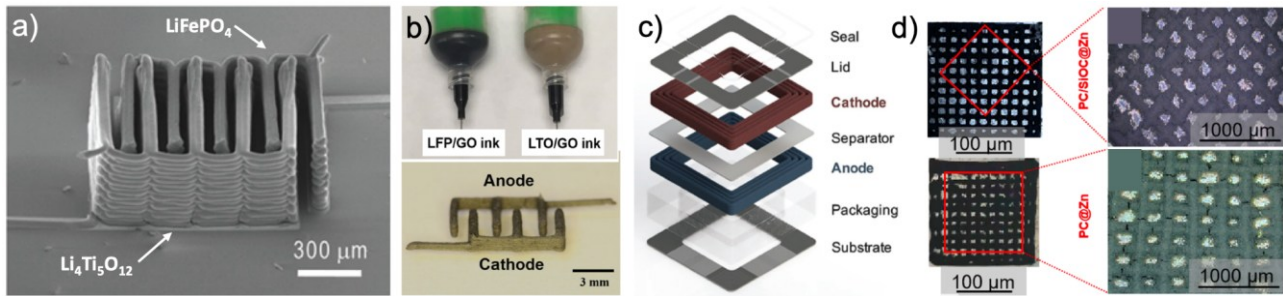

Fig. 4.3: a) SEM image after printing and annealing of the 3D interdigitated microbattery architecture design. Reprinted (adapted) with permission from [289]. Copyright 2013 Wiley Company ; b) Inks loaded in syringes (top) and optical image of the interdigitated electrodes (bottom). Reprinted (adapted) with permission from [295]. Copyright 2016 Wiley Company; c) Schematic representation of fully 3D printed Li-ion square cell battery. Reprinted (adapted) with permission from [304]. Copyright 2018 Wiley Company ; and d) Digital microscope images of the printed composite (PC/SiOC@Zn) and its corresponding annealed form (PC@Zn). Reprinted from [314] with permission from Elsevier.

4.1.4 Ink extrusion: Solving the problem of inadequate rheology

The printability of electrodes via ink extrusion is reliant on the rheological properties of the inks [311]. Viscoelasticity of the ink, for instance, must be modulated with the shear thinning behavior in order to yield stable electrode shapes. To this end, the cellulose-based viscosifiers hydroxypropyl cellulose and hydroxyethyl cellulose have been successfully added to aqueous Li4Ti5O12 and LiFePO4 inks [289]. In the case of a non-aqueous ink loaded with LiMn2O4, PVDF and carbon black ($85.5:8:6.5\ wt.\%$), Li et al. [290] found that by optimizing the solid content to 30 $wt.\%$ in the solvent, the ink was printable (viscosity of 103 $Pa.s$ and 105 Pa shear stress at a shear rate of 0.5 s^{-1}) and exhibited good electrochemical performances. Nonetheless, because of the nature of the NMP solvent, the authors required a very specific manufacturing and drying process.

Another strategy to improve the rheological properties of inks consists in leveraging the good electronic conductivity of reduced GO, to create highly concentrated GO dispersions that have been reported to exhibit gel-like behavior with high elastic modulus [315]. Fu et al. [295] exploited this characteristic by loading aqueous inks with GO to a concentration of 80 mg mL-1 and in a mass ratio $3:7$ of GO/Li4Ti5O12 (or LiFePO4). These inks exhibited high apparent viscosity between $102 - 103\ Pa.s$ at a shear rate of 1 s^{-1}. In contrast, inks heavily loaded with LiFePO4, PVDF and

carbon black in NMP solvent did not present acceptable rheological properties to be printed via ink extrusion [295].

Recently, Almansour et al. [293] claimed to obtain sintered positive electrodes based on LiFePO4 with greater structural stability and a surface area approximately 190% greater than similarly produced devices reported in the literature [316]. The particularity of the ink was that once carbon black was added to increase electronic conductivity, the ink became very viscous and the nozzle became clogged. This group then added different dispersants and a plasticizer to compensate for the $2-3\,wt\%$ of carbon in the ink. The most successful mixture was the mixture of ethylene glycol, glycerol, hydroxypropyl cellulose and Disperbyk DB-130. Other additives that might change rheological properties of the inks are dispersants and binders, which are used to prevent or promote particle aggregation and sedimentation. Perelaer et al. [316] reported the use of substances with hydroxyl or silanol surface groups to favor uniform particle dispersion. Other potentially useful dispersants include glycerol [289], cellulose nanofibers [317] and hyaluronic acid [318], to mention a few. Today numerous polymers are available to control the rheology of active materials for battery electrodes, the choice relies on the ratios of the different components that should match the desired electrochemical performances as well.

4.1.5 Filament and ink extrusion: Solving the problem of electronic conductivity

Analogous to the conventionally fabricated electrodes obtained via a tape casting process (slurry cast in a thin layer onto a flat surface and then dried), both filament and ink feedstocks require conductive additives to allow an efficient electronic conduction across a percolation network in the electrodes. While commercial electrodes contain between $2-6\%$ of conductive carbon additives [319], [320], 3D printed electrodes need a higher amount to counteract the presence of non-conductive fillers (polymer matrix, plasticizer, viscosifier). The pioneering work of Sun et al. [289] in ink extrusion of microbatteries did not use conductive additives, and as a consequence, resulted in limited rate capability.

Given their high surface area, many carbon structures and other materials with at least one dimension in the nanoscale are often used [321]. In the literature different types of carbon black [262], [278], [290], [292], [295], silver nanowires (AgNW) [296], [322], carbon nanotubes (CNT) [261], [297], carbon nanofibers [278], graphite [261], graphene [192], [312] and rGO have been employed. Interestingly, the addition of elongated nanomaterials (CNTs or nanofibers) to the polymer matrix

not only improves electronic conductivity, but also may reinforce the structural stability of the printed object [323].

Concerning ink extrusion, through both simulation and experiments Park et al. [296] found that only $0.7\ vol.\%$ of AgNW is needed to reach the electrical percolation threshold and still present good printability. By adding $1.9\ vol.\%$ of AgNW to an ink of LiFePO$_4$, distilled water and sodium carboxymethyl cellulose (CMC), the conductivity of pure LiFePO$_4$ (normally $\approx 10 - 9\ S\ cm^{-1}$) was improved to $4.21\ x\ 10 - 3\ S\ cm^{-1}$. Despite the good improvements, AgNW are not often the first choice due to their cost. Alternatively, in order to make conductive LiFePO$_4$- and Li$_4$Ti$_5$O$_{12}$-based inks, Zhou et al. [297] added $20\ wt.\%$ of CNT to mixtures of CMC and LiFePO$_4$ (or Li$_4$Ti$_5$O$_{12}$). The final dried electrodes exhibited conductivities of 1.20 and $2.08\ S\ cm^{-1}$, for LiFePO$_4$ and Li$_4$Ti$_5$O$_{12}$, respectively. Similarly, LiFePO$_4$- and Li$_4$Ti$_5$O$_{12}$-based inks loaded with 3:7 wt. of LiFePO$_4$/GO, have been reported to exhibit conductivities of 31.6 and $6.1\ cm^{-1}$,, respectively, after annealing the electrodes to obtain rGO [324]. Note that the use of highly concentrated conductive additives may also present some drawbacks. As studied by Gnanasekaran et al. [325], nozzle wear occurs when using high loading of GO or CNT due to their abrasive behavior, as observed in their high specific Young's modulus.

Concerning filament extrusion, Foster et al. [306] reported that a commercial filament of PLA/Graphene in a weight ratio of $92:8$ exhibited limited electronic conductivity and electrochemical performances. This can be explained by the very high polymer loading that does not allow an efficient percolation network. Moreover, it is worth mentioning that in this study, graphene is at the same time employed as the electroactive material. On the other hand, Ragones et al. [261] used a combination of carbon-based electronic conductors (graphite, graphitized multi-walled CNT and carbon black) with LiFePO$_4$ dispersed in PLA as filaments. In this case, the limited electrochemical performance is not attributed to the lack of conductive additives, but rather to the poor percolation network, along with insufficient electrolyte impregnation and long lithium diffusion path in the PLA matrix. In a similar manner, Reyes et al. [279] fabricated filaments with a combination of PLA, Li$_4$Ti$_5$O$_{12}$ or LiMn$_2$O$_4$ and three carbon-based additives: carbon black, graphene nanoplatelets and multi-walled CNT. They found that the best compromise between printability, electronic conductivity and electrochemical properties existed when conductive additives are kept in $< 30\%\ vol.$ and the ratio carbon additives/electroactive material is $80:20$. Although useful as starting references, these values should not be taken as definitive, as it is still possible to increase the loadings of solid materials without compromising printability. This is the case of the work of Maurel et al. [278] who were able to load a highly loaded printable PLA/graphite filament (up to $60\ wt.\%$ graphite) with up to $10\ wt.\%$ of carbon black (in respect to graphite) and obtain better

electrochemical performance than the previous works, thanks to the addition of a plasticizer. For comparison purposes, the conductivity of $0.4\ S\ cm^{-1}$, at 20 ºC was reported.

As described above, there is no ultimate conductive additive or a combination that allows the electrodes to exhibit perfect printability and optimal electrochemical performance at the same time. Instead, the focus should be directed towards tuning the ratio between polymer matrix, active material and additives. The latter includes not only conductive additives, but also plasticizers and surfactants. As shown in **Fig. 4.4**, samples printed by filament material extrusion printing usually exhibit limited electronic conductivity as conductive species are dispersed within the important yet inactive polymer matrix. Electronic conductivity of the printed samples obtained via filament extrusion can be improved through additional thermal post-processing, enhancing the percolation network, but at the detriment of the mechanical strength and flexibility of the electrodes. Electrodes printed via ink extrusion usually exhibit appropriate electronic conductivity for battery application through the introduction of conductive additives in the ink feedstock.
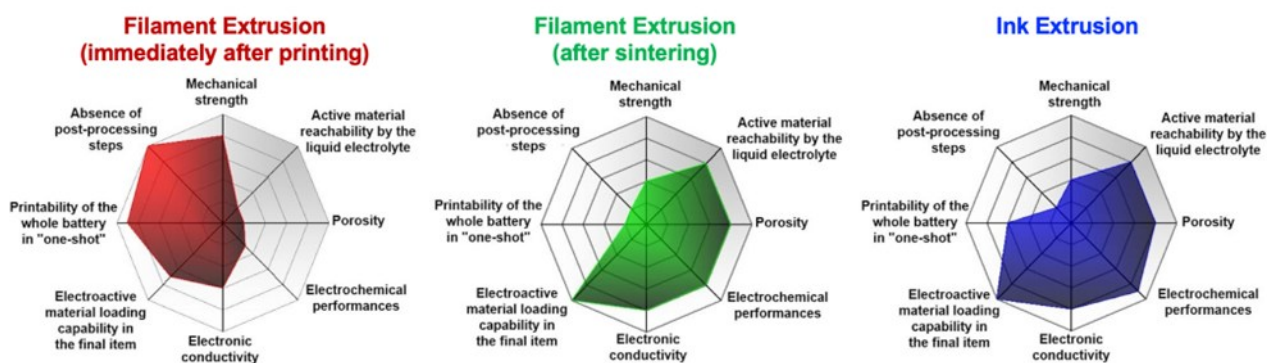

Fig. 4.4: Characteristics summary of 3D printed electrodes manufactured via filament extrusion (before and after additional thermal post-processing step) and ink extrusion.

4.1.6 Towards Environmentally-Friendly and Solvent-Free Material Extrusion of Batteries

Current studies are concentrated on the implementation of environmentally-friendly fabrication processes [284], [326], [327]. Solvent-free formulation of an environmentally-friendly lithium-terephthalate/polylactic acid (Li2TP/PLA) composite 3D printable filament for its use, once 3D printed via filament extrusion, as a negative electrode of a lithium-ion battery was for example reported (**Fig. 4.5 a**) [284]. The process included the introduction of mechanical mixing steps (ball and hand-milling) subsequently followed by the direct introduction within an extruder of the organic electroactive Li2TP particles, polymer matrix powders and additives. Furthermore, future filament extrusion studies must now be focused on the manufacturing of such composite filament using a recycled polymer matrix as new feedstock material as suggested by Zander et al. [328]. Regarding

the ink extrusion process, the fabrication of LiMn2O4 positive electrodes from water-based highly loaded slurries was reported by Airoldi et al. [326]. Environmentally-friendly CMC and Pluronic® P-123 binders were employed here by the authors. Printable pastes were later optimized through the introduction of carbonaceous additives (graphite, multi-walled carbon nanotubes and carbon black). With the same purpose in mind, an additive-free and aqueous GO-based ink was synthesized by Lacey et al. [313] where the authors demonstrated the printing of complex 3D electrode mesh architectures (**Fig. 4.5 b**).
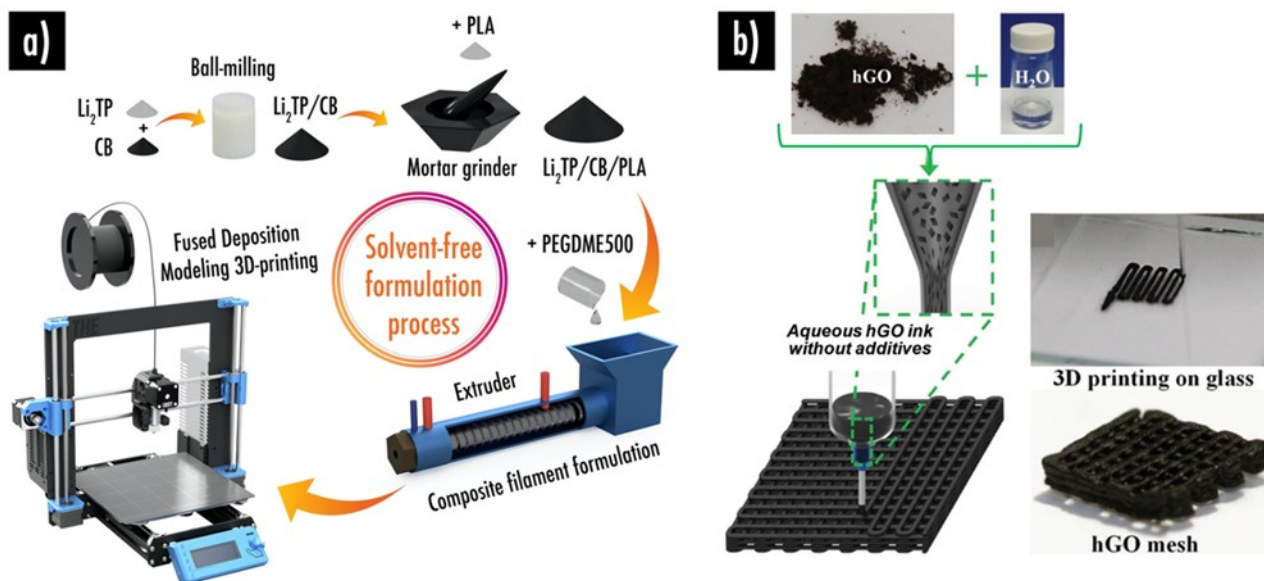

Fig. 4.5: a) Solvent-free formulation of an environmentally-friendly Li2TP/PLA composite 3D-printable filament for its use, once 3D-printed via filament extrusion, as negative electrode of a lithium-ion battery [284]; b) 3D-printing of an additive-free and aqueous graphene oxide-based ink. Reprinted (adapted) with permission from [313]. Copyright 2018 Wiley Company.

4.2   Hardware challenges and required printer modifications

As shown in the previous section, the addition of a high loading of active materials within the filament or ink feedstocks has a detrimental impact on the printability and raises numerous challenges (**Table 4.4**). The incorporation of additives (plasticizers, viscosifiers) thus appears as a first option to improve the mechanical/rheological performances and to facilitate printability. On the other hand, another interesting option often overlooked, consists of performing printer modifications. Hereafter, a summary of the issues faced while printing composite battery materials is presented, and an overview of the filament extrusion and ink extrusion machine modifications that have been specifically implemented in literature to facilitate lithium-ion battery components 3D printing is discussed. Particular attention is paid to custom configurations that were specifically developed to overcome issues related to the printability of composite lithium-ion battery materials.

Table 4.4: Summary of previous studies on the topic of 3D printed lithium-ion batteries.

Lithium-ion battery component	Materials	Printing challenges
Positive electrode	**Filament extrusion →** PLA/LiFePO$_4$ [261] PLA/LiMn$_2$O$_4$/multi-walled CNTs [279] LiFePO$_4$/carbon black/PLA/PEGDME500 [262] LiCoO$_2$/carbon black [282] PP/LiFePO$_4$/paraffinic oil/carbon black [249] PLA/LiFePO$_4$/CNT [281] TPU/LiFePO$_4$/KB [310] **Ink extrusion →** LiFePO$_4$ cellulose aqueous ink [289] LiFePO$_4$/GO aqueous inks [295] LiMn$_2$O$_4$/carbon black/PVDF in N-methyl-2-pyrrolidone solvent [290] LiFePO$_4$/KB/lithium bis (trifluoromethanesulfonyl)imide/PC/polyvinylpyrrolidone [304] LiFePO$_4$/carbon black/CMC in water and 1,4-dioxane [294]	**Filament extrusion →** poor filament mechanical strength and flexibility caused by the high loading of fillers; break within the extruder gears; clogged nozzle leading to non-extrudability; printing speed; under/over extrusion; first layer resolution limitation; retraction parameter; microporosity control **Ink extrusion →** nozzle clogging; poor adhesion to substrate; under/over extrusion; printing speed; ink rheology; microporosity control
Negative electrode	**Filament extrusion →** PLA/graphene [50], [306] PLA/nanographite [307] PLA/Li$_4$Ti$_5$O$_{12}$ [261] PLA/Li$_4$Ti$_5$O$_{12}$/graphene [279] PLA/graphite/carbon black/PEGDME500 [278] Li$_4$Ti$_5$O$_{12}$/carbon black [282] TPU/ Li$_4$Ti$_5$O$_{12}$/KB [310] **Ink extrusion →** Li$_4$Ti$_5$O$_{12}$ cellulose aqueous ink [289] Li$_4$Ti$_5$O$_{12}$/GO aqueous inks [295] Li$_4$Ti$_5$O$_{12}$/KB/lithium bis(trifluoromethanesulfonyl)imide/PC/ polyvinylpyrrolidone [304]	
Current collectors	**Filament extrusion →** Commercial Cu-based filament [279] PLA/Ag-coated Cu [287]	

		Ink extrusion → Cu-based ink [303]	
Electrolyte		**Filament extrusion →** Polyethylene oxide/lithium bistrifluoromethanesulfonyl imide [269], [285] Polyethylene oxide/PLA/lithium bistrifluoromethanesulfonyl imide [280] **Ink extrusion →** PVDF-co-HFP/TiO$_2$/N-Propyl-N-methylpyrrolidinium bis(trifluoromethanesulfonyl)imide (Pyr13TFSI) / lithium bis(trifluoromethanesulfonyl)imide / NMP [277] Ethoxylated trimethylolpropane triacrylate /Al$_2$O$_3$/photoinitiator/LiTFSI/PC [304] Polyethylene oxide/LiClO$_4$/TiO$_2$ [296] LLZO/polyvinyl butyral / benzyl butyl phthalate / n-butanol [285] LLZO/ 441 texanol-based binder / ethanol [302]	**Filament extrusion →** filament buckling phenomenon; printing must ideally be performed in a dry room or glovebox (inert atmosphere) to avoid H$_2$O and O$_2$ exposure; low printing temperature often used (<70°C) requiring firmware modification; only possible for solid polymer electrolyte or hybrid electrolyte; printing speed and retraction parameter optimization **Ink extrusion →** undesirable porosity is induced during the solvent evaporation; ink rheology
Separator		**Filament extrusion →** Pure PLA [262] PLA/PEGDME500/SiO$_2$ [278] PLA/ polyethylene oxide [324] **Ink extrusion →** PVDF-co-HFP/Al$_2$O$_3$ ink [295]	**Filament extrusion →** filament buckling phenomenon; microporosity control **Ink extrusion →** under/over extrusion; ink rheology; microporosity control

4.2.1 Filament extrusion

Due to the high loading composite nature of the filaments specifically designed to print lithium-ion battery components, the material occasionally will not extrude through the heated nozzle properly. This phenomenon can occur randomly, at the start or in the middle of a print, and is either caused by: i) the brittle mechanical behavior of the highly loaded electrode or current collector filaments that often break within the extruder gears (**Fig. 4.6 a**); ii) a buckling phenomenon often reported for flexible filaments (separator or solid polymer electrolyte components) (**Fig. 4.6 a**); or iii) a clogged nozzle occasioned by an accumulation of particles within the nozzle head upon printing. These issues ultimately affect the quality of the 3D printed battery component [278], [324] and could potentially lead to the non-extrudability.

In terms of 3D printers, commercial and custom systems have been used to print battery components via filament extrusion [280], [324], [329]. The main modifications to improve the printability consists of: i) implementing a start-and-stop method [285]; ii) changing the nozzle diameter, and iii) performing mechanical improvements of constitutive 3D printing machine parts (e.g driver, extrusion head). Otherwise, as shown previously, the alteration of the filament composition though the plasticizer addition is a different method to improve the printability, without recurring to any machine modification.

Regarding the start-and-stop method, Reyes et al. [279]or also Maurel et al. [262] used a classical cartesian Prusa machine (Prusa Research, Czech Republic) to fabricate a fully 3D printed lithium-ion battery in a single cycle without requiring any assembly. In order to print all of the components in the same printing cycle and from the same nozzle, the authors modified the G-code file to automatically pause the printing process or the researchers manually interrupted the printing process after depositing each battery component, thus allowing the operator to change the filament manually, switching from the old filament to the new one needed for the fabrication of the next battery component. After changing the filament feedstock, the printing process was resumed, and an entire battery was fabricated in one continuous printing process.

To facilitate the printability, further nozzle alterations and mechanical improvements have been reported on cartesian and delta filament extrusion printers. In conjunction with the preparation of a custom filament specifically developed to be employed as a solid polymer electrolyte in a lithium-ion battery (polyethylene oxide/lithium bistrifluoromethanesulfonyl imide), Maurel et al. [269], [285] modified a cartesian filament extrusion 3D printer with a direct drive "open" extruder, and a larger $0.6mm$ nozzle to prevent clogging (**Fig. 4.6 b**). Original gears were replaced with bondtech drive wheels (BondTech, Sweden) to facilitate the pushing process of the flexible filament into the nozzle. The heatsink part was also removed to reduce the distance between the gears and the nozzle. The latter mechanical improvement was implemented to prevent the buckling phenomenon and to allow the operator to see the filament during the printing process. Likewise, Down et al. [50] used a commercial Zmorph machine (Warsaw, Poland) equipped with a large diameter nozzle of 1mm to prevent blockage. To go further, Maurel et al. [269] developed an inverted delta printer to reduce the forces applied to the filament thus facilitating the printability of highly loaded composite electrode filaments (**Fig. 4.6 c**). In the original architecture, the extruder motor was not directly connected to the nozzle and the filament was required to pass through a polytetrafluoroethylene pipe. Commercial pure polymer filaments can be printed easily but composite filaments were reported to often break inside the flexible pipe due to the forces and vibrations applied during printing. To avoid this phenomenon, a custom inverted delta printer was developed: nozzle position was kept fixed so that

only the bed is moving during printing, and the extrusion motor was directly connected to the head of the nozzle thus facilitating the insertion of the composite filament and printing. Finally, to prevent fracture of a composite filament (ABS/graphene) during the printing process, Dul et al. [330] rolled the filament onto spools with a larger diameter of $20\ cm$, instead of classical spools with $10\ cm$ diameter suitable for standard ABS.

To overcome these common filament extrusion issues while increasing further the active material loading within the feedstock, an innovative manufacturing approach would consist of using direct pellet extrusion process [331], [332]. This technology is also based on the extrusion of thermoplastic materials through a calibrated nozzle, however the main difference with the filament extrusion process is the material feedstock being employed. The pellet extrusion 3D printer is fed directly with pellets or powders through a single [146] (**Fig. 4.6 d**) or multiple feeding ports [333] (**Fig. 4.6 e**) located on the printhead while a motorized screw pushes the pellets into the heated nozzle [334]. This AM technology has been extensively used to fabricate reinforced-thermoplastic parts but the benefits are still underexploited in the field of the battery fabrication. As an example, for the electrodes, thermoplastic materials under the form of pellets can be added into the hopper in conjunction with active materials and conductive additives powders. In particular, the main advantage of this system is that the tedious step of composite filament preparation (mandatory for filament extrusion printing) can be simply removed by using a pellet extrusion printer. Such a system can also overcome the classic breaking of brittle filaments or buckling of flexible filaments within the printhead gears, leading to printing issues. An unprecedented amount of electrochemically active material could be added within the material feedstock (here pellets) thus leading to improved battery performances. Recent understanding of the pellet extrusion process, particularly regarding the printing parameters [146], [335], co-feeding and composite printing [333], microstructure [336], models predicting thermo-fluid dynamics [129], and simulations to predict the fiber orientation during the extrusion process [97], [98], make this process particularly appealing for the fabrication of functionalized materials that can be employed as battery components. Nonetheless, printing resolution appears as the main limitation of this process as an inconsistent material intake and output, or also lack of retraction during printing, can lead to defects.
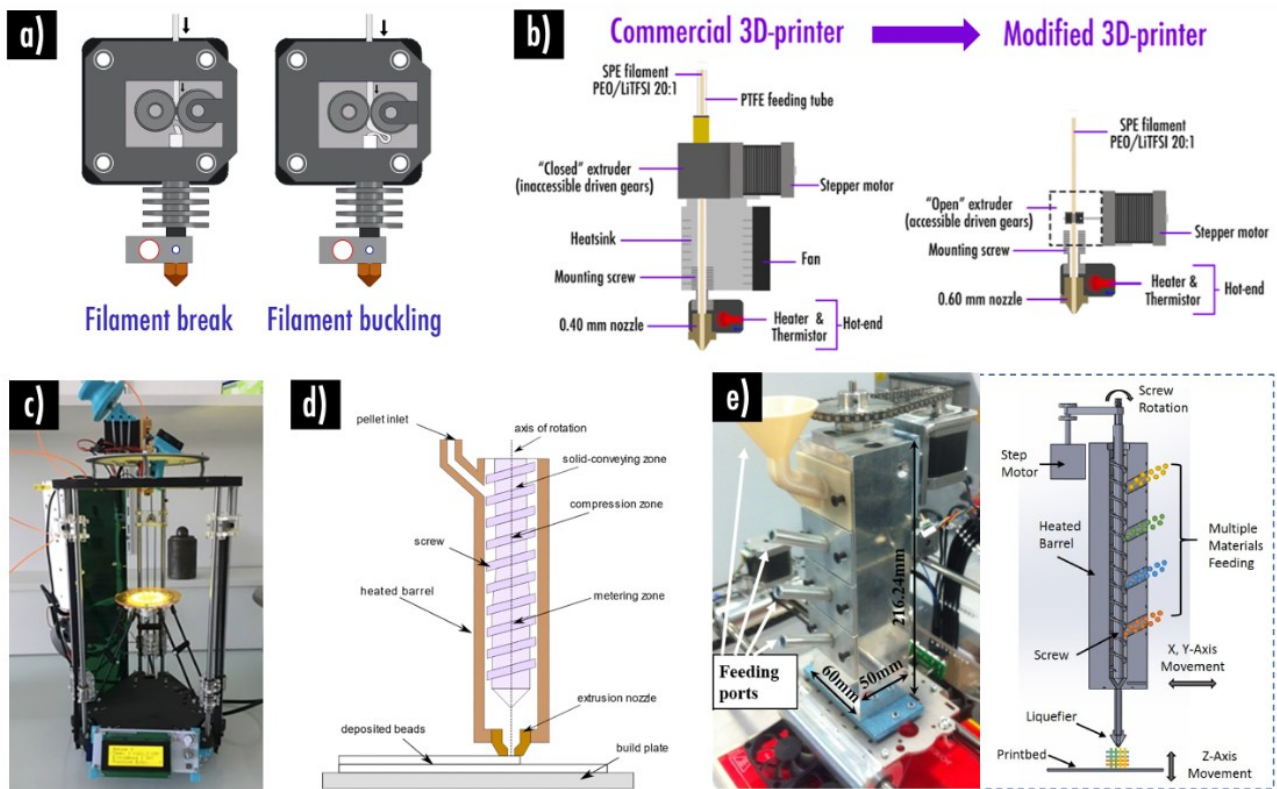
Fig. 4.6: a) Extrusion issues due to filament breakage within the gears and filament buckling [269]*; b) Extruder modifications implemented to facilitate printing of a composite solid polymer electrolyte filament* [285]*; c) Custom-made inverted delta printer facilitating the printability of highly loaded composite electrode filaments* [269]*; d) Pellet extrusion 3D printer equipped with a single* [146]*; and e) multiple feeding ports. Reprinted from* [333] *with permission from Elsevier.*

4.2.2 Ink extrusion

The introduction of a high loading of active material was shown to considerably affect rheological behavior of the ink used to print battery components. As a consequence, a first option (shown previously) to overcome issues such as 1) nozzle clogging [337]; 2) poor adhesion to the substrate [298]; 3) under-extrusion [331] and 4) over-extrusion [301], consists in introducing a viscosifier within the ink material feedstock, without recurring to any machine modification. On the other hand, several printer modifications were explored to overcome the aforementioned problems. Recent work were mostly focused on solving the problems mentioned above, using solutions such as: i) changing the nozzle diameter [302]; ii) thoroughly controlling the ink viscosity thanks to temperature [277]; iii) rheological studies previously the printing phase [299]; iv) the introduction of specific syringe and substrate [293].

Regarding nozzle clogging, different remedies were proposed. Chen et al. [303] used a highly viscous ink loaded with copper particles to print current collectors. To facilitate printability, the authors employed a custom ink extrusion printer with a $200 \mu m$ diameter syringe. The latter was equipped with a ring electric heater set at $120\ °C$ to improve the fluidity of the high-viscosity paste while also

preventing clogging problems in the needle (**Fig. 4.7 a**). Similarly, Nathan-Walleser et al. [338] fabricated graphene-based independent electrodes for capacitors using an ink extrusion printer equipped with a low-temperature print head to control the viscosity. To advance further, a co-planar radio frequency applicator was used by Sarmah et al. [339] to generate an electric field to rapidly heat and cure nano-filled composites. This process consists of a sequential print-and-cure cycle allowing 3D printing of multi-layered and complex structures. Every extruded layer was partially cured using radio frequency before depositing the next layer, so the printed part maintains structural integrity. Another solution to overcome the extrudability problem was presented by Idrees et al. [314] who vacuum filtered the ink to remove any agglomeration and large clusters to prevent the nozzle clogging.

For extrusion problems, Lewis et al. [340] and Liu et al. [339] suggested controlling the ink dynamics during deposition to prevent adhesion and thickness-extrusion problems. To further control the porosity and particles distribution, Li et al. [290] manufactured a macro-/micro-controlled lithium-ion battery by employing a fully-custom ink extrusion 3D printer, with three axis stepper controls and equipped with a $150\ \mu m$ syringe. The fully-custom 3D printer, consisting of a 3-axis micro-positioning stage (Sherline 5400) motorized by stepper motors, was assembled and operated inside an Ar-filled glovebox to prevent external contamination.

To solve extrusion and adhesion issues, Almansour et al. [293] used 3Dn-300 ink extrusion printer (nScrypt, Inc., Orlando, FL, USA), equipped with a special metal syringe tip. As shown in **Fig. 4.7 b**, the electrode samples were printed on a substrate of borosilicate glass that was adhered directly to the print bed (temperature of $40°C$) with a small strip of masking tape. The metal syringe tip was used for the larger initial print runs, but smaller electrodes were printed with yttria-stabilized zirconia nozzles having opening diameters ranging from 75 to $100\ \mu m$. These shorter nozzles led to less material friction and a lower chance of clogging.

Other solutions consist in the use of custom 3D printers used to fabricate battery components: commercial filament extrusion machines equipped/modified with a pressure ink-pump in order to switch from filament to ink extrusion [314]. The main benefit motivating researchers to modify filament extrusion machines into ink extrusion machines can be summarized as follows: i) low cost; ii) the possibility to extrude materials with different viscosities; iii) the possibility to easily modify mechanical parts of the set-up to improve the extrudability (delta or delta-inverted machine, needle-nozzle size, syringe dimensions etc.); and iv) simultaneous multi-material deposition. An example was shown by Airoldi et al. [326]a who fabricated a battery cathode using a home-customized "delta" inverted machine (**Fig. 4.7 c**) equipped with a paste-extrusion head with a syringe of $30\ cm^3$ connected to a controlled pneumatic fluid dispersion (pression up to $5\ bar$), and different needle-

nozzle sizes ($0.45\ mm$, $0.24\ mm$, and $0.20\ mm$) were used. Wang et al. [341] modified a commercial filament extrusion 3D printer (DeltaMaker 3D Printers, United States) by adding a paste extrusion-type tool head to extrude a LiFePO4 base-ink to fabricate lithium-ion battery positive electrode. An interesting custom cartesian filament extrusion 3D printer was used by Tricot et al. [342] equipped with an Arduino Mega 2560/Ramps 1.4 board controller, and a volumetric dosing system to extrude a conductive ink.

With an objective of improving the print quality and accurately controlling the line width, Liu et al. [294] reported the development of a bespoke ink extrusion machine allowing printing at low temperature ($-30\ °C$). After depositing positive electrode inks (LiFePO4, carbon black and CMC dispersed in water and 1,4-dioxane), an additional freeze-drying step was achieved at $-60\ ºC$ during $6\ h$. Employing this low temperature printing process, the resulting electrode was shown to display different microstructure in terms of porosity, pore size and particle distribution in comparison with classical ink extrusion printing achieved at ambient temperature. Ink with a solid content of $0.467\ g.mL-1$ exhibited a specific capacity of $82\ mAh\ g^{-1}$ at current density of $1700\ mA\ g^{-1}$ (10C). Same group [294] also reported a similar study for the negative electrode using Li4Ti5O12 inks via low temperature ink extrusion process. Resulting electrode consisting of 18 layers exhibiting areal capacities of $4.8\ mAh\ cm^{-2}$ at 0.2 C and $3.6\ mAh\ cm^{-2}$ at 2C.
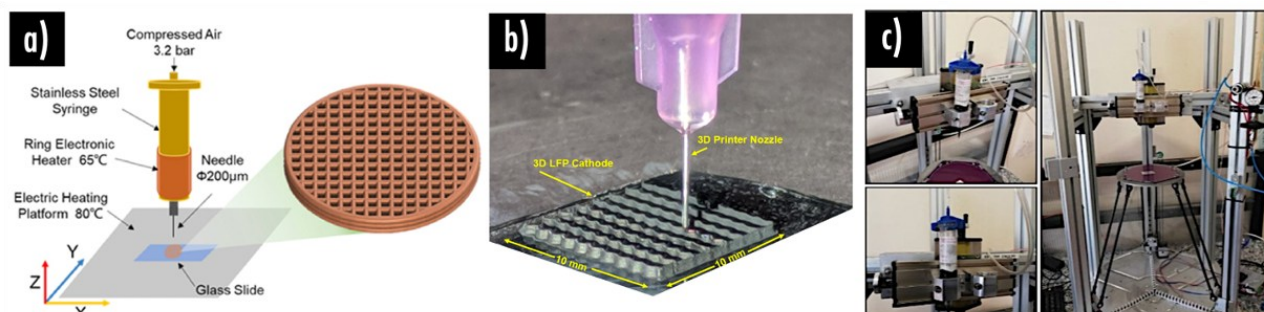

Fig. 4.7: a) Schematic diagram of the ink extrusion printer equipped with a ring heater. Reprinted (adapted) with permission from [303]. *Copyright 2021 American Chemical Society ; b) Printing of a LiFePO4 ink onto a substrate of borosilicate glass to improve adhesion* [293]; *c) Custom-made inverted delta printer facilitating the printability of highly loaded composite electrode inks. Reprinted (adapted) with permission from* [326]. *Copyright 2021 Wiley Company.*

4.3   Optimization of printing and post-processing parameters

In parallel with the printers modification undertaken to facilitate printability of the battery components, one of the most important research topics related to material extrusion printing is the full understanding of the process parameters (**Table 4.1**) in order to i) improve several properties simultaneously (i.e. mechanical, electrical and electrochemical properties, electrode porosity) of 3D printed battery parts and ii) improve the reliability of the extrusion process (i.e. reduction of clogging). An overview about several process parameters for filament and ink extrusion, to improve

the above-mentioned aspects, is presented here. Moreover, post processing treatments are also discussed.

4.3.1 Filament extrusion

In recent years, numerous studies have been specifically investigating the impact of the printing parameters such as the i) infill density and pattern; ii) extrusion-head and build plate temperature; iii) printing speed; and iv) printing layer height on the resulting performances of the printed battery components. In order to improve the electroactive surface area and enhance the liquid electrolyte impregnation, Gupta et al. [281] fabricated micro-architected composite electrodes with varying infill density to achieve desired macroporosity using a custom-made PLA/LiFePO4/CNT filament as feedstock (**Fig. 8.4 a-h**). While fixing an infill density of 30%, Maurel et al. [284] rather proposed to 3D print electrodes with various infill patterns including gyroid, rectilinear and archimedean chord designs to optimize the resulting electrochemical properties upon cycling (**Fig. 4.8 i**). Gnanasekaran et al. [294] took advantage of a multi-material 3D printing machine as polybutylene terephthalate/CNT/graphene and pure PLA were extruded at the same time, using two different nozzles. The authors showed that the best way to prevent warpage was both setting the build plate temperature to $70\,°C$ and using double-sided tape as substrate. The graphene-based composite material proposed in their work could be theoretically employed as anode in a classical lithium-ion battery. A good intralayer adhesion was achieved by Dul et al. [330] while extruding a custom-made ABS/graphene nanoplatelets thanks to a low printing speed of 40 mm.s-1 and a deposition rate of $4\,mm.ss^{1}$. Moreover, a layer height of $0.2\,mm$, a printing temperature of $230\,°C$ and build plate temperature of $60\,°C$ were set as well, in order to obtain good extrudability of the filament. Iffelsberger et al. [283] printed three different PLA/graphite electrodes while setting the nozzle at 185, 200 and $220\,°C$ (**Fig. 4.8 j**). It is possible to appreciate that the electrode printed at $185\,°C$ provides poor quality as the adhesion between single lines and layers is weak. The best quality was achieved for the electrode printed with nozzle temperature of $220\,°C$. At this temperature, the dispersion of graphite particles into the PLA matrix was enhanced and resulted in higher electronic conductivity. Moreover, to avoid the nozzle clogging, high extrusion temperatures must be utilized: Vaneckova et al. [343] set the nozzle and build plate temperatures equal to 215 and $60\,°C$, respectively. In this way, the authors were able to use a very low layer height value ($0.05\,mm$) to fabricate a high-resolution battery anode. Percoco et al. [150] later reported that the total printing force occurring during the manufacturing process is directly linked with the printing temperature. Vernardou et al. [344] deposited over a build plate having a temperature of $50\,°C$, a custom filament made up of PLA and graphene by setting high nozzle temperature ($220\,°C$) and employing a nozzle

having a diameter equal to $0.4mm$. It is important to point out that as soon as fillers (active material and conductive additives) are loaded within a pure polymer filament, the nozzle temperature must be slightly increased to prevent traditional clogging issues. At higher temperature, the viscosity of the melted polymer within the nozzle will decrease, thus ultimately facilitating printability and preventing under-extrusion.

Post-processing treatments such as vacuum drying, vapor polishing, debinding and sintering were also studied in order to improve mechanical, electrical or electrochemical properties. Paz et al. [345] performed acetone vapor polishing at $57\,°C$ for $1\,min$ and subsequently dried the 3D printed item (ABS/graphene nanoplatelets) at $37\,°C$ to ensure surface smoothing, and homogeneous electrical conductivity (**Fig. 4.8 k**). Chen et al. and Ragones et al. [261], [288] dried the 3D printed battery positive electrode under vacuum at $100\,°C$ for $12\,hours$ in order to remove residual solvent and moisture to later improve electrochemical performances. In a similar way, Down et al. [50] additively manufactured NaMnO2 and TiO2 positive and negative electrodes for a sodium-ion battery using a combination of ABS and polyvinyl alcohol (PVA) as polymer matrix. After printing, the electrodes were soaked into water to dissolve the PVA and create porosity. The electrodes were finally dried at 60 °C and stored under vacuum to evaporate the residual water from the parts. To go further, Valera-Jiménez et al. [282] added a slow debinding process (up to $550\,°C$, necessary to ensure slow removal of the polymer matrix while avoiding cracks) and sintering process ($900\,°C$ for $6h$).
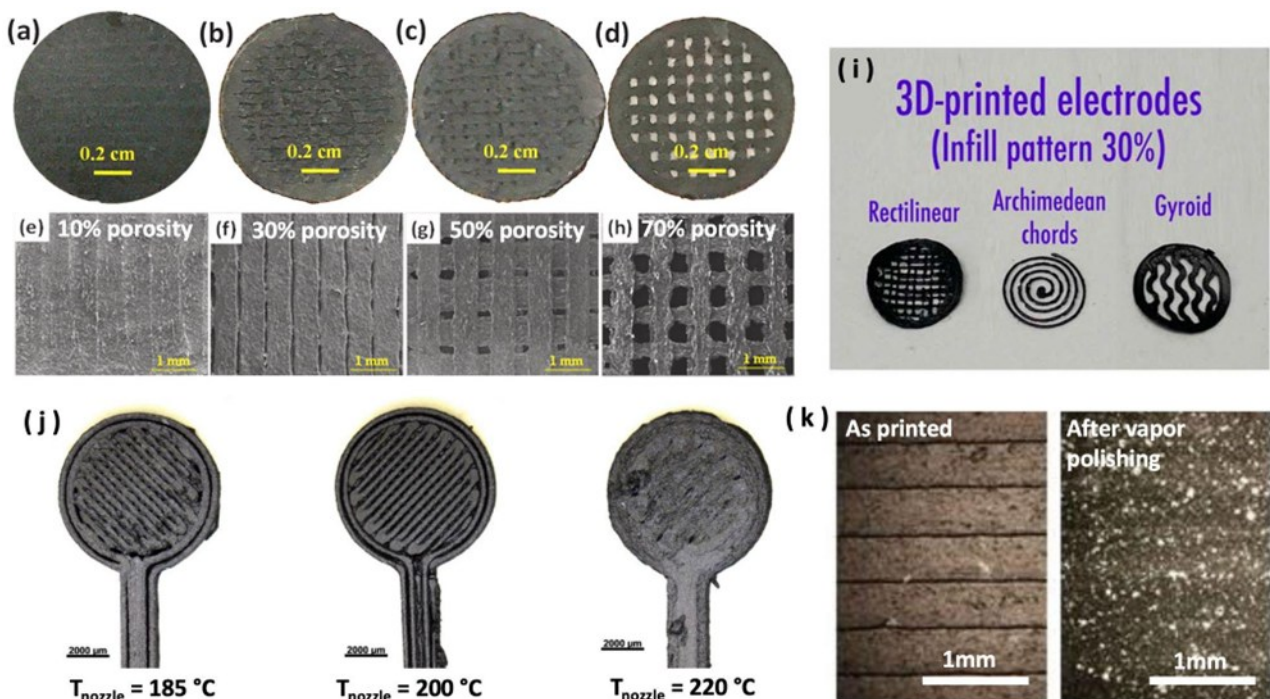

Fig. 4.8: a-h) Optical and SEM images of printed LiFePO4-based electrodes with varying infill density to achieve desired macroporosity of (a, e) 10%, (b, f) 30%, (c, g) 50% and (d, h) 70%. Reprinted from [281] with permission from Elsevier ; i) 3D printed electrodes with various infill patterns [284] ; j) PLA/graphite electrodes printed setting the nozzle temperature at 185, 200 and 220

4.3.2 Ink Extrusion

Regarding ink extrusion printing, the following printing parameters have been investigated to tune selectively the printed battery component performances: i) infill density and patterns; ii) control of pump pressure and printing speed; iii) layer thickness; iv) extrusion-head temperature and diameter; and v) temperature of the build plate or printing chamber. Wang et al. [341] used a custom printer to print a LiFePO4 electrode ink and investigated the impact of various infill patterns (grid, ring, line) on the resulting electrochemical performances during cycling (**Fig. 4.9 a ,b**). While no particular differences were reported at low current densities, the 3D printed electrode with the line infill pattern demonstrated superior performances at higher current densities of 1C, 2C and 4C and better capacity retention after $150\ cycles$ at 1C, in comparison with the 3D printed grid and ring pattern counterparts. The authors thoroughly controlled the applied pressure (between 30 and 50 psi) and printing speed (between 6 and 10 $mm.\,\mathrm{s}^{-1}$). To ensure good printability of their high viscosity inks, Fu et al. [295] optimized the pressure and printing speed (6.8 kPa and 5 mm/s) of an air-powered fluid dispenser to prevent the collapsing of the electrode structures during printing. To fabricate battery separators, Liu et al. [301] used an air-powered fluid dispenser with a fixed extrusion rate of 0.7 mm/min. The authors studied the relationship between the printing pressure (5 Pa and 10 Pa), the separator thickness (29, 50 and 100μm) and separator performance. The best performance of the battery separator was achieved at 10 Pa and 100μm of thickness. Needle geometry, pressure, and print speed were also tuned by Kohlmeyer et al. [300]to maximize print reliability and wetting of the ink. Similar work was pursued by Liu et al. [299] who optimized the printing quality and accuracy by tuning the extrusion speed, scanning speed and layer thickness of printed Li4Ti5O12 negative electrodes (**Fig 4.9 c-e**). While the printing step is usually performed at room temperature in most of the reported studies, here, the authors [282] maintained the printing chamber temperature at $-7\,°C$ to allow the ink to immediately freeze. The 3D printed samples were then stored at $-20\,°C$ and the solvent was subsequently removed to create porosity by applying vacuum freeze-drying. In another study [277], an extrusion temperature of 120 °C was leveraged to overcome the needle clogging. Similarly, Chen et al. [303] increased the extrusion-head temperature to 65 °C and also heated the build plate to 80 °C during the printing step to evaporate the solvent and induce solidification.

Finally, many efforts were attempted to develop relevant pre- and post-treatments such as: i) curing; ii) freeze-drying or vacuum drying; iii) thermal post-processing; and iv) reduction under H2 atmosphere. These additional treatments are performed to solidify the printed structure, remove

moisture and solvent residuals, remove non-electrochemically active polymeric binders, obtain correct sample dimensions, or also to allow electrochemical activation of the printed item. An innovative process reported by Sarmah et al. [339] consisted of immediately adding a curing step for $45-60\,s$ after printing of each layer (*Fig.* 4.9 *f*). The final structure was cured completely for $10\,min$ after the last printed layer. In another study, Wang et al. [341] immersed the 3D printed LiFePO4 electrodes in a water coagulation bath followed by freeze drying to remove solvent residuals and finally obtain free-standing electrodes with increased mechanical strength. Similarly, Gao et al. [291] immediately immersed the printed sulfur positive electrodes in a water coagulation bath to create a phase inversion leading to hierarchical porosity, improved adhesive strength, facilitated electron/ion transport, and enhanced electrochemical performances. After that, freeze-drying at $-50\,°C$ was applied to remove solvent residuals and maintain the 3D structure. As shown in **Fig. 4.9 g**, a freestanding and flexible 3D printed sulfur electrode was obtained after freeze-drying while samples dried in an oven appeared to be very fragile. Freeze-drying was used in other studies to remove the solvent from the electrodes, preventing cracks on the printed structure witnessed when using regular vacuum drying [291], [312]. To remove the remaining solvent from the 3D printed GO electrodes, Fu et al. [291] first employed freeze-drying, followed by thermal post processing at $600\,°C$ in Ar/H2 gas for $2\,hours$ to enable the formation of rGO. An additional thermal post-processing step was also employed by Moyano et al. [346] who subjected a 3D printed GO electrode to a heat treatment up to $1200°C$ under nitrogen atmosphere which assured GO reduction and polymer matrix decomposition.
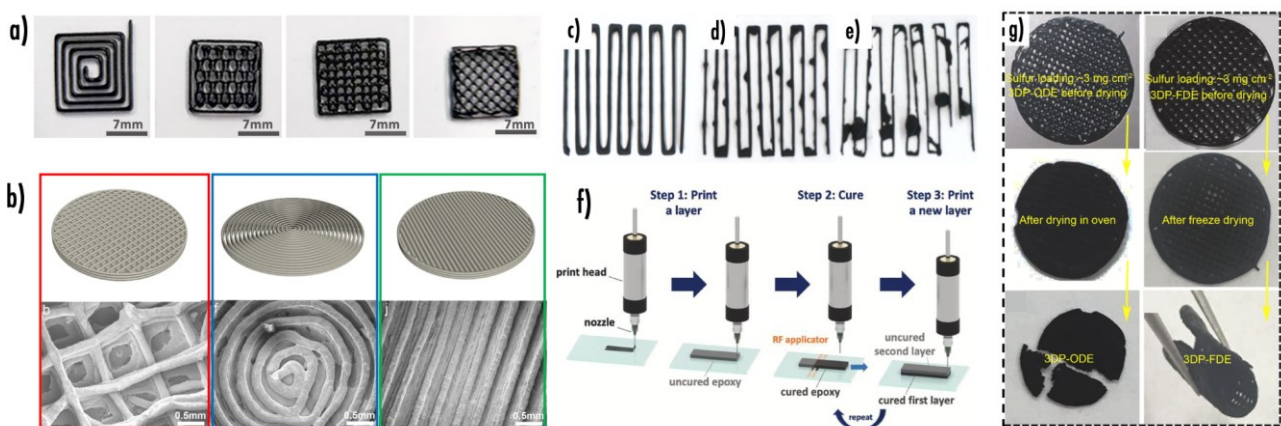

Fig. 4.9: . a,b) Optical, 3D design and SEM images of 3D printed LiFePO4-based electrodes with different infill patterns. Reprinted (adapted) with permission from [341]. Copyright 2018 American Chemical Society ; c-e) Optimization of the printing quality of Li4Ti5O12 electrodes by tuning the extrusion speed, scanning speed and layer thickness. Reprinted from [299] with permission from Elsevier ; f) Schematic representing the ink extrusion printing process using radio-frequency assisted heating and curing. Reprinted from [339] with permission from Elsevier ; g) Optical images of printed sulfur positive electrodes after drying in an oven and after freeze-drying. Reprinted from [291] with permission from Elsevier.

4.4   Conclusions

By leveraging the most recent advancements of additive manufacturing, next-generation shape-conformable 3D lithium-ion batteries can be co-designed together with the final application, so that dead-volume and weight are minimized, while power performance are enhanced. Lithium-ion batteries are the predominant battery type employed in portable consumer electronics, power tools and electric vehicles, due to the current high energy densities, low self-discharge and adequate safety, when compared with other rechargeable battery technologies. Material extrusion 3D printing (filament and ink extrusion), due to simplicity, low cost, flexibility, wide adoption, capability of printing highly loaded composite feedstocks, and multi-material printing options (enabling the printing of a complete battery in a single non assembly process), has been considered for the manufacture of custom-shape lithium-ion batteries in recent years. As shown in this reaserach, state of the art on 3D printed batteries is mainly relegated to manufacturing single battery components (cathode, anode, separator, electrolyte, or current collectors), while only a relatively few works have been focused on 3D printing of complete cells in a single non-assembly printing step. Most of previous studies investigate the preparation and optimization of material feedstock (filament or ink) to facilitate the printability of a single battery component through the addition of a sufficient amount of polymeric matrix, plasticizer (filament extrusion), or viscosities (ink extrusion), while also maximizing the electrochemical performances of the printed item thanks to the introduction of a high loading of battery active material. As a perspective, future studies related to the material feedstock must be focused on environmentally friendly processes to limit drastically the use of non-aqueous solvents for the filament or inks preparation. The simultaneous impact of the battery active material particle size on the printability and electrochemical performances, overlooked until now, should also be optimized. Due to the composite nature of the material feedstocks, material extrusion printing issues are often faced. To overcome these limitations, innovative machine modifications as well as printing and post-processing parameters optimization have been implemented. Still, specific machine modifications and printing parameters optimization must be pursued by coupling modeling and experiments to facilitate the printing of highly loaded composite filaments and inks for the preparation of battery components with superior electrochemical performances. Finally, based on the pioneering efforts was discussed, in-depth research must now be targeted on the development and optimization of innovative multi-material system allowing the manufacturing of complete battery cells in a single step. Manufacturers are encouraged to develop new multi-material systems that consider the composite nature of the material feedstocks and the requirement related to avoiding short-circuit during printing of the complete battery.

5. General conclusions

The aim of the present PhD thesis was to demonstrate the advancements of Additive Manufacturing MEX technologies for the fabrication of smart structures based on the use of electrical and magnetic actuation with embedded sensing systems, through custom-made setups and innovative fabrication approaches. Thanks to research and work done at the Interdisciplinary Additive Manufacturing (IAM) Lab, Polytechnic University of Bari, SMAM 4 Soro, Polytechnic University of Bary, and BruBotics Lab, Vrije University of Bruxelles, the goals of the thesis were achieved: different smart structure, such as electrical, electrothermal or electromagnetic actuators, sensors and different setups for extrusion of non-conventional polymers were studied and characterized.

As shown in previously chapters, the main benefits and advantages that MEX fabrication offers are: i) one-shot fabrication with a reduction of manual tasks, ii) reduction in time and costs fabrication, iii) fabrication of multi-material soft robotics structures ready to be activated using electric and magnetic external stimuli after remotion from the 3D printer build plate, vi) high level of customization of 3D printing machines (custom-made setups), and v) possibility to embedded sensing systems into soft smart structures to provide real-time feedback.

The use of MEX technology enables the fabrication of complex smart structures, such as shown in the PhD thesis, which can self-actuated, self-sensing, and self-healing without expensive materials or machines costs. Multi-material MEX for actuation systems based on electrically or magnetically driven required a low-cost commercial materials and 3D printer. The use of electrical or electromagnetic actuation has demonstrated several advantages, such as reduced activation and deactivation times (i.e., return to the original shape) compared to systems based on shape memory polymers or alloys. It has also been shown to reduce noise levels, unlike pneumatic systems, and offers significantly lower energy consumption. The portability, unlike systems that require light sources, heat, or compressed air, makes these systems highly advantageous for both every day and industrial applications.

Moreover, in this research, the use of non-conventional materials, such as Galinstan, allows to fabricate smart bending gripper and soft frog by incorporating metal filed channels which can be activated via electrical current and external permanent magnet, inducing movements of the smart structures. It has also been shown that the high-level of customization available with 3D printing machine, as shown in the literature, was used in this work to developed several custom-setups: i) entry-level Independent Dual Extrusion (IDEX) 3D machines (500 €) was modified to extrude both thermoplastic polymers and silicone (from a custom-made extrusion-head) at the same time and in the same printing cycle, thereby reducing the extrusion force in order to fabricate thin-layer structures

with high details; ii) similarly, the fabrication of sensing systems with increasing of sensitivity required only a low-cost innovative setup (roller) and implementation of printing approach, such as ironing parameter), with 83% increasing of the sensitivity of the sensors, thereby reduction of voids (53%), for the first time in the literature.

Another achievement reported in the present thesis concerns the possibility to extrude self-healing ink material through low-cost custom-made setup: in this way, multi-material self-healing sensor was developed shown improvements in mechanical, geometrical, conductivity, and healing performance. Additionally, the extrusion force was reduced, and process parameters were improved with the custom-innovative second heating system (SHS) implemented on the 3D printer machines for extrude self-healing ink.

In the author's opinion, MEX technology will be utilized over the next years to develop, study and fabricate the new-generation of smart structures (such as actuators and sensing devices), though customization of 3D printing machine in order to: i) enhance the fabrication process, ii) improve the efficiency of actuators and sensors (e.g., increase of electrical sensitivity), and iii) reduce time, costs, and manual tasks involved in the fabrication processes.

Concluding, despite MEX technology is not yet fully mature, it seems to be suitable for the smart structures field: new advancement and future studies in simulations, customization setups, materials customization, failure-behaviour of the devices and energy consumption will pave the way to overcome the current limitations of Additive Manufacturing.

Appendix A

A1- Magnetic nanopowder dispersion in Ecoflex 00-10

As demonstrated in scientific literature, if the mixing of silicone material with external magnetic/ferromagnetic particles is properly performed, a good dispersion of the particles inside the ink occurs, preventing the stratification. The sedimentation of particles in fluids is governed by the Stoke's equation, and this phenomenon happens at very low sinking velocity v_s which can be calculated as follow:

$$v_s = \frac{d^2 g(\rho_s - \rho_f)}{18\eta}$$

(eq. A1)

Here d is the particle mean diameter (53 nm, accordingly to Fe_3O_4 datasheet), g is the gravity acceleration (9.81 m^2/s), ρ_s is the density of the Fe_3O_4 nanopowder (5170 kg/m^3), ρ_f is the density of the pure silicone (1040 kg/m^3) and η is the dynamic.

From equation (S1), it stands out that the sinking velocity is extremely low, and it ranges from 0.35 nm/s to 0.18 nm/s, when considering 10 $wt\%$ (η=18 $Pa\ s$) and 30 $wt\%$ (η=35 $Pa\ s$) of Fe_3O_4, respectively.

Since the proposed manufacturing approach is envisioned to be used for the fabrication of small-scale silicone structures, which requires very low manufacturing time (no more than 5 min), the sedimentation issue can be considered negligible. It should be noted that, when extruding silicone mixed with 30 $wt\%$ of Fe_3O_4 (highest reduction of force) a very low and neglectable sedimentation of 5.4 μm occurs in 5 min.

In addition, to prove the dispersion of Fe_3O_4 inside the silicone obtained with the mixing method used throughout the whole research and the lack of sedimentation, another test was performed. Two different inks (pure silicone with 0 $wt\%$ of Fe_3O_4, and silicone mixed with 30 $wt\%$ of Fe_3O_4) were extruded in free-air and the extrusion was recorded by using the force sensor placed between the pushing part and the syringe piston. The test was performed by extruding both the inks at the same flow rate Q= 0.1 mL/min for 5 min. Fig. S1 shows the results of the test for both the inks.

As expected, the force recorded to extrude pure silicone was constant over time due to the lack of magnetic nanopowder. On the other hand, also the force applied to extrude the magnetic ink (30 $wt\%$ of Fe_3O_4) resulted to be constant during the whole test (5 min). This result clearly demonstrate that the mixing technique used to add magnetic nanopowder inside the silicone ensured the full dispersion of Fe_3O_4 without creating stratification regions. It is important to point out that the absence of spikes in the extrusion force is a direct measure of the dispersion of the Fe_3O_4 nanopowder inside the silicone.
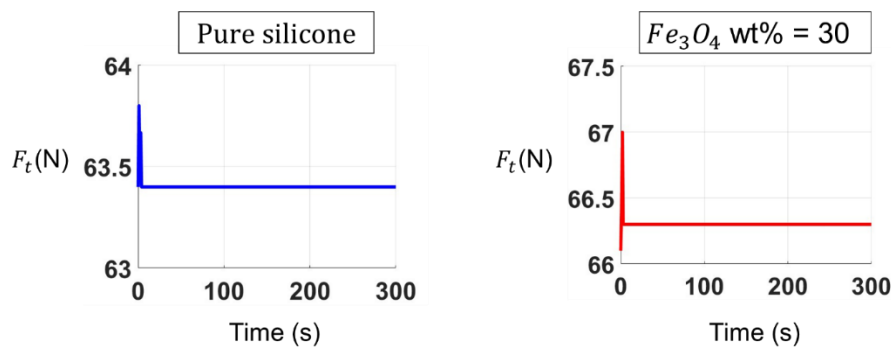

Fig.A1-Extrusion in free air for 5 min to prove the dispersion of magnetic nanopowder inside the silicone and the lack of stratification regions

A2- Force sensor and methodology for recording every force contribution

Force-Pressure Sensor RP-C18.3-ST was used to evaluate the extrusion force of the pushing part. The sensor was installed between the syringe piston and the 3D printer pushing part, as shown in Fig. A2 a). The sensor was connected

to Arduino UNO using the circuit scheme shown in Fig. A2 b). The resistance changes read by the sensor was shown on the PC screen through Arduino sketch and collected in Excel file.
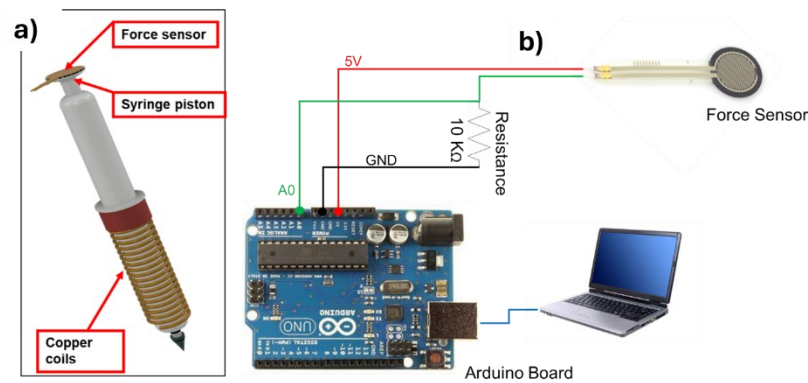

Fig.S2- a) Schematic representation of the force sensor attached on the syringe piston, and b) Force sensor circuit using Arduino UNO

To convert the resistance value in force value, the following code was used:

```
void setup() {
  pinMode(13, OUTPUT);
  pinMode(7, INPUT);
  Serial.begin(9600);
}
 void loop() {
  int v = analogRead(A0);
   Serial.println(v);
  if (v < 900) {
    digitalWrite(13, HIGH);
  } else {
    digitalWrite(13, LOW);
  }
  delay(200);
}
```

.

Every force contribution has been calculated using the following methodology:

1) The selected flow parameter was set (i.e. Q = 0.1 mL/min)
2) The extrusion was run in free-air (around 50 cm away from the build plate) for a total of 7 s. In this way, the counter-pressure force (F_{C-P}) has been avoided and the force recorded from the strain gauge F_T (total printing force) was equal to F_S (force generated inside the syringe), F_S has been experimentally found out.
3) At this point the bead described in 3.2 (70mm long, and 1.02 mm wide) was extruded on the build plate. The select layer height was set (i.e. 0.1 mm)
4) The strain gauge measured the overall printing force F_T which, at this time, also includes the counter-pressure force F_{C-P}
5) By deducting the F_S (found out at point 2) by F_T (found out at point 4), the counterpressure force F_{C-P} was found out.

The following procedure has been used when the copper coils were not provided with electrical current (traditional approach). By keeping the process parameters unchanged (same value of Q and same value of layer height), electrical current (4.5 A) was provided to the copper coils. At this point another bead (70 mm long and 1.02 mm wide) was extruded on the build-plate and the strain gauge sensor recorded the overall printing force (F_T) which includes the electromagnetic force F_{EM}, as shown in equation (2). It should be noted that F_T calculated when exploiting the electromagnetic force is smaller than F_T calculated when extruding in accordance with the traditional approach, because F_{EM} is a subtractive term.

At this point the new F_T was deducted to F_T calculated at point 5), and in this way the electromagnetic force F_{EM} was computed.

A3- Bio-inspired soft robots

In Fig. A3 all the dimensions of the soft bio-inspired robots described in Fig. 3.9 (chapter 3) are presented.
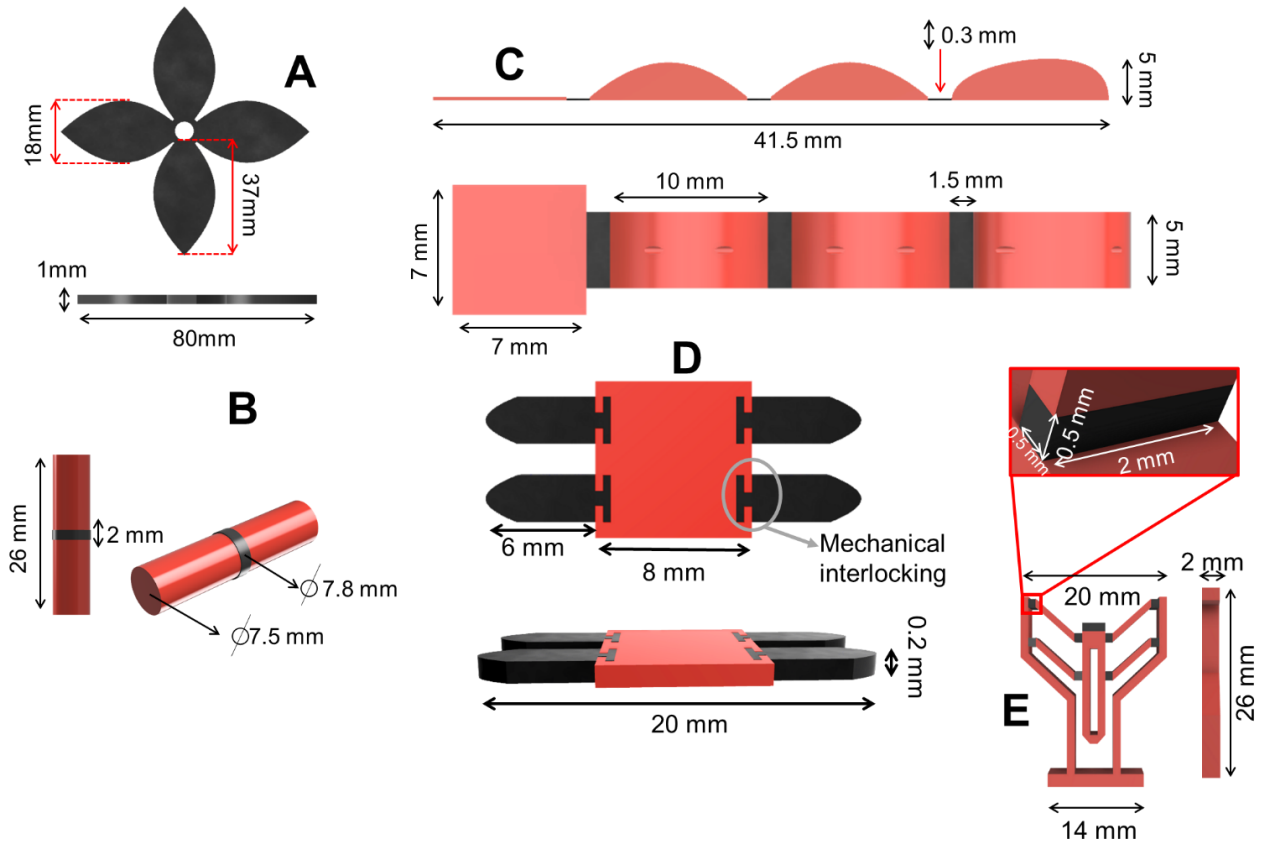

Fig. A3- Dimensions (mm) of the 3D printed bio-inspired soft robots presented in Fig 3.9 (main text): A) magnetic soft flower, B) knee-like structure, C) bio-inspired finger, D) spider-inspired soft robot, and E) bistable actuator.

Additionally, Fig. A4 shows a direct comparison between the same bio-inspired structure fabricated with the proposed electromagnetic and traditional approach. The dimensions of the bio-inspired finger are shown in Fig A9. In particular, the main idea underlying the present comparison is that the silicone joint (magnetic for the proposed approach, pure for the traditional approach) has to be composed of 3 consecutive extruded layers. Such number of layers was experimentally found to ensure a good adhesion and reduces delamination problems when the finger was bent. The minimum layer height achievable with the proposed approach of 0.1 mm was set, and a total thickness of the magnetic ink joint of 0.3 mm (corresponding to 3 layers of 0.1 mm each) was set. On the other hand, the minimum layer height achievable with the traditional approach was 0.3 mm (smaller layer height values resulted in over-extrusion and distortion problems due to extremely high printing forces) resulting in a total thickness of the pure silicone of 0.9 mm (3 layers of 0.3 mm each).

Thus, the only difference in the dimension of the finger between the proposed and traditional approach is the thickness of the soft silicone joint: 0.3 mm in the proposed approach, and 0.9 mm in the traditional approach.

The same testing procedure was used for both the bio-inspired fingers: a nylon tendon (0.2 mm) was integrated inside the finger holes and connected to a stepper motor which was moved at 300 RPM for a total of 3 s. When the motor pulled the tendon, the whole finger was bent. The main difference in the performance of the finger fabricated with the proposed and traditional approach are shown in Fig. A4. The finger fabricated with the proposed approach results in greater bending performance and flexibility since the thickness of the soft joint is just 0.3 mm (against 0.9 mm for the finger fabricated with the traditional approach). The present comparison clearly shows the benefits of the electromagnetic-assisted

approach in fabricating high performance soft robotic devices having small-scale features.
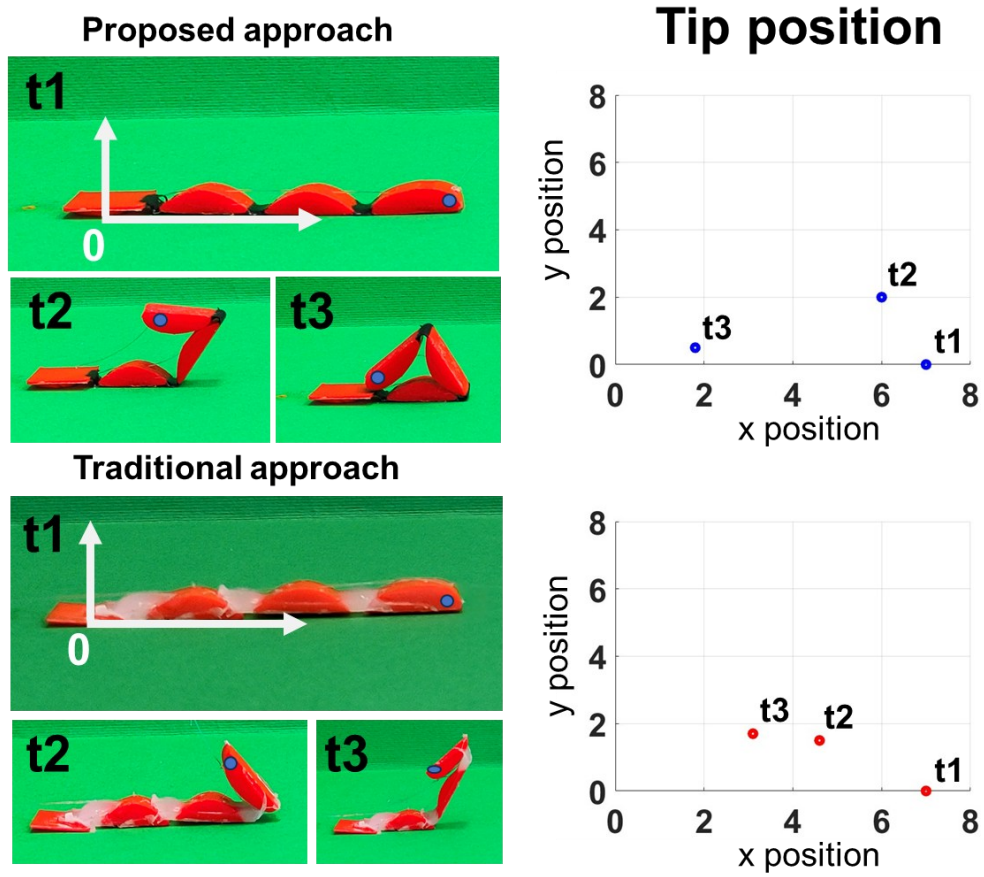

Fig.A4- Comparison between the same bio-inspired finger (soft joint composed of 3 extruded layers) fabricated with the proposed and traditional approach: the proposed approach produces a finger with improved bending behavior and flexibility.

APPENDIX B

B1- Diels-Alder self-healing materials: Characterization

The self-healing materials Pripol1040_DPBM was characterized using Differential scanning calorimetry (DSC) with a temperature window of -100 to 150 °C and rate of 5 K/min (see Fig. B1 a). The glass transition temperature (T_g) was found at 53°C.

Regarding the rheology, Dynamic rheometry was performed to determine T_{gel}, resulting to be 135°C.
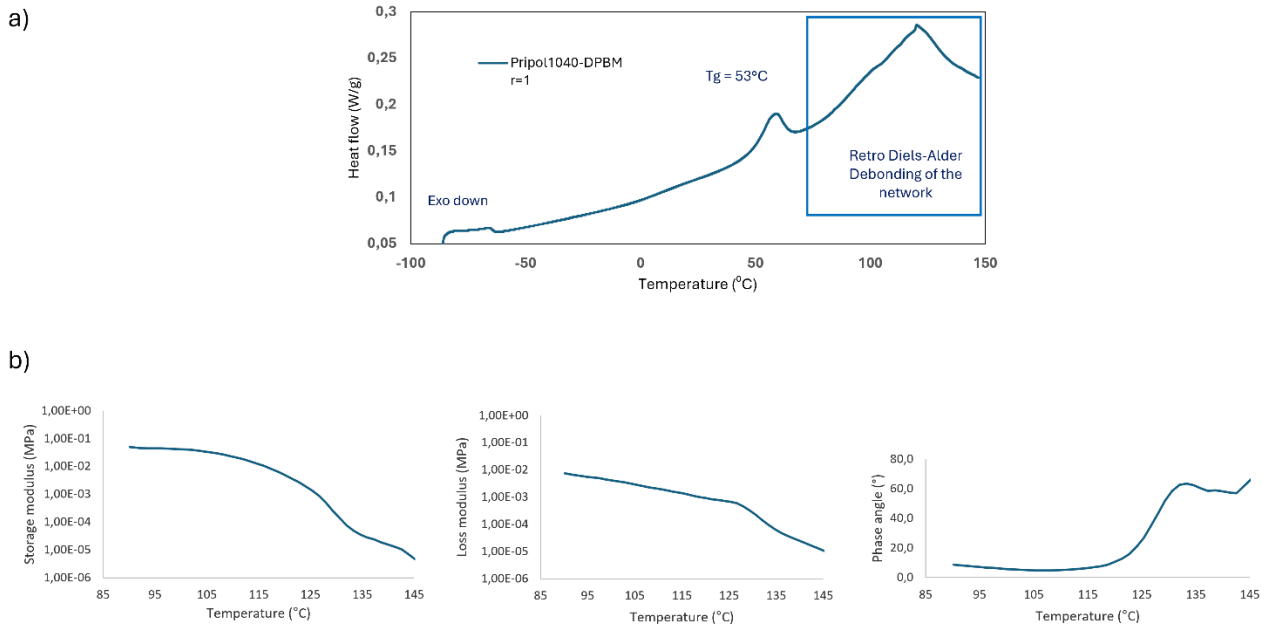
a)

b)

Fig.B1- a) Thermal analysis using Differential Scanning Calorimetry (DSC, and b) Dynamic rheometry.

B2- Force sensor for recording extrusion force

Pressure force Sensor CP 150 (RS Components, Belgium) was used to evaluate the extrusion force of the pushing part. The sensor was installed between the metal-custom syringe piston and the metal pushing part, as shown in Fig. B2 a). A 3D printed support was used to fix the sensor to the syringe-piston.

Arduino UNO R3-board (RS Components, Belgium) was used to control the sensor through the circuit schema shown in Fig. B2 b). The sensor resistance values were shown on the computer screen using Arduino sketch. Excel file was used to collect the data.

The following sketch was used to convert the resistance values in force value:

```
int fsrPin = 0;
int fsrReading;

void setup(void) {
  Serial.begin(9600);
}
 void loop(void) {
  fsrReading = analogRead(fsrPin);
   Serial.print("Analog reading = ");
   Serial.print(fsrReading);    // print the
  raw analog reading
   if (fsrReading < 10) {
     Serial.println(" - No pressure");

     Serial.println(" - Light squeeze");
  } else if (fsrReading < 800) {
     Serial.println(" - Medium squeeze");
  } else {
     Serial.println(" - Big squeeze");
  }
  delay(1000);
}
```
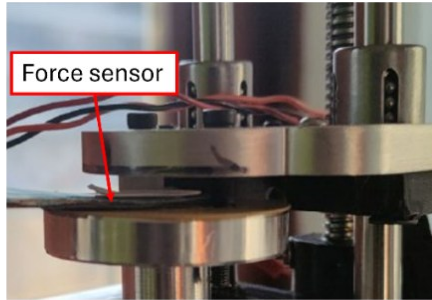
```
} else if (fsrReading < 200) {
  Serial.println(" - Light touch");
} else if (fsrReading < 500)
```
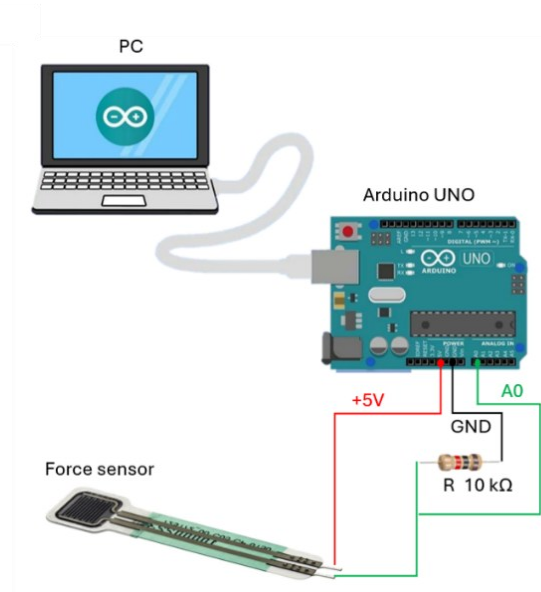
a)

b)

Fig.B3- a) Force sensor attached on the syringe piston, and b) Force sensor circuit using Arduino UNO R3-board.

B3- Printer modification

The ToolChanger motion system was modified in order to extrude ink-based self-healing materials.

The following part were used to modify the printer (Tab B1):

Part name	Realization	Cost (€/pz)	Img
Pushing element	CNC	--	
Linear Bearing (x2)	RS Components	13,00	
Lead screw	Rs Components	8,00	
Linear rail (x2)	Rs Components	14,00	
Joint	3D printed	--	

Stepper motor	E3D ToolChanger	22,64	
Custom-plate	CNC	--	
ToolChanger-plate	E3D ToolChanger	34,95	
Heating element	Rs Components	55,27	
Heating block (metal element + thermocouple + heating)	E3D ToolChanger	9,99	
Dock	3D printed	--	
Motor Fan	E3D ToolChanger	--	
Cooling-Fan	E3D ToolChanger	--	
Nozzle	E3D ToolChanger	--	
Thermal isolator	Rs Components	11,00	

The external PID temperature controller (See Fig. B3 a) was used to implement the Dual Temperature Control (DTC) approach. The PID is composed of control-plate with monitor and buttons for setting the temperature, solid state relay (SSR), and a thermocouple. The thermocouple was fixed to the syringe-barrel to read the temperature of heating element in real-time.
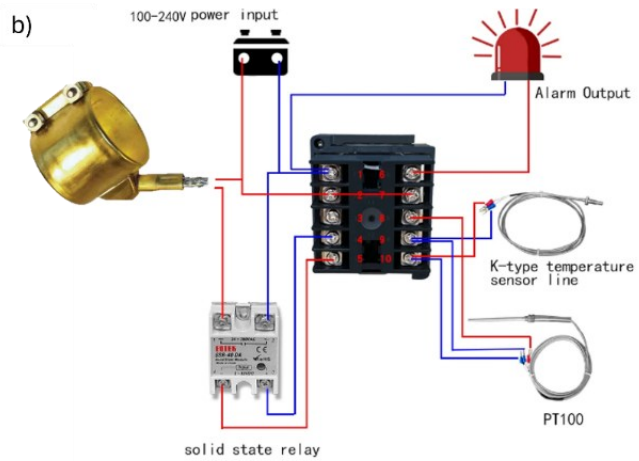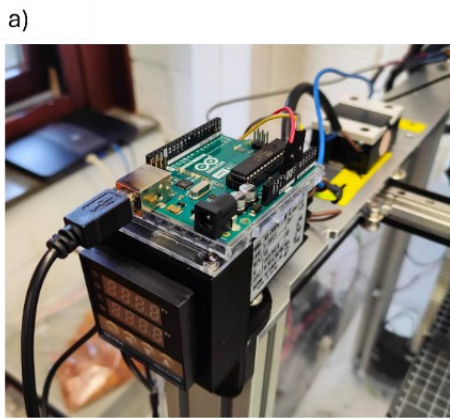
Fig.B3- a) PID temperature controller fixed to the ToolChanger Frame, and b) wiring of the PID.

The heating element (RS Components, Belgium) could work up to 340°C, with a maximum watt density of 6.5 W/cm2. The diameter ranges from 25 to 100 mm, according to the rotation of the bull. The heating element is powered directly by the PID controller, such as shown in the Fig. B3 b.

The schematic presentation of the modified extrusion ink-based head is shown in Fig. B3- c and d.
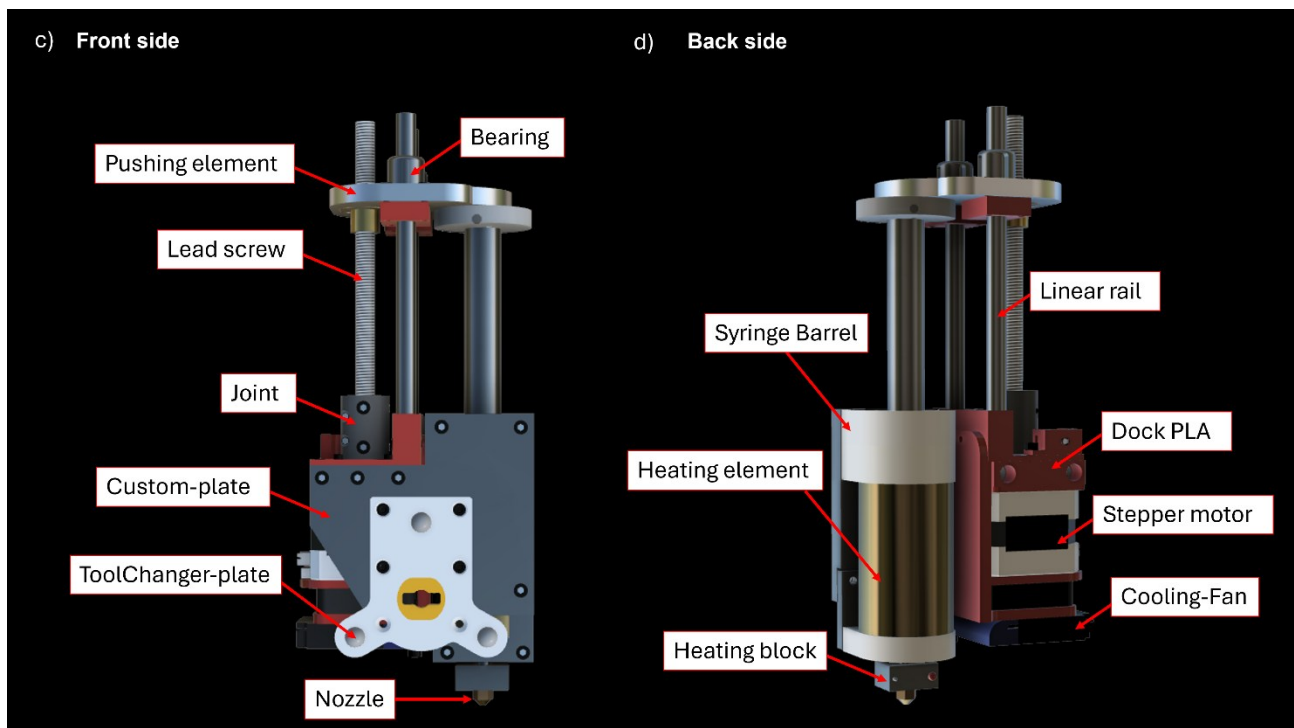
Fig.B3- c) front side of the modified ink-based extrusion head, and d) back side.

B4- Custom-made hot metal syringe

The hot custom-made syringe for self-healing materials extrusion was based on 40 ml syringe model with the following dimensions:

- internal height: 75 mm
- internal diameter: 13 mm

- external height: 89 mm
- external diameter: 28 mm

The syringe was manufactured using Computer Numerical Control (CNC) machine in aluminum metal. The syringe was designed according to the CNC manufacturing and to easy clean the internal surface, as shown in Fig B4- b, c, and d
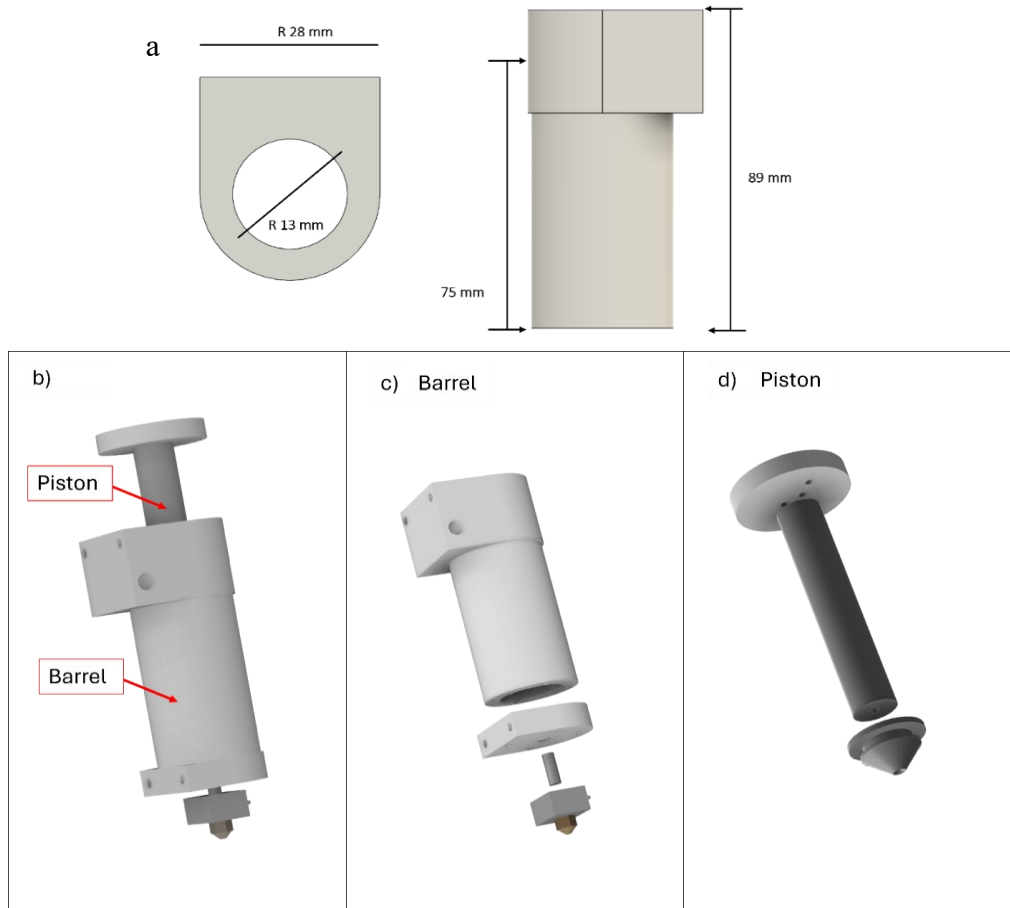
Fig.B4-: Custom-made hot metal syringe schema: a) geometrical dimensions of custom-made hot metal syringe b) assembled schema of the syringe, c) barrel exploded CAD, and d) piston exploded CAD.

.B5- Mechanical test

For the tensile test the ASTM D638-14 Type V standard was used to design the dogbones, and for the compression test the used standard was the ASTM D695.

The samples were fabricated using three different extrusion temperature to evaluate the relationship between extrusion temperature (Fig. B5 a) and mechanical performance, when the DTC is enabled. 90° and 0° printing direction, respectively parallel and perpendicular to the y-axis was tested. A total of 12 samples were tested: two repetitions for each printing direction and temperature.

As shown in Fig. B5 b, four different layers were printed resulting in a good adhesion.

Moreover, the breaking sections of the several samples, after the tensile tests, were shown in Fig. B5 c, when the extrusion temperature is equal to 145°C.

a) Text = 145°C

Text = 150°C

Text = 155°C

b)

L4
L3
L2
L1
Build plate

c)
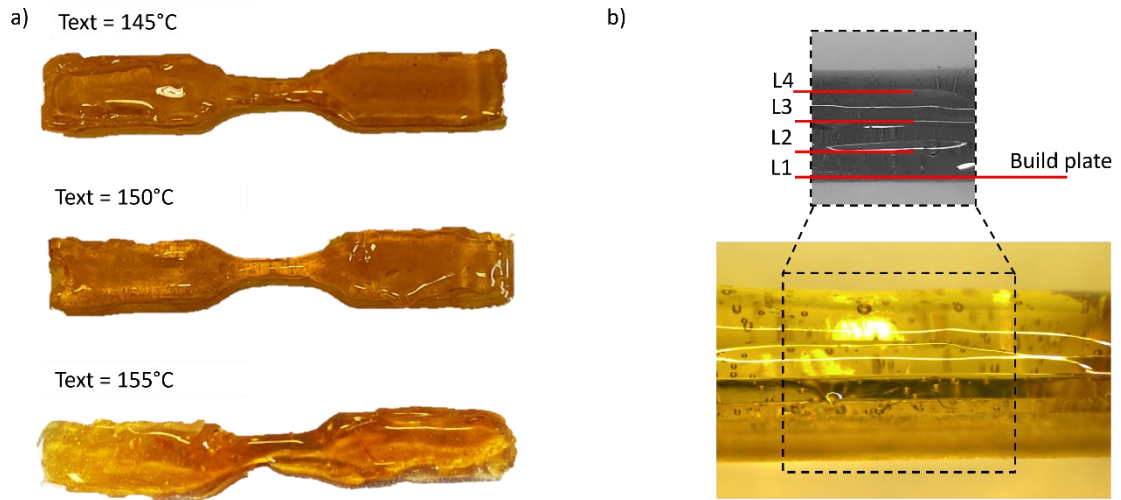
BREAKING SECTION - DOGBONES T$_{ext}$ = 145°C

Raster 0°   Raster 90°

Front view

Top view
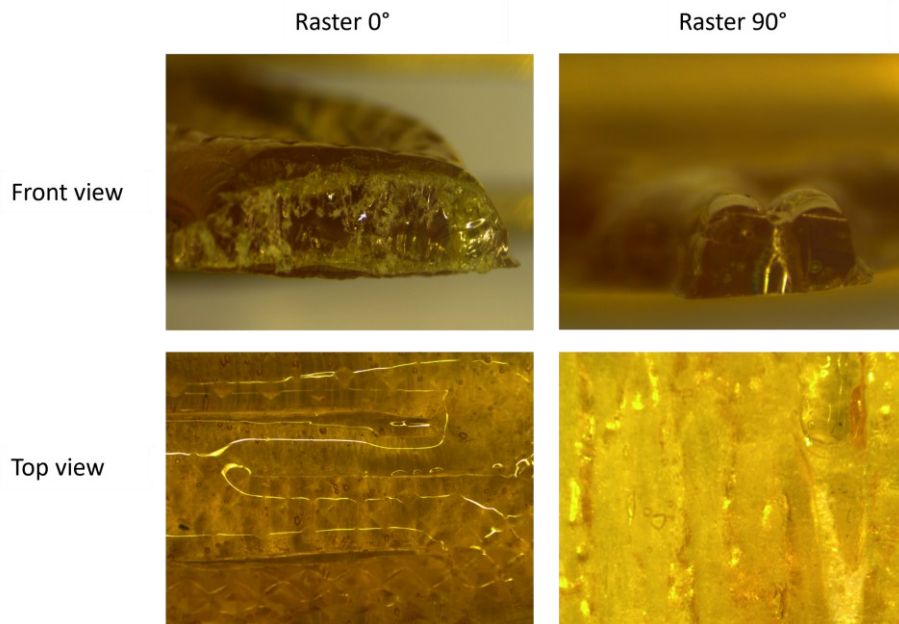
Fig.B5-: a) printed dogbones for tensile tests, b) printed layers, c) breaking section of the dogbones after the tensile test.

In order to demostrate the potenziality of the proposed DTC approac, the following pictures shown the deposition of the selg-jealing materials during the printing of the dogbones when the DTC is enalbed and the extrusion temperature is equal to 145°C. The latter prining parameter allows to print with a good quality the specimens, resulting in a trade-off between geometrical accuracy and mechanical performance.

Fig.B5-: d) printing of the dogbone specimen (DCT = On, Text = 145°C).

B6- Printing quality

The impact of the DTC, when the extrusion temperature is equal to the better (145°C), is possible to print complex-shape structures which result in a good geometrical accuracy and printing quality, as shown in Fig. S6 a. Following the printed shape were compared with the original STL shape in order to evaluate the accuracy of the printer:
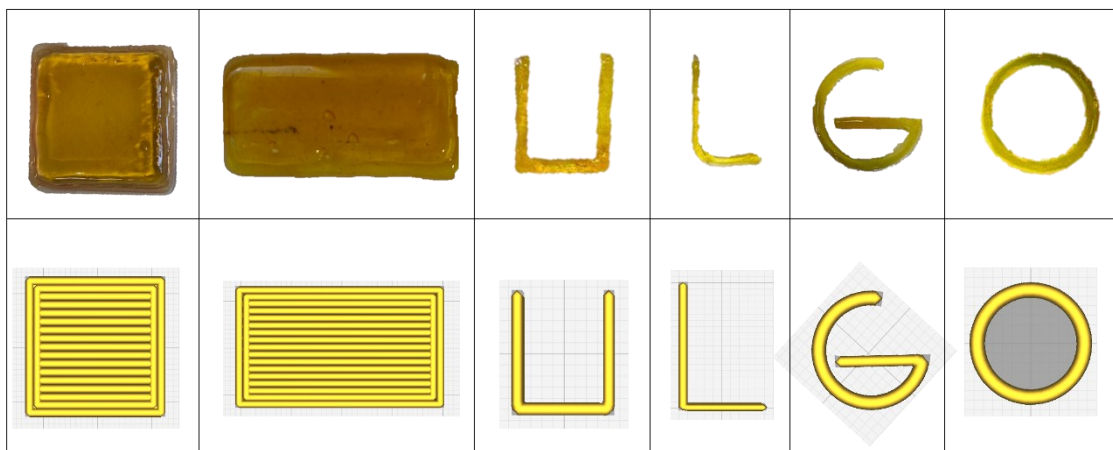
Fig.B6 a: printed shapes quality vs STL shapes

The 2D linear and snake structures 3D printed using the traditional approach shown a different size of the same printed bead resulting in a lower printing accuracy. The error of the filament deviation (σ_f) of the 3D printed structures results respectively 0.64, 0.58, 0.83 mm, for 145, 150, and 155°C of set extrusion temperature (only barrel was on). Indeed, the

width of the filament (when the best temperature of 145°C is used) ranges from 0.42 to 1.13 mm, with printing error 36% bigger than the structures printed using the proposed approach (SHS=On).

Barrel-Traditional approach

Text = 145°C – Barrel On
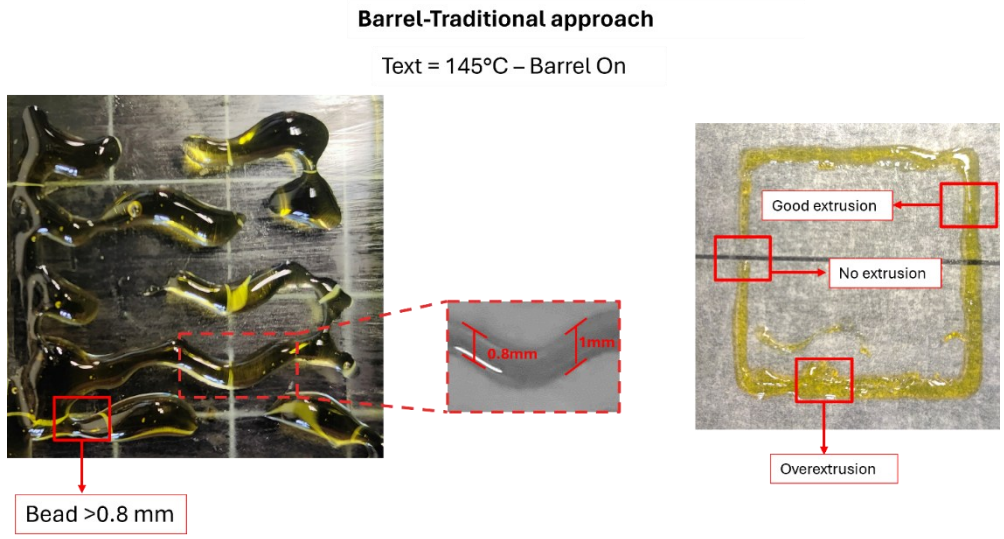
Fig.B6 b: printed shapes quality vs STL shapes

B7- Smart structures: Sensor

The smart structures gained a lot of attention from the scientific community. The sensor was manufactured using two different self-healing materials deposited through two different printing heads (Fig. B7-a). The filament-based self-healing conductive material was extruded by a commercial Titan extruder (E3D, UK), and the dielectric one was extruded by the custom-made ink-based printing head. The sensor was fabricated in order to be flexible: a total of three layers (one of dielectric and two of conductive) were printed, enabling a bending angle of 38.6°, as shown in Fig. SB- b. Finally, in Fig. SB- c was presented the real setup used to test the sensors.
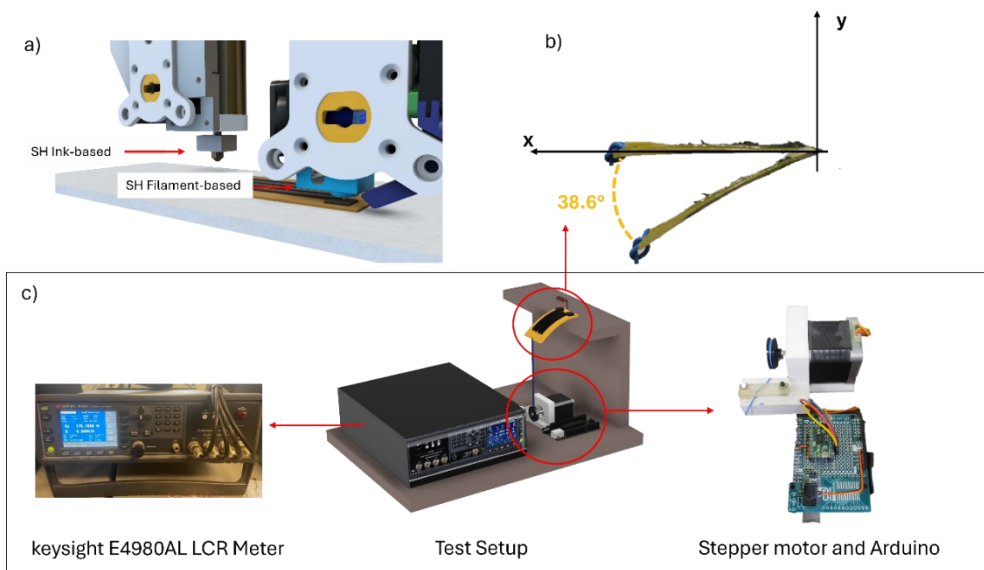
Fig.B7-: a) multimaterial printing for ink- and filament-based deposition, b) bending angle of the tested sensors, c) real setup.

References

[1] J. Butt, "Exploring the Interrelationship between Additive," pp. 1–33, 2020.

[2] U. M. Dilberoglu, B. Gharehpapagh, U. Yaman, and M. Dolen, "The Role of Additive Manufacturing in the Era of Industry 4.0," *Procedia Manuf.*, vol. 11, no. June, pp. 545–554, 2017, doi: 10.1016/j.promfg.2017.07.148.

[3] J. S. Cuellar, G. Smit, D. Plettenburg, and A. Zadpoor, "Additive manufacturing of non-assembly mechanisms," *Addit. Manuf.*, vol. 21, no. May 2017, pp. 150–158, 2018, doi: 10.1016/j.addma.2018.02.004.

[4] B. Shih *et al.*, "Design considerations for 3D printed, soft, multimaterial resistive sensors for soft robotics," *Front. Robot. AI*, vol. 6, no. APR, pp. 1–12, 2019, doi: 10.3389/frobt.2019.00030.

[5] K. V. Wong and A. Hernandez, "A Review of Additive Manufacturing," *ISRN Mech. Eng.*, vol. 2012, pp. 1–10, 2012, doi: 10.5402/2012/208760.

[6] M. Lalegani Dezaki, R. Sales, A. Zolfagharian, H. Yazdani Nezhad, and M. Bodaghi, "Soft pneumatic actuators with integrated resistive sensors enabled by multi-material 3D printing," *Int. J. Adv. Manuf. Technol.*, vol. 128, no. 9–10, pp. 4207–4221, 2023, doi: 10.1007/s00170-023-12181-8.

[7] J. De Santiago *et al.*, "Electrical motor drivelines in commercial all-electric vehicles: A review," *IEEE Trans. Veh. Technol.*, vol. 61, no. 2, pp. 475–484, 2012, doi: 10.1109/TVT.2011.2177873.

[8] M. Ehsani, Y. Gao, and S. Gay, "Characterization of Electric Motor Drives for Traction Applications," *IECON Proc. (Industrial Electron. Conf.*, vol. 1, pp. 891–896, 2003, doi: 10.1109/IECON.2003.1280101.

[9] L. Hsu, G. Yan, and M. Tsai, "Novel flexible printed circuit windings for slotless linear motor design," in *2010 International Conference on Electrical Machines and Systems*, 2010, pp. 1578–1582.

[10] A. Pavone, G. Stano, and G. Percoco, "On the Fabrication of modular linear electromagnetic actuators with 3D printing technologies," *Procedia CIRP*, vol. 110, no. C, pp. 139–144, 2022, doi: 10.1016/j.procir.2022.06.026.

[11] N. A. Mansour, B. Shin, B. Ryu, and Y. Kim, "Development of a novel miniaturized electromagnetic actuator for a modular serial manipulator," *Actuators*, vol. 10, no. 1, pp. 1–13, 2021, doi: 10.3390/act10010014.

[12] A. C. De Leon *et al.*, "Plastic Metal-Free Electric Motor by 3D Printing of Graphene-Polyamide Powder," *ACS Appl. Energy Mater.*, vol. 1, no. 4, pp. 1726–1733, 2018, doi: 10.1021/acsaem.8b00240.

[13] D. Sehrawat and N. S. Gill, "Smart Sensors: Analysis of Different Types of IoT Sensors," in *2019 3rd International Conference on Trends in Electronics and Informatics (ICOEI)*, 2019, pp. 523–528. doi: 10.1109/ICOEI.2019.8862778.

[14] J. D. Pereira, "Pressure Sensors: Working Principles of Static and Dynamic Calibration," *Sensors*, vol. 24, no. 2, 2024, doi: 10.3390/s24020629.

[15] J. F. Tressler, S. Alkoy, and R. E. Newnham, "Piezoelectric sensors and sensor materials," *J. Electroceramics*, vol. 2, no. 4, pp. 257–272, 1998, doi: 10.1023/A:1009926623551.

[16] Y. Yue, D. Ji, Y. Liu, and D. Wei, "Chemical Sensors Based on Covalent Organic Frameworks," *Chem. - A Eur. J.*, vol. 30, no. 3, 2024, doi: 10.1002/chem.202302474.

[17] A. S. Fiorillo, C. D. Critello, and S. A. Pullano, "Theory, technology and applications of piezoresistive sensors: A review," *Sensors Actuators A Phys.*, vol. 281, pp. 156–175, 2018, doi: https://doi.org/10.1016/j.sna.2018.07.006.

[18] X. Hu and W. Yang, "Planar capacitive sensors – designs and applications," *Sens. Rev.*, vol. 30, no. 1, pp. 24–39, Jan. 2010, doi: 10.1108/02602281011010772.

[19] A. J. Cheng *et al.*, "Recent Advances of Capacitive Sensors: Materials, Microstructure Designs, Applications,

and Opportunities," *Adv. Mater. Technol.*, vol. 8, no. 11, pp. 1–34, 2023, doi: 10.1002/admt.202201959.

[20]   O. H. Elibol, D. Morisette, D. Akin, J. P. Denton, and R. Bashir, "Integrated nanoscale silicon sensors using top-down fabrication," *Appl. Phys. Lett.*, vol. 83, no. 22, pp. 4613–4615, Dec. 2003, doi: 10.1063/1.1630853.

[21]   G. Stano, A. Pavone, M. A. Jafor, K. Matalgah, G. Percoco, and T. J. Fleck, "Enhancing the sensitivity of 3D printed sensors via ironing and void reduction," *Virtual Phys. Prototyp.*, vol. 19, no. 1, 2024, doi: 10.1080/17452759.2024.2331153.

[22]   G. Stano, A. Di Nisio, A. M. Lanzolla, M. A. Ragolia, and G. Percoco, "Additive manufacturing for capacitive liquid level sensors," *Int. J. Adv. Manuf. Technol.*, vol. 123, no. 7–8, pp. 2519–2529, 2022, doi: 10.1007/s00170-022-10344-7.

[23]   G. Mogli *et al.*, "Self-Powered Integrated Tactile Sensing System Based on Ultrastretchable, Self-Healing and 3D Printable Ionic Conductive Hydrogel," *Adv. Funct. Mater.*, vol. 34, no. 7, pp. 1–12, 2024, doi: 10.1002/adfm.202307133.

[24]   D. Bourell *et al.*, "Materials for additive manufacturing," *CIRP Ann.*, vol. 66, no. 2, pp. 659–681, 2017, doi: https://doi.org/10.1016/j.cirp.2017.05.009.

[25]   J. Y. Lee, J. An, and C. K. Chua, "Fundamentals and applications of 3D printing for novel materials," *Appl. Mater. Today*, vol. 7, pp. 120–133, 2017, doi: 10.1016/j.apmt.2017.02.004.

[26]   Y. L. Yap, S. L. Sing, and W. Y. Yeong, "A review of 3D printing processes and materials for soft robotics," *Rapid Prototyp. J.*, vol. 26, no. 8, pp. 1345–1361, Jan. 2020, doi: 10.1108/RPJ-11-2019-0302.

[27]   S. Gharaie *et al.*, "Direct 3D printing of a two-part silicone resin to fabricate highly stretchable structures," *Prog. Addit. Manuf.*, no. 0123456789, 2023, doi: 10.1007/s40964-023-00421-y.

[28]   A. Saxena and M. Kamran, "A Comprehensive Study on 3D Printing Technology," *MIT Int. J. Mech. Eng.*, vol. 6, no. 2, pp. 63–69, 2016, [Online]. Available: https://www.researchgate.net/publication/310961474_A_Comprehensive_Study_on_3D_Printing_Technology %0Ahttps://www.researchgate.net/publication/310961474

[29]   C. G. Harris, N. J. S. Jursik, W. E. Rochefort, and T. W. Walker, "Additive Manufacturing With Soft TPU – Adhesion Strength in Multimaterial Flexible Joints," *Front. Mech. Eng.*, vol. 5, no. July, pp. 1–6, 2019, doi: 10.3389/fmech.2019.00037.

[30]   E. H. Tümer and H. Y. Erbil, "Extrusion-based 3d printing applications of pla composites: A review," *Coatings*, vol. 11, no. 4, pp. 1–42, 2021, doi: 10.3390/coatings11040390.

[31]   G. Stano, S. M. A. I. Ovy, J. R. Edwards, M. Cianchetti, G. Percoco, and Y. Tadesse, "One-shot additive manufacturing of robotic finger with embedded sensing and actuation," *Int. J. Adv. Manuf. Technol.*, pp. 467–485, 2022, doi: 10.1007/s00170-022-10556-x.

[32]   S. I. Koltsov, T. G. Statsenko, and S. M. Morozova, "Modification of Commercial 3D Fused Deposition Modeling Printer for Extrusion Printing of Hydrogels," *Polymers (Basel).*, vol. 14, no. 24, 2022, doi: 10.3390/polym14245539.

[33]   E. MacDonald and R. Wicker, "Multiprocess 3D printing for increasing component functionality," *Science (80-.).*, vol. 353, no. 6307, 2016, doi: 10.1126/science.aaf2093.

[34]   E. MacDonald *et al.*, "3D printing for the rapid prototyping of structural electronics," *IEEE Access*, vol. 2, pp. 234–242, 2014, doi: 10.1109/ACCESS.2014.2311810.

[35]   X. Kuang, K. Chen, C. K. Dunn, J. Wu, V. C. F. Li, and H. J. Qi, "3D Printing of Highly Stretchable, Shape-Memory, and Self-Healing Elastomer toward Novel 4D Printing," *ACS Appl. Mater. Interfaces*, vol. 10, no. 8,

pp. 7381–7388, 2018, doi: 10.1021/acsami.7b18265.

[36]   J. Patadiya, A. Gawande, G. Joshi, and B. Kandasubramanian, "Additive manufacturing of shape memory polymer composites for futuristic technology," *Ind. Eng. Chem. Res.*, vol. 60, no. 44, pp. 15885–15912, 2021, doi: 10.1021/acs.iecr.1c03083.

[37]   A. Mitchell, U. Lafont, M. Hołyńska, and C. Semprimoschnig, "Additive manufacturing — A review of 4D printing and future applications," *Addit. Manuf.*, vol. 24, no. October, pp. 606–626, 2018, doi: 10.1016/j.addma.2018.10.038.

[38]   A. Zapciu, C. G. Amza, C. Rontescu, and G. Tasca, "3D-Printed, Non-assembly, Pneumatically Actuated Mechanisms from Thermoplastic Materials," *Mater. Plast.*, vol. 55, no. 31, pp. 517–520, 2018, doi: 10.37358/mp.18.4.5065.

[39]   F. Pahlevanzadeh *et al.*, *Three-dimensional printing constructs based on the chitosan for tissue regeneration: State of the art, developing directions and prospect trends*, vol. 13, no. 11. 2020. doi: 10.3390/ma13112663.

[40]   A. Zolfagharian, A. Z. Kouzani, S. Y. Khoo, A. A. A. Moghadam, I. Gibson, and A. Kaynak, "Evolution of 3D printed soft actuators," *Sensors Actuators, A Phys.*, vol. 250, pp. 258–272, 2016, doi: 10.1016/j.sna.2016.09.028.

[41]   P. Boyraz, G. Runge, and A. Raatz, "An overview of novel actuators for soft robotics," *High-Throughput*, vol. 7, no. 3, pp. 1–21, 2018, doi: 10.3390/act7030048.

[42]   A. Maurel, A. Pavone, G. Stano, A. C. Martinez, E. MacDonald, and G. Percoco, "Manufacturing-oriented review on 3D printed lithium-ion batteries fabricated using material extrusion," *Virtual Phys. Prototyp.*, vol. 18, no. 1, 2023, doi: 10.1080/17452759.2023.2264281.

[43]   J. Shintake, V. Cacucciolo, D. Floreano, and H. Shea, "Soft Robotic Grippers," *Adv. Mater.*, vol. 30, no. 29, 2018, doi: 10.1002/adma.201707035.

[44]   X. Cao, S. Xuan, S. Sun, Z. Xu, J. Li, and X. Gong, "3D Printing Magnetic Actuators for Biomimetic Applications," vol. 30136, 2021, doi: 10.1021/acsami.1c08252.

[45]   C. Yan, X. Zhang, Z. Ji, X. Wang, and F. Zhou, "3D-Printed Electromagnetic Actuator for Bionic Swimming Robot," *J. Mater. Eng. Perform.*, no. Ref 38, 2021, doi: 10.1007/s11665-021-05918-7.

[46]   R. Tao, J. Shi, F. Granier, M. Moeini, A. Akbarzadeh, and D. Therriault, "Multi-material fused filament fabrication of flexible 3D piezoelectric nanocomposite lattices for pressure sensing and energy harvesting applications," *Appl. Mater. Today*, vol. 29, no. July, p. 101596, 2022, doi: 10.1016/j.apmt.2022.101596.

[47]   Q. Wu *et al.*, "3D Printed Sensors for Wearable Electronics and Smart Gesture Recognition," *Adv. Mater. Technol.*, vol. 2302048, pp. 1–11, 2024, doi: 10.1002/admt.202302048.

[48]   J. Liu, X. Zhang, J. Liu, X. Liu, and C. Zhang, "3D Printing of Anisotropic Piezoresistive Pressure Sensors for Directional Force Perception," vol. 2309607, pp. 1–10, 2024, doi: 10.1002/advs.202309607.

[49]   T. Košir and J. Slavič, "Manufacturing of single-process 3D-printed piezoelectric sensors with electromagnetic protection using thermoplastic material extrusion," *Addit. Manuf.*, vol. 73, no. April, p. 103699, 2023, doi: 10.1016/j.addma.2023.103699.

[50]   M. P. Down, E. Martínez-Periñán, C. W. Foster, E. Lorenzo, G. C. Smith, and C. E. Banks, "Next-Generation Additive Manufacturing of Complete Standalone Sodium-Ion Energy Storage Architectures," *Adv. Energy Mater.*, vol. 9, no. 11, 2019, doi: 10.1002/aenm.201803019.

[51]   Y. Pang *et al.*, "Additive Manufacturing of Batteries," *Adv. Funct. Mater.*, vol. 30, no. 1, 2020, doi: 10.1002/adfm.201906244.

[52]   G. Stano and G. Percoco, "Additive manufacturing aimed to soft robots fabrication: A review," *Extrem. Mech.*

Lett., vol. 42, p. 101079, 2021, doi: 10.1016/j.eml.2020.101079.

[53]   S. Walker, O. D. Yirmibeşoğlu, U. Daalkhaijav, and Y. Mengüç, "14 - Additive manufacturing of soft robots," in *Woodhead Publishing in Materials*, S. M. Walsh and M. S. B. T.-R. S. and A. P. Strano, Eds., Woodhead Publishing, 2019, pp. 335–359. doi: https://doi.org/10.1016/B978-0-08-102260-3.00014-7.

[54]   H. Dong, T. Weng, K. Zheng, H. Sun, and B. Chen, "Review: Application of 3D Printing Technology in Soft Robots," *3D Print. Addit. Manuf.*, vol. 11, no. 3, pp. 954–976, 2024, doi: 10.1089/3dp.2023.0127.

[55]   S. Singh, G. Singh, C. Prakash, and S. Ramakrishna, "Current status and future directions of fused filament fabrication," *J. Manuf. Process.*, vol. 55, no. April, pp. 288–306, 2020, doi: 10.1016/j.jmapro.2020.04.049.

[56]   A. Pavone, G. Stano, and G. Percoco, "One-Shot 3D Printed Soft Device Actuated Using Metal-Filled Channels and Sensed with Embedded Strain Gauge," *3D Print. Addit. Manuf.*, vol. 10, no. 6, pp. 1251–1259, 2023, doi: 10.1089/3dp.2022.0263.

[57]   "Advanced Intelligent Systems - 2021 - Tawk - A Review of 3D-Printable Soft Pneumatic Actuators and Sensors Research.pdf."

[58]   A. Zolfagharian, M. A. P. Mahmud, S. Gharaie, M. Bodaghi, A. Z. Kouzani, and A. Kaynak, "3D/4D-printed bending-type soft pneumatic actuators: fabrication, modelling, and control," *Virtual Phys. Prototyp.*, vol. 15, no. 4, pp. 373–402, Oct. 2020, doi: 10.1080/17452759.2020.1795209.

[59]   H. Watschke, K. Hilbig, and T. Vietor, "Design and characterization of electrically conductive structures additively manufactured by material extrusion," *Appl. Sci.*, vol. 9, no. 4, pp. 1–25, 2019, doi: 10.3390/app9040779.

[60]   T. Chen and K. Shea, "An Autonomous Programmable Actuator and Shape Reconfigurable Structures Using Bistability and Shape Memory Polymers," *3D Print. Addit. Manuf.*, vol. 5, no. 2, pp. 91–101, May 2018, doi: 10.1089/3dp.2017.0118.

[61]   S. Bodkhe, L. Vigo, S. Zhu, O. Testoni, N. Aegerter, and P. Ermanni, "3D Printing To Integrate Actuators Into Composites," *Addit. Manuf.*, vol. 35, no. January, p. 101290, 2020, doi: 10.1016/j.addma.2020.101290.

[62]   M. A. H. Khondoker, N. Baheri, and D. Sameoto, "Tendon-Driven Functionally Gradient Soft Robotic Gripper 3D Printed with Intermixed Extrudate of Hard and Soft Thermoplastics," *3D Print. Addit. Manuf.*, vol. 6, no. 4, pp. 191–203, Aug. 2019, doi: 10.1089/3dp.2018.0102.

[63]   W. Wang and S. H. Ahn, "Shape Memory Alloy-Based Soft Gripper with Variable Stiffness for Compliant and Effective Grasping," *Soft Robot.*, vol. 4, no. 4, pp. 379–389, 2017, doi: 10.1089/soro.2016.0081.

[64]   R. Guo, L. Sheng, H. Y. Gong, and J. Liu, "Liquid metal spiral coil enabled soft electromagnetic actuator," *Sci. China Technol. Sci.*, vol. 61, no. 4, pp. 516–521, 2018, doi: 10.1007/s11431-017-9063-2.

[65]   N. El-Atab *et al.*, "Soft Actuators for Soft Robotic Applications: A Review," *Adv. Intell. Syst.*, vol. 2, no. 10, p. 2000128, 2020, doi: 10.1002/aisy.202000128.

[66]   H. Peng, F. Guimbretière, J. McCann, and S. E. Hudson, "A 3D printer for interactive electromagnetic devices," *UIST 2016 - Proc. 29th Annu. Symp. User Interface Softw. Technol.*, no. October, pp. 553–562, 2016, doi: 10.1145/2984511.2984523.

[67]   W. Wang, H. Rodrigue, H. Il Kim, M. W. Han, and S. H. Ahn, "Soft composite hinge actuator and application to compliant robotic gripper," *Compos. Part B Eng.*, vol. 98, pp. 397–405, 2016, doi: 10.1016/j.compositesb.2016.05.030.

[68]   G. Stano, A. Pavone, and G. Percoco, "3D Printing of Shape Memory Polymers: Embedding Nichrome-Wires to Enhance Their Performance BT - Selected Topics in Manufacturing: Emerging Trends from the Perspective of

AITeM's Young Researchers," L. Carrino, L. M. Galantucci, and L. Settineri, Eds., Cham: Springer Nature Switzerland, 2024, pp. 3–18. doi: 10.1007/978-3-031-41163-2_1.

[69] M. Mehrpouya, H. Vahabi, S. Janbaz, A. Darafsheh, T. R. Mazur, and S. Ramakrishna, "4D printing of shape memory polylactic acid (PLA)," *Polymer (Guildf).*, vol. 230, no. July, p. 124080, 2021, doi: 10.1016/j.polymer.2021.124080.

[70] Q. Ji, X. V. Wang, L. Wang, and L. Feng, "Online reinforcement learning for the shape morphing adaptive control of 4D printed shape memory polymer," *Control Eng. Pract.*, vol. 126, no. June, p. 105257, 2022, doi: 10.1016/j.conengprac.2022.105257.

[71] S. Suethao, T. Prasopdee, K. Buaksuntear, D. U. Shah, and W. Smitthipong, "Recent Developments in Shape Memory Elastomers for Biotechnology Applications," *Polymers (Basel).*, vol. 14, no. 16, 2022, doi: 10.3390/polym14163276.

[72] A. Koualiarella *et al.*, "Tuning of shape memory polymer properties by controlling 3D printing strategy," *CIRP Ann.*, vol. 69, no. 1, pp. 213–216, 2020, doi: 10.1016/j.cirp.2020.04.070.

[73] S. Valvez, P. N. B. Reis, L. Susmel, and F. Berto, "Fused filament fabrication-4d-printed shape memory polymers: A review," *Polymers (Basel).*, vol. 13, no. 5, pp. 1–25, 2021, doi: 10.3390/polym13050701.

[74] A. Leonés, A. Sonseca, D. López, S. Fiori, and L. Peponi, "Shape memory effect on electrospun PLA-based fibers tailoring their thermal response," *Eur. Polym. J.*, vol. 117, no. May, pp. 217–226, 2019, doi: 10.1016/j.eurpolymj.2019.05.014.

[75] L. Du *et al.*, "From a body temperature-triggered reversible shape-memory material to high-sensitive bionic soft actuators," *Appl. Mater. Today*, vol. 18, p. 100463, 2020, doi: 10.1016/j.apmt.2019.100463.

[76] S. Pandini *et al.*, "Two-way reversible shape memory behaviour of crosslinked poly(ε-caprolactone)," *Polymer (Guildf).*, vol. 53, no. 9, pp. 1915–1924, 2012, doi: 10.1016/j.polymer.2012.02.053.

[77] Y. Bai, X. Zhang, Q. Wang, and T. Wang, "A tough shape memory polymer with triple-shape memory and two-way shape memory properties," *J. Mater. Chem. A*, vol. 2, no. 13, pp. 4771–4778, 2014, doi: 10.1039/C3TA15117D.

[78] S. K. Melly, L. Liu, Y. Liu, and J. Leng, "Active composites based on shape memory polymers: overview, fabrication methods, applications, and future prospects," *J. Mater. Sci.*, vol. 55, no. 25, pp. 10975–11051, 2020, doi: 10.1007/s10853-020-04761-w.

[79] K. Takashima, R. Miyazaki, and T. Mukai, "Surface Shape Changeable Tactile Sensor Using Shape-Memory Polymer," *2021 60th Annu. Conf. Soc. Instrum. Control Eng. Japan, SICE 2021*, pp. 1169–1174, 2021.

[80] S. Nam and E. Pei, "The influence of shape changing behaviors from 4D printing through material extrusion print patterns and infill densities," *Materials (Basel).*, vol. 13, no. 17, 2020, doi: 10.3390/MA13173754.

[81] X. Huang, M. Panahi-Sarmad, K. Dong, R. Li, T. Chen, and X. Xiao, "Tracing evolutions in electro-activated shape memory polymer composites with 4D printing strategies: A systematic review," *Compos. Part A Appl. Sci. Manuf.*, vol. 147, no. April, p. 106444, 2021, doi: 10.1016/j.compositesa.2021.106444.

[82] F. Cesarano, M. Maurizi, C. Gao, F. Berto, F. Penta, and C. Bertolin, "ScienceDirect Structural ScienceDirect ScienceDirect Preliminary optimization of shape memory polymers geometric Preliminary optimization shape memory geometric parameters to enhance of the thermal loads ' polymers activation range parameters loads ' acti," *Procedia Struct. Integr.*, vol. 42, no. 2019, pp. 1282–1290, 2022, doi: 10.1016/j.prostr.2022.12.163.

[83] G. Ehrmann and A. Ehrmann, "Investigation of the shape-memory properties of 3D printed pla structures with different infills," *Polymers (Basel).*, vol. 13, no. 1, pp. 1–11, 2021, doi: 10.3390/polym13010164.

[84] N. Roudbarian, M. Baniasadi, P. Nayyeri, M. Ansari, R. Hedayati, and M. Baghani, "Enhancing shape memory properties of multi-layered and multi-material polymer composites in 4D printing," *Smart Mater. Struct.*, vol. 30, no. 10, 2021, doi: 10.1088/1361-665X/ac1b3b.

[85] Y. Yang, Y. Chen, Y. Wei, and Y. Li, "3D printing of shape memory polymer for functional part fabrication," *Int. J. Adv. Manuf. Technol.*, vol. 84, no. 9–12, pp. 2079–2095, 2016, doi: 10.1007/s00170-015-7843-2.

[86] Y. Mao, K. Yu, M. S. Isakov, J. Wu, M. L. Dunn, and H. Jerry Qi, "Sequential Self-Folding Structures by 3D Printed Digital Shape Memory Polymers," *Sci. Rep.*, vol. 5, pp. 1–12, 2015, doi: 10.1038/srep13616.

[87] S. Yamamura and E. Iwase, "Hybrid hinge structure with elastic hinge on self-folding of 4D printing using a fused deposition modeling 3D printer," *Mater. Des.*, vol. 203, p. 109605, 2021, doi: 10.1016/j.matdes.2021.109605.

[88] M. Y. Khalid, Z. U. Arif, A. Tariq, M. Hossain, K. Ahmed Khan, and R. Umer, "3D printing of magneto-active smart materials for advanced actuators and soft robotics applications," *Eur. Polym. J.*, vol. 205, no. January, p. 112718, 2024, doi: 10.1016/j.eurpolymj.2023.112718.

[89] T. N. Do, H. Phan, T. Q. Nguyen, and Y. Visell, "Miniature Soft Electromagnetic Actuators for Robotic Applications," *Adv. Funct. Mater.*, vol. 28, no. 18, pp. 1–11, 2018, doi: 10.1002/adfm.201800244.

[90] N. Kohls, B. Dias, Y. Mensah, B. P. Ruddy, and Y. C. Mazumdar, "Compliant Electromagnetic Actuator Architecture for Soft Robotics," *Proc. - IEEE Int. Conf. Robot. Autom.*, pp. 9042–9049, 2020, doi: 10.1109/ICRA40945.2020.9197442.

[91] G. Mao *et al.*, "Soft electromagnetic actuators," *Sci. Adv.*, vol. 6, no. 26, 2020, doi: 10.1126/sciadv.abc0251.

[92] H. Tiismus, A. Kallaste, T. Vaimann, and A. Rassõlkin, "State of the art of additively manufactured electromagnetic materials for topology optimized electrical machines," *Addit. Manuf.*, vol. 55, no. March, 2022, doi: 10.1016/j.addma.2022.102778.

[93] M. Saari, B. Cox, E. Richer, P. S. Krueger, and A. L. Cohen, "Fiber Encapsulation Additive Manufacturing: An Enabling Technology for 3D Printing of Electromechanical Devices and Robotic Components," *3D Print. Addit. Manuf.*, vol. 2, no. 1, pp. 32–39, Mar. 2015, doi: 10.1089/3dp.2015.0003.

[94] C. Kim, C. Sullivan, A. Hillstrom, and R. Wicker, "Intermittent Embedding of Wire into 3D Prints for Wireless Power Transfer," *Int. J. Precis. Eng. Manuf.*, vol. 22, no. 5, pp. 919–931, 2021, doi: 10.1007/s12541-021-00508-y.

[95] M. Saari, B. Xia, B. Cox, P. S. Krueger, A. L. Cohen, and E. Richer, "Fabrication and Analysis of a Composite 3D Printed Capacitive Force Sensor," *3D Print. Addit. Manuf.*, vol. 3, no. 3, pp. 136–141, Sep. 2016, doi: 10.1089/3dp.2016.0021.

[96] A. Hamidi and Y. Tadesse, "Single step 3D printing of bioinspired structures via metal reinforced thermoplastic and highly stretchable elastomer," *Compos. Struct.*, vol. 210, no. March 2018, pp. 250–261, 2019, doi: 10.1016/j.compstruct.2018.11.019.

[97] Z. Wang and D. E. Smith, "Finite element modelling of fully-coupled flow/fiber-orientation effects in polymer composite deposition additive manufacturing nozzle-extrudate flow," *Compos. Part B Eng.*, vol. 219, p. 108811, 2021, doi: https://doi.org/10.1016/j.compositesb.2021.108811.

[98] Z. Wang, D. E. Smith, and D. A. Jack, "A statistical homogenization approach for incorporating fiber aspect ratio distribution in large area polymer composite deposition additive manufacturing property predictions," *Addit. Manuf.*, vol. 43, p. 102006, 2021, doi: https://doi.org/10.1016/j.addma.2021.102006.

[99] A. P. Taylor, C. V. Cuervo, D. P. Arnold, S. Member, L. F. Velásquez-garcía, and S. Member, "Fully 3D-Printed

, Monolithic , Mini Magnetic Actuators for Low-Cost , Compact Systems," vol. 28, no. 3, pp. 481–493, 2019, doi: 10.1109/JMEMS.2019.2910215.

[100] G. Stano, A. Di, A. Lanzolla, and G. Percoco, "Additive manufacturing and characterization of a load cell with embedded strain gauges," *Precis. Eng.*, vol. 62, no. November 2019, pp. 113–120, 2020, doi: 10.1016/j.precisioneng.2019.11.019.

[101] K. Kim, J. Park, J. Suh, M. Kim, Y. Jeong, and I. Park, "Sensors and Actuators A : Physical 3D printing of multiaxial force sensors using carbon nanotube (CNT)/ thermoplastic polyurethane (TPU) filaments," *Sensors Actuators A. Phys.*, vol. 263, pp. 493–500, 2017, doi: 10.1016/j.sna.2017.07.020.

[102] L. Yeong *et al.*, "3D Printed Metamaterial Capacitive Sensing Array for Universal Jamming Gripper and Human Joint Wearables," vol. 2001082, pp. 1–9, 2021, doi: 10.1002/adem.202001082.

[103] M. Boltez, "Design principles for a single-process 3d-printed accelerometer – theory and experiment," vol. 152, 2021, doi: 10.1016/j.ymssp.2020.107475.

[104] S. Lathers, M. Mousa, and J. La Belle, "Additive Manufacturing Fused Filament Fabrication Three-Dimensional Printed Pressure Sensor for Prosthetics with Low Elastic Modulus and High Filler Ratio Filament Composites," *3D Print. Addit. Manuf.*, vol. 4, no. 1, pp. 30–40, Mar. 2017, doi: 10.1089/3dp.2016.0051.

[105] B. M. Kilbourne and J. R. Hutchinson, "Morphological diversification of biomechanical traits: Mustelid locomotor specializations and the macroevolution of long bone cross-sectional morphology," *BMC Evol. Biol.*, vol. 19, no. 1, pp. 1–16, 2019, doi: 10.1186/s12862-019-1349-8.

[106] A. Dey and N. Yodo, "A systematic survey of FDM process parameter optimization and their influence on part characteristics," *J. Manuf. Mater. Process.*, vol. 3, no. 3, 2019, doi: 10.3390/jmmp3030064.

[107] D. Dairabayeva, A. Perveen, and D. Talamona, "Investigation on the mechanical performance of mono-material vs multi-material interface geometries using fused filament fabrication," *Rapid Prototyp. J.*, vol. 29, no. 11, pp. 40–52, 2022, doi: 10.1108/RPJ-07-2022-0221.

[108] G. Stano, S. M. A. I. Ovy, G. Percoco, R. Zhang, H. Lu, and Y. Tadesse, "Additive Manufacturing for Bioinspired Structures: Experimental Study to Improve the Multimaterial Adhesion Between Soft and Stiff Materials," *3D Print. Addit. Manuf.*, Jan. 2023, doi: 10.1089/3dp.2022.0186.

[109] M. Zeraatkar, M. D. De Tullio, and G. Percoco, "Fused filament fabrication (FFF) for manufacturing of microfluidic micromixers: An experimental study on the effect of process variables in printed microfluidic micromixers," *Micromachines*, vol. 12, no. 8, 2021, doi: 10.3390/mi12080858.

[110] M. Zeraatkar, M. D. de Tullio, A. Pricci, F. Pignatelli, and G. Percoco, "Exploiting limitations of fused deposition modeling to enhance mixing in 3D printed microfluidic devices," *Rapid Prototyp. J.*, vol. 27, no. 10, pp. 1850–1859, Jan. 2021, doi: 10.1108/RPJ-03-2021-0051.

[111] G. Stano, A. Di Nisio, A. M. Lanzolla, M. Ragolia, and G. Percoco, "Fused filament fabrication of commercial conductive filaments: experimental study on the process parameters aimed at the minimization, repeatability and thermal characterization of electrical resistance," *Int. J. Adv. Manuf. Technol.*, vol. 111, no. 9–10, pp. 2971–2986, 2020, doi: 10.1007/s00170-020-06318-2.

[112] A. M. Soomro *et al.*, "Flexible Fluidic-Type Strain Sensors for Wearable and Robotic Applications Fabricated with Novel Conductive Liquids: A Review," *Electron.*, vol. 11, no. 18, 2022, doi: 10.3390/electronics11182903.

[113] A. M. Soomro *et al.*, "Fully 3D printed multi-material soft bio-inspired frog for underwater synchronous swimming," *Int. J. Mech. Sci.*, vol. 210, p. 106725, 2021, doi: https://doi.org/10.1016/j.ijmecsci.2021.106725.

[114] K. Lussenburg, A. Sakes, and P. Breedveld, "Design of non-assembly mechanisms: A state-of-the-art review,"

Addit. Manuf., vol. 39, p. 101846, 2021, doi: https://doi.org/10.1016/j.addma.2021.101846.

[115]   M. Chen, A. Sinha, K. Hu, and M. I. Shah, "Impact of technological innovation on energy efficiency in industry 4.0 era: Moderation of shadow economy in sustainable development," *Technol. Forecast. Soc. Change*, vol. 164, p. 120521, 2021, doi: https://doi.org/10.1016/j.techfore.2020.120521.

[116]   J. Gardan, "Smart materials in additive manufacturing: state of the art and trends," *Virtual Phys. Prototyp.*, vol. 14, no. 1, pp. 1–18, 2019, doi: 10.1080/17452759.2018.1518016.

[117]   J. Oh and J. Bae, "A direct ink writing based fabric-embedded soft sensor for improved durability and sewability," *Smart Mater. Struct.*, vol. 31, no. 6, p. 65020, 2022, doi: 10.1088/1361-665X/ac6d31.

[118]   "Adv Funct Materials - 2023 - Ansari - 3D Printing of Small-Scale Soft Robots with Programmable Magnetization.pdf."

[119]   G. Stano, A. Pricci, A. Pavone, and G. Percoco, "Electromagnetic assistance enables 3D printing of silicone-based thin-walled bioinspired soft robots," *Addit. Manuf.*, vol. 81, no. November 2023, p. 104028, 2024, doi: 10.1016/j.addma.2024.104028.

[120]   F. B. Coulter and A. Ianakiev, "4D Printing Inflatable Silicone Structures," *3D Print. Addit. Manuf.*, vol. 2, no. 3, pp. 140–144, Sep. 2015, doi: 10.1089/3dp.2015.0017.

[121]   "Adv Materials Technologies - 2023 - Mohammadi - 3D-Printed Phase-Change Artificial Muscles with Autonomous Vibration.pdf."

[122]   V. S. Joseph *et al.*, "Silicone/epoxy hybrid resins with tunable mechanical and interfacial properties for additive manufacture of soft robots," *Appl. Mater. Today*, vol. 22, p. 100979, 2021, doi: https://doi.org/10.1016/j.apmt.2021.100979.

[123]   S. M. A. I. Ovy, G. Stano, G. Percoco, M. Cianchetti, and Y. Tadesse, "Inexpensive monolithic additive manufacturing of silicone structures for bio-inspired soft robotic systems," *Eng. Res. Express*, 2023, doi: 10.1088/2631-8695/acb587.

[124]   E. Luis *et al.*, "Silicone 3D Printing: Process Optimization, Product Biocompatibility, and Reliability of Silicone Meniscus Implants," *3D Print. Addit. Manuf.*, vol. 6, no. 6, pp. 319–332, Dec. 2019, doi: 10.1089/3dp.2018.0226.

[125]   A. Zolfagharian *et al.*, "Silicon-based soft parallel robots 4D printing and multiphysics analysis," *Smart Mater. Struct.*, vol. 31, no. 11, p. 115030, 2022, doi: 10.1088/1361-665X/ac976c.

[126]   A. Hamidi and Y. Tadesse, "3D printing of very soft elastomer and sacrificial carbohydrate glass/elastomer structures for robotic applications," *Mater. Des.*, vol. 187, p. 108324, 2020, doi: https://doi.org/10.1016/j.matdes.2019.108324.

[127]   O. D. Yirmibeşoğlu, T. Oshiro, G. Olson, C. Palmer, and Y. Mengüç, "Evaluation of 3D printed soft robots in radiation environments and comparison with molded counterparts," *Front. Robot. AI*, vol. 6, no. MAY, pp. 1–14, 2019, doi: 10.3389/frobt.2019.00040.

[128]   O. D. Yirmibesoglu *et al.*, "Direct 3D printing of silicone elastomer soft robots and their performance comparison with molded counterparts," in *2018 IEEE International Conference on Soft Robotics (RoboSoft)*, 2018, pp. 295–302. doi: 10.1109/ROBOSOFT.2018.8404935.

[129]   S. Walker *et al.*, "Zero-Support 3D Printing of Thermoset Silicone Via Simultaneous Control of Both Reaction Kinetics and Transient Rheology," *3D Print. Addit. Manuf.*, vol. 6, no. 3, pp. 139–147, Apr. 2019, doi: 10.1089/3dp.2018.0117.

[130]   J. Plott and A. Shih, "The extrusion-based additive manufacturing of moisture-cured silicone elastomer with minimal void for pneumatic actuators," *Addit. Manuf.*, vol. 17, pp. 1–14, 2017, doi:

https://doi.org/10.1016/j.addma.2017.06.009.

[131] D. A. Porter, A. L. Cohen, P. S. Krueger, and D. Y. Son, "Additive Manufacturing with Ultraviolet Curable Silicones Containing Carbon Black," *3D Print. Addit. Manuf.*, vol. 5, no. 1, pp. 73–86, Mar. 2018, doi: 10.1089/3dp.2017.0019.

[132] S. Zheng, M. Zlatin, P. R. Selvaganapathy, and M. A. Brook, "Multiple modulus silicone elastomers using 3D extrusion printing of low viscosity inks," *Addit. Manuf.*, vol. 24, pp. 86–92, 2018, doi: https://doi.org/10.1016/j.addma.2018.09.011.

[133] M. Schaffner, J. A. Faber, L. Pianegonda, P. A. Rühs, F. Coulter, and A. R. Studart, "3D printing of robotic soft actuators with programmable bioinspired architectures," *Nat. Commun.*, vol. 9, no. 1, p. 878, 2018, doi: 10.1038/s41467-018-03216-w.

[134] C. Marquez *et al.*, "Direct Ink-Write Printing of Ceramic Clay with an Embedded Wireless Temperature and Relative Humidity Sensor," *Sensors*, vol. 23, no. 6. 2023. doi: 10.3390/s23063352.

[135] D. Espalin, D. W. Muse, E. MacDonald, and R. B. Wicker, "3D Printing multifunctionality: structures with electronics," *Int. J. Adv. Manuf. Technol.*, vol. 72, no. 5, pp. 963–978, 2014, doi: 10.1007/s00170-014-5717-7.

[136] E. Yarali *et al.*, "Magneto-/ electro-responsive polymers toward manufacturing, characterization, and biomedical/ soft robotic applications," *Appl. Mater. Today*, vol. 26, p. 101306, 2022, doi: https://doi.org/10.1016/j.apmt.2021.101306.

[137] X. Peng *et al.*, "Integrating digital light processing with direct ink writing for hybrid 3D printing of functional structures and devices," *Addit. Manuf.*, vol. 40, p. 101911, 2021, doi: https://doi.org/10.1016/j.addma.2021.101911.

[138] M. Bodaghi, R. Noroozi, A. Zolfagharian, M. Fotouhi, and S. Norouzi, "4D printing self-morphing structures," *Materials (Basel).*, vol. 12, no. 8, 2019, doi: 10.3390/ma12081353.

[139] A. Zolfagharian, A. Kaynak, S. Y. Khoo, and A. Kouzani, "Pattern-driven 4D printing," *Sensors Actuators A Phys.*, vol. 274, pp. 231–243, 2018, doi: https://doi.org/10.1016/j.sna.2018.03.034.

[140] A. Kania, K. Berent, T. Mazur, and M. Sikora, "3D printed composites with uniform distribution of Fe3O4 nanoparticles and magnetic shape anisotropy," *Addit. Manuf.*, vol. 46, p. 102149, 2021, doi: https://doi.org/10.1016/j.addma.2021.102149.

[141] S. Roh *et al.*, "3D-Printed Silicone Soft Architectures with Programmed Magneto-Capillary Reconfiguration," *Adv. Mater. Technol.*, vol. 4, no. 4, p. 1800528, Apr. 2019, doi: https://doi.org/10.1002/admt.201800528.

[142] Y. Kim, H. Yuk, R. Zhao, S. A. Chester, and X. Zhao, "Printing ferromagnetic domains for untethered fast-transforming soft materials," *Nature*, vol. 558, no. 7709, pp. 274–279, 2018, doi: 10.1038/s41586-018-0185-0.

[143] J. Stieghorst and T. Doll, "Rheological behavior of PDMS silicone rubber for 3D printing of medical implants," *Addit. Manuf.*, vol. 24, pp. 217–223, 2018, doi: https://doi.org/10.1016/j.addma.2018.10.004.

[144] Y. Tu, A. Hassan, A. Siadat, and G. Yang, "Analytical modeling of deposited filaments for high viscosity material-based piston-driven direct ink writing," *Int. J. Adv. Manuf. Technol.*, vol. 123, no. 9, pp. 3387–3398, 2022, doi: 10.1007/s00170-022-10511-w.

[145] D. Ma, X. Tian, J. Han, and L. Xia, "Modeling for silicone foam material extrusion with liquid rope coiling," *Int. J. Mech. Sci.*, vol. 249, p. 108234, 2023, doi: https://doi.org/10.1016/j.ijmecsci.2023.108234.

[146] A. Pricci, M. D. de Tullio, and G. Percoco, "Semi-analytical models for non-Newtonian fluids in tapered and cylindrical ducts, applied to the extrusion-based additive manufacturing," *Mater. Des.*, vol. 223, p. 111168, 2022, doi: https://doi.org/10.1016/j.matdes.2022.111168.

[147] A. Colpani, A. Fiorentino, and E. Ceretti, "Feasibility analysis and characterization of an extrusion-based AM process for a two-component and biocompatible silicone," *J. Manuf. Process.*, vol. 49, pp. 116–125, 2020, doi: https://doi.org/10.1016/j.jmapro.2019.11.017.

[148] J. Plott, X. Tian, and A. J. Shih, "Voids and tensile properties in extrusion-based additive manufacturing of moisture-cured silicone elastomer," *Addit. Manuf.*, vol. 22, pp. 606–617, 2018, doi: https://doi.org/10.1016/j.addma.2018.06.010.

[149] S. Walker, E. Lingle, N. Troxler, T. Wallin, and K. Healy, "Predicting interfacial layer adhesion strength in 3D printable silicone," vol. 47, no. September, 2021, doi: 10.1016/j.addma.2021.102320.

[150] G. Percoco, L. Arleo, G. Stano, and F. Bottiglione, "Analytical model to predict the extrusion force as a function of the layer height, in extrusion based 3D printing," *Addit. Manuf.*, vol. 38, no. December 2020, p. 101791, 2021, doi: 10.1016/j.addma.2020.101791.

[151] J. Plott, X. Tian, and A. Shih, "Measurement and Modeling of Forces in Extrusion-Based Additive Manufacturing of Flexible Silicone Elastomer With Thin Wall Structures," *J. Manuf. Sci. Eng.*, vol. 140, no. 9, Jun. 2018, doi: 10.1115/1.4040350.

[152] S. Terryn, E. Roels, J. Brancart, G. Van Assche, and B. Vanderborght, "Self-healing and high interfacial strength in multi-material soft pneumatic robots via reversible diels-alder bonds," *Actuators*, vol. 9, no. 2, 2020, doi: 10.3390/ACT9020034.

[153] Y. Ji, C. Luan, X. Yao, J. Fu, and Y. He, "Recent Progress in 3D Printing of Smart Structures: Classification, Challenges, and Trends," *Adv. Intell. Syst.*, vol. 2000271, p. 2000271, 2021, doi: 10.1002/aisy.202000271.

[154] B. Li, P. F. Cao, T. Saito, and A. P. Sokolov, "Intrinsically Self-Healing Polymers: From Mechanistic Insight to Current Challenges," *Chem. Rev.*, vol. 123, no. 2, pp. 701–735, 2023, doi: 10.1021/acs.chemrev.2c00575.

[155] S. R. White *et al.*, "Autonomic Healing of Polymer Composites," *Nature*, vol. 409, no. February, p. 794, 2001, [Online]. Available: https://www.nature.com/articles/35057232.pdf

[156] I. Roppolo, M. Caprioli, C. F. Pirri, and S. Magdassi, "3D Printing of Self-Healing Materials," *Adv. Mater.*, 2023, doi: 10.1002/adma.202305537.

[157] Y. Yang, B. Zhu, D. Yin, and J. Wei, "Flexible self-healing nanocomposites for recoverable motion sensor," pp. 1–9, 2015, doi: 10.1016/j.nanoen.2015.07.023.

[158] H. Tu, M. Zhou, Y. Gu, and Y. Gu, "Conductive, self-healing, and repeatable graphene/carbon nanotube/polyurethane flexible sensor based on Diels-Alder chemothermal drive," *Compos. Sci. Technol.*, vol. 225, no. November 2021, p. 109476, 2022, doi: 10.1016/j.compscitech.2022.109476.

[159] E. Roels *et al.*, "Self-healing sensorized soft robots," *Mater. Today Electron.*, vol. 1, no. June, p. 100003, 2022, doi: 10.1016/j.mtelec.2022.100003.

[160] K. Cerdan, J. Brancart, E. Roels, B. Vanderborght, and P. Van Puyvelde, "Humins Blending in Thermoreversible Diels–Alder Networks for Stiffness Tuning and Enhanced Healing Performance for Soft Robotics," *Polymers (Basel).*, vol. 14, no. 9, 2022, doi: 10.3390/polym14091657.

[161] S. Terryn, G. Mathijssen, J. Brancart, D. Lefeber, G. Van Assche, and B. Vanderborght, "Development of a self-healing soft pneumatic actuator: A first concept," *Bioinspiration and Biomimetics*, vol. 10, no. 4, 2015, doi: 10.1088/1748-3190/10/4/046007.

[162] X. Li, T. Zhang, B. Song, K. Yang, X. Hao, and J. Ma, "Polyurethane toughened covalent adaptive networks epoxy composite based on thermoreversible Diels-Alder reaction: Self-healable, shape memory, and recyclable," *J. Appl. Polym. Sci.*, vol. 141, no. 1, pp. 1–11, 2024, doi: 10.1002/app.54762.

[163] A. Safaei *et al.*, "Fast Self-Healing at Room Temperature in Diels–Alder Elastomers," *Polymers (Basel).*, vol. 15, no. 17, 2023, doi: 10.3390/polym15173527.

[164] S. Terryn, J. Brancart, E. Roels, G. Van Assche, and B. Vanderborght, "Room Temperature Self-Healing in Soft Pneumatic Robotics: Autonomous Self-Healing in a Diels-Alder Polymer Network," *IEEE Robot. Autom. Mag.*, vol. 27, no. 4, pp. 44–55, 2020, doi: 10.1109/MRA.2020.3024275.

[165] Y. Shan, Z. Li, T. Yu, X. Wang, K. Yang, and Y. Cui, "Self-healing strain sensor based on silicone elastomer for human motion detection," *Compos. Sci. Technol.*, vol. 218, no. November 2021, p. 109208, 2022, doi: 10.1016/j.compscitech.2021.109208.

[166] B. Vanderborght *et al.*, "Effect of Secondary Particles on Self-Healing and Electromechanical Properties of Polymer Composites Based on Carbon Black and a Diels − Alder Network," 2023, doi: 10.1021/acsapm.3c01043.

[167] R. Guo *et al.*, "Dynamic borate ester bond-based 3D printing fluorescence polysiloxane with self-healing, antimicrobial, and shape memory," *Chem. Eng. J.*, vol. 485, no. November 2023, p. 149850, 2024, doi: 10.1016/j.cej.2024.149850.

[168] E. Roels, S. Terryn, J. Brancart, R. Verhelle, G. Van Assche, and B. Vanderborght, "Additive Manufacturing for Self-Healing Soft Robots," *Soft Robot.*, vol. 7, no. 6, pp. 711–723, 2020, doi: 10.1089/soro.2019.0081.

[169] Z. Li *et al.*, "Self-Healing and shape memory reconfigurable Poly(urethane-urea-amide) elastomers containing multiple dynamic bonds for improving performance of 4D printout," *Chem. Eng. J.*, vol. 485, no. October 2023, p. 149933, 2024, doi: 10.1016/j.cej.2024.149933.

[170] S. Shaffer, K. Yang, J. Vargas, M. A. Di, and W. Voit, "On reducing anisotropy in 3D printed polymers via ionizing radiation," *Polymer (Guildf).*, vol. 55, no. 23, pp. 5969–5979, 2014, doi: 10.1016/j.polymer.2014.07.054.

[171] Y. Jia *et al.*, "Recent Progress on the 3D Printing of Dynamically Cross-Linked Polymers," *Adv. Funct. Mater.*, vol. 34, no. 2, pp. 1–35, 2024, doi: 10.1002/adfm.202307279.

[172] J. Wang, X. Lin, R. Wang, Y. Lu, and L. Zhang, "No Title," *Adv. Funct. Mater.*, no. 15, pp. 1–14, 2023, doi: 10.1002/adfm.202211579.

[173] K. Cerdan, C. Moya, P. Van Puyvelde, G. Bruylants, and J. Brancart, "Magnetic Self-Healing Composites : Synthesis and Applications," 2022.

[174] V. Nguyen-Van, H. Nguyen-Xuan, B. Panda, and P. Tran, "3D concrete printing modelling of thin-walled structures," *Structures*, vol. 39, no. March, pp. 496–511, 2022, doi: 10.1016/j.istruc.2022.03.049.

[175] S.-D. Wu and S. Hsu, "4D bioprintable self-healing hydrogel with shape memory and cryopreserving properties," *Biofabrication*, vol. 13, no. 4, p. 45029, 2021, doi: 10.1088/1758-5090/ac2789.

[176] S. Terryn *et al.*, "Structure-Property Relationships of Self-Healing Polymer Networks Based on Reversible Diels-Alder Chemistry," *Macromolecules*, vol. 55, no. 13, pp. 5497–5513, 2022, doi: 10.1021/acs.macromol.2c00434.

[177] M. A. S. R. Saadi *et al.*, "Direct Ink Writing : A 3D Printing Technology for Diverse Materials," vol. 2108855, pp. 1–57, 2022, doi: 10.1002/adma.202108855.

[178] Z. Guo, P. Yu, Y. Liu, and J. Zhao, "High-precision resistance strain sensors of multilayer composite structure via direct ink writing : Optimized layer flatness and interfacial strength," *Compos. Sci. Technol.*, vol. 201, no. September 2020, p. 108530, 2021, doi: 10.1016/j.compscitech.2020.108530.

[179] I. H. Abd Elzahra and M. H. Al-Sherrawi, "Enhancement of self-healing to mechanical properties of concrete," *IOP Conf. Ser. Mater. Sci. Eng.*, vol. 1117, no. 1, p. 12026, 2021, doi: 10.1088/1757-899X/1117/1/012026.

[180] T. Yuan, L. Zhang, T. Li, R. Tu, and H. A. Sodano, "3D Printing of a self-healing, high strength, and reprocessable thermoset," *Polym. Chem.*, vol. 11, no. 40, pp. 6441–6452, 2020, doi: 10.1039/d0py00819b.

[181] K. Yang *et al.*, "Diels–Alder Reversible Thermoset 3D Printing: Isotropic Thermoset Polymers via Fused Filament Fabrication," *Adv. Funct. Mater.*, vol. 27, no. 24, pp. 1–11, 2017, doi: 10.1002/adfm.201700318.

[182] K. M. M. Billah, J. L. Coronel, L. Chavez, Y. Lin, and D. Espalin, "Additive manufacturing of multimaterial and multifunctional structures via ultrasonic embedding of continuous carbon fiber," *Compos. Part C Open Access*, vol. 5, p. 100149, 2021, doi: https://doi.org/10.1016/j.jcomc.2021.100149.

[183] T. Košir and J. Slavič, "Single-process fused filament fabrication 3D-printed high-sensitivity dynamic piezoelectric sensor," *Addit. Manuf.*, vol. 49, p. 102482, 2022, doi: https://doi.org/10.1016/j.addma.2021.102482.

[184] N. Blaž, M. Kisić, L. Živanov, and M. Damnjanović, "Capacitive Sensor with Stretchable Membrane Fabricated by 3D Printing for Displacement Application," in *IEEE EUROCON 2019 -18th International Conference on Smart Technologies*, 2019, pp. 1–5. doi: 10.1109/EUROCON.2019.8861960.

[185] J. Oprel, G. Wolterink, J. Schilder, and G. Krijnen, "Novel 3D printed capacitive shear stress sensor," *Addit. Manuf.*, vol. 73, p. 103674, 2023, doi: https://doi.org/10.1016/j.addma.2023.103674.

[186] A. Dijkshoorn *et al.*, "Embedded sensing: integrating sensors in 3-D printed structures," *J. Sensors Sens. Syst.*, vol. 7, no. 1, pp. 169–181, 2018, doi: 10.5194/jsss-7-169-2018.

[187] M. Schouten, G. Wolterink, A. Dijkshoorn, D. Kosmas, S. Stramigioli, and G. Krijnen, "A Review of Extrusion-Based 3D Printing for the Fabrication of Electro- and Biomechanical Sensors," *IEEE Sens. J.*, vol. 21, no. 11, pp. 12900–12912, 2021, doi: 10.1109/JSEN.2020.3042436.

[188] J. D. Banks and A. Emami, "Carbon-Based Piezoresistive Polymer Nanocomposites by Extrusion Additive Manufacturing: Process, Material Design, and Current Progress," *3D Print. Addit. Manuf.*, vol. 11, no. 2, pp. e548–e571, Dec. 2022, doi: 10.1089/3dp.2022.0153.

[189] J. C. Tan and H. Y. Low, "Embedded electrical tracks in 3D printed objects by fused filament fabrication of highly conductive composites," *Addit. Manuf.*, vol. 23, pp. 294–302, 2018, doi: https://doi.org/10.1016/j.addma.2018.06.009.

[190] N. Lazarus, J. B. Tyler, J. A. Cardenas, B. Hanrahan, H. Tsang, and S. S. Bedair, "Direct electroless plating of conductive thermoplastics for selective metallization of 3D printed parts," *Addit. Manuf.*, vol. 55, p. 102793, 2022, doi: https://doi.org/10.1016/j.addma.2022.102793.

[191] J. C. Tan and H. Y. Low, "Multi-materials fused filament printing with embedded highly conductive suspended structures for compressive sensing," *Addit. Manuf.*, vol. 36, p. 101551, 2020, doi: https://doi.org/10.1016/j.addma.2020.101551.

[192] O. Urra Sanchez, H. Besharatloo, J. Yus, A. J. Sanchez-Herencia, and B. Ferrari, "Material thermal extrusion of conductive 3D electrodes using highly loaded graphene and graphite colloidal feedstock," *Addit. Manuf.*, vol. 72, p. 103643, 2023, doi: https://doi.org/10.1016/j.addma.2023.103643.

[193] T. Li, Z. Saadatnia, T. Chen, J. X. M. Chen, H. T. H. Shi, and H. E. Naguib, "Facile material extrusion of 3D wearable conductive-polymer micro-super-capacitors," *Addit. Manuf.*, vol. 74, p. 103714, 2023, doi: https://doi.org/10.1016/j.addma.2023.103714.

[194] A. Potnuru and Y. Tadesse, "Investigation of polylactide and carbon nanocomposite filament for 3D printing," *Prog. Addit. Manuf.*, vol. 4, no. 1, pp. 23–41, 2019, doi: 10.1007/s40964-018-0057-z.

[195] Z. Wang *et al.*, "A magnetic soft robot with multimodal sensing capability by multimaterial direct ink writing," *Addit. Manuf.*, vol. 61, no. June 2022, p. 103320, 2023, doi: 10.1016/j.addma.2022.103320.

[196] G. L. Goh, W. Y. Yeong, J. Altherr, J. Tan, and D. Campolo, "3D printing of soft sensors for soft gripper applications," *Mater. Today Proc.*, vol. 70, pp. 224–229, 2022, doi: https://doi.org/10.1016/j.matpr.2022.09.025.

[197] D. Singh, C. Tawk, R. Mutlu, E. Sariyildiz, V. Sencadas, and G. Alici, "A 3D Printed Soft Force Sensor for Soft Haptics," in *2020 3rd IEEE International Conference on Soft Robotics (RoboSoft)*, 2020, pp. 458–463. doi: 10.1109/RoboSoft48309.2020.9115991.

[198] P. Singh Matharu, Z. Wang, J. H. Costello, S. P. Colin, R. H. Baughman, and Y. T. Tadesse, "SoJel –A 3D printed jellyfish-like robot using soft materials for underwater applications," *Ocean Eng.*, vol. 279, p. 114427, 2023, doi: https://doi.org/10.1016/j.oceaneng.2023.114427.

[199] M. Maurizi *et al.*, "Dynamic Measurements Using FDM 3D-Printed Embedded Strain Sensors," *Sensors*, vol. 19, no. 12. 2019. doi: 10.3390/s19122661.

[200] M. Arh, J. Slavič, and M. Boltežar, "Experimental identification of the dynamic piezoresistivity of fused-filament-fabricated structures," *Addit. Manuf.*, vol. 36, p. 101493, 2020, doi: https://doi.org/10.1016/j.addma.2020.101493.

[201] A. Georgopoulou, B. Vanderborght, and F. Clemens, "Fabrication of a Soft Robotic Gripper With Integrated Strain Sensing Elements Using Multi-Material Additive Manufacturing," vol. 8, no. November, pp. 1–16, 2021, doi: 10.3389/frobt.2021.615991.

[202] S. Mousavi, D. Howard, F. Zhang, J. Leng, and C. H. Wang, "Direct 3D Printing of Highly Anisotropic, Flexible, Constriction-Resistive Sensors for Multidirectional Proprioception in Soft Robots," *ACS Appl. Mater. Interfaces*, vol. 12, no. 13, pp. 15631–15643, 2020, doi: 10.1021/acsami.9b21816.

[203] S. J. Leigh, R. J. Bradley, C. P. Purssell, D. R. Billson, and D. A. Hutchins, "A Simple, Low-Cost Conductive Composite Material for 3D Printing of Electronic Sensors," *PLoS One*, vol. 7, no. 11, p. e49365, Nov. 2012.

[204] Y. Yang, Y. Chen, Y. Li, Z. Wang, and Y. Li, "Novel Variable-Stiffness Robotic Fingers with Built-In Position Feedback," *Soft Robot.*, vol. 4, no. 4, pp. 338–352, Jun. 2017, doi: 10.1089/soro.2016.0060.

[205] Q. Ji, J. Jansson, M. Sjöberg, X. V. Wang, L. Wang, and L. Feng, "Design and calibration of 3D printed soft deformation sensors for soft actuator control," *Mechatronics*, vol. 92, p. 102980, 2023, doi: https://doi.org/10.1016/j.mechatronics.2023.102980.

[206] F. Grønborg, T. G. Zsurzsan, A. E. Daugaard, J. Spangenberg, and D. B. Pedersen, "Conductive compliant mechanisms: Geometric tuning of 3D printed flexural sensors," *Addit. Manuf. Lett.*, vol. 3, p. 100088, 2022, doi: 10.1016/j.addlet.2022.100088.

[207] B. Li, S. Zhang, L. Zhang, Y. Gao, and F. Xuan, "Strain sensing behavior of FDM 3D printed carbon black filled TPU with periodic configurations and flexible substrates," *J. Manuf. Process.*, vol. 74, no. June 2021, pp. 283–295, 2022, doi: 10.1016/j.jmapro.2021.12.020.

[208] R. Yu *et al.*, "Highly Sensitive Flexible Piezoresistive Sensor with 3D Conductive Network," *ACS Appl. Mater. Interfaces*, vol. 12, no. 31, pp. 35291–35299, Aug. 2020, doi: 10.1021/acsami.0c09552.

[209] S. N. Kwon, S. W. Kim, I. G. Kim, Y. K. Hong, and S. I. Na, "Direct 3D Printing of Graphene Nanoplatelet/Silver Nanoparticle-Based Nanocomposites for Multiaxial Piezoresistive Sensor Applications," *Adv. Mater. Technol.*, vol. 4, no. 2, pp. 1–9, 2019, doi: 10.1002/admt.201800500.

[210] K. Dembek, B. Podsiadły, and M. Słoma, "Influence of Process Parameters on the Resistivity of 3D Printed Electrically Conductive Structures," *Micromachines*, vol. 13, no. 8. 2022. doi: 10.3390/mi13081203.

[211] T. Barši Palmić, J. Slavič, and M. Boltežar, "Process Parameters for FFF 3D-Printed Conductors for Applications in Sensors," *Sensors*, vol. 20, no. 16. 2020. doi: 10.3390/s20164542.

[212] G. L. Goh *et al.*, "A 3D Printing-Enabled Artificially Innervated Smart Soft Gripper with Variable Joint Stiffness," *Adv. Mater. Technol.*, vol. 8, no. 24, p. 2301426, Dec. 2023, doi: https://doi.org/10.1002/admt.202301426.

[213] A. Pavone *et al.*, "Additive manufacturing of Diels-Alder self-healing polymers: Separate heating system to enhance mechanical, healing properties and assembly-free smart structures," *Addit. Manuf.*, vol. 95, no. November, 2024, doi: 10.1016/j.addma.2024.104535.

[214] T. J. Coogan and D. O. Kazmer, "Prediction of interlayer strength in material extrusion additive manufacturing," *Addit. Manuf.*, vol. 35, no. November 2019, p. 101368, 2020, doi: 10.1016/j.addma.2020.101368.

[215] S. Sharafi, M. H. Santare, J. Gerdes, and S. G. Advani, "A review of factors that influence the fracture toughness of extrusion-based additively manufactured polymer and polymer composites," *Addit. Manuf.*, vol. 38, p. 101830, 2021, doi: https://doi.org/10.1016/j.addma.2020.101830.

[216] X. Sun, M. Mazur, and C. T. Cheng, "A review of void reduction strategies in material extrusion-based additive manufacturing," *Addit. Manuf.*, vol. 67, no. February, p. 103463, 2023, doi: 10.1016/j.addma.2023.103463.

[217] Y. Tao *et al.*, "A review on voids of 3D printed parts by fused filament fabrication," *J. Mater. Res. Technol.*, vol. 15, pp. 4860–4879, 2021, doi: 10.1016/j.jmrt.2021.10.108.

[218] T. Xu, J. Zhang, M. Salehizadeh, O. Onaizah, and E. Diller, "Millimeter-scale flexible robots with programmable three-dimensional magnetization and motions," *Sci. Robot.*, vol. 4, no. 29, p. eaav4494, Apr. 2019, doi: 10.1126/scirobotics.aav4494.

[219] A. Pricci, S. M. Al Islam Ovy, G. Stano, G. Percoco, and Y. Tadesse, "Semi-analytical and numerical models to predict the extrusion force for silicone additive manufacturing, as a function of the process parameters," *Addit. Manuf. Lett.*, vol. 6, p. 100147, 2023, doi: https://doi.org/10.1016/j.addlet.2023.100147.

[220] "(Dario Lunni et al .2020)Plant-Inspired Soft Bistable Structures Based on Hygroscopic Electrospun Nanofibers.pdf."

[221] H. Lee *et al.*, "3D-printed programmable tensegrity for soft robotics," *Sci. Robot.*, vol. 5, no. 45, pp. 1–11, 2020, doi: 10.1126/SCIROBOTICS.AAY9024.

[222] L. Rossing, R. B. N. Scharff, B. Chömpff, C. C. L. Wang, and E. L. Doubrovski, "Bonding between silicones and thermoplastics using 3D printed mechanical interlocking," *Mater. Des.*, vol. 186, p. 108254, 2020, doi: https://doi.org/10.1016/j.matdes.2019.108254.

[223] R. Mutlu, G. Alici, M. in het Panhuis, and G. M. Spinks, "3D Printed Flexure Hinges for Soft Monolithic Prosthetic Fingers," *Soft Robot.*, vol. 3, no. 3, pp. 120–133, Sep. 2016, doi: 10.1089/soro.2016.0026.

[224] J. C. S. McCaw *et al.*, "Vibration-assisted printing of highly viscous food," *Addit. Manuf.*, vol. 56, p. 102851, 2022, doi: https://doi.org/10.1016/j.addma.2022.102851.

[225] T. J. Fleck, J. C. S. McCaw, S. F. Son, I. E. Gunduz, and J. F. Rhoads, "Characterizing the vibration-assisted printing of high viscosity clay material," *Addit. Manuf.*, vol. 47, p. 102256, 2021, doi: https://doi.org/10.1016/j.addma.2021.102256.

[226] H. Nassar, M. Ntagios, W. T. Navaraj, and R. Dahiva, "Multi-Material 3D Printed Bendable Smart Sensing Structures," in *2018 IEEE SENSORS*, 2018, pp. 1–4. doi: 10.1109/ICSENS.2018.8589625.

[227] K. H. Teng *et al.*, "Embedded Smart Antenna for Non-Destructive Testing and Evaluation (NDT&E) of Moisture Content and Deterioration in Concrete," *Sensors*, vol. 19, no. 3. 2019. doi: 10.3390/s19030547.

[228] T. J. Coogan and D. O. Kazmer, "Healing simulation for bond strength prediction of FDM," *Rapid Prototyp. J.*, vol. 23, no. 3, pp. 551–561, 2017, doi: 10.1108/RPJ-03-2016-0051.

[229] G. Stano, N. Sayah, D. E. Smith, and T. J. Fleck, "Effect of Process Parameters in Additively Manufactured Sensors prepared via Material Extrusion Processes: Correlation among Electrical, Mechanical and Microstructure Properties," *Addit. Manuf. Lett.*, vol. 9, no. March 2023, p. 100194, 2024, doi: 10.1016/j.addlet.2024.100194.

[230] A. Andreu, S. Kim, J. Dittus, M. Friedmann, J. Fleischer, and Y. J. Yoon, "Hybrid material extrusion 3D printing to strengthen interlayer adhesion through hot rolling," *Addit. Manuf.*, vol. 55, no. November 2021, pp. 1–9, 2022, doi: 10.1016/j.addma.2022.102773.

[231] M. Qasaimeh, D. Ravoori, A. Jain, and A. Adnan, "Modeling the Effect of In Situ Nozzle-Integrated Compression Rolling on the Void Reduction and Filaments-Filament Adhesion in Fused Filament Fabrication (FFF)," *Multiscale Sci. Eng.*, vol. 4, no. 1, pp. 37–54, 2022, doi: 10.1007/s42493-022-00073-0.

[232] J. F. Christ, N. Aliheidari, P. Pötschke, and A. Ameli, "Bidirectional and Stretchable Piezoresistive Sensors Enabled by Multimaterial 3D Printing of Carbon Nanotube/Thermoplastic Polyurethane Nanocomposites," *Polymers*, vol. 11, no. 1. 2019. doi: 10.3390/polym11010011.

[233] D. Xiang *et al.*, "Enhanced performance of 3D printed highly elastic strain sensors of carbon nanotube/thermoplastic polyurethane nanocomposites via non-covalent interactions," *Compos. Part B Eng.*, vol. 176, p. 107250, 2019, doi: https://doi.org/10.1016/j.compositesb.2019.107250.

[234] J. F. Christ, N. Aliheidari, A. Ameli, and P. Pötschke, "3D printed highly elastic strain sensors of multiwalled carbon nanotube/thermoplastic polyurethane nanocomposites," *Mater. Des.*, vol. 131, pp. 394–401, 2017, doi: https://doi.org/10.1016/j.matdes.2017.06.011.

[235] J. Diani, B. Fayolle, and P. Gilormini, "A review on the Mullins effect," *Eur. Polym. J.*, vol. 45, no. 3, pp. 601–612, 2009, doi: https://doi.org/10.1016/j.eurpolymj.2008.11.017.

[236] F. Daniel, N. H. Patoary, A. L. Moore, L. Weiss, and A. D. Radadia, "Temperature-dependent electrical resistance of conductive polylactic acid filament for fused deposition modeling," *Int. J. Adv. Manuf. Technol.*, vol. 99, no. 5, pp. 1215–1224, 2018, doi: 10.1007/s00170-018-2490-z.

[237] M. Mohiuddin and S. V Hoa, "Temperature dependent electrical conductivity of CNT–PEEK composites," *Compos. Sci. Technol.*, vol. 72, no. 1, pp. 21–27, 2011, doi: https://doi.org/10.1016/j.compscitech.2011.08.018.

[238] H. Gao, J. An, C. K. Chua, D. Bourell, C.-N. Kuo, and D. T. H. Tan, "3D printed optics and photonics: Processes, materials and applications," *Mater. Today*, vol. 69, pp. 107–132, 2023, doi: https://doi.org/10.1016/j.mattod.2023.06.019.

[239] L. Chow *et al.*, "3D Printing Auxetic Architectures for Hypertrophic Scar Therapy," *Macromol. Mater. Eng.*, vol. 307, no. 5, p. 2100866, May 2022, doi: https://doi.org/10.1002/mame.202100866.

[240] J. Zhang, G. Lu, and Z. You, "Large deformation and energy absorption of additively manufactured auxetic materials and structures: A review," *Compos. Part B Eng.*, vol. 201, p. 108340, 2020, doi: https://doi.org/10.1016/j.compositesb.2020.108340.

[241] R. Johnston and Z. Kazancı, "Analysis of additively manufactured (3D printed) dual-material auxetic structures under compression," *Addit. Manuf.*, vol. 38, p. 101783, 2021, doi: https://doi.org/10.1016/j.addma.2020.101783.

[242] K. Günaydın, C. Rea, and Z. Kazancı, "Energy absorption enhancement of additively manufactured hexagonal and re-entrant (auxetic) lattice structures by using multi-material reinforcements," *Addit. Manuf.*, vol. 59, p. 103076, 2022, doi: https://doi.org/10.1016/j.addma.2022.103076.

[243] F. Sahraeeazartamar *et al.*, "Effect of Secondary Particles on Self-Healing and Electromechanical Properties of Polymer Composites Based on Carbon Black and a Diels-Alder Network," *ACS Appl. Polym. Mater.*, vol. 5, no. 10, pp. 7813–7830, 2023, doi: 10.1021/acsapm.3c01043.

[244] E. Roels *et al.*, "Processing of Self-Healing Polymers for Soft Robotics," *Adv. Mater.*, vol. 34, no. 1, pp. 1–27, 2022, doi: 10.1002/adma.202104798.

[245] B. Zhang, S. H. Chung, S. Barker, D. Craig, R. J. Narayan, and J. Huang, "Direct ink writing of polycaprolactone

/ polyethylene oxide based 3D constructs," *Prog. Nat. Sci. Mater. Int.*, vol. 31, no. 2, pp. 180–191, 2021, doi: 10.1016/j.pnsc.2020.10.001.

[246] A. Andreu, H. Lee, J. Kang, and Y. J. Yoon, "Self-Healing Materials for 3D Printing," *Adv. Funct. Mater.*, vol. 2315046, pp. 1–25, 2024, doi: 10.1002/adfm.202315046.

[247] J. W. Long, B. Dunn, D. R. Rolison, and H. S. White, "Three-Dimensional Battery Architectures," *Chem. Rev.*, vol. 104, no. 10, pp. 4463–4492, Oct. 2004, doi: 10.1021/cr020740l.

[248] B. Trembacki, E. Duoss, G. Oxberry, M. Stadermann, and J. Murthy, "Mesoscale Electrochemical Performance Simulation of 3D Interpenetrating Lithium-Ion Battery Electrodes," *J. Electrochem. Soc.*, vol. 166, no. 6, pp. A923–A934, 2019, doi: 10.1149/2.0031906jes.

[249] A. Maurel *et al.*, "Considering lithium-ion battery 3D-printing via thermoplastic material extrusion and polymer powder bed fusion," *Addit. Manuf.*, vol. 37, no. July 2020, 2021, doi: 10.1016/j.addma.2020.101651.

[250] A. Maurel *et al.*, "Toward High Resolution 3D Printing of Shape-Conformable Batteries via Vat Photopolymerization: Review and Perspective," *IEEE Access*, vol. 9, pp. 140654–140666, 2021, doi: 10.1109/ACCESS.2021.3119533.

[251] A. Maurel *et al.*, "Overview on Lithium-Ion Battery 3D-Printing By Means of Material Extrusion," *ECS Meet. Abstr.*, vol. MA2020-02, no. 69, pp. 3690–3690, 2020, doi: 10.1149/ma2020-02693690mtgabs.

[252] H. Bikas, P. Stavropoulos, and G. Chryssolouris, "Additive manufacturing methods and modeling approaches: A critical review," *Int. J. Adv. Manuf. Technol.*, vol. 83, no. 1–4, pp. 389–405, 2016, doi: 10.1007/s00170-015-7576-2.

[253] M. P. Browne, E. Redondo, and M. Pumera, "3D Printing for Electrochemical Energy Applications," *Chem. Rev.*, vol. 120, no. 5, pp. 2783–2810, Mar. 2020, doi: 10.1021/acs.chemrev.9b00783.

[254] P. Chang, H. Mei, S. Zhou, K. G. Dassios, and L. Cheng, "3D printed electrochemical energy storage devices," *J. Mater. Chem. A*, vol. 7, no. 9, pp. 4230–4258, 2019, doi: 10.1039/C8TA11860D.

[255] M. Zhang, H. Mei, P. Chang, and L. Cheng, "3D printing of structured electrodes for rechargeable batteries," *J. Mater. Chem. A*, vol. 8, no. 21, pp. 10670–10694, 2020, doi: 10.1039/D0TA02099K.

[256] Y. Yang *et al.*, "Overview on the applications of three-dimensional printing for rechargeable lithium-ion batteries," *Appl. Energy*, vol. 257, p. 114002, 2020, doi: https://doi.org/10.1016/j.apenergy.2019.114002.

[257] V. Egorov, U. Gulzar, Y. Zhang, S. Breen, and C. O'Dwyer, "Evolution of 3D Printing Methods and Materials for Electrochemical Energy Storage," *Adv. Mater.*, vol. 32, no. 29, 2020, doi: 10.1002/adma.202000556.

[258] L. Zeng, P. Li, Y. Yao, B. Niu, S. Niu, and B. Xu, "Recent progresses of 3D printing technologies for structural energy storage devices," *Mater. Today Nano*, vol. 12, p. 100094, 2020, doi: https://doi.org/10.1016/j.mtnano.2020.100094.

[259] D. B. Ahn, S.-S. Lee, K.-H. Lee, J.-H. Kim, J.-W. Lee, and S.-Y. Lee, "Form factor-free, printed power sources," *Energy Storage Mater.*, vol. 29, pp. 92–112, 2020, doi: https://doi.org/10.1016/j.ensm.2020.04.007.

[260] L. E. Asp *et al.*, "A Structural Battery and its Multifunctional Performance," *Adv. Energy Sustain. Res.*, vol. 2, no. 3, p. 2000093, Mar. 2021, doi: https://doi.org/10.1002/aesr.202000093.

[261] H. Ragones *et al.*, "Towards smart free form-factor 3D printable batteries," *Sustain. Energy Fuels*, vol. 2, no. 7, pp. 1542–1549, 2018, doi: 10.1039/c8se00122g.

[262] A. Maurel *et al.*, "Three-Dimensional Printing of a LiFePO4/Graphite Battery Cell via Fused Deposition Modeling," *Sci. Rep.*, vol. 9, no. 1, pp. 1–14, 2019, doi: 10.1038/s41598-019-54518-y.

[263] S.-H. Kim, K.-H. Choi, S.-J. Cho, S. Choi, S. Park, and S.-Y. Lee, "Printable Solid-State Lithium-Ion Batteries:

A New Route toward Shape-Conformable Power Sources with Aesthetic Versatility for Flexible Electronics," *Nano Lett.*, vol. 15, no. 8, pp. 5168–5177, Aug. 2015, doi: 10.1021/acs.nanolett.5b01394.

[264] J. B. Goodenough and K.-S. Park, "The Li-Ion Rechargeable Battery: A Perspective," *J. Am. Chem. Soc.*, vol. 135, no. 4, pp. 1167–1176, Jan. 2013, doi: 10.1021/ja3091438.

[265] S. H. Park, G. Goodall, and W. S. Kim, "Perspective on 3D-designed micro-supercapacitors," *Mater. Des.*, vol. 193, p. 108797, 2020, doi: https://doi.org/10.1016/j.matdes.2020.108797.

[266] L. Chen, Y. He, Y. Yang, S. Niu, and H. Ren, "The research status and development trend of additive manufacturing technology," *Int. J. Adv. Manuf. Technol.*, vol. 89, no. 9–12, pp. 3651–3660, 2017, doi: 10.1007/s00170-016-9335-4.

[267] B. Berman, "3-D printing: The new industrial revolution," *Bus. Horiz.*, vol. 55, no. 2, pp. 155–162, 2012, doi: https://doi.org/10.1016/j.bushor.2011.11.003.

[268] W. Gao *et al.*, "The status, challenges, and future of additive manufacturing in engineering," *CAD Comput. Aided Des.*, vol. 69, pp. 65–89, 2015, doi: 10.1016/j.cad.2015.04.001.

[269] A. Maurel, "Thermoplastic composite filaments formulation and 3D-printing of a lithium-ion battery via fused deposition modeling To cite this version : HAL Id : tel-03626274 Thèse de Doctorat de l ' Université de Picardie Jules Verne," 2022.

[270] Y. Gao, B. Li, W. Wang, W. Xu, C. Zhou, and Z. Jin, "Watching and Safeguarding Your 3D Printer: Online Process Monitoring Against Cyber-Physical Attacks," *Proc. ACM Interact. Mob. Wearable Ubiquitous Technol.*, vol. 2, no. 3, 2018, doi: 10.1145/3264918.

[271] Y. Zhang, Y. Zhang, G. Liu, Y. Yang, M. Wu, and B. Pang, "Fresh properties of a novel 3D printing concrete ink," *Constr. Build. Mater.*, vol. 174, pp. 263–271, 2018, doi: https://doi.org/10.1016/j.conbuildmat.2018.04.115.

[272] A. Pasricha and R. Greeninger, "Exploration of 3D printing to create zero-waste sustainable fashion notions and jewelry," *Fash. Text.*, vol. 5, no. 1, 2018, doi: 10.1186/s40691-018-0152-2.

[273] S. J. Trenfield *et al.*, "Shaping the future: recent advances of 3D printing in drug delivery and healthcare," *Expert Opin. Drug Deliv.*, vol. 16, no. 10, pp. 1081–1094, Oct. 2019, doi: 10.1080/17425247.2019.1660318.

[274] B. Blakey-Milner *et al.*, "Metal additive manufacturing in aerospace: A review," *Mater. Des.*, vol. 209, p. 110008, 2021, doi: https://doi.org/10.1016/j.matdes.2021.110008.

[275] R. Jones *et al.*, "RepRap – the replicating rapid prototyper," *Robotica*, vol. 29, no. 1, pp. 177–191, 2011, doi: DOI: 10.1017/S026357471000069X.

[276] E. Malone and H. Lipson, "Fab@Home: the personal desktop fabricator kit," *Rapid Prototyp. J.*, vol. 13, no. 4, pp. 245–255, Jan. 2007, doi: 10.1108/13552540710776197.

[277] M. Cheng *et al.*, "Elevated-Temperature 3D Printing of Hybrid Solid-State Electrolyte for Li-Ion Batteries," *Adv. Mater.*, vol. 30, no. 39, p. 1800615, Sep. 2018, doi: https://doi.org/10.1002/adma.201800615.

[278] A. Maurel *et al.*, "Highly Loaded Graphite-Polylactic Acid Composite-Based Filaments for Lithium-Ion Battery Three-Dimensional Printing," *Chem. Mater.*, vol. 30, no. 21, pp. 7484–7493, 2018, doi: 10.1021/acs.chemmater.8b02062.

[279] C. Reyes *et al.*, "Three-Dimensional Printing of a Complete Lithium Ion Battery with Fused Filament Fabrication," *ACS Appl. Energy Mater.*, vol. 1, no. 10, pp. 5268–5279, 2018, doi: 10.1021/acsaem.8b00885.

[280] H. Ragones *et al.*, "On the Road to a Multi-Coaxial-Cable Battery: Development of a Novel 3D-Printed Composite Solid Electrolyte," *J. Electrochem. Soc.*, vol. 167, no. 7, p. 070503, 2020, doi: 10.1149/2.0032007jes.

[281] V. Gupta, F. Alam, P. Verma, A. M. Kannan, and S. Kumar, "Additive manufacturing enabled, microarchitected,

hierarchically porous polylactic-acid/lithium iron phosphate/carbon nanotube nanocomposite electrodes for high performance Li-Ion batteries," *J. Power Sources*, vol. 494, no. December 2019, p. 229625, 2021, doi: 10.1016/j.jpowsour.2021.229625.

[282] J. F. Valera-Jiménez, J. C. Pérez-Flores, M. Castro-García, and J. Canales-Vázquez, "Development of full ceramic electrodes for lithium-ion batteries via desktop-fused filament fabrication and further sintering," *Appl. Mater. Today*, vol. 25, 2021, doi: 10.1016/j.apmt.2021.101243.

[283] C. Iffelsberger, C. W. Jellett, and M. Pumera, "3D Printing Temperature Tailors Electrical and Electrochemical Properties through Changing Inner Distribution of Graphite/Polymer," *Small*, vol. 17, no. 24, 2021, doi: 10.1002/smll.202101233.

[284] A. Maurel, R. Russo, S. Grugeon, S. Panier, and L. Dupont, "Environmentally Friendly Lithium-Terephthalate/Polylactic Acid Composite Filament Formulation for Lithium-Ion Battery 3D-Printing via Fused Deposition Modeling," *ECS J. Solid State Sci. Technol.*, vol. 10, no. 3, p. 037004, 2021, doi: 10.1149/2162-8777/abedd4.

[285] A. Maurel *et al.*, "Poly(Ethylene Oxide)−LiTFSI Solid Polymer Electrolyte Filaments for Fused Deposition Modeling Three-Dimensional Printing," *J. Electrochem. Soc.*, vol. 167, no. 7, p. 070536, 2020, doi: 10.1149/1945-7111/ab7c38.

[286] D. J. Bischoff and M. E. Mackay, "Plasticization of a Diels-Alder Covalent Adaptable Network for Fused Filament Fabrication," *ACS Appl. Polym. Mater.*, 2023, doi: 10.1021/acsapm.3c03156.

[287] A. Maurel *et al.*, "Ag-Coated Cu/Polylactic Acid Composite Filament for Lithium and Sodium-Ion Battery Current Collector Three-Dimensional Printing via Thermoplastic Material Extrusion," *Front. Energy Res.*, vol. 9, no. April, pp. 1–10, 2021, doi: 10.3389/fenrg.2021.651041.

[288] C. Chen, J. Jiang, W. He, W. Lei, Q. Hao, and X. Zhang, "3D Printed High-Loading Lithium-Sulfur Battery Toward Wearable Energy Storage," *Adv. Funct. Mater.*, vol. 30, no. 10, pp. 1–7, 2020, doi: 10.1002/adfm.201909469.

[289] K. Sun, T.-S. Wei, B. Y. Ahn, J. Y. Seo, S. J. Dillon, and J. A. Lewis, "3D Printing of Interdigitated Li-Ion Microbattery Architectures," *Adv. Mater.*, vol. 25, no. 33, pp. 4539–4543, Sep. 2013, doi: https://doi.org/10.1002/adma.201301036.

[290] J. Li, X. Liang, F. Liou, and J. Park, "Macro-/Micro-Controlled 3D Lithium-Ion Batteries via Additive Manufacturing and Electric Field Processing," *Sci. Rep.*, vol. 8, no. 1, pp. 1–11, 2018, doi: 10.1038/s41598-018-20329-w.

[291] X. Gao *et al.*, "Toward a remarkable Li-S battery via 3D printing," *Nano Energy*, vol. 56, no. October 2018, pp. 595–603, 2019, doi: 10.1016/j.nanoen.2018.12.001.

[292] J. Li, M. C. Leu, R. Panat, and J. Park, "A hybrid three-dimensionally structured electrode for lithium-ion batteries via 3D printing," *Mater. Des.*, vol. 119, pp. 417–424, 2017, doi: 10.1016/j.matdes.2017.01.088.

[293] A. S. Almansour, A. J. Gorven, and M. Singh, "Additive manufacturing of novel 3D ceramic electrodes for high-power-density batteries," *Int. J. Appl. Ceram. Technol.*, vol. 19, no. 2, pp. 979–991, Mar. 2022, doi: https://doi.org/10.1111/ijac.13952.

[294] C. Liu *et al.*, "Comparative study on the electrochemical performance of LiFePO4 cathodes fabricated by low temperature 3D printing, direct ink writing and conventional roller coating process," *Ceram. Int.*, vol. 45, no. 11, pp. 14188–14197, 2019, doi: https://doi.org/10.1016/j.ceramint.2019.04.124.

[295] K. Fu *et al.*, "Graphene Oxide-Based Electrode Inks for 3D-Printed Lithium-Ion Batteries," *Adv. Mater.*, vol. 28,

no. 13, pp. 2587–2594, Apr. 2016, doi: https://doi.org/10.1002/adma.201505391.

[296] J. S. Park, T. Kim, and W. S. Kim, "Conductive Cellulose Composites with Low Percolation Threshold for 3D Printed Electronics," *Sci. Rep.*, vol. 7, no. 1, pp. 1–10, 2017, doi: 10.1038/s41598-017-03365-w.

[297] L. Zhou *et al.*, "3D-Printed Microelectrodes with a Developed Conductive Network and Hierarchical Pores toward High Areal Capacity for Microbatteries," *Adv. Mater. Technol.*, vol. 4, no. 2, p. 1800402, Feb. 2019, doi: https://doi.org/10.1002/admt.201800402.

[298] I. Ben-Barak, D. Schneier, Y. Kamir, M. Goor, D. Golodnitsky, and E. Peled, "Drop-on-demand 3D-printed silicon-based anodes for lithium-ion batteries," *J. Solid State Electrochem.*, vol. 26, no. 1, pp. 183–193, 2022, doi: 10.1007/s10008-021-05056-z.

[299] C. Liu *et al.*, "High mass loading ultrathick porous Li4Ti5O12 electrodes with improved areal capacity fabricated via low temperature direct writing," *Electrochim. Acta*, vol. 314, pp. 81–88, 2019, doi: https://doi.org/10.1016/j.electacta.2019.05.082.

[300] R. R. Kohlmeyer *et al.*, "Composite batteries: a simple yet universal approach to 3D printable lithium-ion battery electrodes," *J. Mater. Chem. A*, vol. 4, no. 43, pp. 16856–16864, 2016, doi: 10.1039/C6TA07610F.

[301] Y. Liu *et al.*, "3D printed separator for the thermal management of high-performance Li metal anodes," *Energy Storage Mater.*, vol. 12, pp. 197–203, 2018, doi: https://doi.org/10.1016/j.ensm.2017.12.019.

[302] D. W. McOwen *et al.*, "3D-Printing Electrolytes for Solid-State Batteries," *Adv. Mater.*, vol. 30, no. 18, p. 1707132, May 2018, doi: https://doi.org/10.1002/adma.201707132.

[303] C. Chen *et al.*, "3D Printed Lithium-Metal Full Batteries Based on a High-Performance Three-Dimensional Anode Current Collector," *ACS Appl. Mater. Interfaces*, 2021, doi: 10.1021/acsami.1c03997.

[304] "Advanced Materials - 2018 - Wei - 3D Printing of Customized Li-Ion Batteries with Thick Electrodes.pdf."

[305] X. Wei *et al.*, "3D Printable Graphene Composite," *Sci. Rep.*, vol. 5, no. 1, p. 11181, 2015, doi: 10.1038/srep11181.

[306] C. W. Foster *et al.*, "3D Printed Graphene Based Energy Storage Devices," *Sci. Rep.*, vol. 7, no. October 2016, pp. 1–11, 2017, doi: 10.1038/srep42233.

[307] C. W. Foster, H. M. Elbardisy, M. P. Down, E. M. Keefe, G. C. Smith, and C. E. Banks, "Additively manufactured graphitic electrochemical sensing platforms," *Chem. Eng. J.*, vol. 381, p. 122343, 2020, doi: https://doi.org/10.1016/j.cej.2019.122343.

[308] D. Golodnitsky, E. Livshits, and E. Peled, "Highly conductive oriented PEO-based polymer electrolytes," *Macromol. Symp.*, vol. 203, no. 1, pp. 27–46, Oct. 2003, doi: https://doi.org/10.1002/masy.200351303.

[309] G. B. T.-H. of P. (Second E. Wypych, Ed., "10 - EFFECT OF PLASTICIZERS ON PROPERTIES OF PLASTICIZED MATERIALS," Boston: William Andrew Publishing, 2012, pp. 209–306. doi: https://doi.org/10.1016/B978-1-895198-50-8.50012-6.

[310] X. Hu *et al.*, "3D-Printed Thermoplastic Polyurethane Electrodes for Customizable, Flexible Lithium-Ion Batteries with an Ultra-Long Lifetime," *Small*, vol. 19, no. 34, p. 2301604, Aug. 2023, doi: https://doi.org/10.1002/smll.202301604.

[311] S. Tagliaferri, A. Panagiotopoulos, and C. Mattevi, "Direct ink writing of energy materials," *Mater. Adv.*, vol. 2, no. 2, pp. 540–563, 2021, doi: 10.1039/D0MA00753F.

[312] K. Shen, H. Mei, B. Li, J. Ding, and S. Yang, "3D Printing Sulfur Copolymer-Graphene Architectures for Li-S Batteries," *Adv. Energy Mater.*, vol. 8, no. 4, p. 1701527, Feb. 2018, doi: https://doi.org/10.1002/aenm.201701527.

[313]   S. D. Lacey *et al.*, "Extrusion-Based 3D Printing of Hierarchically Porous Advanced Battery Electrodes," *Adv. Mater.*, vol. 30, no. 12, p. 1705651, Mar. 2018, doi: https://doi.org/10.1002/adma.201705651.

[314]   M. Idrees *et al.*, "3D printed PC/SiOC@Zn hybrid composite as dendrite-free anode for Zn-Ion battery," *Nano Energy*, vol. 100, p. 107505, 2022, doi: https://doi.org/10.1016/j.nanoen.2022.107505.

[315]   S. Naficy *et al.*, "Graphene oxide dispersions: tuning rheology to enable fabrication," *Mater. Horiz.*, vol. 1, no. 3, pp. 326–331, 2014, doi: 10.1039/C3MH00144J.

[316]   J. Perelaer, P. J. Smith, C. E. Hendriks, A. M. J. van den Berg, and U. S. Schubert, "The preferential deposition of silica micro-particles at the boundary of inkjet printed droplets," *Soft Matter*, vol. 4, no. 5, pp. 1072–1078, 2008, doi: 10.1039/B715076H.

[317]   D. Cao *et al.*, "3D Printed High-Performance Lithium Metal Microbatteries Enabled by Nanocellulose," *Adv. Mater.*, vol. 31, no. 14, p. 1807313, Apr. 2019, doi: https://doi.org/10.1002/adma.201807313.

[318]   S. R. Shin *et al.*, "A Bioactive Carbon Nanotube-Based Ink for Printing 2D and 3D Flexible Electronics," *Adv. Mater.*, vol. 28, no. 17, pp. 3280–3289, May 2016, doi: https://doi.org/10.1002/adma.201506420.

[319]   W. B. Hawley and J. Li, "Electrode manufacturing for lithium-ion batteries—Analysis of current and next generation processing," *J. Energy Storage*, vol. 25, p. 100862, 2019, doi: https://doi.org/10.1016/j.est.2019.100862.

[320]   L. Fransson, T. Eriksson, K. Edström, T. Gustafsson, and J. O. Thomas, "Influence of carbon black and binder on Li-ion batteries," *J. Power Sources*, vol. 101, no. 1, pp. 1–9, 2001, doi: https://doi.org/10.1016/S0378-7753(01)00481-5.

[321]   K. Fu, Y. Yao, J. Dai, and L. Hu, "Progress in 3D Printing of Carbon Materials for Energy-Related Applications," *Adv. Mater.*, vol. 29, no. 9, p. 1603486, Mar. 2017, doi: https://doi.org/10.1002/adma.201603486.

[322]   Y. Jo *et al.*, "3D-printable{,} highly conductive hybrid composites employing chemically-reinforced{,} complex dimensional fillers and thermoplastic triblock copolymers," *Nanoscale*, vol. 9, no. 16, pp. 5072–5084, 2017, doi: 10.1039/C6NR09610G.

[323]   Z. Jiang, B. Diggle, M. L. Tan, J. Viktorova, C. W. Bennett, and L. A. Connal, "Extrusion 3D Printing of Polymeric Materials with Advanced Properties," *Adv. Sci.*, vol. 7, no. 17, pp. 1–32, 2020, doi: 10.1002/advs.202001379.

[324]   A. Vinegrad *et al.*, "Plasticized 3D-Printed Polymer Electrolytes for Lithium-Ion Batteries," *J. Electrochem. Soc.*, vol. 168, no. 11, p. 110549, 2021, doi: 10.1149/1945-7111/ac39d5.

[325]   K. Gnanasekaran *et al.*, "3D printing of CNT- and graphene-based conductive polymer nanocomposites by fused deposition modeling," *Appl. Mater. Today*, vol. 9, pp. 21–28, 2017, doi: 10.1016/j.apmt.2017.04.003.

[326]   L. Airoldi, U. Anselmi-Tamburini, B. Vigani, S. Rossi, P. Mustarelli, and E. Quartarone, "Additive Manufacturing of Aqueous-Processed LiMn2O4 Thick Electrodes for High-Energy-Density Lithium-Ion Batteries," *Batter. Supercaps*, vol. 3, no. 10, pp. 1040–1050, Oct. 2020, doi: https://doi.org/10.1002/batt.202000058.

[327]   N. Verdier, G. Foran, D. Lepage, A. Prébé, D. Aymé-Perrot, and M. Dollé, "Challenges in solvent-free methods for manufacturing electrodes and electrolytes for lithium-based batteries," *Polymers (Basel).*, vol. 13, no. 3, pp. 1–26, 2021, doi: 10.3390/polym13030323.

[328]   N. E. Zander, M. Gillan, and R. H. Lambeth, "Recycled polyethylene terephthalate as a new FFF feedstock material," *Addit. Manuf.*, vol. 21, no. March, pp. 174–182, 2018, doi: 10.1016/j.addma.2018.03.007.

[329]   V. Gupta, F. Alam, P. Verma, A. M. Kannan, and S. Kumar, "Additive manufacturing enabled, microarchitected,

hierarchically porous polylactic-acid/lithium iron phosphate/carbon nanotube nanocomposite electrodes for high performance Li-Ion batteries," *J. Power Sources*, vol. 494, p. 229625, 2021, doi: https://doi.org/10.1016/j.jpowsour.2021.229625.

[330] S. Dul, L. Fambri, and A. Pegoretti, "Fused deposition modelling with ABS-graphene nanocomposites," *Compos. Part A Appl. Sci. Manuf.*, vol. 85, pp. 181–191, 2016, doi: 10.1016/j.compositesa.2016.03.013.

[331] T. Cersoli, A. Cresanto, C. Herberger, E. MacDonald, and P. Cortes, "3D Printed Shape Memory Polymers Produced via Direct Pellet Extrusion," *Micromachines*, vol. 12, no. 1. 2021. doi: 10.3390/mi12010087.

[332] A. La Gala, D. V. A. Ceretti, R. Fiorio, L. Cardon, and D. R. D'hooge, "Comparing pellet- and filament-based additive manufacturing with conventional processing for ABS and PLA parts," *J. Appl. Polym. Sci.*, vol. 139, no. 44, p. e53089, Nov. 2022, doi: https://doi.org/10.1002/app.53089.

[333] Z. Zhou, I. Salaoru, P. Morris, and G. J. Gibbons, "Additive manufacturing of heat-sensitive polymer melt using a pellet-fed material extrusion," *Addit. Manuf.*, vol. 24, pp. 552–559, 2018, doi: https://doi.org/10.1016/j.addma.2018.10.040.

[334] L. B. Silva, R. O. de Oliveira, G. F. Barbosa, S. B. Shiki, and K. Fu, "Influence of the single-screw extruder nozzle diameter on pellet-based filaments for additive manufacturing," *J. Brazilian Soc. Mech. Sci. Eng.*, vol. 44, no. 7, pp. 1–11, 2022, doi: 10.1007/s40430-022-03590-z.

[335] S. Singamneni, D. Smith, M.-J. LeGuen, and D. Truong, "Extrusion 3D Printing of Polybutyrate-Adipate-Terephthalate-Polymer Composites in the Pellet Form," *Polymers*, vol. 10, no. 8. 2018. doi: 10.3390/polym10080922.

[336] N. Sayah and D. E. Smith, "Effect of Process Parameters on Void Distribution, Volume Fraction, and Sphericity within the Bead Microstructure of Large-Area Additive Manufacturing Polymer Composites," *Polymers*, vol. 14, no. 23. 2022. doi: 10.3390/polym14235107.

[337] J. Hu *et al.*, "3D-Printed Cathodes of LiMn1−FePO4 Nanocrystals Achieve Both Ultrahigh Rate and High Capacity for Advanced Lithium-Ion Battery," *Adv. Energy Mater.*, vol. 6, no. 18, p. 1600856, Sep. 2016, doi: https://doi.org/10.1002/aenm.201600856.

[338] T. Nathan-Walleser *et al.*, "3D Micro-Extrusion of Graphene-based Active Electrodes: Towards High-Rate AC Line Filtering Performance Electrochemical Capacitors," *Adv. Funct. Mater.*, vol. 24, no. 29, pp. 4706–4716, Aug. 2014, doi: https://doi.org/10.1002/adfm.201304151.

[339] A. Sarmah *et al.*, "Additive manufacturing of nanotube-loaded thermosets via direct ink writing and radio-frequency heating and curing," *Carbon N. Y.*, vol. 200, pp. 307–316, 2022, doi: https://doi.org/10.1016/j.carbon.2022.08.063.

[340] J. A. Lewis, "Direct Ink Writing of 3D Functional Materials," *Adv. Funct. Mater.*, vol. 16, no. 17, pp. 2193–2204, Nov. 2006, doi: https://doi.org/10.1002/adfm.200600434.

[341] J. Wang *et al.*, "Toward High Areal Energy and Power Density Electrode for Li-Ion Batteries via Optimized 3D Printing Approach," *ACS Appl. Mater. Interfaces*, vol. 10, no. 46, pp. 39794–39801, Nov. 2018, doi: 10.1021/acsami.8b14797.

[342] F. Tricot *et al.*, "Fabrication of 3D conductive circuits: print quality evaluation of a direct ink writing process," *RSC Adv.*, vol. 8, no. 46, pp. 26036–26046, 2018, doi: 10.1039/C8RA03380C.

[343] E. Vaněčková *et al.*, "3D printed polylactic acid/carbon black electrodes with nearly ideal electrochemical behaviour," *J. Electroanal. Chem.*, vol. 857, p. 113745, 2020, doi: 10.1016/j.jelechem.2019.113745.

[344] D. Vernardou, K. C. Vasilopoulos, and G. Kenanakis, "3D printed graphene-based electrodes with high

electrochemical performance," *Appl. Phys. A Mater. Sci. Process.*, vol. 123, no. 10, pp. 1–7, 2017, doi: 10.1007/s00339-017-1238-1.

[345] R. Paz, R. Moriche, M. Monzón, and J. García, "Influence of manufacturing parameters and post processing on the electrical conductivity of extrusion-based 3D printed nanocomposite parts," *Polymers (Basel).*, vol. 12, no. 4, pp. 1–16, 2020, doi: 10.3390/POLYM12040733.

[346] J. J. Moyano, A. Gómez-Gómez, D. Pérez-Coll, M. Belmonte, P. Miranzo, and M. I. Osendi, "Filament printing of graphene-based inks into self-supported 3D architectures," *Carbon N. Y.*, vol. 151, pp. 94–102, 2019, doi: https://doi.org/10.1016/j.carbon.2019.05.059.